Nanoscale mechanics of collagen in articular cartilage

Sheetal Rajendra Inamdar

Institute of Bioengineering

School of Engineering and Material Science

Queen Mary University of London

A thesis submitted in fulfillment of the requirements for the degree of Doctor of Philosophy, University of London

I, Sheetal Rajendra Inamdar, confirm that the research included within this thesis is my own work or that where it has been carried out in collaboration with, or supported by others, that this is duly acknowledged below and my contribution indicated. Previously published material is also acknowledged below.

I attest that I have exercised reasonable care to ensure that the work is original, and does not to the best of my knowledge break any UK law, infringe any third party's copyright or other Intellectual Property Right, or contain any confidential material.

I accept that the College has the right to use plagiarism detection software to check the electronic version of the thesis.

I confirm that this thesis has not been previously submitted for the award of a degree by this or any other university.

Signature:

Date:

Details of collaboration and publications:

- Inamdar, S. R. *et al.* The Secret Life of Collagen : Temporal Changes in Nanoscale Fibrillar Pre-Strain and Molecular Cartilage. (2017). doi:10.1021/acsnano.7b00563

Abstract

Articular cartilage is a mechanically important soft tissue whose organisation at the micro- and nanoscale is critical for healthy joint function and where degeneration is associated with widespread disorders such as osteoarthritis. The tissue possesses a complex, graded and depth-dependent structure and at the nanoscale, cartilage mechanical functionality is dependent on the collagen and hydrated proteoglycans that form the extracellular matrix. The structure and *in situ* dynamic response of the collagen fibrils at the nanoscale, however, remain unclear. Here we utilise small angle X-ray diffraction to measure the depth-wise structure of the fibrillar architecture whilst performing time-resolved measurements during compression of bovine and human cartilage explants. We demonstrate the existence of a depth-dependent fibrillar pre-strain as determined by the D-periodicity, estimated at approximately 1-2%, due to osmotic swelling pressure from the proteoglycans. Furthermore, we reveal a rapid reduction and recovery of this pre-strain during stress relaxation, approximately 60 seconds after onset of peak load. Selective proteoglycan removal disrupts both collagen fibril pre-strain and transient responses during stress relaxation. Additionally, we show that IL-1β induced tissue inflammation also results in a reduction in fibrillar pre-strain and altered fibrillar mechanics. Cyclic loading induces a dynamic reduction and recovery in the D-period that is present regardless of loading rate or treatment, along with changes in diffraction peak intensities and widths. These findings suggest that the fibrils respond to loading via *intra*- and *inter*-fibrillar disordering alongside a transient response that is mediated by changes in hydration. These are the first studies to highlight previously unknown transient and cyclic responses to loading at the fibrillar level, and are likely to transform our understanding of the role of collagen fibril nano-mechanics in cartilage and other hydrated soft tissues. These methods can now be used to better understand cartilage in aging and other muscoskeletal diseases.

Acknowledgements

Firstly, I would like to thank my supervisors Dr. Himadri Gupta and Prof. Martin Knight, both of whom have provided precious guidance throughout the duration of my PhD. Dr. Gupta, you have worked tirelessly beside me not only in developing my knowledge and skills, but also in providing unlimited support and enthusiasm in every element of this project. Prof. Knight, you have been my supervisor throughout my academic conquests over the past 8 years at Queen Mary, through your continued support and faith in my abilities, you have mentored me into becoming a more confident scientist. I am eternally grateful to you both.

To my parents (Kashmira and Arpan Brahmbhatt), your unconditional love and support is something that can never be matched. From a very young age you have always reminded me to work hard in order to achieve my goals and as a result of your tenacious guidance I have made it this far. I owe you everything.

Finally, to my Husband (Sunny) who has been endlessly by my side through all of my academic adventures and is the most selfless and compassionate person I will ever meet. This would be meaningless without you.

I dedicate this thesis to my loving parents and my wonderful husband, without whom none of my success would be possible.

This work was supported by The Engineering and Physical Sciences Research Council (EPSRC).

Publications, Presentations and Prizes

Publications

Inamdar, S. R., Knight, D. P., Terrill, N. J., Karunaratne, A., Cacho-Nerin, F., Knight, M. M., Gupta, H. S., *The Secret Life of Collagen : Temporal Changes in Nanoscale Fibrillar Pre-Strain and Molecular Cartilage.* (2017). doi:10.1021/acsnano.7b00563

Presentations

- Poster presentation: Inamdar, S.R., et al, *Depth-dependent Fibrillar Pre-strain Found in Bovine Articular Cartilage Collagen*. Presented at Diamond Light Source user meeting, September 2015.
- Poster Presentation: Inamdar, S .R., et al, *Depth-dependent Fibrillar Pre-strain Found in Bovine Articular Cartilage Collagen*. Presented at Queen Mary University of London, Institute of Bioengineering Launch Event, October 2015.
- Oral presentation: Inamdar, S. R., et al, *Depth-dependent Fibrillar Pre-strain Found in Bovine Articular Cartilage Collagen (I22)*. Presented at Diamond Light Source seminar series, March 2016.
- Poster presentation: Inamdar, S. R., et al, *Fibrillar nanomechanics of cartilage collagen and changes associated with compositional degradation.* Presented at the World Congress of Biomaterials (Montreal, Canada), April 2016.

Prizes

- Best poster – 3rd Prize for poster presented at QMUL, IoB Launch, October 2015.
- Merit award – One of the 42 top scoring abstracts out of 3500 submitted for the World Congress of Biomaterials (Montreal, Canada), April 2016.

List of Abbreviations

AFM	Atomic force microscopy
BL	Beam line
BSA	Bovine serum albumin
DLS	Diamond light source
DMEM	Dulbecco's Modified Eagles Medium
DMMB	1,9-dimethylmethylene blue
DZ	Deep zone
ECM	Extracellular matrix
EPICS	Experimental physics and industrial control system
ESRF	European synchrotron radiation facility
FCS	Fetal calf serum
FRPVE	Fibril-reinforced poroviscoelastic
GAG	Glycosaminoglycan
GDA	Generic data acquisition
HA	Hyaluronan
IGF	Insulin-like growth factor
IL-1β	Inter-leukin -1 beta
IMS	Industrial methylated spirit
IR	Infrared
LINAC	Linear accelerator
LP	Link protein
MC	Mineralised cartilage
MMPs	Matrix metalloproteinases
OA	Osteoarthritis
PBS	Phosphate buffered saline

PG	Proteoglycan
SAXD	Small angle X-ray diffraction
SAXS	Small angle X-ray scattering
SB	Subchondral bone
SEM	Standard error of mean
SZ	Superficial zone
TGF	Transforming growth factor
TNF	Tumor necrosis factor
TTL	Transistor-Transistor Logic
TZ	Transitional zone
WAXD	Wide angle X-ray diffraction

Table of Contents

Table of Figures

Table of Equations

Chapter 1

Structure and function of articular cartilage

1. Structure and function of articular cartilage

Cartilage is a specialised connective tissue present within the human body. The tissue can be subdivided into elastic, fibro-cartilage, fibro-elastic and hyaline cartilage based on variations in the composition of the extracellular matrix. This thesis investigates hyaline cartilage, more specifically articular cartilage, which is an avascular, aneural and alymphatic tissue that lines the articulating surfaces of synovial joints. The tissue functions as a low-friction bearing surface, which reduces the stress to the underlying bone by deforming during physiological loading thereby increasing the contact area [1,2]. With its ability to withstand high and varying load levels over years of constant use, the wear-resistant surface is vital for providing safe load support and transfer within the joint. Articular cartilage is composed of an abundant extracellular matrix with a relatively sparse population of cells called chondrocytes which make up less than 10% of the tissue volume. The biomechanical properties of cartilage are governed by the composition and structure of the extracellular matrix[3]. The heterogeneous tissue exhibits a depth-dependent variation in composition and structure, which leads to nonlinear and anisotropic properties during physiological compressive loading[2].

1.1. Structural components of articular cartilage

1.1.1. Type II collagen

A major component in all connective tissue, collagen is found to be the most abundant structural protein in mammals[4]. Collagen fibrils are cylindrical structures that play a crucial role in providing such tissues with a vast range of tensile properties as well as performing a structural role at multiple length scales. Collagen also has the ability to interact with other materials such as proteoglycans, minerals and elastic fibers, which in turn allows complex structures to form[5]. There is a variety in collagen type as well as both

homotypic and heterotypic fibrils found in most tissues. The differences in the intramolecular packing as well as interfibrillar interactions dictate the mechanical properties of the fibrils as well as determining collagen type[6].

In articular cartilage the predominant form of collagen is type II and is almost exclusive to this tissue; however there are also other minor collagens and non-collagenous glycoproteins present, including collagen IX and XI. There secondary collagens are thought to have specific functions in the regulation of the collagen II phase[7], whilst modulating fibril diameter, surface properties, and interfibrillar interactions[5]. Collagen XI is thought to regulate fibrillogenesis via fibril initiation and limiting fibril diameter and is located in the core of the collagen II fibrils[5]. Collagen IX is thought to be involved with crosslinking the collagen network, and is located on the surface of the collagen II fibrils[5,7].

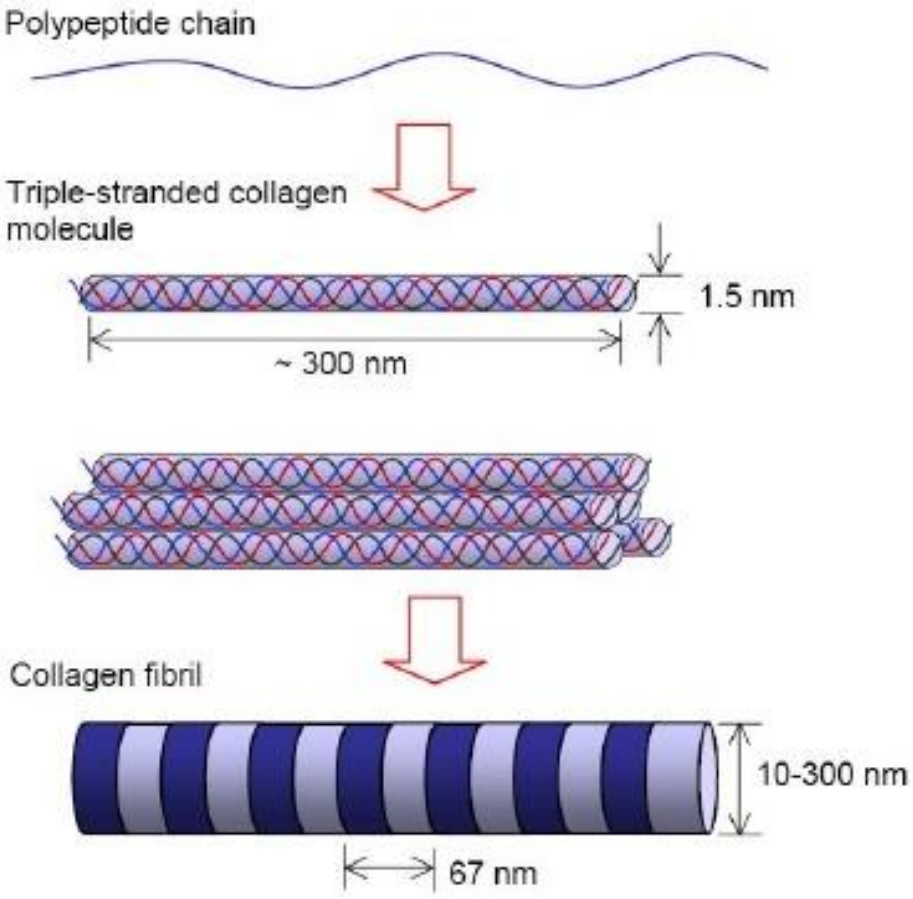

Figure 1.1: Schematic of collagen fibril structure at the ultrastructural level, from the polypeptide chains that form the tropocollagen molecules to the fibrillar structure with the associated 67nm periodicity from the underlying overlap and gap regions represented [8].

Formed of three polypeptide chains, collagen molecules are in general right-handed triple helices that contain characteristically the repeating peptide sequence glycine-X-Y, where X and Y represent mainly proline or hydroxyproline. The glycine residues are found facing towards the interior of the protein core whilst the remaining amino acids are outward facing. Found most commonly as cylindrical fibrillar structures with radii of 10-300 nm, the collagen network can be distinguished by the axial periodicity of 65-67nm (depending on hydration and tissue type) as shown by Figure 1.1, as a result of the molecular packing. This periodicity, from here referred to as the Density (D)-period, is as a result of collagen molecules forming a staggered array axially leading to zones

denoted as gap and overlap regions. The interactions that occur between molecules are directed by electrostatic and hydrophobic regions which provide optimal contact, thus leading to the D stagger that can be observed. Alongside these interactions, the fibrils are further stabilised by the intermolecular cross-links that are also mediated by collagen type IX[5,9,10].

1.1.2. Proteoglycans

There are a variety of proteoglycans found in cartilage and play a crucial role in the normal function of the tissue. The key proteins present are aggrecan, decorin, biglycan, fibromodulin and lumican, each with structural differences in terms of their core proteins and glycosaminoglycan (GAG) chains. Aggrecan is the most abundant of these macromolecules found in cartilage[11]. Aggrecan is found as aggregates bound to a single chain of hyaluronan (HA) via link protein (LP)[12] as shown by Figure 1.2a.

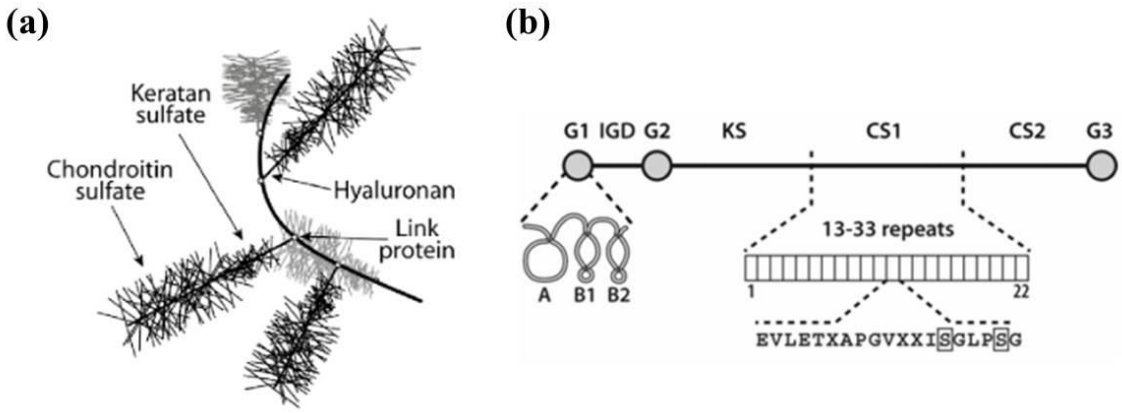

Figure 1.2: The subcomponents and structure of aggrecan (a) Aggrecan molecules are comprised of a hyaluronan molecule with an associated core protein, stabilised by a link protein, to which there are branches of keratin and chondroitin sulphate attached forming a bottle brush-like structure [12] (b) The protein core of the GAG chains where there are structural domains G1-G3 which are required for the bond formation between the polysaccharides and the link protein[12].

The glycosaminoglycan side chains are made up of the dominant polysaccharides, chondroitin and keratin sulphate in fully developed cartilage[12] and more than 100 chains

can be found in individual aggrecan molecules[13]. Within each GAG chain there are structural domains including the G1-G3 which contain cysteine residues that are required for bond formation[11] (Figure 1.2b). The GAG chains are responsible for giving the PGs a negative charge due to the presence of carboxyl and sulphate groups resulting in a fixed charge density within the tissue. This is the factor that causes water flow into the tissue and resultant swelling pressure, and the importance of this will be later discussed.

1.1.3. Chondrocytes

Unlike most other tissues in the human body, the cell population in cartilage is sparse[12]. Originating from mesenchymal stem cells, these highly specialised cells regulate matrix metabolism by synthesizing the components such as type II collagen, proteoglycan aggregates and non-collagenous proteins, whilst also removing them[1,14]. The cells only occupy around 2-10% of the tissue volume; however are highly sensitive to their surrounding environment. The structure, size and shape vary dependent on the position within the tissue with the highest density of cells found at the superficial zone (Figure 1.3). The chondrocytes are encapsulated within a local microenvironment and do not migrate around the tissue. Within this microenvironment, the cells have the capacity to interpret signals through mechanotransduction[13] – an important factor given the mechanical role of the tissue.

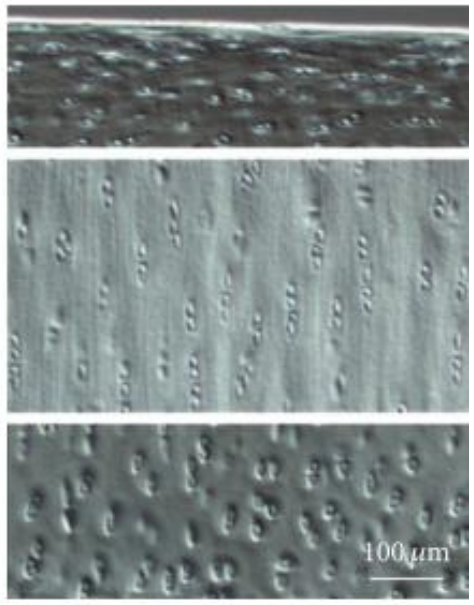

Figure 1.3: Light microscopy images showing the shape and distribution of chondrocytes throughout full thickness cartilage. It can be observed that the cells form an ellipsoid-like shape which are orientated in the direction of the fibrillar structure i.e. parallel to the surface in the superficial zone and both perpendicular and columnar in the deep zone [15].

1.1.4. Hierarchical composition of articular cartilage

The components of the cartilage extracellular matrix contribute to the tissue's structure and biomechanics[13]. Throughout the full-thickness of the tissues, these key elements vary in content and distribution. The microstructure of cartilage is shown schematically in Figure 1.4, in which the left side of the schematic represents the collagen leaves that are in the plane parallel to the axis of split line. The split line is as a result of preferential orientation of the collagen fibrils along the surface of the tissue, which reflect the orientation of stress lines which are found in this optimal configuration to resist tensile forces[16].

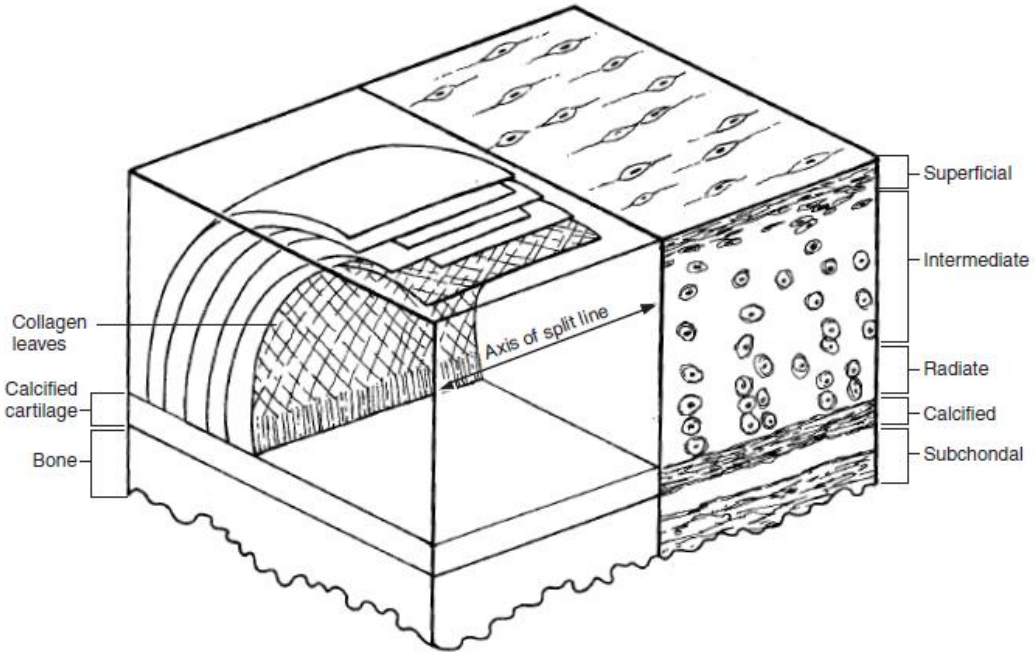

Figure 1.4: Schematic of a transverse cut through full thickness cartilage on two mutually orthogonal planes. It has been previously suggested that the collagen fibrils are found in a leaf like structure, with an orientation parallel to the surface in the superficial zone, random orientation in the transitional zone and perpendicular to the surface in the deep zone prior to a fusion of fibrils into the calcified region.[14]

The orientation and distribution of the collagen fibrils (10-20% of wet weight) in these leaves vary across the full thickness of cartilage. In the superficial zone the fibrils are found to lay parallel to the articulating surface, while further down in the transitional/medial zone the fibrils are less well orientated and more sparsely distributed. Finally in the deep/radial zone the fibrils (where they connect to the subchondral bone) are found to orient perpendicular to the articulating surface, in tightly packed bundles[1]. There is also a variation in collagen content in relation to the thickness of the tissue, such that the highest volume of fibrils can be found in the superficial and deep zones[17,18].

Entrapped within the network of collagen fibrils reside the proteoglycans[19]. The proteoglycans that are found in cartilage constitute 10-20% of the wet weight. These protein structures are responsible for drawing water into the tissue (which makes up 65-

80% of the wet weight). Previous studies have also shown that there is a depth-dependent concentration of proteoglycan such that the highest concentration can be found within the deep zone[17,18]. This compositional variation has direct influence on the depth-dependent water content and contributes widely to the tissues nonlinear behaviour.

Alongside the fibrils and proteoglycans exist the chondrocytes, whose distribution and phenotypic features also vary throughout the thickness of the tissue as. Towards the superficial zone, the cells are flattened and elliptical with an orientation parallel to the joint surface, in the medial region these cells are predominantly spherical with a lower cell density (number of cells), and finally in the radial zone the cells are arranged in columns perpendicular to the surface[1,14].

1.2. Articular cartilage degradation in disease

1.2.1. Etiology of osteoarthritis

Cartilage has poor ability to regenerate given its aneural, avascular and alymphatic features. As a result, when there is a mechanical instability or musculoskeletal disorder leading to osteoarthritis (OA), there is a cascade of catabolic events which result in clinical characteristics such as inflammation of the joint, varying degrees of joint pain, stiffness, deformity and overall loss of tissue function[20]. OA affects the entire synovial joint, and the residing chondrocytes are independently responsible for their response to injury which leads to the long term degeneration of the tissue due to an imbalance of anabolic and catabolic activities of the cells[21]. OA and the degradation associated with the disease lead to dysfunction at multiple length scales and contribute to changes in both structural and mechanical function of the tissue[22]. Furthermore, the prevalence of this disease increases significantly with age, and with an ever growing/aging population, it is

important to fully characterise the mechanisms behind the disease and decipher the links between structure and mechanical function of the tissue[23].

1.2.2. Structural and compositional changes in OA

The onset of OA and progressive degradation can be split into two phases; the biosynthetic phase and the degradative phase. The first refers to the attempt to repair the ECM made by the chondrocytes and the second refers to the digestion of the ECM and matrix synthesis inhibition by the enzyme activity produced by the cells[21]. The imbalance of these two processes ultimately lead to degeneration of the tissue as a whole, resulting in changes in tissue composition in a depth-wise manner.

1.2.3. Cellular response

In healthy cartilage, the chondrocytes are involved in a relatively slow balance of matrix synthesis and degradation leading to a stringent matrix turnover. However, in diseases such as OA, this balance is perturbed leading to an upregulation of both processes and furthermore an imbalance in matrix turnover[21]. There are both genetic and biochemical factors alongside changes to the mechanical stresses within that tissue that are believed to play a role in the disruption of chondrocyte-matrix associations that leads to the altered metabolic response[24] (Figure 1.5).

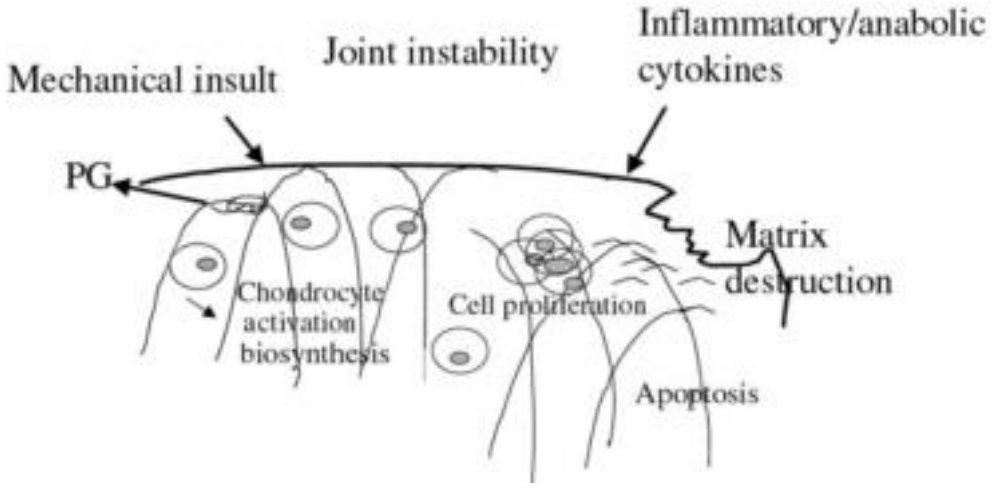

Figure 1.5: The response of chondrocytes to external injury in cartilage following a mechanical insult. Matrix activation via joint instability leads to an imbalance in anabolic and catabolic activity, which in the longer term leads to matrix destruction[21].

Whilst anabolic cytokines such as insulin-like growth factor 1 (IGF-1) and transforming growth factor (TGF)-β are continuously produced resulting in enhanced synthesis of the ECM components, an upregulation of inflammatory cytokines such as inter-leukin 1 (IL-1) and tumor necrosis factor (TNF)-α is also produced by the cells (Figure 1.6). This leads to an increased synthesis of matrix metalloproteinases (MMPs) which are degradative enzymes that cause destruction of the matrix components and further causing a metabolic imbalance. There is also a decrease in measured MMP enzyme inhibitors, resulting in an overall reduction in matrix synthesis[21].

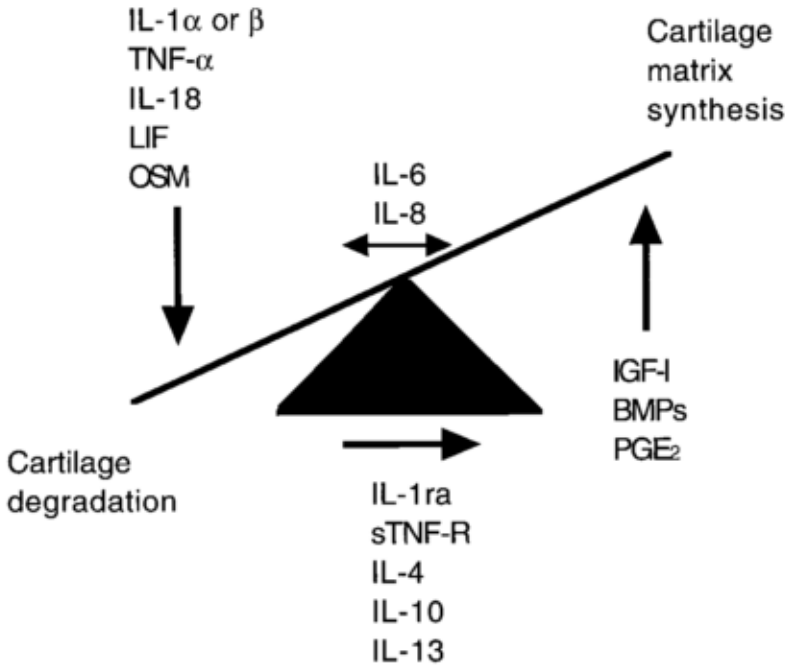

Figure 1.6: The imbalance of cartilage degradation versus matrix synthesis is accompanied and driven by changes to the relative amount of both catabolic and inhibitory cytokines that are produced by the cells.

1.2.4. Compositional changes

In OA what can be observed at the macroscopic scale is chondromalacia (softening of the tissue), fibrillation of the collagen and areas of lesions and ulceration. Furthermore, there are obvious areas of total loss of tissue layers – particularly the superficial zone which is usually the first region to be implicated by the onset of OA as can be seen in Figure 1.7 [20].

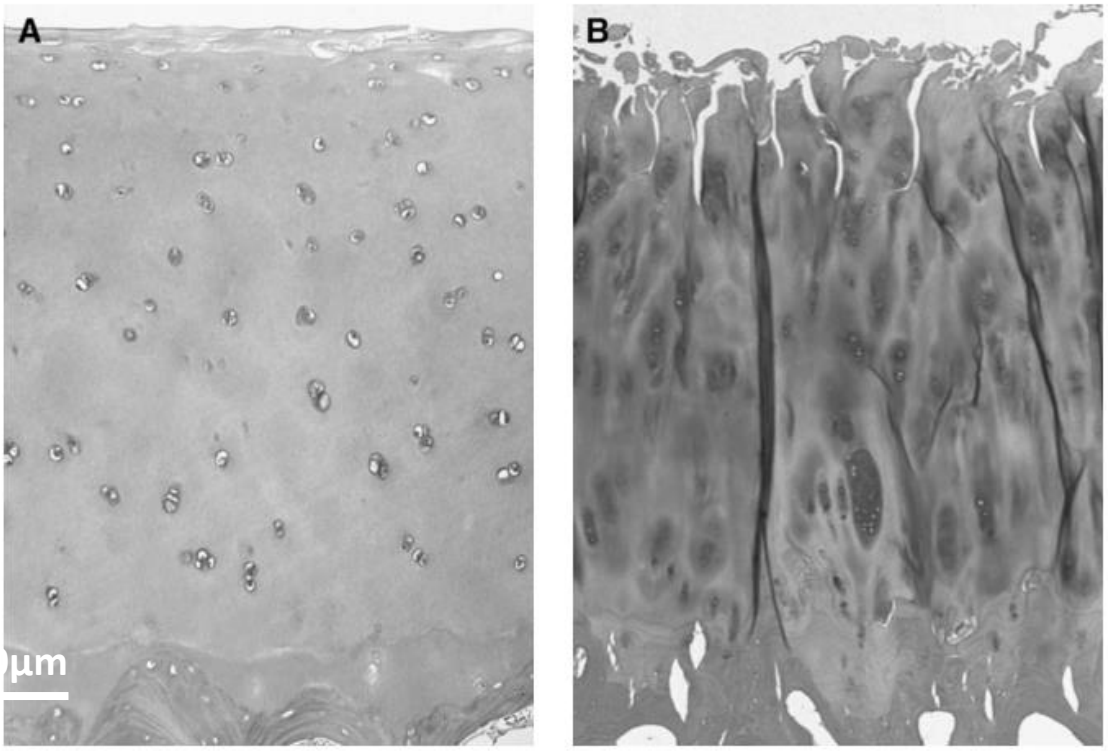

Figure 1.7: Light microscope section of full thickness cartilage in (a) healthy adult and (b) early OA, where a disruption in the structure of the tissue can be observed, as indicated by the fissuring of the superficial zone and collapse in structure through to the deep zone. [20]

Further indications that OA is present within a joint is the increase in cartilage hydration, narrowing of the joint space, changes to the subchondral bone structure and osteophyte formation[22]. The biochemical changes found in OA have been extensively investigated and the loss of normal tissue function have been directly linked to the loss of normal composition i.e. proteoglycan content[20]. In terms of the proteoglycan content, the proteolytic degradation prevents the formations of the regular macromolecular structure and results in shorter chain length of the molecules. This leads to a higher proportion of proteoglycans existing in a non-aggregated form, the matrix then becomes more permeable thus reducing the localised hydrostatic pressure causing the subsequent chondromalacia found in OA[20].

Alongside the progressive loss of PG with depth from the superficial zone, this trend is also found in terms of the collagen[25]. Although there is some loss of collagen associated with OA, the main feature is the changes in collagen organization[20]. Changes to the 3D architecture of the different zones lead to alterations in tissues ability to withstand compression. These involve changes to the orientation of the fibrils, density of collagen fibrils and type or amount of collagen cross-linking[22]. Studies have shown that throughout disease progression there is a disorganisation and disruption of the fibrils in terms of the direction and degree of orientation, this however is also depth dependent[26]. In a study by Moger *et al*. (2007), the predominant orientation of the fibrils in the deep/radial through to the subchondral bone was reoriented through the progression of OA within a lesion. Furthermore, the study found that in severe cases there was thickening of the transitional zone which may rise from the disorganisation of the top region within the radial zone, further implicating the depth dependent relationship the tissue possesses. The collagen content seems to only be dramatically reduced in the advanced stages of OA[27]. However, there is an age related modification of the collagen fibrils such that there is an accumulation of non-enzymatic glycation end products which result in stiffening of the collagen fibrils[28]. Changes to the localised mechanics of the fibrils in turn affect the chondrocytes, which are mechanosensitive to their local environment, contributing further to the metabolic imbalance[25]. Furthermore, it is known that the tissue has a higher ability to imbibe water in OA which would be suggestive that the collagen network no longer has the ability to restrain swelling as it would in a healthy state[22].

1.3. Introduction to cartilage mechanics

1.3.1. Macroscale mechanical properties

There have been various studies that have shown the knee joint in particular can experience around 3.5 times total bodyweight, and forces between 0-10 times body weight during joint articulation at the joint surface, with a experimentally measured modulus of around 10 MPa[12,29,30]. The mechanical properties of cartilage are very specific to the tissue's function and are widely different to other tissues within the body. Most importantly, the modulus of bone is in the range of 2-20 GPa depending on bone type[30,31] as shown in Figure 1.8, which is significantly higher than that of cartilage. Without the presence of cartilage, the articulation of bone to bone contact would cause high contact stresses given the higher modulus. Therefore, it is essential that cartilage mediates the stress between the two bones within a joint and this is achieved through the gradient in modulus.

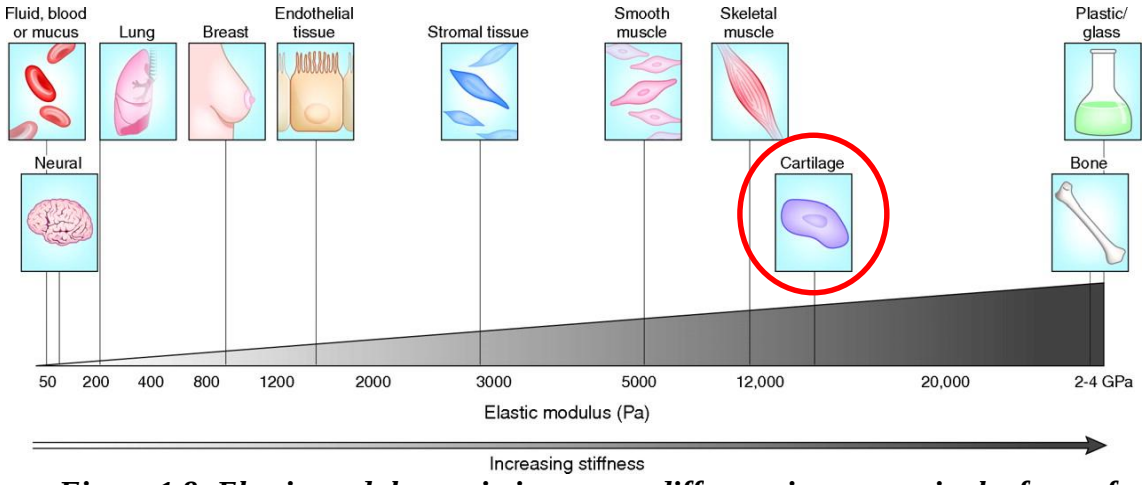

Figure 1.8: Elastic modulus variation across different tissue types in the form of elastic modulus measured in Pascals, highlighting the stiffness gradient between cartilage and bone[32].

The mechanical properties of cartilage have been extensively quantified previously at the macroscopic level, using a variety of techniques, such as confined and unconfined compression[2,33,34]. Cartilage experiences different types of mechanical stresses, but the primary type is compressive loading which varies along the thickness of the tissue. The measured Young's modulus varies between 5 to 25 MPa depending on the joint location and depth within the tissue[12] as indicated by Figure 1.9.

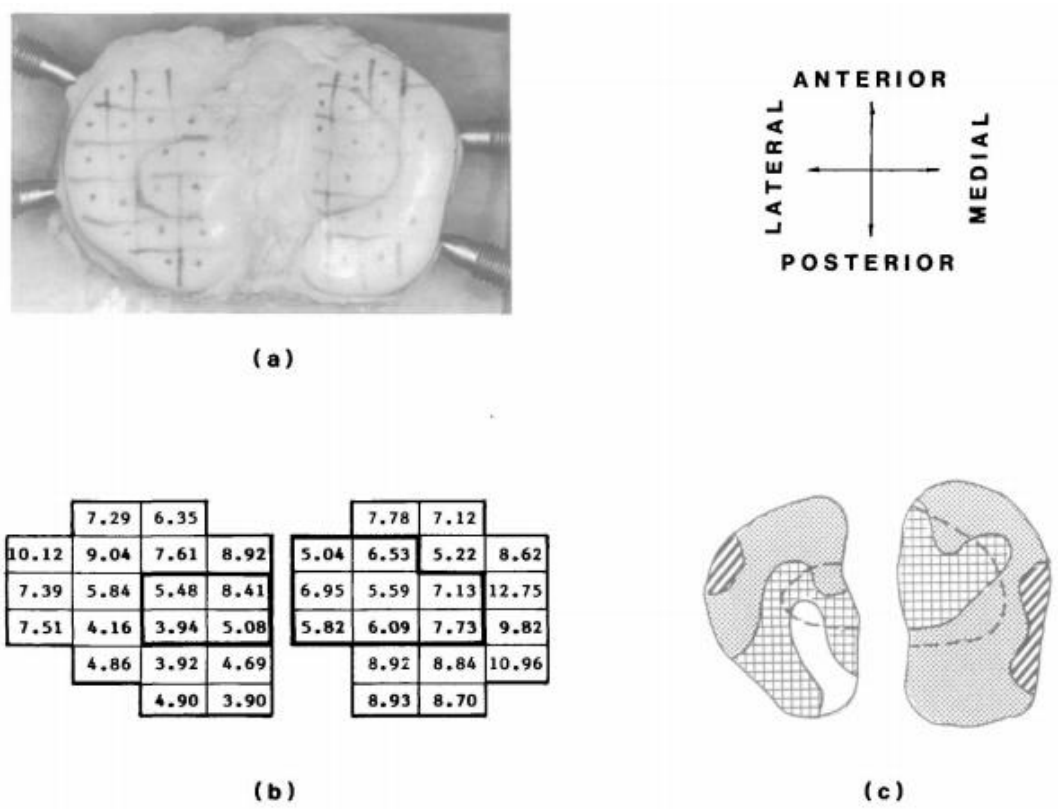

Figure 1.9: (a) Tibial surface (with orthogonal reference grid) split into regions of interest with the dots indicating indentation points, (b) 2 second creep modulus values for each region, (c) Contour map of stiffness determined from the creep modulus values[29].

A method of understanding the regional variation in tissue mechanics within a joint is shown above in Figure 1.9 where the 2 second creep modulus can vary from 40 to over 100Kg/cm^{2}and represents the local stiffness of the tissue on instantaneous compression[35]. At an equilibrium state the compressive aggregate modulus (H_A) ranges between 0.08 to

2 MPa[12], which is largely determined by the hydrostatic pressure formed by the PG's[3,14]. Tensile forces are also experienced by the tissue both on the surface during joint motion and during compression, in which the collagen fibrils stretch along the axis of loading. During normal rotational and translational movement in joints, pure shear stresses of the tissue occur where no compression of the tissue is observed. The associated shear modulus of cartilage can vary between 0.05 to 0.25 MPa[12].

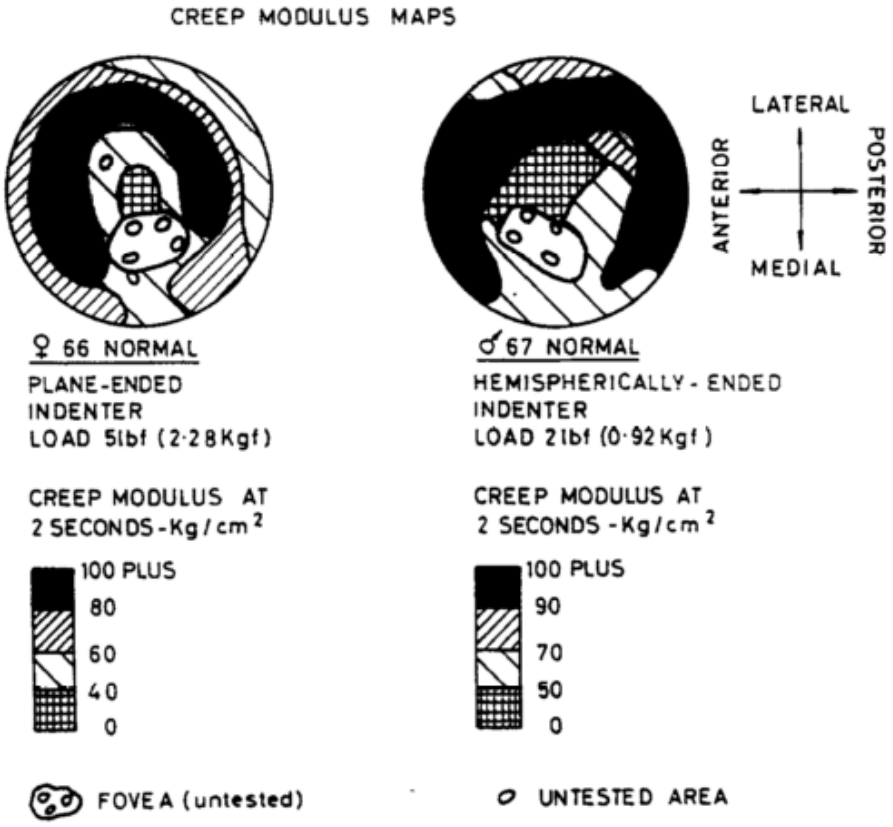

Figure 1.10: Maps of the 2 second creep modulus across the femoral heads from two human donors. The left map shows the stiffness of the tissue across the joint when measured using a plane-ended indenter whilst the right map resulted from a hemispherically-ended indenter. The shape of the indenter influences the measured creep modulus across the surface of the joint, however, the region of 100+ Kg/cm² creep modulus are found within a similar central region of the joint surface[35].

The mechanics of cartilage can be further investigated within different length scales as indicated by Figure 1.11. Given the complexity of the tissue structure, it is important to understand the levels of load sharing at different scales. The tissue's ability to withstand

high load levels is determined by the tissues ability to transmit and share the body level loads. At the joint level, the equilibrium is achieved by the active contraction forces generated by the muscles whilst opposing forces are held by the passive joint components such as ligaments alongside the cartilage[36] (Figure 1.11b). The tissue and micro-scale level is far more complex leading to an inhomogeneous and anisotropic time/depth-dependent strain profile which will now be further discussed.

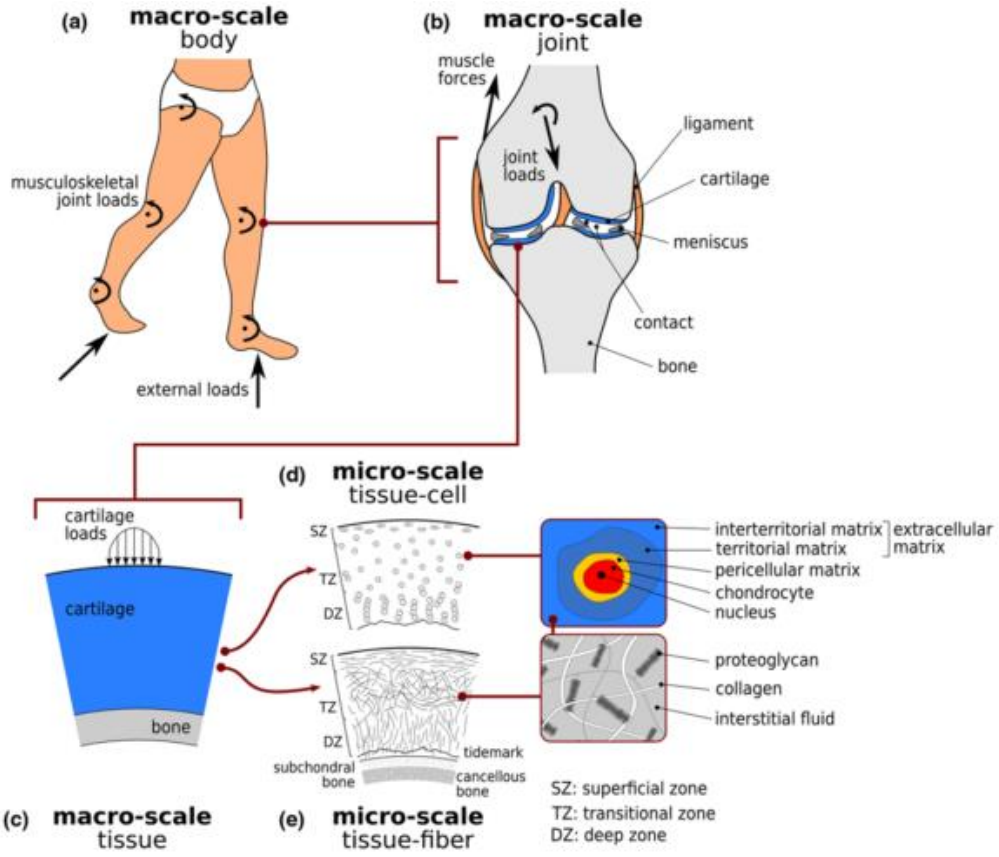

Figure 1.11: (a) Load generation found at body level, (b) schematic of joint structure with influence of structural components on joint forces, (c) macro-scale level structure including full thickness cartilage connected to bone surface, (d,e) micro-scale structure including the complex composition of the tissue with depth-dependent structure[36].

1.3.2. Mechanical changes in OA

There is a direct structure-function relationship in cartilage and the structural changes involved in OA lead to detrimental changes in the tissue mechanics. Furthermore, changes to the mechanics lead to further degradation of the tissue. Alteration to the regular

function of the tissue leads to impaired joint mobility which is as a result in the changes to the joint mechanics. As described previously there is a loss in the total volume of cartilage associated with OA which, in turn, reduces the capacity of the remaining tissue to withstand the large repetitive loading that is found in normal joint motion[37]. Many studies have found that OA results in a reduction in stiffness of the tissue, a study by Kleeman *et al.* (2005) found that this reduction was directly associated with progression of the disease with a loss of stiffness at around 25% with increasing degradation as measured by the ICRS grade (International Cartilage Repair Society system used to classify the level of osteoarthritic degradation). In normal healthy cartilage, under compression, the PG and interstitial water play a dominant role in the resultant compressive stiffness and flow-dependent transient behaviour[22]. The dramatic reduction in stiffness in OA can therefore be correlated with PG loss. Furthermore, given the close relationship and balance between the collagen network and PG, in OA the degradation and loss of the macromolecular structures are directly linked to the changes in the tissue mechanics.

When loaded under tensile conditions, the ECM deforms in response along the direction of loading, and the resistance is believed to be a measure of the intrinsic tensile properties of the collagen. However, in OA the tensile modulus of cartilage has been found to reduce to around 90% compared to healthy tissue. The reduced tensile stiffness is a direct product of the collagen network disruption found in OA and is the reduction is also directly correlated with age[22]. Studies have also found that under shear testing, OA tissue is more compliant, which may be as a result of the surface fibrillation[22].

1.3.3. Time dependent macroscale mechanical properties

Articular cartilage exhibits a time dependent behaviour in terms of macroscale tissue mechanics. This time dependent property is directly linked to the interactions of the structural elements of the ECM, and this behaviour has been largely quantified and modelled. Alongside this, cartilage does not deform in a homogenous manner and both the rate of compression and level of strain has an impact in the measured tissue response[38]. Furthermore, there is no constant proportionality factor between stress and strain due to the fact that the material response is sensitive to the rate at which it is loaded[39]. To demonstrate this compressive behaviour at the macroscale, standardised tests to measure the stress-relaxation and creep response have been conducted by many groups (Figure 1.12)[40].

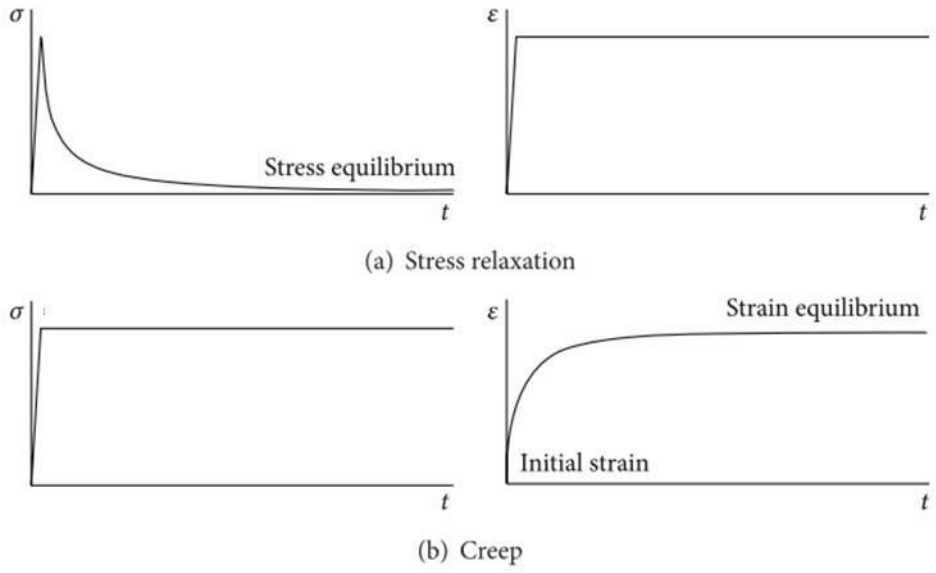

Figure 1.12: (a) stress-relaxation and (b) creep behaviour of cartilage under compression, where σ represents stress and ε represents strain and time t[40].

An early study by Mow et a. (1980) utilised confined creep compression tests to measure the tissue response, with the interpretation of cartilage as a biphasic material composed of a both a solid porous-permeable matrix phase (constituting ~20% of the total tissue

mass) and an interstitial fluid phase (~80% of the total tissue mass). This study quantified the creep behaviour through the movement of fluid in the tissue and the fluid pressure gradient within the tissue (which will be discussed in more detail later).

Figure 1.13 shows a schematic of the tissue response during a typical creep compression test, as simulated by such poroelastic models. Under compression, a combination of fluid exudation and reorganisation of the extracellular matrix is observed. The rate of creep (B) is dependent on the fluid exudation and which continues until an equilibrium position is met (C). During compression, the matrix constitution is the key regulator of the tissues time-dependent response.

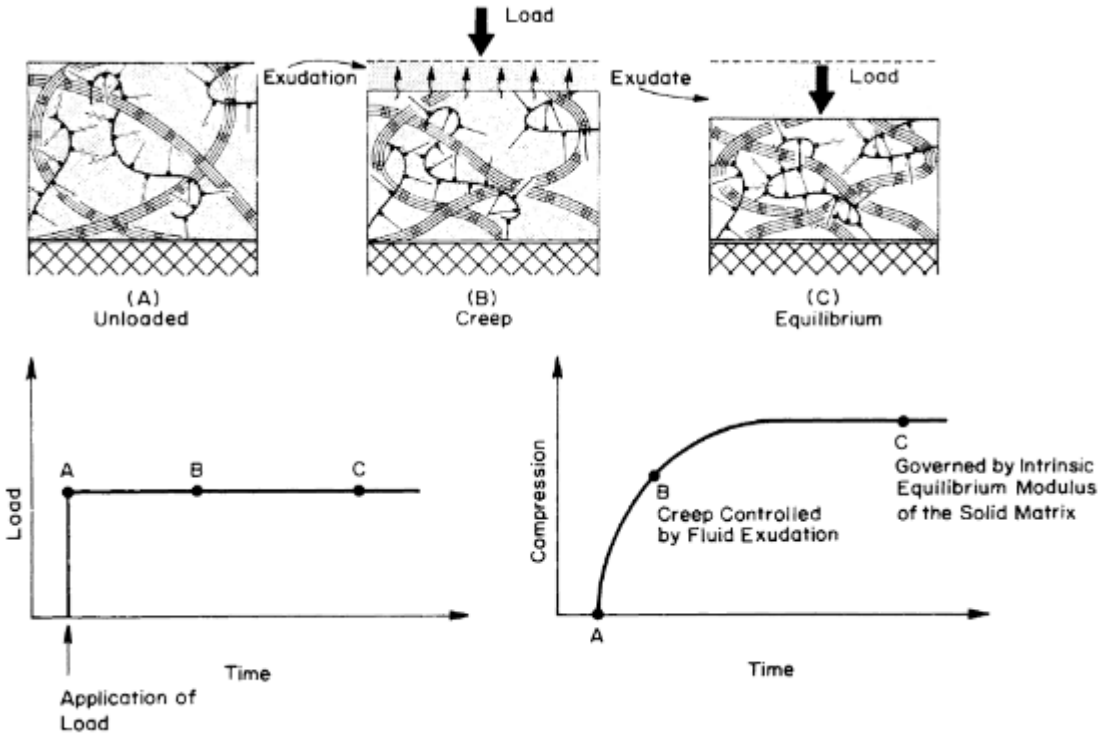

Figure 1.13: Schematic response of cartilage under confined compression during a creep test in the (a) unloaded state, (b) during the application of a fixed load and (c) during the relaxation of the tissue to an equilibrium state where the tissue no longer further compresses [39]**.**

The resultant mechanical properties derived from these tests have shown that articular cartilage is highly permeable whilst possessing a time-dependent stiffness. Figure 1.14 indicates the compressive properties of three different types of bovine cartilage revealing that articular cartilage is significantly more penetrable with a permeability factor (k) of 4.67 when compared to both nasal and meniscal cartilage. This can be explained by the importance of fluid flow in balancing the stress application. Alongside this, the aggregate modulus is lower in cartilage at 0.85 MPa when compared to nasal cartilage at 5.64 MPa, again likely due to the structural differences in terms of function and composition, with articular cartilage's requirement to be more compressible than that of the nasal tissue.

Tissue	Aggregate modulus (HA) (MPa)	Permeability (k), 10–15 $m^4/N\ s$	H_2O by weight (%)
Nasal cartilage	5.64	0.49	75.6
Articular cartilage	0.85	4.67	80.9
Meniscus	0.41	0.81	73.9

From Woo et al. (1987)

Figure 1.14: Compressive properties found in three types of bovine cartilage indicating the variation in aggregate modulus, permeability and water content[41].

What is evident here from these studies is that the time-dependency of the tissue response is linked directly to the tissues composition and the interactions of these constituent ECM components. In order to fully understand how each component contributes to the biomechanical behaviour and how the tissue functions mechanically overall, a structural hypothesis is investigated prior to discussion into mechanical models for these interfaces.

1.3.4. Structural hypotheses for time-dependent mechanics

The time-dependent behaviour is largely due to the structural and fluid components of the extracellular matrix. The tissue is made up of a viscoelastic solid scaffold forming the ECM with water flowing through the porous structure. However, it is important to

understand how the individual ECM components are involved in resisting compression whilst also performing to return the tissue to its initial state when uncompressed.

To begin with, the proteoglycan aggregates contain negatively charged sites creating a fixed charge density which, in turn, results in repulsive forces pushing the molecules away from one another. The repulsion of these chains alongside the attraction of water molecules causes the aggregates to occupy a large volume of the tissue, whilst creating a high osmotic pressure and associated swelling pressure within the tissue[15,42]. The experimentally measured osmotic pressure in cartilage can range between 0.05 to 0.35 MPa[43].

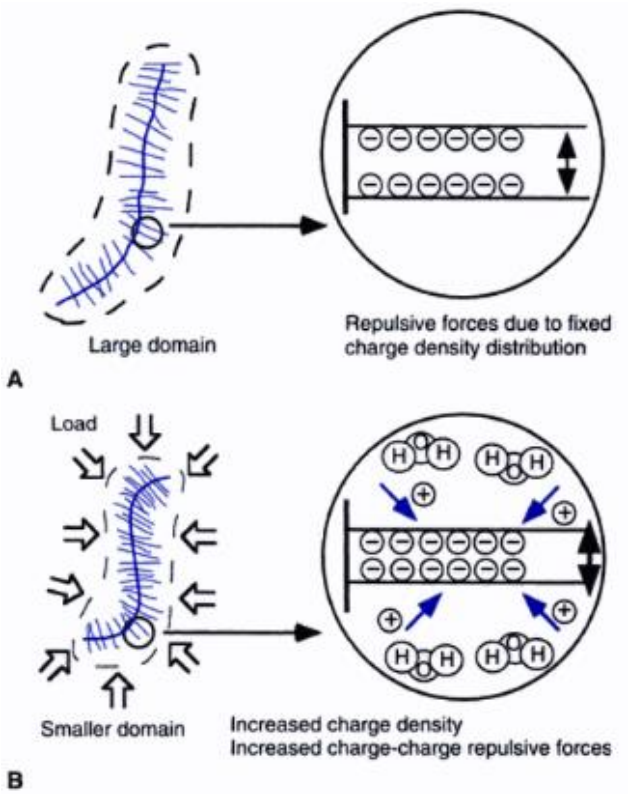

Figure 1.15: Schematic representation of a proteoglycan aggregate before (a) and after (b) external load application where on compression there is a smaller domain occupied by the GAG chains and thus an increase in associated charge density and charge-charge repulsion[30].

These PG aggregates are packed so tightly that they are unable to fully extend to their aqueous volume[43] and under compression the proteoglycans are forced to occupy a smaller domain which further increases the localised charge density and associated intermolecular repulsive forces in an attempt to resist confinement[30] as indicated by Figure 1.15. Under compression there is a loss of the volume of water but the number of mobile ions remains constant, to preserve electroneutrality, resulting in an increase in osmotic pressure[44].

In the event of the external stress causing the internal pressure to exceed that of the swelling pressure, the water begins to flow out of the tissue. The resultant loss of fluid causes the localised PG concentration to increase by drawing them closer together and this creates further increases in the bulk compressive stress alongside the osmotic swelling pressure and charge related repulsion forces until equilibrium is reached[30](Figure 1.16). Furthermore, the fluid flow is resisted by the low permeability of the matrix and thus creating further resistance to compression[15].

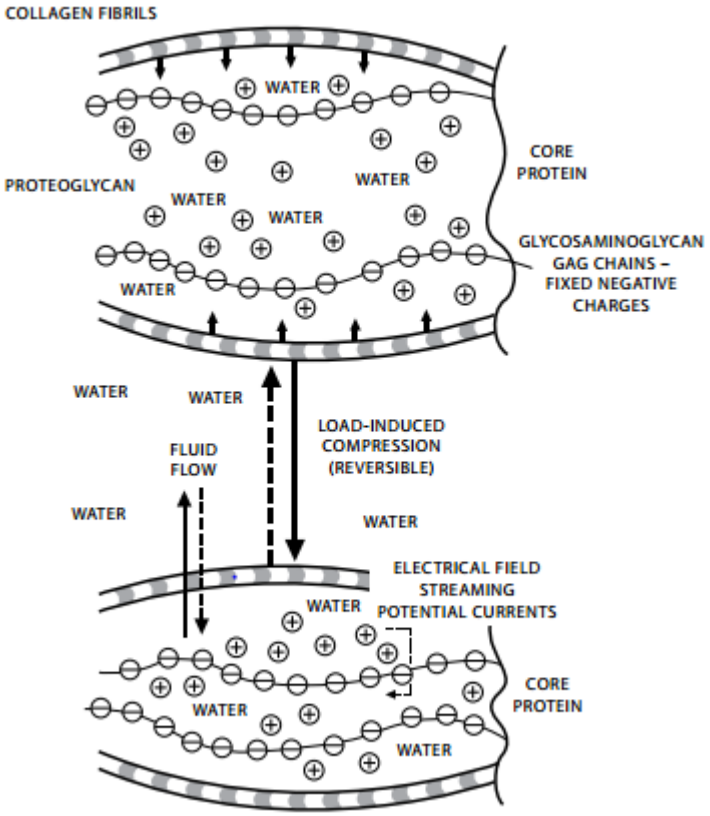

***Figure 1.16: Reversible fluid flow out of collagen and PG matrix following compression where a change in the osmotic gradient drives the reversible flow of water from between the GAG chains*[45].**

The mechanism is further support by the presence of the collagen fibrillar network[46]. The collagen network restrains the PG's from swelling whilst anchoring the PG matrix; this resistance in turn contributes to the swelling pressure and together the two components provide the bulk compressive stiffness found in cartilage (Figure 1.17). As a result, the swelling pressure causes the fibrillar network to remain in tension and thus results in an associated 'pre-strain' of the fibrils even when the tissue is not under any immediate compression[47].

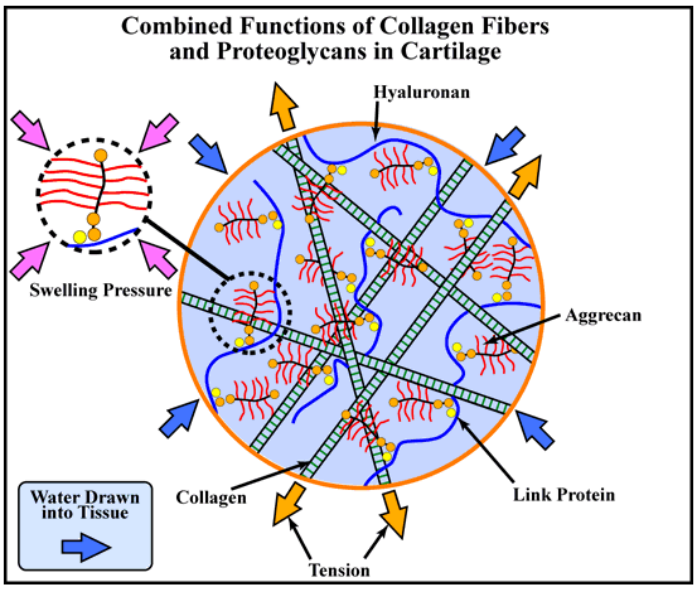

***Figure 1.17: Combined contribution of the proteoglycan and water content in creating the swelling pressure found in cartilage which is restrained by the collagenous network*[48].**

1.3.5. Modelling of time-dependent articular cartilage mechanics

In an attempt to understand the complex interactions in cartilage mechanics, many groups have developed models of the tissue incorporating the ECM components. Early models, such as that of Mow *et al*. (1980) proposed the biphasic theory such that the tissue is formed of an incompressible elastic solid alongside and incompressible, inviscid fluid. This theory suggests that the frictional drag of fluid flow by the solid phase causes high interstitial fluid pressurization and this contributes to the tissues ability to withstand loads, resulting in the observed poroviscoelastic behaviour[20,34]. The time-dependent, i.e. the viscoelastic, behaviour of cartilage, as mentioned earlier, is as a result of the interstitial fluid flow and associated drag from the ECM. Mow *et al.* (1980) described this phenomenon caused by the interstitial fluid flow as that biphasic viscoelastic behaviour, whilst the contribution from the macromolecules is known as the intrinsic viscoelastic behaviour or flow-independent response of the solid phase[49]. However, this model would

suggest that cartilage is a fluid-filled porous-permeable biphasic medium with no consideration of charge effects[43].

When considering the role of the PG charge and ion contribution, the phases are further subdivided into an ion phase, a fluid phase and a charged solid phase – introducing the triphasic theory proposed by Lai *et al.* (1991). This theory combines the biphasic theory with the physico-chemical theory for ionic and polyionic PG solutions, to form a tertiary mixture based model. This model found that a contribution of three different effects was important in determining the compressive stiffness of cartilage, these included the osmotic pressure, chemical expansion stress and the solid matrix elastic stress[50]. This particular model measured average tissue responses, whereas a further developed model by Buschmann and Grodinsky (1995) investigated the molecular level role of charge in the tissue. This particular model incorporates regional variations in electrical charge and they found that the results of this model matched the experimentally measured swelling pressure, whereas the triphasic theory overestimated this value[30].

Other models have investigated the role of the collagen fibrils in cartilage mechanics. There has been some evidence to suggest that the fibrils play a role in the flow-independent viscoelasticity of cartilage mechanics and therefore fibril-reinforced poroelastic models have been developed to predict the mechanical behaviour of cartilage in relation to the fibrillar network[51]. Li *et al.* (1999) investigated the depth-dependence of fibrillar structure on the nonlinear fibril reinforced poroelastic model (Figure 1.18). Here, the composite consisted of three phases; a nonfibrillar isotropic matrix (comprised of the proteoglycans), the collagen fibrillar network and the fluid. This model provides information as to how the tissue responds throughout the thickness for example suggesting that the most deformation occurs in the top 25% of the tissue[52].

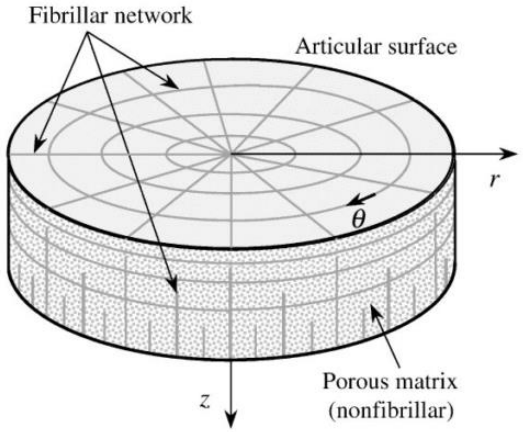

***Figure 1.18: Nonhomogeneous fibril-reinforced poroelastic model of cartilage representation where the depth dependent angular orientation is incorporated into the model*[52].**

A further extension of this model was investigated by Wilson *et al.* (2004), where the swelling behaviour was accounted for. Through the combination of their fibril –reinforced poroviscoelastic finite element model and biphasic swelling model with experimental results, they were able to explain cartilage behaviour in tests such as indentation and unconfined tests. Here, they combined the constitutive model (biphasic) with a fibrillar contribution, whereby the fibrils are described as arcade-like in structure as described by Benninhhoff's model (1925)[53].

More recent models have investigated the importance of including depth-dependent properties. A fibril-reinforced cartilage swelling model, which accounts for the depth-dependent collagen structure and composition, was used by Hosseini *et al.* (2014) to determine the importance of the superficial zone when the tissue is under loading. Utilising this model alongside channel indentation tests, they were able to show that the superficial zone was capable of recruiting regions of the deep zone via the transitional fibrils[38,54]. A fibril-reinforced poroviscoelastic (FRPVE) model was used by Halonen *et al.* (2013) to characterise the effect of collagen orientation and distribution, alongside PG

distribution, on the 3D joint stresses and strains. The 3D finite element model created investigated different depth-wise structures during normal gait cycle and at mechanical equilibrium (Figure 1.19) and found that the arcade-like collagen architecture derived significantly lower stresses when compared to a homogenous model[55]. Such studies highlight the importance of evaluating localised structure in terms of tissue depth and further exemplifies that cartilage cannot be assumed to be a homogenous structure given the associated microscale mechanical properties observed.

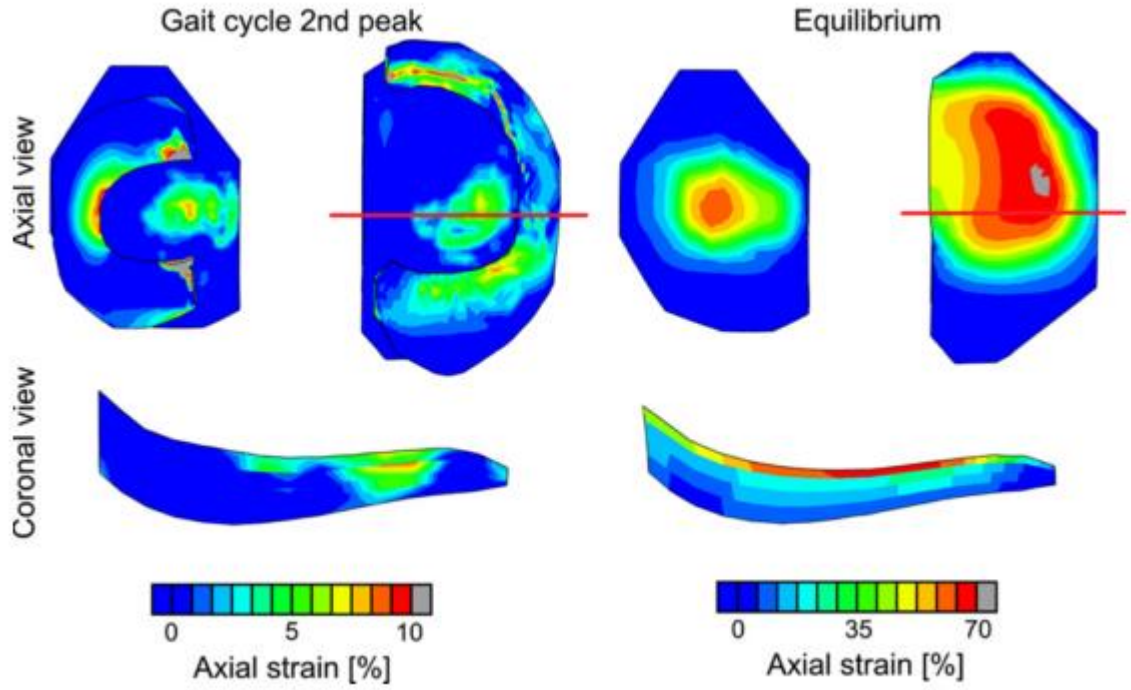

Figure 1.19: Axial strain maps at the tissue surface and through the depth during normal gait and at equilibrium derived through a FRPVE model which accounts for the 3D architecture in cartilage[55].

1.3.6. Microscale mechanical properties

Given that the tissue possesses a depth-dependent ECM structure and composition, there is also an associated inhomogeneous strain profile visible throughout the thickness. As previously mentioned there is an increased PG content with depth which would intuitively mean an increase in fixed charge density and thus an increase in swelling pressure as a result. Furthermore, there is a depth wise variation in both architecture and concentration

of collagen. Combining these two factors, with the association of compressive stiffness and PG concentration as measured via biochemical analysis of sections through the thickness of the tissue, there is an altered compressive resistance throughout the different zones of cartilage which was measured by using fluorescently labelled chondrocytes as markers for strain within the zones (Figure 1.20)[56,57].

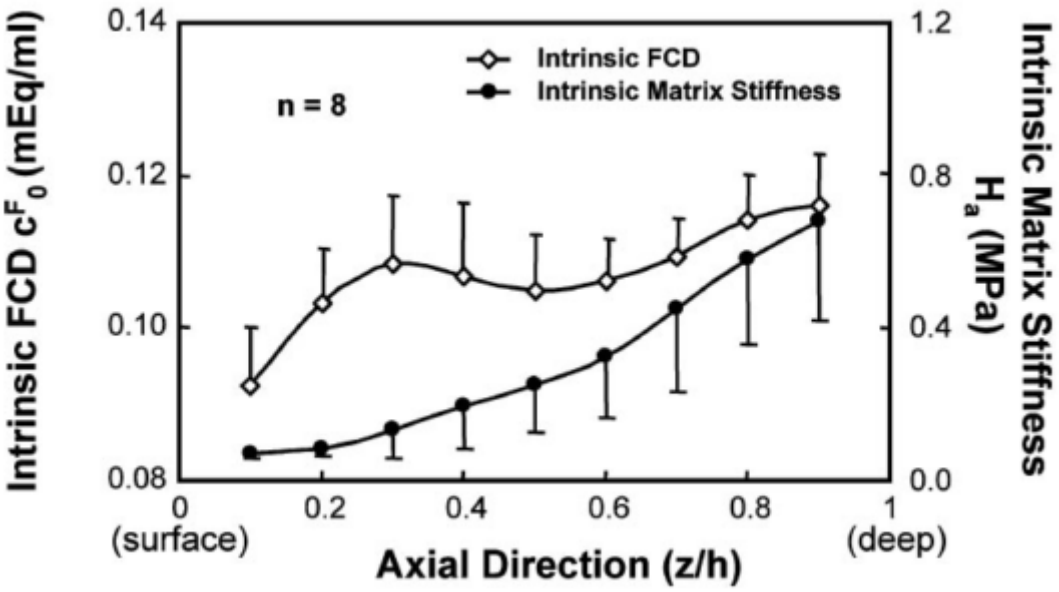

Figure 1.20: The distribution of the intrinsic fixed charge density and the intrinsic matrix stiffness. With increasing FCD there is an associated increase in matrix stiffness as mediated by the localised changes in composition in terms of PG content and associated swelling pressure[57].

Understanding the depth-dependent microstructural mechanics of cartilage has been of great interest[15,56,58]. A study by Szarko and Xia (2012) used the chondrocytes as markers for tracking displacement within sections of cartilage under compression as shown by Figure 1.21. They found that non-uniform tissue deformation occurring in cartilage such that the greater cell displacement was found significantly higher in the superficial zone ($p<0.01$ when compared to both transitional and deep zones) through to the transitional zone ($p<0.05$ when compared to the deep zone) with the greatest resistance to compression found in the deep zone[56].

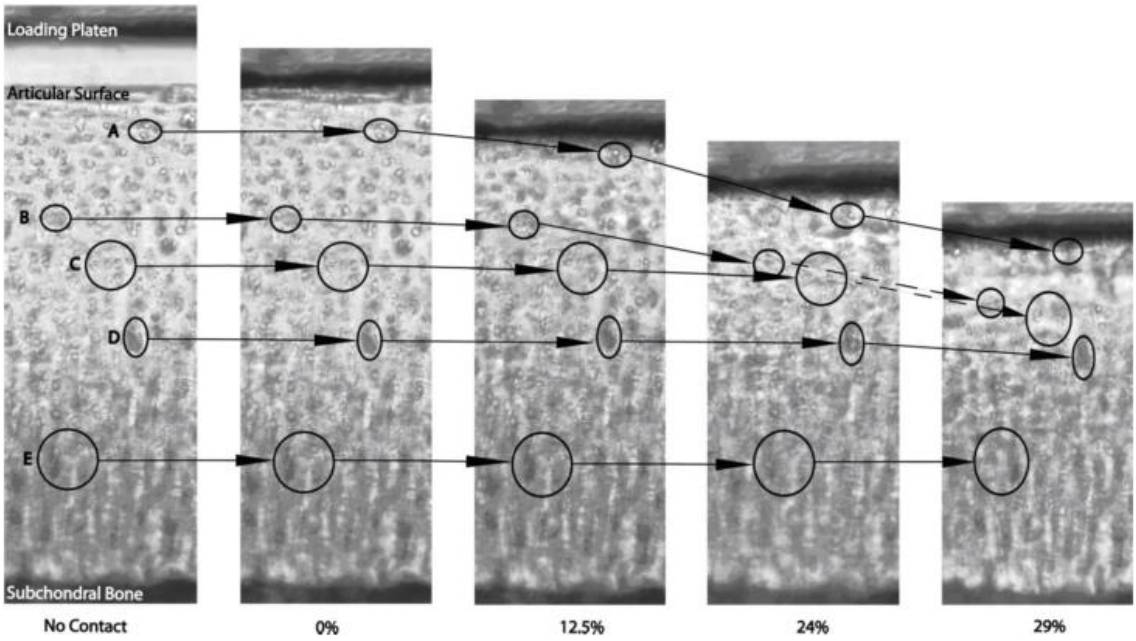

Figure 1.21: Microscope images of full thickness cartilage sections under various different strain levels indicating the depth-dependent strain field observed in full thickness articular cartilage where regions closest to the articular surface are more compressible than the zone adjacent to the subchondral bone*[56]*.

An earlier study by Schinagl *et al.* (1997) utilised a similar methodology to determine the equilibrium confined compression modulus of bovine cartilage as a function of depth. They found that there was a significant increase in compressive modulus with depth such that the superficial zone had a modulus of around 0.079 +/- 0.039 MPa whereas the deepest layer had a modulus value of 2.10 +/- 2.69 MPa, thus suggesting that different zones contribute significantly differently to the macroscale level mechanics that are observed through simple stress-relaxation/creep tests[58]. These findings correlate with the study by Tomkoria *et al.* (2004) who used nanoindentation by atomic force microscopy (AFM) to determine the average Young's modulus as a function of depth as shown in Figure 1.22.

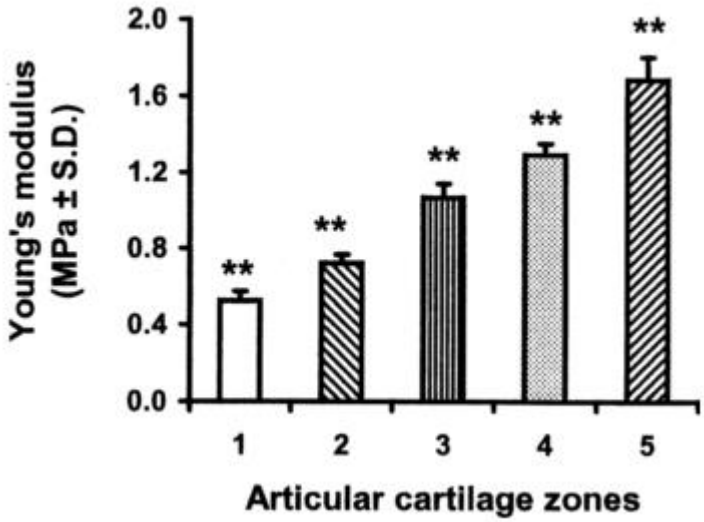

***Figure 1.22: Average Young's modulus as a function of depth determined by nanoindentation during AFM scanning where 1 represents the superficial zone and 5 the deep zone/calcified*[59].**

Thambyah and Broom (2013) studied the effect of stress relaxation via a channel indenter to investigate the response of the matrix adjacent to the directly loaded regions as well as the zonal responses to three different strain rates. They utilised light microscopy to image the chondrons within the tissue and measured changes to chondron aspect ratios within all the zones to identify any changes associated with loading (Figure 1.23). They found that at the lowest level of strain only the superficial zone provided any immediate changes to the measured ratios. The medium rate extended the level of deformation to the transitional zone whilst at all compression levels the deep zone chondrons remained undeformed. These findings coincide with the localised resistance to compression whereby the deep zone is the stiffest of all three zones and this shields the local clusters of cells from experiencing deformation[15].

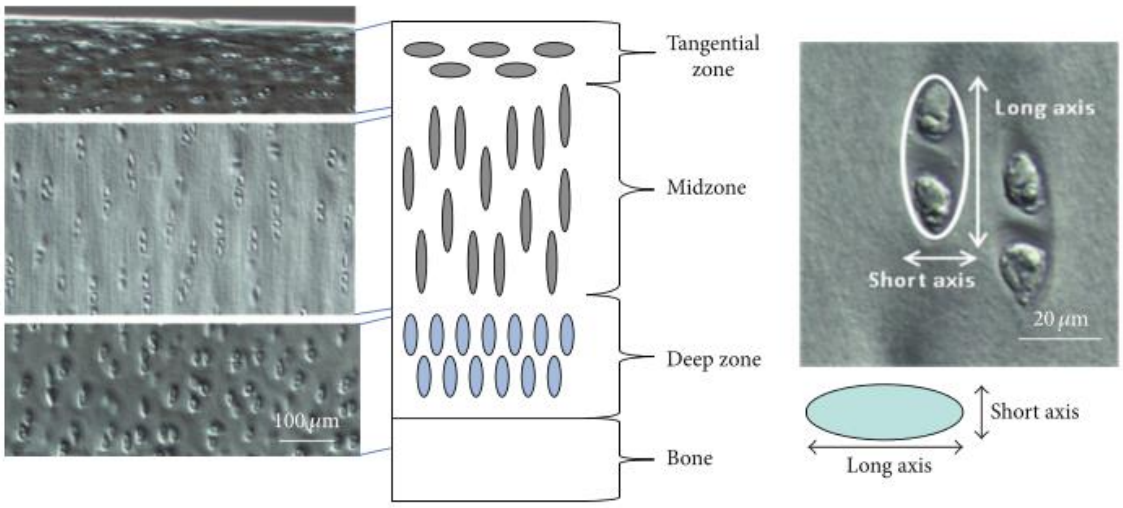

Figure 1.23: Light microscopy images of different regions within cartilage where the tangential zone is referring to the superficial zone and the chondron aspect ratio measurements were used to indicate changes in localised strain under tissue level compression[15].

Recent work has focused on the role of the superficial zone in cartilage mechanics given its important role in lubrication and articulation within joints and the loss associated with tissue degradation. As mentioned earlier, models have indicated that the superficial zone is highly influential in transducing stresses through the tissue via the transitional zone[54]. A study by Grenier *et al.* (2014) investigated changes to the instantaneous and equilibrium confined compression moduli of the superficial zone with surface fibrillation and associated proteoglycan removal and found a reduction in both[60]. Another study by Griffin *et al.* utilised confocal strain mapping to determine the effect of collagen degradation (and associated PG loss) and found a reduction in dynamic (viscoelastic) shear modulus and an increased energy dissipation within the upper 400um of the tissue (within the superficial zone) as show in Figure 1.24[61].

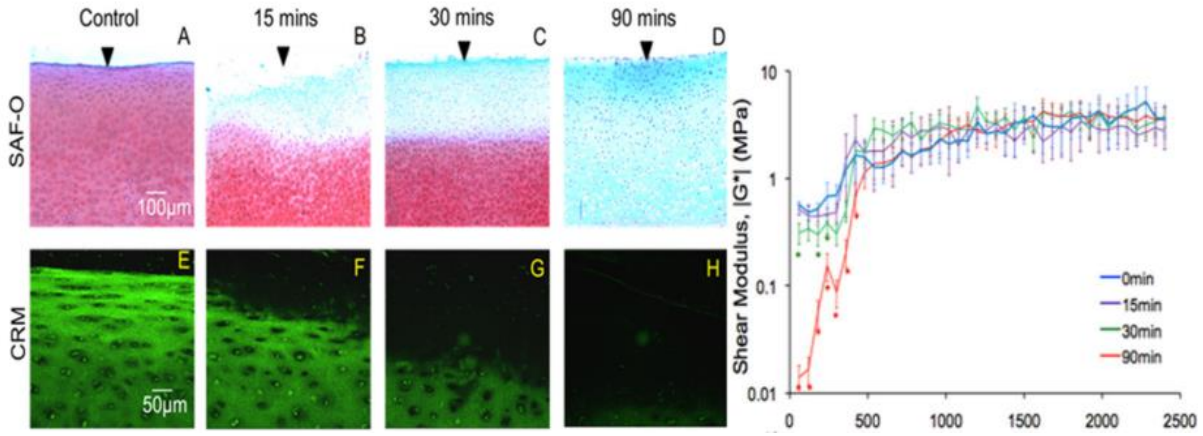

Figure 1.24: Safranin-O histology (A-D) and confocal reflectance micrographs (E-H) of cartilage before and after varying levels of collagenase digestion and the shear modulus as a function of depth from the surface of the tissue[61]

1.4. Nanoscale mechanical properties

The proteoglycans within the extracellular matrix have been investigated at the nanoscale to determine how they contribute to tissue level mechanics using atomic force microscopy (AFM) based techniques. Han *et al.* 2011 used an AFM probe to apply dynamic deformation in cartilage tissue within the same length scales as the proteoglycans and measured both untreated and proteoglycan depleted tissue. They found that whilst the proteoglycans are important in determining tissue properties such as the permeability and modulus, at the nanoscale they are also important in constraining collagen fibrillar mobility i.e. they prevent the fibrils from excessive release of tension via buckling[62,63].

Alongside the contribution of the PG's in providing cartilage with its mechanical properties, the collagen fibrillar network also has a mechanical role in resisting compression whilst having the flexibility to allow the tissue to return to its fully hydrated state when decompressed. Given that the fibrils are largely associated with the PGs, it is likely that there are nanomechanical effects, such as changes to the intramolecular packing, which may not be observed using traditional techniques. Studies that have modelled the behaviour of the fibrils have suggested that the collagen network only plays

a role in dynamic loading and has little effect on the equilibrium response however there is no experimental evidence to confirm this theory[51,64,65].

Very little is known about how exactly the collagen fibrils are able to respond to loading in cartilage however there have been a few studies that have investigated depth-dependent fibrillar organisation and changes associated with uniaxial compression. Early studies by Aspden and Hukins (1979) showed that the fibrils in cartilage produce characteristic X-ray diffraction patterns that provided a direct measurement of the both the orientation and distribution of orientations within articular cartilage[66,67]. A later study by Moger *et al.* (2009) used small angle X-ray scattering to infer changes in the fibrillar orientation under loading and found that at surface pressures of up to ~1.5 MPa the observed compression of the superficial and transitional fibrils was reversible. At higher surface pressures of around 4.8-6 MPa the load increase led to further deformation which propagated down the deep zone and a rotation of fibrils at around 10 degrees from the predominant radial direction was observed. Furthermore, they were able to show with progressive increase in loading, there was an associated 'crimping' of the fibrils such that the entire fibrillar structure was altered, but no intra-fibrillar changes were reported[68]. However, this does not provide further insight as to what mechanisms underpin these changes and whether there is any intra-fibrillar disordering associated with localised changes to strain.

Extensive studies have been performed in other collagen rich tissues such as tendon and bone and have indicated the flexibility of fibrils when placed under loading. Stress-relaxation tests performed using X-ray diffraction have shown that the fibrils are extensible and the measured changes in axial D-period can be from 67nm to 69nm prior to any observable failure. This elongation of the fibrils is believed to be only partly down the extension of the helical structure of the molecules but more so due to molecular

rearrangement[5]. A study by Gupta *et al.* (2005) investigated the deformation mechanisms in bone and more specifically measured the fibrillar level strain whilst comparing this to tissue level deformation. They found that although the fibrillar deformation was homogenous along the bone there was a difference between the fibrillar and tissue level strain (Figure 1.25). They concluded that the tissue level deformation could be attributed by two factors; firstly the tensile stretching of the mineralised fibrils as indicated by the increase in axial D-period but also via the presence of shear deformation of the interfibrillar matrix[69].

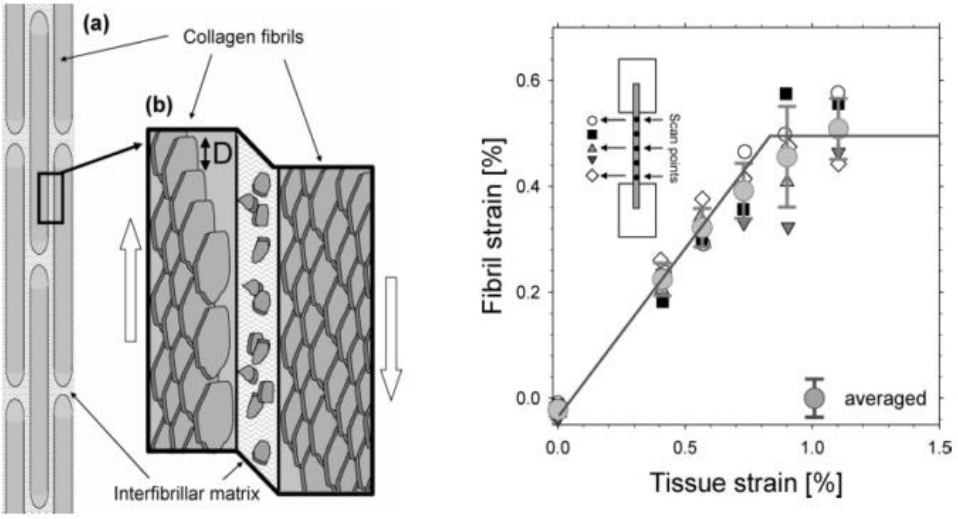

Figure 1.25: Schematic indicating the nanometer-level deformation mechanism in mineralised bone, where there is the presence of mineralised collagen alongside an extrafibrillar matrix, alongside a chart indicating that the fibrillar level strain is not equal to the tissue level strain[69].

The mechanisms behind the time-dependent properties of tendon were investigated by Screen *et al.* (2011). The nanoscale structural changes were measured simultaneously with tensile stress relaxation alongside both confocal scanning microscopy small angle and X-ray scattering. They tracked both the transverse and axial changes to the fibres and measured the contribution of the fibrillar level mechanics. They found that the fibrils expanded upon stress relaxation and suggested that this was likely down to volume

conservation via fluid flow from the extrafibrillar to the intrafibrillar space (Figure 1.26)[70]. This would suggest that the interactions between the interfibrillar PG and associated water molecules mediate the fibrillar level mechanics and this may have some relevance when investigating the role of collagen fibrils in the ECM of cartilage.

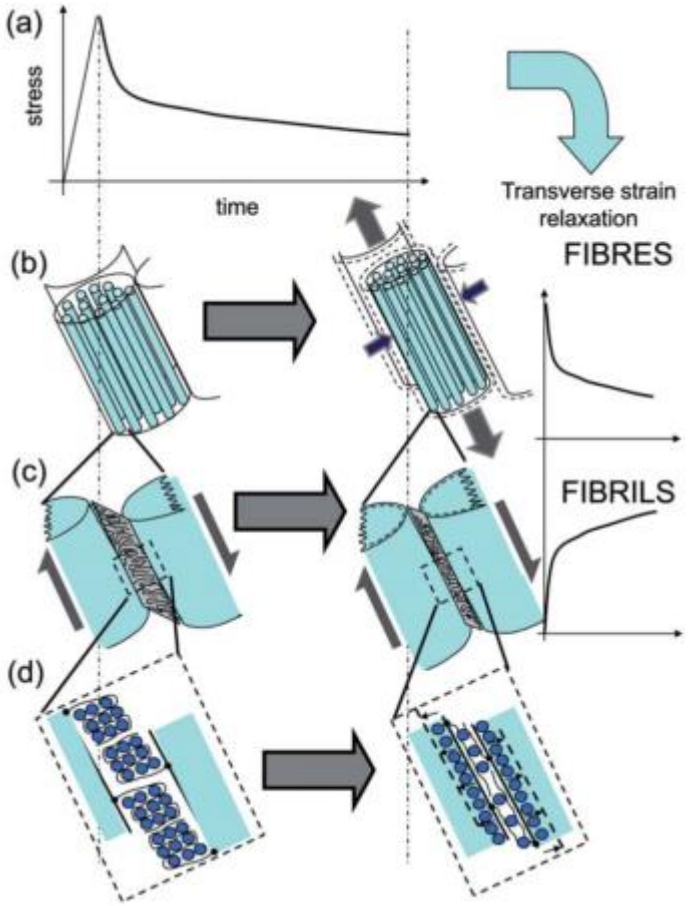

Figure 1.26: Schematic of macroscale stress relaxation (a), fibre contraction (b), and fibrillar expansion associated with localised changes in hydrations as proposed by the hypothesis of movement of water molecules from the extrafibrillar space to the intrafibrillar space (d)[70].

Aims & Objectives

In view of the open questions concerning the role of the collagen fibrillar network in cartilage mechanics as summarized above, this thesis has the following **Aims and Objectives**.

Aims

1. To understand the nanostructural parameters associated with the architecture of the fibrillar network in cartilage using *in-situ* synchrotron SAXD, i.e. the fibrillar D-period, orientation and the level of both inter- and intra-fibrillar disorder.
2. To investigate the nano-mechanical response of the collagen fibrillar network in articular cartilage via dynamic *in situ* SAXD measurements and determine how selective ECM compositional alterations changes these properties.
3. To understand the changes in dynamic mechanical response of the collagen fibrils in cartilage under conditions mimicking physiological tissue-level inflammation in both animal and human models.

Objectives

- To define the spatial variation of the nanostructural parameters of the collagen network across the full thickness of articular cartilage using SAXD.
- To design an adaptive sample holder for the existing *in situ* micromechanical testing machine to allow compression of cartilage explants.
- To develop experimental protocols for determining collagen fibrillar response under macroscopic stress-relaxation and cyclic loading, to be conducted at synchrotron facilities with simultaneous application of SAXD to measure real-time fibrillar level mechanics.

- To apply methods of structural manipulation – both enzymatic and inflammation related degradation – to cartilage explants, in order to mimic the changes in cartilage associated with osteoarthritis, and utilise chemical assays to measure the level of degradation.
- To conduct transient viscoelastic mechanical tests at the macroscale, concurrent with time-resolved *in situ* SAXD, to determine the nanoscale fibrillar response in healthy tissue, as well as in enzymatically degraded cartilage.
- In a similar manner to the above, to carry out dynamic cyclic compression in the mechanically physiological range on healthy and inflamed cartilage, and to determine short- and long-term fibrillar deformation mechanisms under such a loading regimen.
- To determine the effect of macroscopic loading rate, in cyclic compressive loading, on the fibrillar dynamics in both bovine and human cartilage.

Chapter 2

Methods: Synchrotron techniques

2. Methods: Synchrotron techniques

2.1. Introduction to X-ray diffraction

2.1.1. History and background of x-rays

X-rays were first discovered in 1895 by Wilhelm Conrad Roentgen in his laboratory at the University of Würzburg. In the years following, methods of understanding X-rays and the practical uses were developed in order to study crystal structures. The diffraction of X-rays through crystalline structures was first discovered by Max von Laue who had an initial idea that regularly spaced atoms in a crystal may act as a diffraction grating for X-rays and that only secondary X-rays would interfere constructively. These ideas and findings were later developed by William Henry Bragg and his son, William Lawrence Bragg, who subsequently constructed Bragg's law of diffraction[71].

X-rays are formed of electromagnetic waves with relatively short wavelengths between 0.01nm to 10nm with an associated photon energy ranging between 100keV to 100eV as indicated by Figure 2.1. The shorter wavelength permits the use of X-rays in characterising nanoscale structures in a vast range of materials through the interpretation of diffracted and scattered X-rays[72]. In order to use X-rays as a tool for interpreting small scale structure within a material it must possesses a crystalline structure with periodic repeating units. It is not necessary that this periodicity be at the atomic scale only (although this is by far the most common), as the D-periodicity of ~65-67 nm observed in collagen can also lead to a diffraction signal. The repeating units, with fixed spacing, give rise to a periodic electron density distribution, and this charge distribution leads to organised interactions between the electromagnetic waves of the X-ray (which can be considered as oscillating electric and magnetic fields) and the negatively charged electrons within the atoms of the structure. If the X-rays are in the same order of

magnitude as the periodic spacing, then the resultant spatial patterns of scattered light provide indirectly ultrastructural information about the materials, such as the intermolecular spacing, crystal structure and other parameters [73,74], as will be discussed in more detail in the following sections.

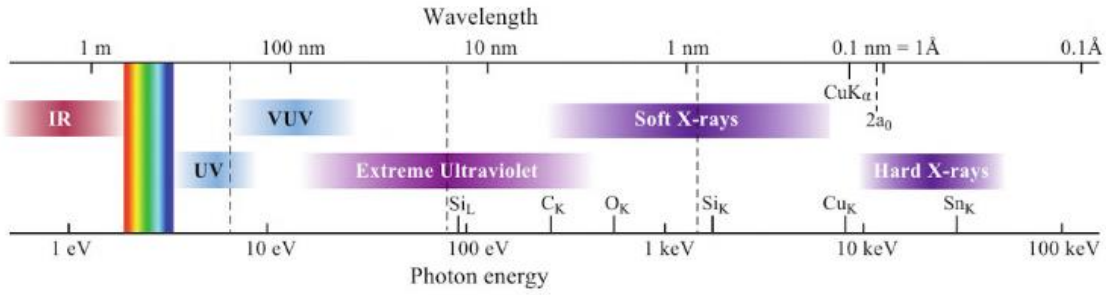

Figure 2.1. The electromagnetic spectrum ranging between infrared (IR) wavelengths to hard x-ray wavelengths, with wavelengths indicated along the top and photon energies along the bottom. Visible light is indicated to the left which is made up of red (650nm), green (530nm) and blue (470nm) wavelengths*[72]*.

2.2. Small angle X-ray scattering (SAXS) and diffraction (SAXD)

2.2.1. Principles of X-ray diffraction

The phenomenon underlying X-ray diffraction and scattering can be understood by considering the basic atomistic level interactions of X-rays with matter. Two processes occur when an X-ray beam is incident on an atom within a material: it is either absorbed with an ejection of electrons (photoelectric effect) or the beam may be scattered (mainly but not only coherent scattering). The coherent scattered radiation arises from photons that are deviated from their course but possess the same wavelength as the incident beam[75]. The interaction of the electromagnetic field of the incident radiation with the electron density distribution of the material leads to elastic (or Rayleigh) scattering from the atoms comprising the material, which manifests as spherical electromagnetic waves originating at each of the atoms. When a material has a particular crystalline structure at

the atomic or molecular level, there are periodic variations in electron density due to the periodicity of the crystalline lattice. Due to the phenomenon of constructive and destructive interference from regularly spaced sources of radiation (such as the atoms on the crystalline lattice), an inhomogeneous angular distribution of the maxima and minima of scattered X-ray radiation results which is dependent on the specific molecular arrangement of the material. Therefore, in an inverse procedure, when an X-ray is incident on the material, the characteristic spatial pattern of the scattered radiation can – in principle – be used to obtain information on the sample's electron density distribution.

This is of particular relevance to understanding collagen nanostructure, because the collagen fibrils in cartilage exhibits periodic crystalline structure at the nano-scale (the D-period) which can result in scattered diffraction in X-ray scattering. In this case the D-periodicity arises from the periodic low- and high density regions of tropocollagen molecule packing, forming the gap and overlap regions, as described by the Hodge-Petruska model for collagen packing[76]. As detailed below, the diffraction pattern arising from this meridional D-periodicity can be used to quantify numerous parameters which characterize the collagen/PG fibrillar composite at the nanoscale.

To demonstrate how lattice periodicity of a material leads to constructive and destructive interference in X-ray diffraction, the well-known Bragg's Law for atomic diffraction is reviewed[75]. Bragg's law relates the wavelength (λ) of the X-rays to the spacing d between each atomic plane (D-spacing). This can be applied to determine when the scattered waves from adjacent rows of atoms are in phase, leading to only beams diffracted in specific angles (directions) interfering constructively[77], as shown in Figure 2.2.

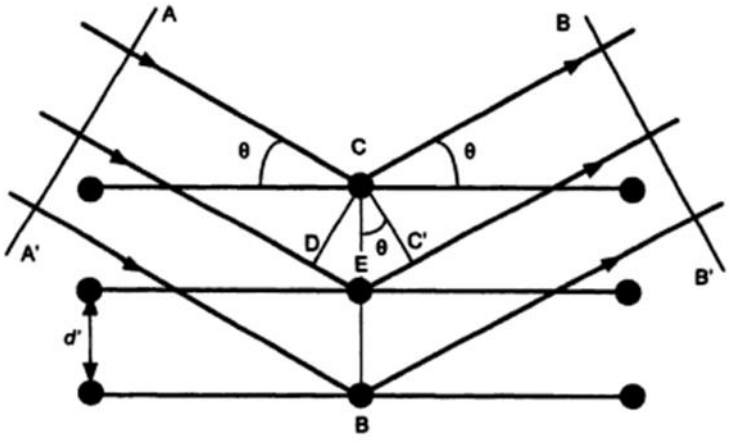

Figure 2.2. Diffraction of X-ray beams in a crystal, where the distance between two parallel places is indicated as d`, A and A` are the incident rays, B and B` are the diffracted rays at angle ϑ. In order for constructive interference the distance between DEC` must equal a multiple of a complete wavelength (nλ)[77].

The following equation is the expression of Bragg's Law, shown schematically in Figure 2.3:

$$\boldsymbol{\lambda = 2\frac{d`}{n}\sin\theta} \qquad \textbf{Equation 1}$$

where λ is the wavelength, n is the order of reflection, θ is the diffraction angle and d` is the spacing between crystallographic lattice planes which are indexed by a series of integers (hkl, the Miller indices of the crystallographic plane)[75]. It is conventional to write a generalized form of this relation for a continuous (arbitrary) electron density distribution, and to define a class of physical quantities called wave-vectors (usually denoted *k* or *q*) which have the dimension of inverse length. Bragg's law can be related to the scattering vector $\vec{q}$ whose direction is the difference between the wavevector of the scattered radiation (**k**') and the wavevector of the beam incident on the sample (**k**). The intensity of the scattered radiation is then a function of the scattering angle 2θ (as shown by Figure 2.3) and the nature of the electron density distribution in the scattering object:

essentially, by considering a continuous electron density distribution in place of the discrete array of atomic lattice planes used in the pictorial representation of Bragg's law.

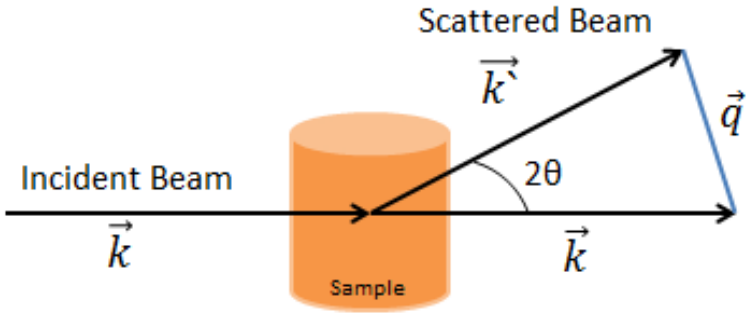

Figure 2.3. Schematic representing the scattering vector that is defined by the scattering angle relative to the incident and scattered beam.

The scattering wavevector is related to the Bragg angle 2θ as follows:

$$\vec{q} = \frac{4\pi}{\lambda} \cdot \sin\frac{2\theta}{2} \qquad \textbf{Equation 2}$$

The coordinate in reciprocal space q is inversely related to the coordinate in real space, when in a one dimensional space. It may be shown that, for the specific angles $2\theta_n$ for which Bragg's law indicates a constructive interference of scattered radiation, the scattering vector q has the magnitude inversely proportional to the lattice spacing d for the corresponding lattice planes:

$$q = n\frac{2\pi}{d} \qquad \textbf{Equation 3}$$

where d is the spacing between lattice planes (and, in our particular case, will be shown to correspond to the D-periodicity in the collagen fibrils), and n is the integer order of the diffraction peak.

2.2.2. Factors that modulate SAXS patterns

Based on the principles described above, the scattered radiation for an arbitrary distribution of matter can be written in terms of the scattering wavevector $\vec{q}$ and the electron density distribution in the sample as:

$$\boldsymbol{I(\vec{q}) = |A(q)|^2} \qquad \textbf{Equation 4}$$

$$\boldsymbol{A(q) \equiv \int \rho(\vec{x}) e^{-i\vec{q}\cdot\vec{x}} d\vec{x}} \qquad \textbf{Equation 5}$$

where I(q) is X-ray intensity, A(q) is scattering amplitude and ρ(x) is the spatially varying electron density of the sample. It can be seen that for a general electron density distribution, the scattered intensity can have both periodic and smoothly varying components. The variation of intensity with wavevector q which occurs in reciprocal space can be mapped to a variation of intensity by scattering angle. In this manner, an angle dependent intensity distribution is obtained, denoted by the X-ray scattering pattern. Besides containing diffraction peaks from crystalline (periodically ordered) components in the scattering sample, the pattern also contains diffuse scattering from amorphous or less ordered material. In general the shape of the scattering patterns that are gained from SAXS/SAXD (the terms arising from the evaluated integrals in Equations (4) and (5) above) are directly correlated to the ultrastructure of the tissue that is being investigated. Detailed analysis of X-ray scattering from specific shapes like spheres, cylinders or plates are described in standard textbooks on SAXS[75], but some qualitative and simple statements can be made. Where there is a large dimension of the sample along a specific direction in real space, the shape of the scattering intensity appears small (foreshortened) in the same direction in reciprocal space (i.e. as captured on the X-ray detector). This is shown by Figure 2.4, where a long fibril with a small radius R << L would produce an anisotropic intensity distribution (of roughly elliptical shape), which is narrow vertically but wide horizontally.

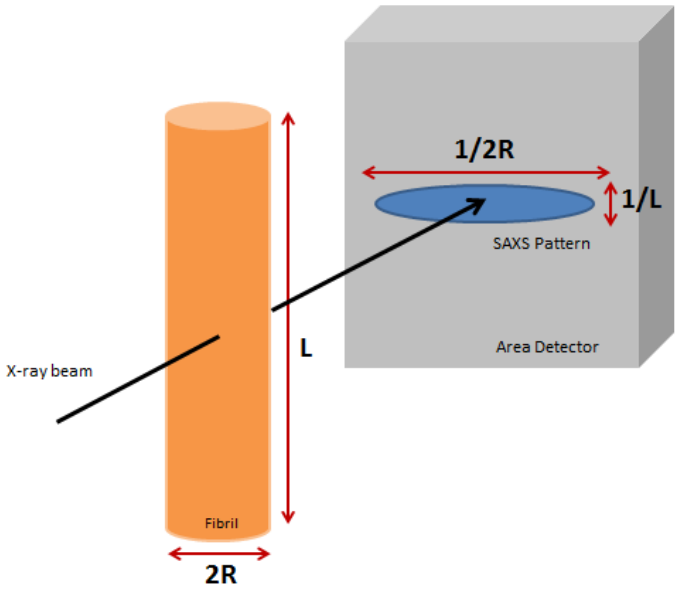

Figure 2.4. Schematic representing the SAXS pattern that is obtained from a fibril that has a length L and diameter 2R, where the reciprocal space is inversely proportional to the real space.

The variation in SAXS patterns, in terms of the qualitative differences, can be simply described as shown by Figure 2.5. Where the fibrils are in parallel to the direction of the beam one would see a thin elongated disc or ellipse shaped intensity distribution oriented at right angles to the fibril axis (Figure 2.5(I)). When there is a degree of misorientation (Figure 2.5(II)) one would observe a more rounded ellipse as the sum of narrow ellipses oriented in different directions is (approximately) a broadened elliptical pattern.

When analysing the diffraction rings (e.g the small angle X-ray diffraction peaks arising from the meridional D-stagger in the fibrils) a very similar analysis holds: for fibrils distributed over a range of angles in the scattering volume, the X-ray diffraction intensity lies on an arc, rather than a single spot (or angular coordinate) and the extent of arcing is increased as the degree of misorientation increases.

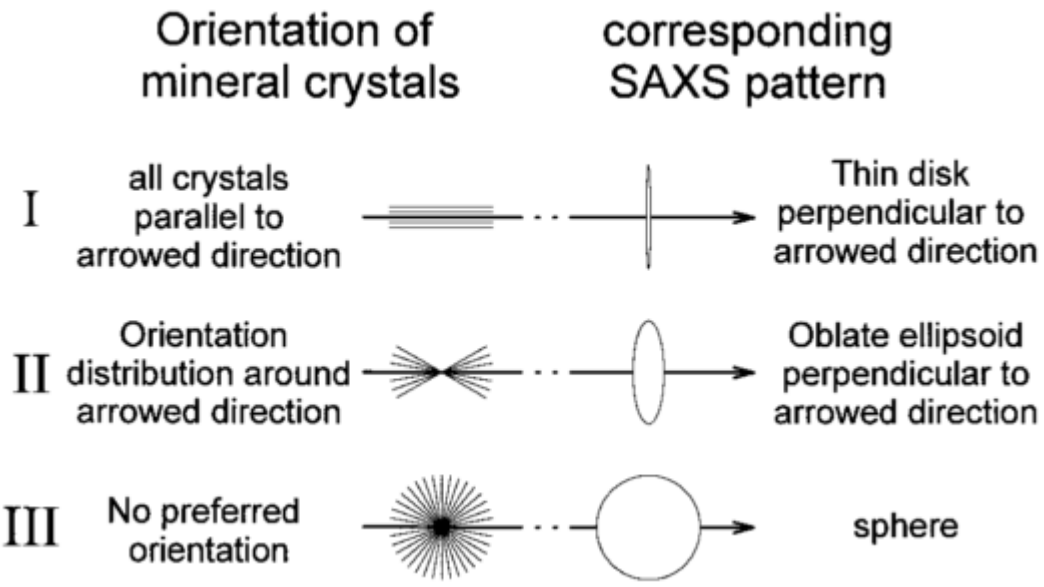

***Figure 2.5. Schematic showing the way in which real space organisations of fibrils affect the reciprocal space patterns that are generated*[78].**

2.3. Applications in analysis of fibrillar structure of collage via X-ray diffraction and scattering

Early studies into collagen structure via X-ray methods were conducted in the 1940's by Richard Bear[79], who studied the triple-helical structure of collagen molecules and the axial arrangement observed in collagen fibrils. These studies showed that the scattering pattern obtained from collagen consisted of a series of reflections that indexed on a periodicity of 64nm[79,80]. Just over a decade later North *et al.* (1954) found at higher scattering angles the presence of high intensity at 1.3nm which reflected the spacing between neighbouring collagen molecules[80,81]. From this point onwards, many groups have utilised X-ray diffraction to further investigate the nanoscale structure of collagen, and the results of some studies relevant to collagenous tissues are summarized below.

Orgel *et al.* (2001) utilised synchrotron radiation to determine the static structure of type I collagen fibrils. They confirmed the three-dimensional molecular packing previously described within collagen fibrils consisting of a quasi-hexagonal lattice. Furthermore they

confirmed the presence of crosslinking between the tropocollagen molecules that both strengthen and stabilise the fibrils[82]. The same group later investigated the microfibrillar structure from whole rat tail tendons confirming periodic spacing D at a length of 67nm as described in the Hodge-Petruska model[76,83].

Tendon is a prototypical example of a collagenous tissue whereby the fibrillar structure within the tissue permits the use of SAXS to measure underlying mechanisms. Early studies by Mosler *et al.* (1985) and Folkhard *et al.* (1987) investigated the molecular rearrangement in tendon collagen that occurs during stress-relaxation. They utilised time-resolved synchrotron radiation to measure the D-periodicity and changes related to tension. An increase in the D-period was observed which was reversible upon unloading. This mechanism behind this structural change was described as result of sliding of the triple helices which, in turn, changes the length of the gap and overlap regions. Furthermore, upon loading there are changes in the meridional intensities which are also reversible[84]. A later study showed that under stress relaxation, the change in D-period followed a similar trend to the tissue level stress such that a strain of 6.5% and held caused an initial increase of D-period from 67 nm to ~68nm followed by a relaxation of the D-period back down to around 67.25nm during tissue relaxation[85]. This study shows that the fibrils are flexible structures and such changes are measurable using X-ray diffraction studies.

A study by Fratzl *et al.* performed *in situ* measurements at the synchrotron where strains were applied to rat tail tendon and the fibrillar response measured. They were able to show that at low level strains (< 3%) there is an initial straightening of the molecular kinks and at higher strains this leads to molecular gliding within the fibrils (Figure 2.6). They also observed that strain within the fibrils were always an order of magnitude

smaller than the tissue level strain. This was further investigated by Gupta *et al.* (2009) and Screen *et al.* (2011) in determining the time-dependent kinetics of tendon fibrils and fibres during stress relaxation as discussed in **Chapter 1** in terms of nanoscale fibrillar mechanics.

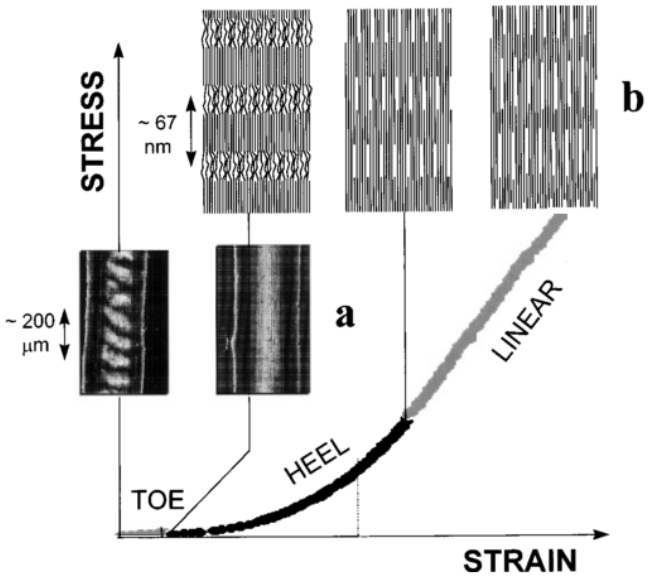

Figure 2.6. Stress-strain curve from a rat tail tendon where at the toe region the stress levels are significantly lower due to the macroscopic crimping of the fibrils followed by (a) where the molecular kinks are straightened and finally the linear region indicated by (b) where further extension leads to a 'fuzziness' of the gap/overlap interface[86].

The nanoscale deformation mechanism of bone – being largely mineralized Type I collagen fibrils at the nanoscale has been also investigated using time-resolved SAXD combined with *in situ* mechanical testing. This is due to the intrinsic periodic structure formed by the tropocollagen molecules in the collagen fibrils that can be measured alongside the information on size, orientation and shape of mineral platelets that can be inferred from the SAXS patterns[69,78,87,88] as shown by Figure 2.5. As an example of the insight into nanoscale mechanisms that such techniques can provide, Gupta et al (2013) investigated the toughening mechanisms of antler bone. The group were interested in

tracking the fibrillar deformations during cyclic loading to determine the nanoscale mechanisms that lead to high work of fracture. With experimental data combined with model predictions they provided strong evidence that the key energy dissipating mechanism was intrafibrillar sliding between the mineral and collagen fibrils, leading to permanent plastic strain at tissue and fibrillar level, providing the antler bone with such high toughness[87].

In contrast to the extensive work on tendon, and recent studies on bone, relatively few previous studies have investigated the nanostructural features of collagen in cartilage using SAXS techniques. Wachtel and Maroudas (1998) investigated the effects of pH and ionic strength on the intrafibrillar hydration in cartilage, given that the hydration of cartilage is important in the tissues load bearing ability. They used the lateral spacing of tropocollagen molecules (arising from the equatorial diffuse scattering peak as indicated in Figure 2.7) They were able to show that intermolecular spacing is mediated by ionic strength such that at higher levels the spacing is reduced due to the lowered repulsion between the tropocollagen molecules. It is plausible that a Debye-Hueckel type screening effect is the underlying cause. Furthermore, pH levels lower than 1.8 cause an increase in intrafibrillar water as there is an associated increase in the intrafibrillar positive charge. They concluded that the localised charge within the fibril determines the intermolecular spacing more so than the overall charge of the fibril.

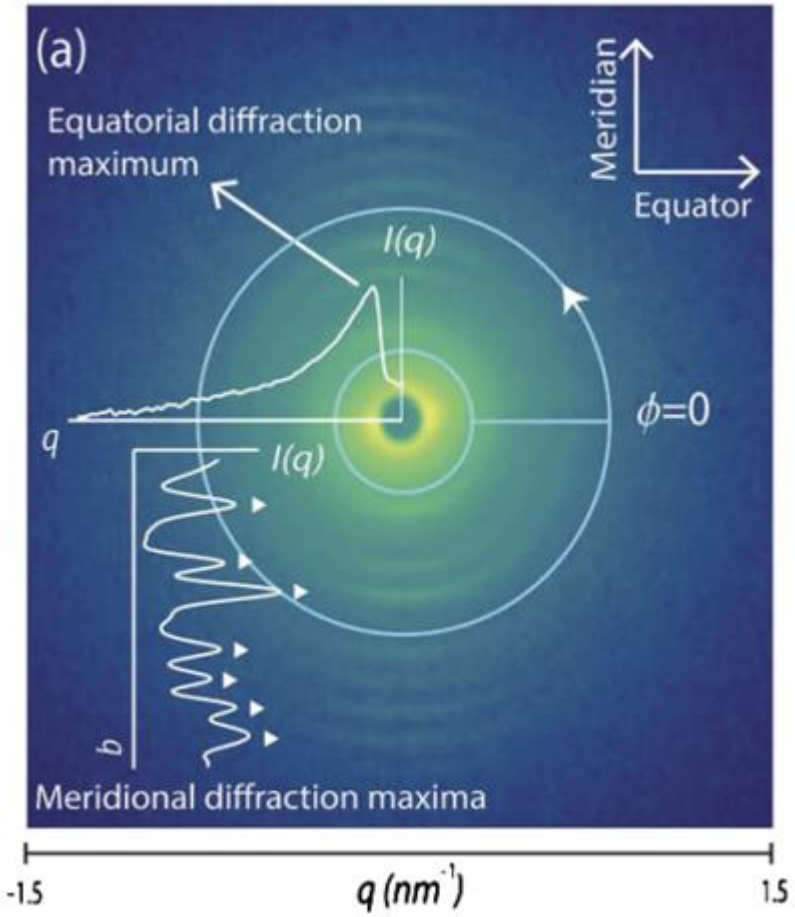

Figure 2.7. 2D SAXS pattern from cartilage which is constituted by the meridional diffraction maxima are indicated (from which the D-period is determined), the equatorial diffraction maxima and background diffuse scatter[89].

Mollenhauer *et al.* (2003) used SAXS to identify the orientation of collagen fibrils in the cartilage from both normal and osteoarthritic ankle and knee joints of human cadavers, using the position of maximum SAXD intensity in a radially integrated azimuthal SAXD profile. They found that in the severely degenerated cartilage from OA patients, the fibrils within the deep zone reoriented from transverse to the joint surface – the predominant orientation that is normally found in healthy cartilage. By plotting the intensity distribution as a function of angle and finding the peak intensity angle, the orientation of the fibrils from the horizontal plane was found, supporting existing knowledge of the depth-dependent variation of the orientation of fibrils in cartilage[90]: parallel to the joint

surface in the superficial zone, transitioning to a perpendicular orientation in the deep zone. However, no analysis of the D-period was performed, nor were the kinetics of fibrillar deformation investigated.

In a similar manner, Moger *et al.* (2007) investigated the orientation of collagen in normal and diseased cartilage and subchondral bone of equine metacarpophalangeal joints. They investigated the degree of orientation alongside the direction of orientation via the third order collagen diffraction maxima. Their findings are indicated via colour maps showing the degree of fibrils at a particular orientation through the full thickness sections of cartilage, where the colour represents the scattering peak intensity at a specific orientation and the width of the plot represented the amount of scatter in the distribution as shown in Figure 2.8.

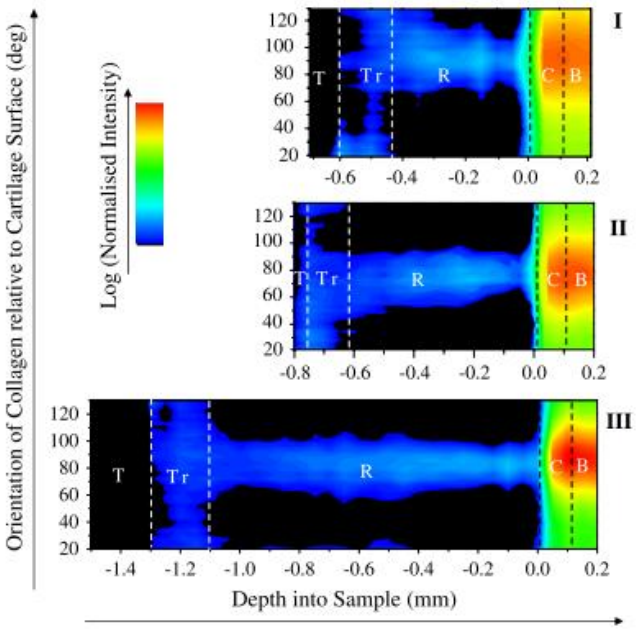

Figure 2.8. Colour maps showing the orientation of collagen fibrils with depth to the surface for different regions within the joint where T refers to the superficial zone, Tr the transitional zone, R the deep zone, C the calcified zone and B the underlying bone[26].

This was then further developed by the same group who investigated the effects of compressive load on fibril reorientation[68]. Using a flat tipped 6 mm long and 2 mm wide indenter, load was applied to the surface of the cartilage in an unconfined indentation test, however data acquisition was triggered at a minimum of 5 minutes after load application in which case the tissue would have relaxed to a particular level and therefore did not represent the immediate response following compression. The load values applied resulted in a range of deformations, from barely perceptible surface deformations to irreversible damage. With surface pressures up to 1.5MPa there were reversible changes in orientation as a result of the compression of the tangential fibers, and as the load was then increased the reorientation propagated into the radial zone. At loads above 6MPa, fibers began to 'crimp' in the radial zone (Figure 2.9). Finally, failure was found to be characterized by a radial split in the deep cartilage which was identified by taking a micrograph[68].

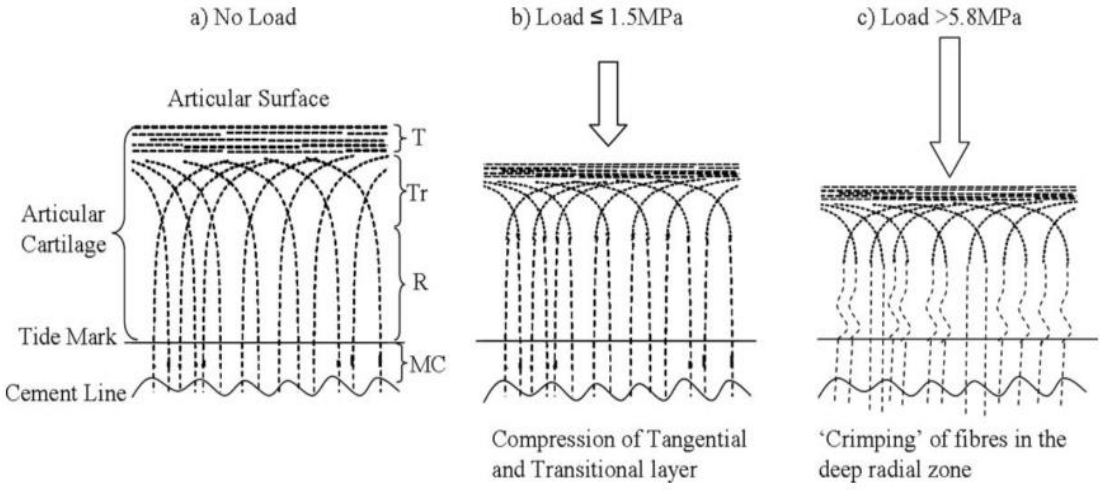

Figure 2.9. Schematic showing the changes in regional collagen orientation in response to (a) no load, (b) loads up to 1.5MPa and loads above 5.8MPa in the superficial zone (T), transitional zone (Tr), deep zone (R) and mineralised cartilage (MC)[68].

While these initial studies provide important information on the SAXS spectra of cartilage, a complete understanding of the biomechanical structure function relations in cartilage – and their alterations in OA – requires a multiscale characterization of fibrillar level strains, stresses, and changes in fibril orientation distribution, in particular in a time-resolved manner as cartilage is subjected to periodic loading. Furthermore, other ultrastructural parameters, including the level of intra and inter-fibrillar disordering or fibril radial distribution changes can be potentially extracted from the SAXS spectra. Such ultrastructural parameters will allow a deeper understanding linking the mechanisms by which load is dissipated throughout the tissue to nanoscale structural changes that have not been previously quantified or observed in cartilage.

2.4. Synchrotrons as high brilliance X-ray sources

To carry out spatially-(~micron scale) or temporally (~ 1 second or below)-resolved kinetic measurements using SAXS on cartilage, high brilliance sources of X-ray radiation are needed. Synchrotrons are highly specialised sources of high brilliance radiation used in the study of advanced materials and their properties. The very first synchrotron radiation was observed in 1947 and only became a research tool during the mid-1960s primarily as a by-product of experiments in nuclear and particle physics, utilising very low energy in the range of several hundred MeV, whereby radiation was a side effect of particle accelerators[91]. Since then synchrotron radiation has been developed such that a much wider range of X-ray sources are available with an equally wide range of applications. The light generated by synchrotron is through the generation of electrons via an electron gun which are then fired into the three particle accelerators, the linear accelerator (LINAC), the booster synchrotron and the large storage ring, where the particles are accelerated to very high speeds (Figure 2.10(a)). Once inside the storage ring (which is maintained as a vacuum), the path of the electron beam is bent by the magnetic

undulators (insertion device), forcing the electrons to follow an undulating trajectory, which cause the electrons to emit energy in the form of light. The undulators are made up of a complex array of small magnets and changes in the gaps between the rows of magnets allow fine tuning in the wavelength of the generated X-rays (Figure 2.10 (b)). The photons that are generated are then channelled from the storage ring into the individual beamlines, where the beam can be further refined to the specification of the user[92,93].

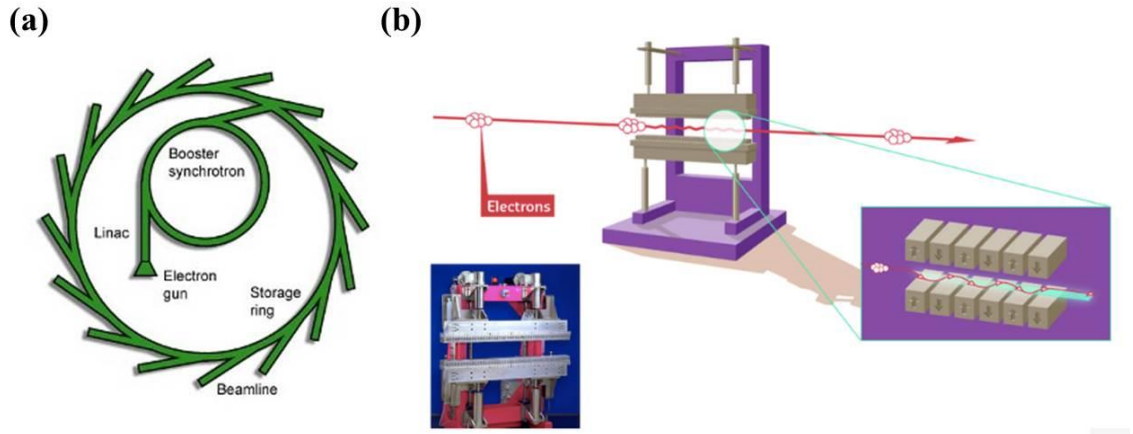

Figure 2.10. (a) Schematic of a synchrotron facility[92], (b) schematic of an undulator where the incoming electrons are indicated and are passed through a panel of magnets that alter the path of the electrons causing them to emit photons[93].

2.4.1. Design of a synchrotron SAXS Beamline

The photon beams generated from the storage ring is sent first through an optical hutch which contains a series of optical components (mirrors and lenses) designed to filter and focus the beam down to the specifications required. These components include silicon mirrors, slits and crystals that are capable of removing certain colours within the synchrotron light as well as to resize the beam down to the μm range. Once the beam is reformed, it is passed through into the experimental hutch where the sample stage is mounted a known distance away from either a single X-ray detector or multiple detectors. When the X-ray beam is applied to the sample, scattered radiation emitted (via the processes described in the previous sections) are incident on the detector, leading to the

acquisition of usually 2D X-ray scattering and diffraction patterns. Controlling exposure times, beam positions on the sample via motorised stages and switching between X-ray scattering and X-ray transmission scanning, and the application of stimuli (mechanical, chemical or otherwise) can be adjusted by users in the adjacent control cabin Figure 2.11.

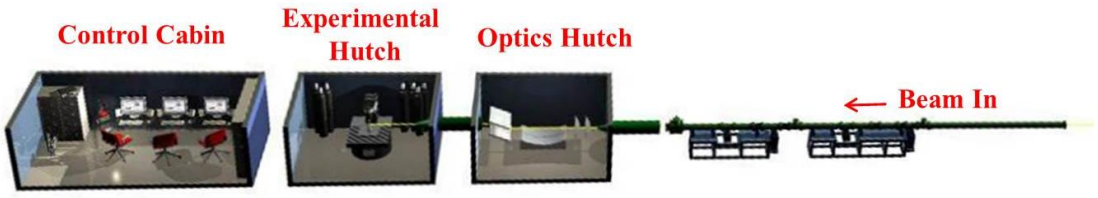

***Figure 2.11. Schematic of a beamline including the control cabin, experimental hutch and optics hutch*[92].**

Two beamlines were primarily used during this project; these were the Non-Crystalline Diffraction beamline I22 at Diamond Light Source (DLS), Harwell (UK) and the High Brilliance beamline ID02 at the European Synchrotron Radiation Facility (ESRF), Grenoble (France). Both beamlines are equipped for SAXS with relatively similar high energy beams (~10-15 keV) with high flux which refers to the number of photons delivered per second and low beam divergence which indicates the spread of the beam at the sample interface. The major difference between the two beamlines is that at ID02 (ESRF) the sample to detector distances can be increased to a (unprecedented worldwide) value of 34m which allows users to access very low wave-vectors (i.e. perform ultra-SAXS or USAXS) – which allows analysis of structural features at scales of ~500 nm and larger, well above the ~1-100 nm typical for SAXS, thus providing resolution at larger dimensions. Furthermore, flux is several (~4-6) orders of magnitude higher at ESRF than at DLS, providing more scattered photons at the sample, higher scattering intensity and better count statistics. At DLS a long-term access programme was granted under the

project specification and therefore provided access twice a year over the course of the project. An ESRF access grant provided one visit per year over two years. The specifications of the beamlines used in this project are presented below in Figure 2.12.

	Diamond Light Source (DLS)	**European Synchrotron Radiation Facility (ESRF)**
Location	I22 Beamline, DLS, Oxfordshire, UK	ID02 Beamline, ESRF, Grenoble, France
Radiation energy (keV)	14	12.4
Flux (photons/s)	3.57×10^{9}	1×10^{14}
Detector type	Pilatus P3-2M (Silicon hybrid pixel detector, DECTRIS)	Rayonix MX-170HS
Average sample to detector distance (m)	1	1
Beam size (μm)	~10-15	~50
Average exposure time (s)	0.5	0.03

Figure 2.12. Specifications of the DLS (left) and ESRF (right) beamlines used for the SAXD X-ray studies described in the current thesis.

2.5. Effects of radiation

2.5.1. Radiation damage

Radiation damage is a factor that must be considered when using high photon flux beams such as those used in this project. It is known that gamma irradiation is able to break down collagen and thus leading to changes in biological and mechanical properties of tissues[94]. The gamma radiation has dose dependent effects and causes splitting of the polypeptide chains of collagen. Gamma radiation is regularly used as a way of sterilization in orthopaedic applications at low levels between 10 to 70 kGy (where 1 Gy refers to the 1 joule of energy per kilogram of matter), however scientific studies that involve X-ray diffraction can lead to exposures exceeding 1 MGy[94,95]. Previous studies investigating the effect of X-ray radiation on the macroscale mechanics of cortical bone (which has largely type I collagen molecules) found that with small doses of radiation the fracture toughness

of bone is reduced[94]. A further study by the same group investigated fibrillar strains which were decreased by ~40% following low doses at ~70 kGy[95].Whilst radiation damage is inevitable when attempting to scan through samples, the effects of the X-ray radiation can be limited by adjusting the radiation dose by controlling the exposure times[96]. Furthermore, the beam can be attenuated via an X-ray absorbing filter made up of metals such as molybdenum or aluminium, which reduce the total dose of photons per exposure by defined levels which can be calculated for each absorber at given energy levels of the X-ray radiation. Finally, it is also important to consider the thicknesses of the samples to be tested, as there is a direct correlation whereby a thicker sample will absorb more of the radiation and thus provide a pathway for radiation damage.

2.5.2. Testing radiation damage

Radiation damage will, potentially, affect both the structure of the collagenous tissue in cartilage at the nanoscale, and alter the mechanics of the tissue as well. Changes in structure at the nanoscale will manifest themselves in changes in the X-ray scattering signal, in particular the loss of peaks arising from periodic stacking of collagen molecules due to radiation-induced breakdown of the staggered arrangement. By minimizing the X-ray exposure time, the radiation damage can be minimized, but too low an exposure time will lead to poor count statistics and too much noise for the SAXS signal to be analysable. Initial tests were conducted at DLS to learn what type of beam settings would provide a sufficient signal from the test sample without exposing the tissue for too long which would lead to radiation damage. A simple exposure time test was performed where between 0.1-5 seconds exposure times were applied to bovine cartilage tissue at different points across the cross-section of the tissue across 5 distinct zones in the depth of the tissue, with and without a X-ray absorbing filter (a 0.05mm sheet of molybdenum), as

indicated by Figure 2.13. Laterally displaced columns indicated progressively increasing X-ray exposure times.

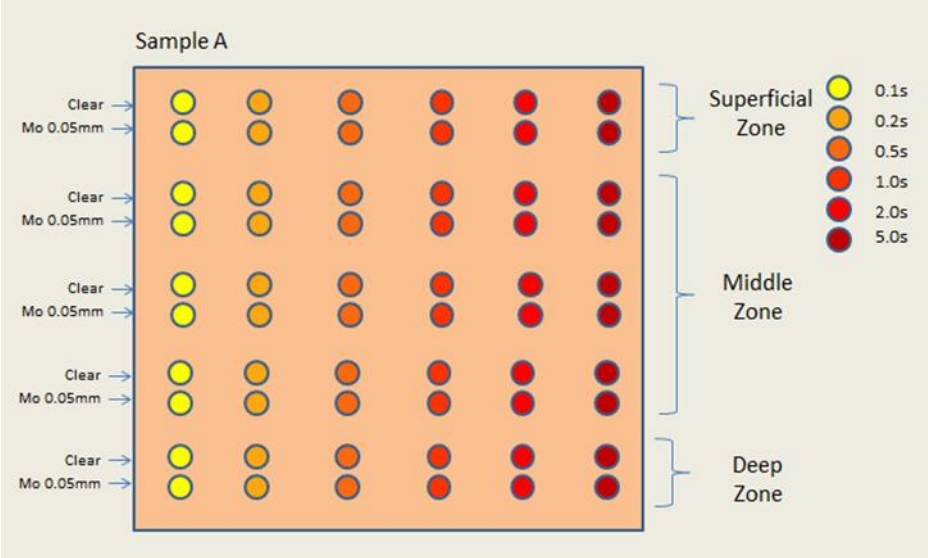

Figure 2.13. Schematic of exposure time test conducted at DLS with varying exposure times, with and without a molybdenum filter.

During the tests it could be identified qualitatively through the SAXS patterns that the longer exposure time combined with the molybdenum filter produced the best observable signal as indicated in Figure 2.14, where representative 2D SAXS patterns from the deep zone are shown.

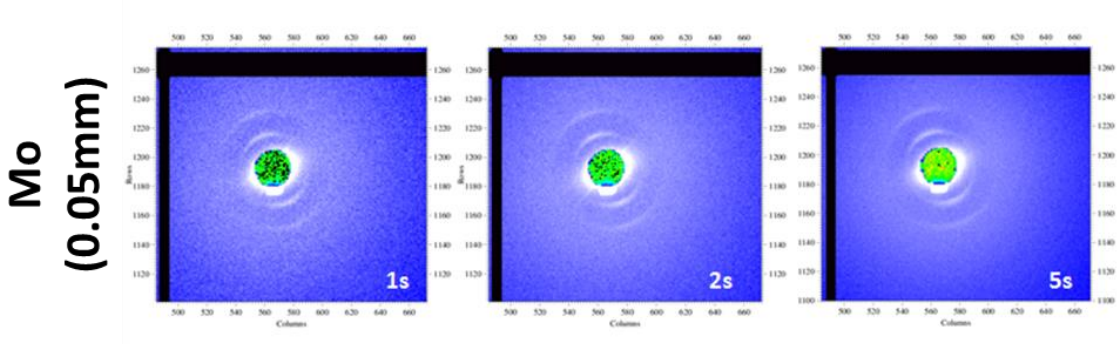

Figure 2.14. Representative SAXS patterns with varying exposure times within the deep zone with a molybdenum filter.

Based on prior work in bone conducted by the Gupta group, a molybdenum (Mo-) filter was used to attenuate the beam to the lowest possible exposure time consistent with good signal statistics. Specifically, to quantify the effect on the SAXD signal due to the difference in exposure times, and to consequently identify the lowest time needed to get a sufficient signal, the standard SAXS/WAXD analysis tool Fit2D[97] was used to generate integrated intensity plots that measured the scattered intensity across the radial (q) direction from the beam centre, with a special focus on the strongest (third order) meridional Bragg-peak. In Fit2D the radial coordinate is *q* and the angular coordinate is denoted χ as shown in Figure 2.15.

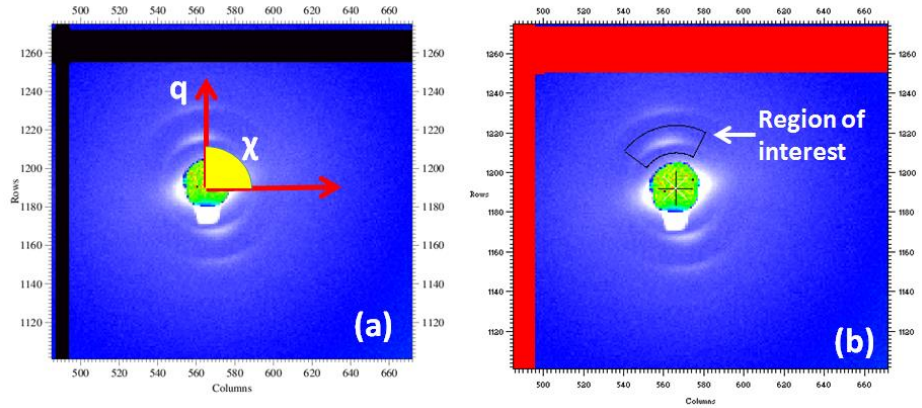

Figure 2.15. (a) Coordinate system used in Fit2D where q represents the radial coordinate (i.e. scattering vector position away from the centre) and χ represents the angular coordinate, (b) region of interest (i.e. cake sector) that is integrated over to generate intensity profiles.

The total peak intensity was then determined by taking the area under the I(q) intensity plots. What can be observed (Figure 2.16) is that there is a linear correlation between exposure time and peak intensity for the times that were used within this test. Radiation damage will damage the staggered D-periodic arrangement of collagen, which will in turn reduce and eliminate the meridional Bragg-peaks. As a result, no further intensity will accumulate in the wavevector region corresponding to these peaks. It can be therefore

seen that during a long exposure time during which radiation damage is occurring, the Bragg peak intensity would first increase proportional to the exposure time (and photons incident), but then saturate to a constant value when further exposure does not continue to increase the scattered intensity in the Bragg peaks. We observe no such sign of a reduction in intensity or approach to a saturation value, and it may therefore be concluded that an exposure time of 0.5 seconds was adequate to gain an analysable signal with minimal radiation damage.

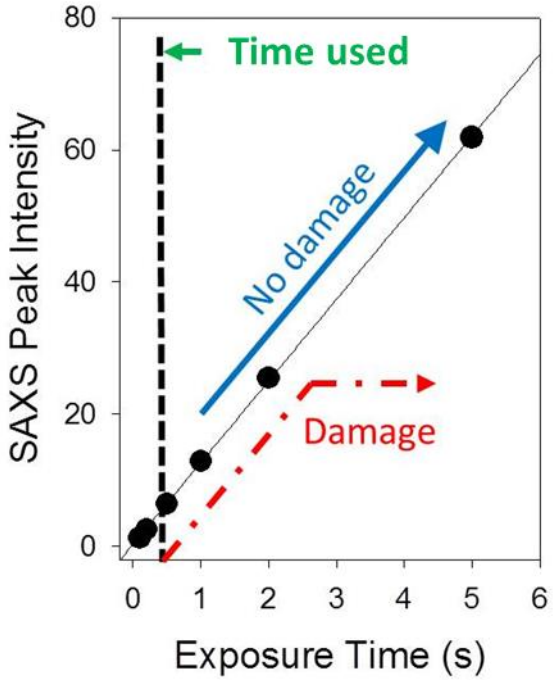

Figure 2.16. SAXS peak intensity with varying exposure times (from the data acquired as in Figure 2.14) showing a linear trend.

2.5.3. Methods of dose control

Alongside exposure times and attenuation, there are other methods that can be used to minimise radiation damage further. To begin with, the beam sizes used across all experiments were in the micron range (~10-15 μm) whereas the sample itself was between 500-1000 μm in terms of tissue thickness perpendicular to the beam. Therefore, the whole

tissue is not exposed each time a measurement is taken, but a narrow tunnel region through the sample with a 10-50 micron diameter (Figure 2.17).

Alongside this, the cartilage sample can be moved relative to the beam, as it is mounted in a micromechanical setup which is itself on a two-axis sample stage driven by DC-motors, in the experimental hutch. Progressive translation of the sample stage between X-ray diffraction measurements can be set up such that the same region was never exposed more than once (Figure 2.17). The step-size for each movement was twice that of the beam diameter. In some instances, a motor-control script can be written (with the help of the technical staff at DLS I22 or ESRF ID02) to perform continuous motion of the sample stage within a fixed region as opposed to a complex stepwise script for every individual motor movement. Given that the beam size (~10 μm) is very small relative to the zones within cartilage (~100s of μm), it is possible to carry out sequential offset exposures for multiple points whilst still remaining within the same zone. Here we assumed, given the zonal isotropy transverse to the joint surface (vertical surface of the cartilage sample), that the relative response of the fibrils laterally within a region could be assumed to be on average the same.

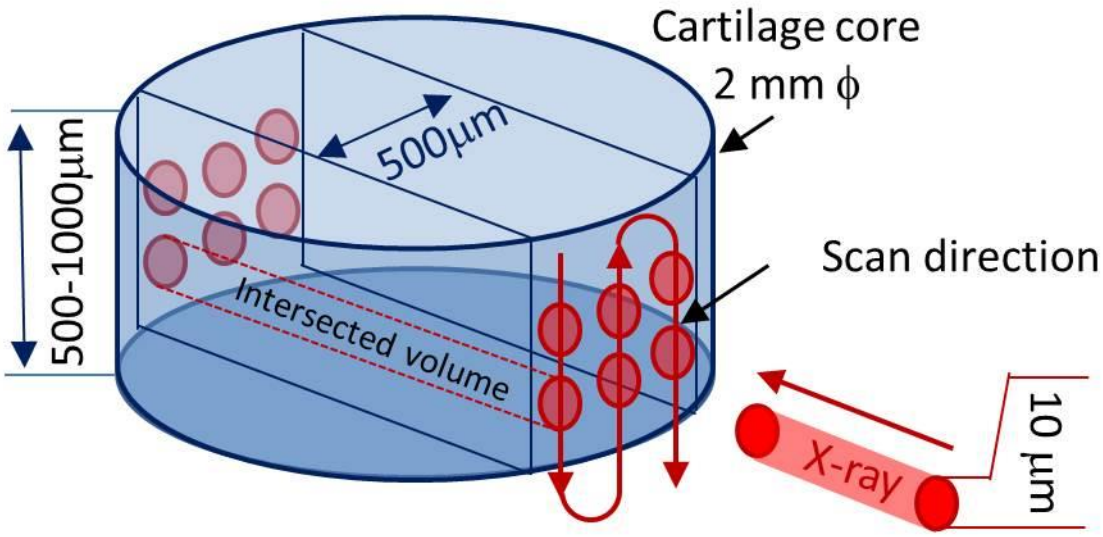

Figure 2.17. Schematic of beam application during SAXS measurements. The X-ray beam ranges from 10-15µm and is applied within a fixed region of 500µm within the centre of the sample to maintain the scattering/intersected volume.

Finally, to check whether the radiation is affecting the cartilage mechanical properties, the tissue level mechanics measured without X-ray exposure were compared to those obtained during synchrotron experiments. It was observed that there were no differences in parameters such as tangent modulus where both the in house and beamline measurements were around 5MPa.

2.6.Synchrotron in-situ and scanning experimental design

2.6.1. SAXS scanning

Micro-beam synchrotron SAXS can be used as a tool to measure both the time-variation of ultrastructural parameters in a particular region of interest within a sample as well as providing a way of measuring 2D variations in a sample with microscale heterogeneities in the average nanoscale structure. Given the ability to acquire a SAXS pattern with sufficient statistics within a second or less at the synchrotron, large areas of a tissue can be scanned within 10-15 minutes dependent on step sizes, allowing for microscale maps

of 2D SAXS patterns to be formed, with each pattern containing information on nanostructural parameters that are obtained on further reduction of the 2D pattern, and their gradients evaluated[98]. When combined with a small diameter (tens of microns down to a few hundred nm) X-ray beam at modern micro- and nano-focus beamlines, the ability to control the sample relative to the incoming X-ray allows for highly accurate position resolved analysis of the localised nanostructure.

A well-established example where SAXS scanning has been used to image the hierarchical structure is in the case of bone[78,99]. Given that bone is characterized by the presence of a structural hierarchy formed of collagen type I fibrils with embedded mineral particles, SAXS has been used to study both structures (mineral and fibrils) in terms of size and positional variations across the tissue, although the majority of published work concerns mineral as it scatters much more strongly than collagen. SAXS scanning in trabecular bone is one of the original examples where SAXS scanning was used to measure nanostructural parameters such as the particle orientation, degree of orientation and thickness as indicated in Figure 2.18[99,100].

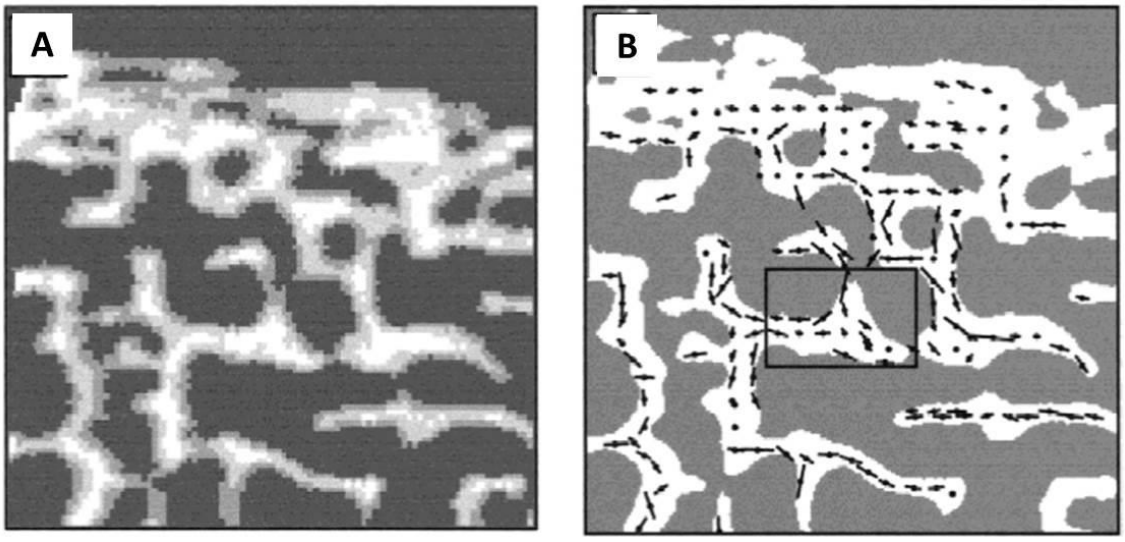

Figure 2.18. (A) Radiography of a trabecular one specimen where the light grey shows the trabecular structure whilst the darker region corresponds to the marrow space filled with resin, (B) Arrows indicating the predominant orientation of the mineral crystals via their directions whilst the length of the arrows indicate the degree of orientation (adapted from Rinnerthaler et al. (1999)).

As a second example, Figure 2.19 below shows an example of a 2D SAXS scan performed on the osteon (the building block of cortical bone) to generate a binned intensity plot as shown in inset (a). This plot is generated by rebinning (down-sampling) the 2D SAXS image from a scan (to enable smaller total memory size when rendering) and plotting the rebinned patterns in terms of a greyscale. What can be observed qualitatively from the individual SAXS patterns (b,c) is that there is scattered intensity shaped in the form of an ellipsoid. The shape (and degree of anisotropy) of the ellipsoid can be linked to the dimensions of the plate shaped mineral particles in this particular bone type. For collagen, the evaluation of the 2D SAXS patterns – in particular, the analysis of the D-period, and fibril orientation from each pattern and its representation – will be described later in this chapter.

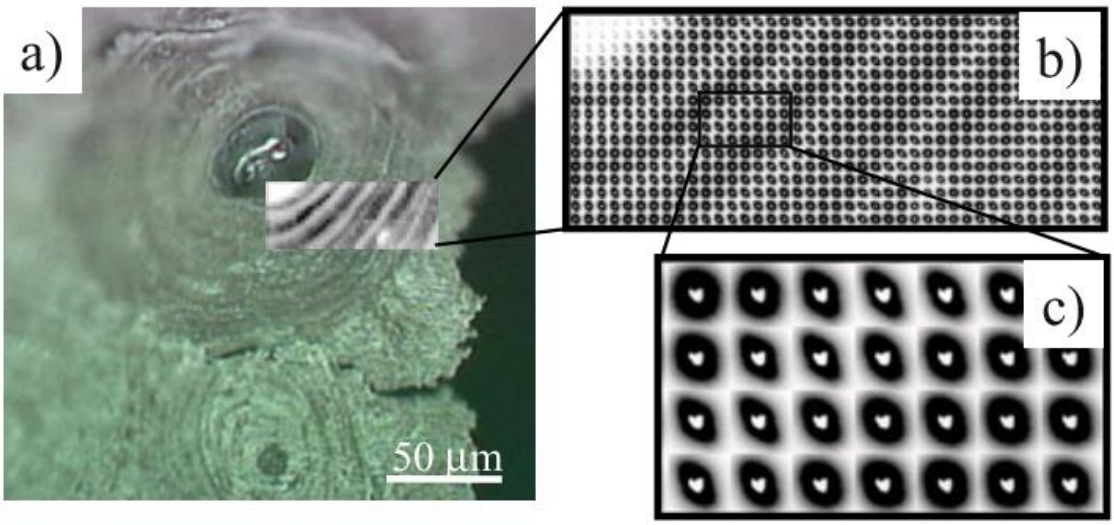

Figure 2.19. SAXS imaging of a single osteon where (a) is a light microscopy image with an inset image of SAXS intensity within the region. The SAXS intensity derived from the 2D SAXS scan (b) which when looked at individually shows the minerals in the individual scattering patterns (c) possess a preferred orientation.

2.6.2. Area scanning of cartilage

On the subject of 2D area scans of biological tissues, we here describe an example of a 2D SAXS area scan of a full thickness bovine cartilage sample carried out at DLS. The experiments (described in more detail in **Chapter 4**) were carried out to gain a better understanding of the variation in collagen fibrillar ultrastructure both in the depth from the surface as well as laterally within each zone. A zone within the middle of the sample (sample size 20 x ~7 mm) of width 0.5 mm was used to perform the scan in order to ensure that the scattering volume remained relatively constant. The motorised sample stage was used to move the sample relative to the beam with step sizes in the vertical (y-) direction (perpendicular to the tissue surface) of 45µm (~3× beam diameter) and in the horizontal(x-) direction (parallel to the tissue surface) of 50µm as indicated by Figure 2.20. The 2D SAXS scan was performed in an unstrained sample which was kept hydrated throughout, with a fixed exposure time of 0.5s. What can be observed qualitatively (without any further analysis of each SAXS pattern) is that there is not a great deal of

variation in the x-direction, as would be expected from the tissue homogeneity in this direction, while the main heterogeneity in the 2D patterns exists in the y-direction i.e. through the thickness of the sample.

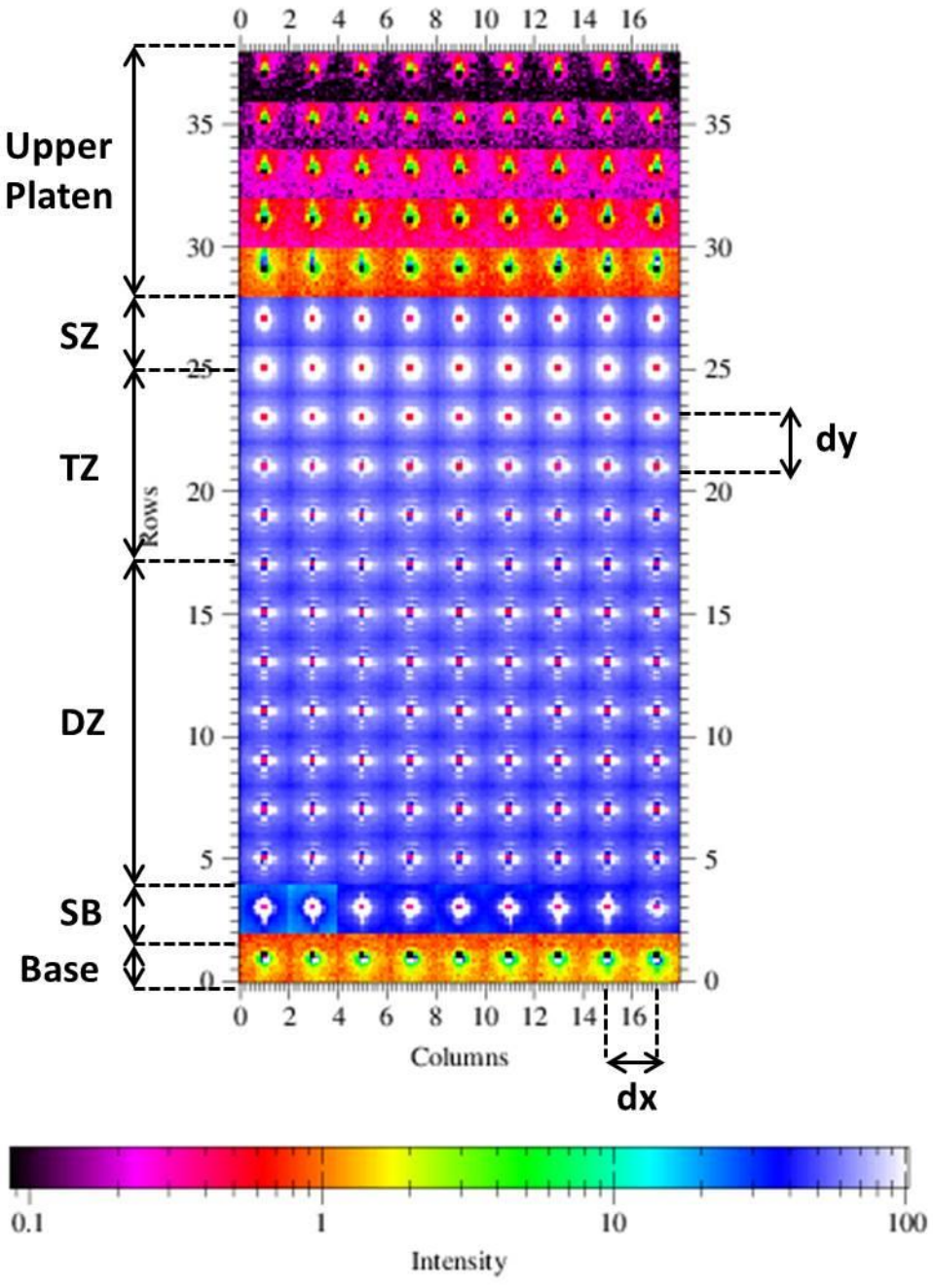

Figure 2.20. 2D SAXS scan grid in full thickness bovine cartilage, where the superficial zone (SZ), transitional zone (TZ), deep zone (DZ) and subchondral bone (SB) can be observed. Grid plot generated using Fit2D[101].

2.6.3. Depth-dependent scanning

Given that the SAXS patterns are homogenous along the horizontal (x-) axis, as would be expected from the structure of cartilage, we then turned our focus to the depth-dependent nanoscale properties (as a function of the y- or vertical direction). More refined single line scans were performed with 2× the beam diameter steps, to further increase the spatial resolution of observed differences through the thickness of the tissue. It was observed that there are 3 distinct and qualitatively different SAXS patterns obtained from each zone within the tissue. Figure 2.21 shows sample SAXS patterns that were gained for each zone of cartilage. The first pattern (a) shows that the predominant orientation is parallel to the surface which can be identified qualitatively through the peaks being found on the left and right of the beam stop. The next pattern taken 6% further down the sample into the transitional zone (b), there seems to be no preferred orientation as suggested by the peaks being almost full rings of intensity. Finally, in the deep zone the fibrils show preferred orientation close to perpendicular to the articular surface as shown by the strong peaks above and below the beam stop.

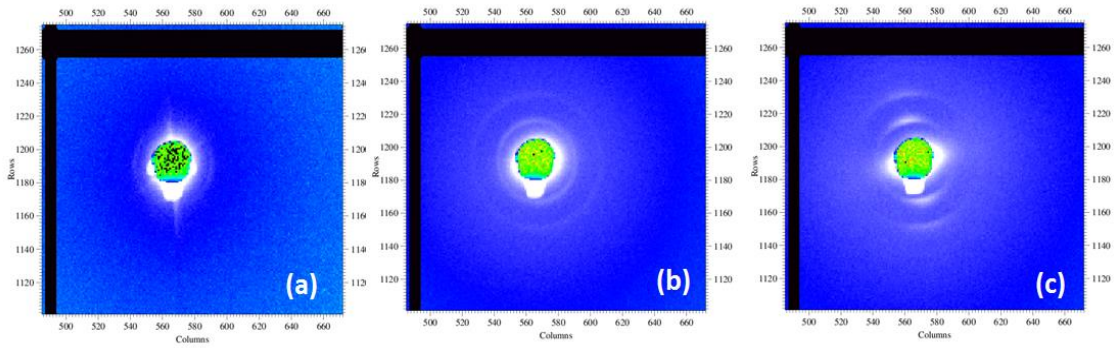

Figure 2.21. Representative SAXS patterns obtained from the (a) superficial zone (SZ), (b) transitional zone (TZ) and (c) deep zone.

2.6.4. In-situ mechanics

The complementary synchrotron SAXS analysis to microbeam mapping is *in situ* analysis, which is based on localizing the beam to a spot (or homogeneous region) while

applying an external stimulus to the sample. In this thesis, that stimulus is a mechanical load. SAXS patterns were acquired simultaneously with *in situ* mechanical deformation data by integrating a micromechanical tester into the beam line. Based on a previously made micro-mechanical frame[102], a modified micro-compression tester was mounted onto the motorized stage within the experimental hutch as indicated in Figure 2.22. This sample stage can be moved in the x, y and z direction and therefore allows alignment of the sample in relation to the beam.

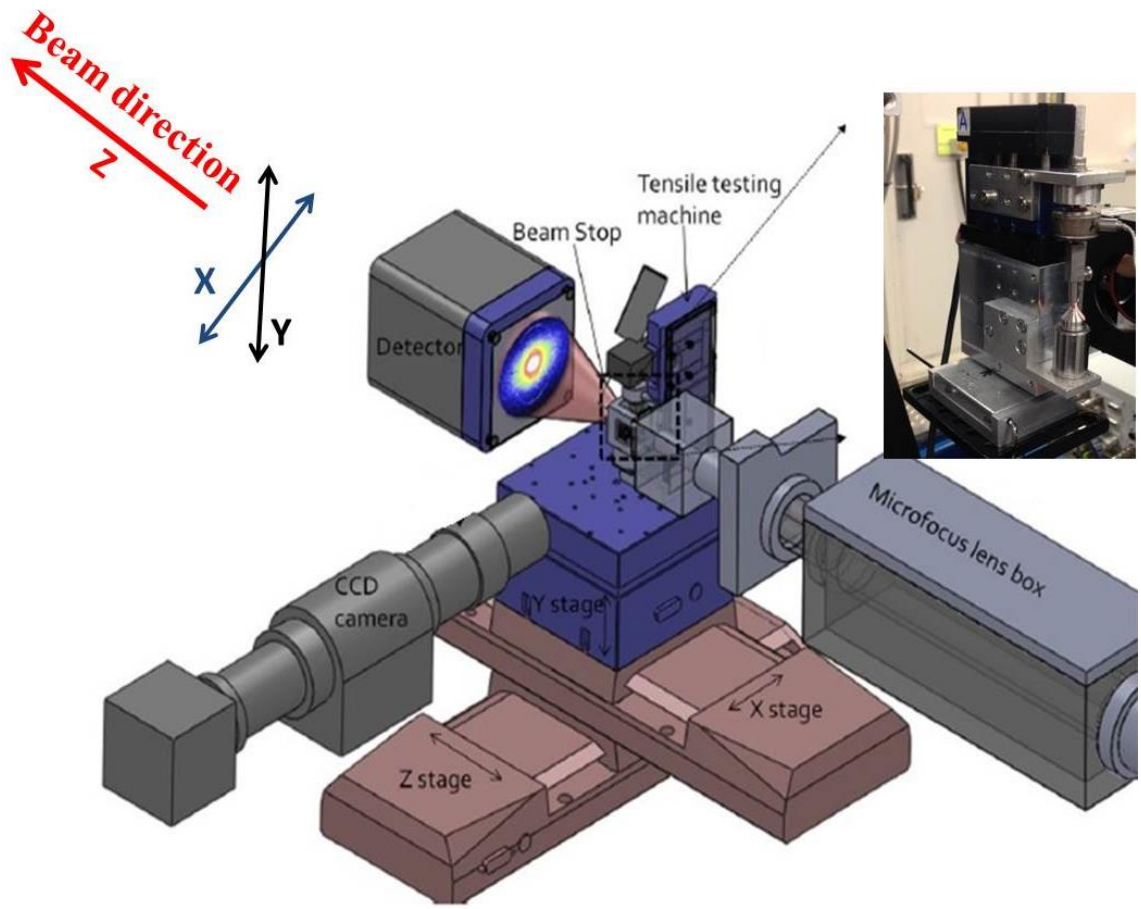

Figure 2.22. Beamline setup at DLS where the micro-mechanical tester is mounted onto the motorised stage.

2.6.5. Sample holder design

The micro-compression tester consists of a frame on which a M110.1dg motor is mounted (Physik Instrumente (PI) GmbH & Co, Germany)) to which a 22N load cell (Richmond Industries Ltd, UK)) with the custom made loading platen are attached. The newly designed base holds the specialized sample holder. Initially, a method of implementing confined compression was designed and used to both simplify parameters required to analyse the mechanics whilst also performing tests that are closer to what occurs in regular physiological conditions in the joint. Confined compression refers to confining or eliminating the lateral deformation of the tissue when loaded vertically. The details of the confined compression tester can be found in the Appendix A.1. Taking into account the confining walls (which absorb X-ray radiation), it was essential that there be an inlet and outlet for the beam (which is ~ 10-20 μm). The inlet had to be wide enough to scan an area of the tissue whilst the outlet had to provide a wide enough exit for the diffracted radiation to emerge without shadowing. As only very low Bragg diffraction angles $2\theta < 5°$ are of relevance for the meridional Bragg peaks from collagen, a relatively narrow 0.5mm slot was sufficient.

However, for the majority of the experiments in this thesis, the confined compression design was later simplified to an unconfined compression setup, as we found that beam absorption from the side-walls due to imperfect alignment of the confined compression chamber with the direction of the beam was unavoidable in practice. An unconfined compression test also allowed access to the sample from outside to allow sufficient hydration of the sample during longer term tests. A schematic of the setup is shown in Figure 2.23).

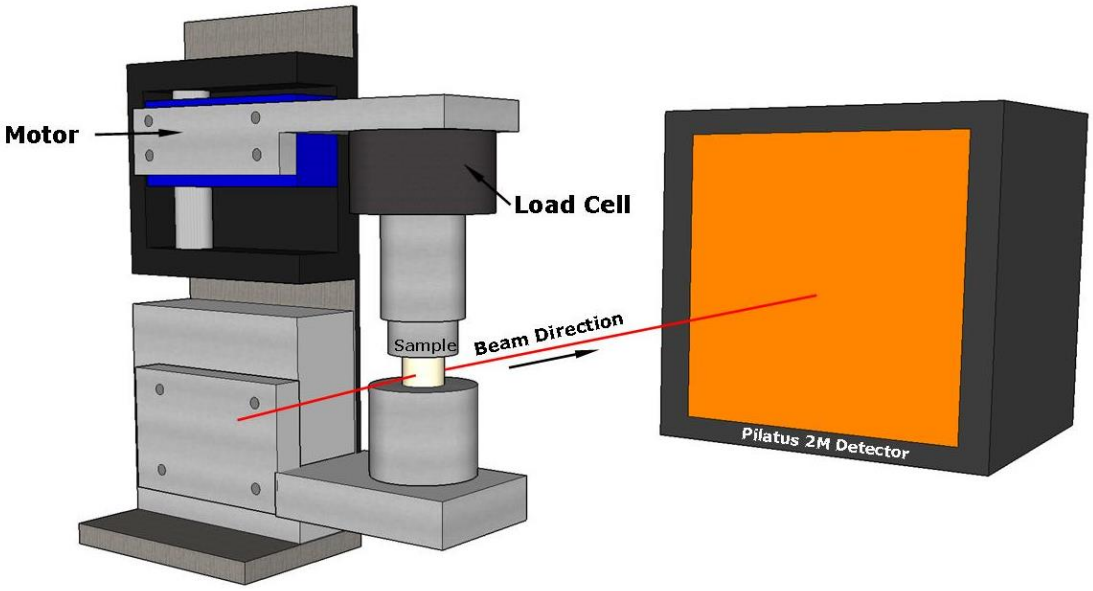

Figure 2.23. Schematic of micro-mechanical tester setup showing the upper arm attached to the motor consisting of the load cell and loading platen alongside the lower block and base in line with the beam, with the detector indicated in the background.

To finalize the designs of the parts discussed above, many different prototype designs were generated using 3D modelling software such as SolidWorks (2012, x64 edition), which were regularly evaluated and critiqued in group meetings, and modified until the final design was produced. Part drawings of the final concept can be found in Appendix A.2. The final design included a 2mm circular indenter than was controlled with the upper drive motor, and a cone shaped sample base which the 2mm discs of cartilage were placed as shown in Figure 2.24. For hydration, a droplet of PBS was used to hydrate the sample, which was adequate for the time frame of 5-10minutes during each test.

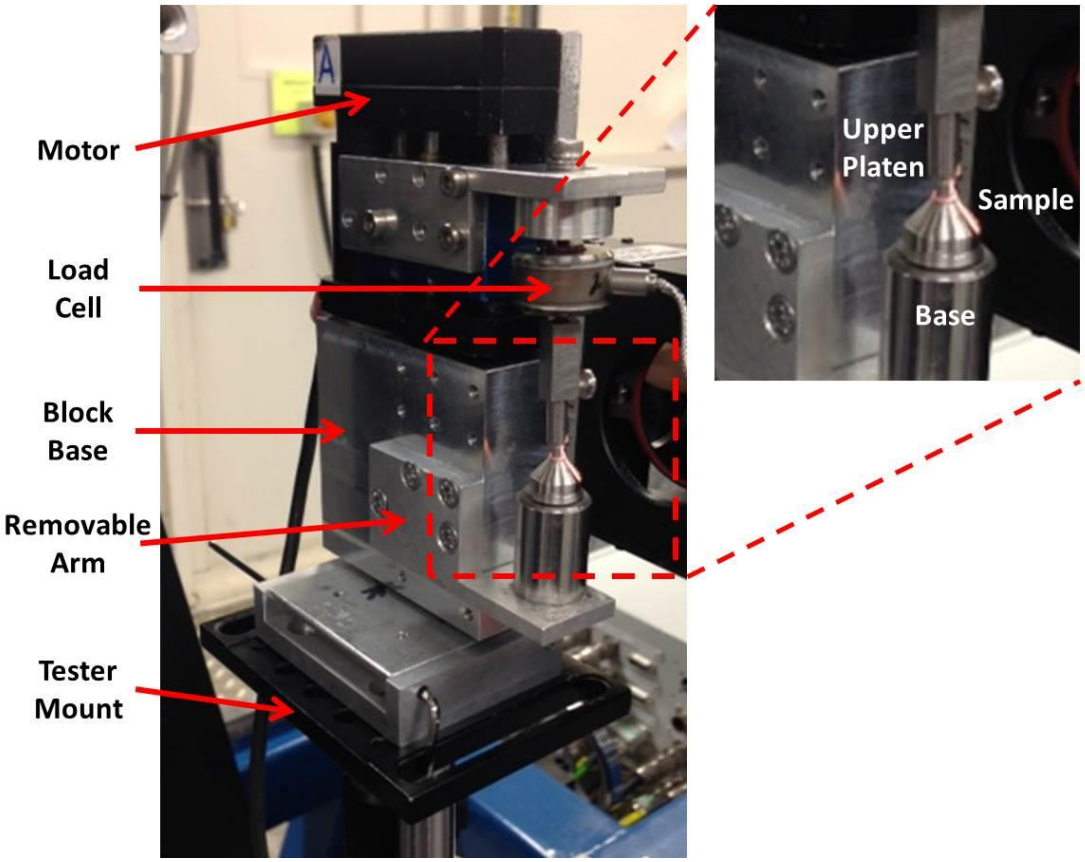

Figure 2.24. Image of micro-mechanical tester with adapted sample holder and loading platen.

2.6.6. Stress-relaxation loading protocols

Two main types of time-dependent loading protocols were applied, during the *in situ* loading of cartilage combined with synchrotron SAXS. These are (a) stress-relaxation, which is the application of a strain during a ramp-up phase, followed by a hold-period where the tissue strain is constant and (b) cyclic loading, where a cyclic strain profile is applied to the tissue. During the stress relaxation tests, the SAXS measurements involved a combination of line scans and single acquisitions. These experiments were conducted at the I22 beamline at DLS. The micro-mechanical tester was controlled by a customised LabView (National Instruments, UK) programme designed for stress-relaxation compression tests, developed with the help of Jun Ma (technician, SEMS QMUL). The laptop with the control software was kept within the experimental hutch and connected

to the local-area network so that it could be managed remotely from the control cabin, using the Windows Remote Desktop feature. Sample thickness was first measured using a calibrated digital Vernier calliper to input into the programme, and used to convert strain rates and levels to applied motor speeds and displacements. Samples were then mounted onto the tester and a 0.1N tare load was applied to the sample to ensure that the loading platen was correctly in place on the sample prior to commencing the test.

Transmission scanning (with the use of a diode) was utilised to find the central position within the sample where each line scan was initiated from using a relative scan (details of the commands and scripting can be found in Appendix A.3/A.4). Initially a line scan was performed through the thickness of the sample in the unstrained state, followed by the stress-relaxation test, and then finally a line scan performed in the strained state- what will now be referred to as static scanning. Figure 2.25 shows a schematic of the static scanning protocol with a representative plot of load versus time for a stress-relaxation test at 20% strain level loaded at a rate of 20%/min. As indicated by the figure, there were less SAXS patterns acquired within the sample post compression, as expected due to the displacement of the upper platen and the compression of the tissue. However, the tissue strain in cartilage cannot be considered uniform: given that cartilage possesses a depth-dependent strain profile[15,58] with higher strain in the superficial compared to transitional zones, point to point comparisons of SAXS patterns are quite difficult in this configuration.

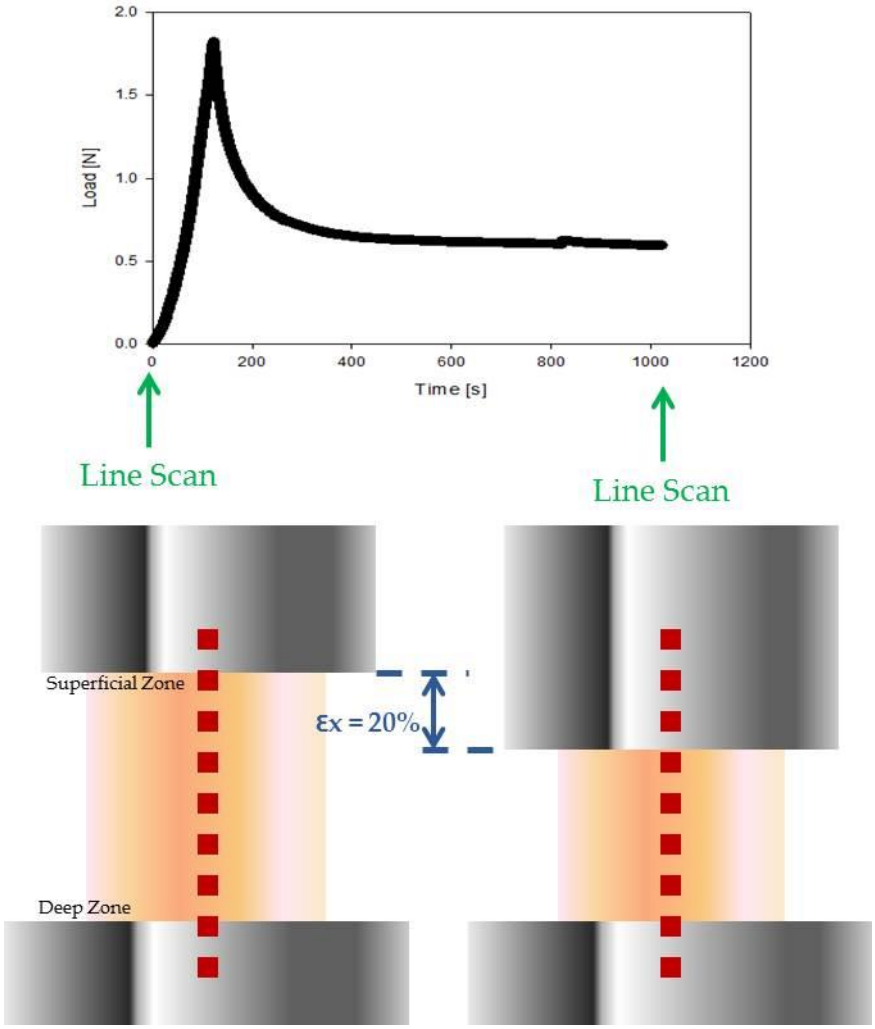

Figure 2.25. Schematic of static scanning with representative mechanics data from a stress-relaxation test at 20% strain level at 20%/min strain rate. Here a line scan was first performed through the full thickness of the tissue prior to strain application and a further line scan performed on relaxation of the tissue.

A new method was then developed to perform scripted scanning of the tissue *during* the stress-relaxation tests, which we refer to as dynamic scanning to distinguish it from the pre-compression and post-compression scanning tests described in the previous paragraph. A region of interest was first identified by first performing a SAXS line scan and looking qualitatively at the resultant patterns. The sample stage was then positioned so that the beam was within the region of interest i.e. the deep zone. Initial experiments involved scanning during the relaxation phases alone as indicated by Figure 2.26. The

stress-relaxation test would be started using the control software, and at the start of relaxation a customised script to acquire a series of SAXS images was initiated to begin scanning within the region of interest (Appendix A.4). These scripts were written in Python, integrated into the control systems Generic Data Acquisition (GDA) framework at BL I22 (Diamond) and Experimental Physics and Industrial Control System (EPICS) framework at ID02 (ESRF). As stated earlier, the sample stage was shifted between each acquisition within a 500μm window to prevent repeat exposures on the same point. Given that the bulk of the tissue level relaxation occurs during the first ~150 seconds, a higher sampling frequency was used for the earlier part of the relaxation. Specifically, the first 15 exposures were every 10 seconds followed by an exposure every 60 seconds for the remainder of the relaxation phase.

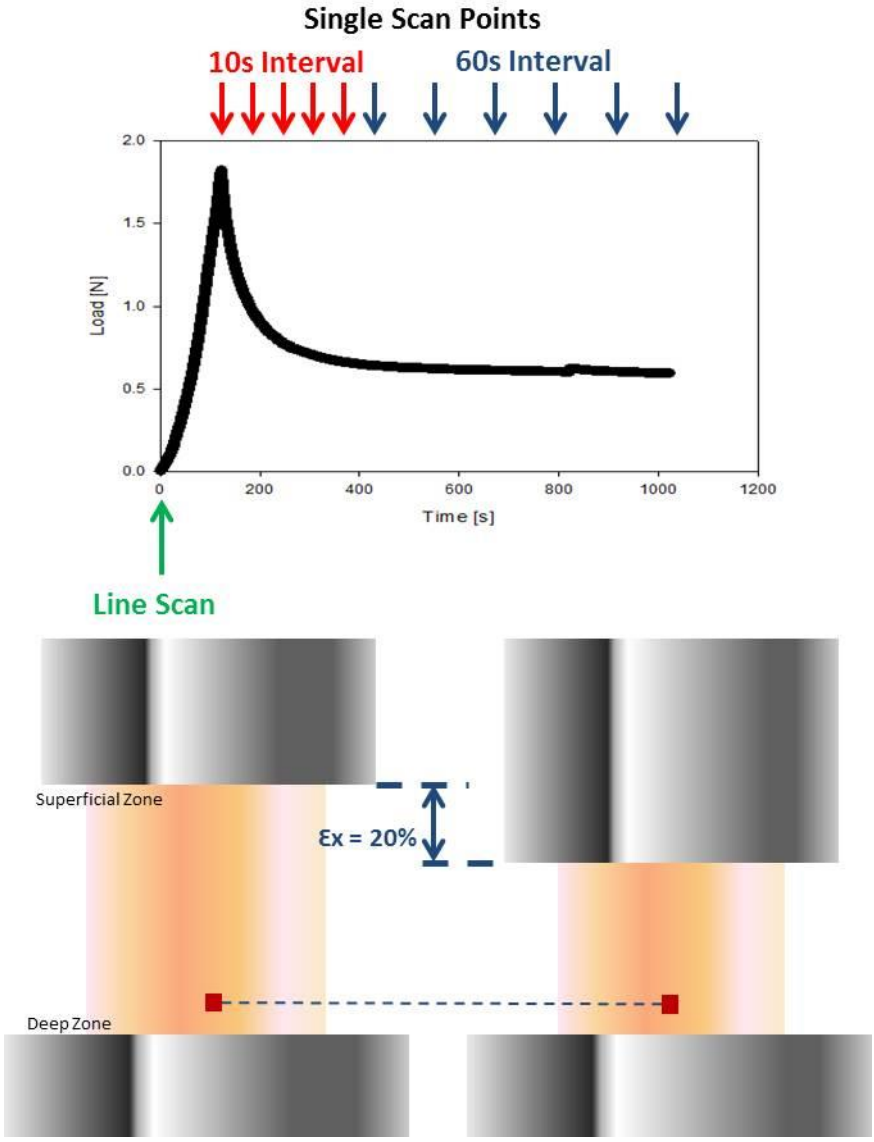

Figure 2.26. Schematic of dynamic scanning regime, where single SAXS spectra are acquired within a region of interest during the relaxation phase at fixed time intervals.

This method was later further refined to also perform SAXS measurements tracking the ramp up phase to measure changes associated with loading, as well as the subsequent relaxation. The scripting was adjusted so that the detector acquisition could be triggered 10 seconds prior to the LabView programme in order to capture the ramp up phase (Appendix A.4.2).

2.6.7. Cyclic loading protocols on cartilage

Cyclic loading tests were carried out to simulate the repetitive loading environment encountered by joints during physiological loading[103–105]. Cyclic tests were conducted at beamline ID02 (ESRF, Grenoble) using the micro-mechanical tester in the unconfined configuration. As with DLS, the tester was mounted onto the motorised sample stage at ID02 beam line as indicated in Figure 2.27. The principles of using this beamline are the same as ESRF with different scripting and user interfaces on control computers.

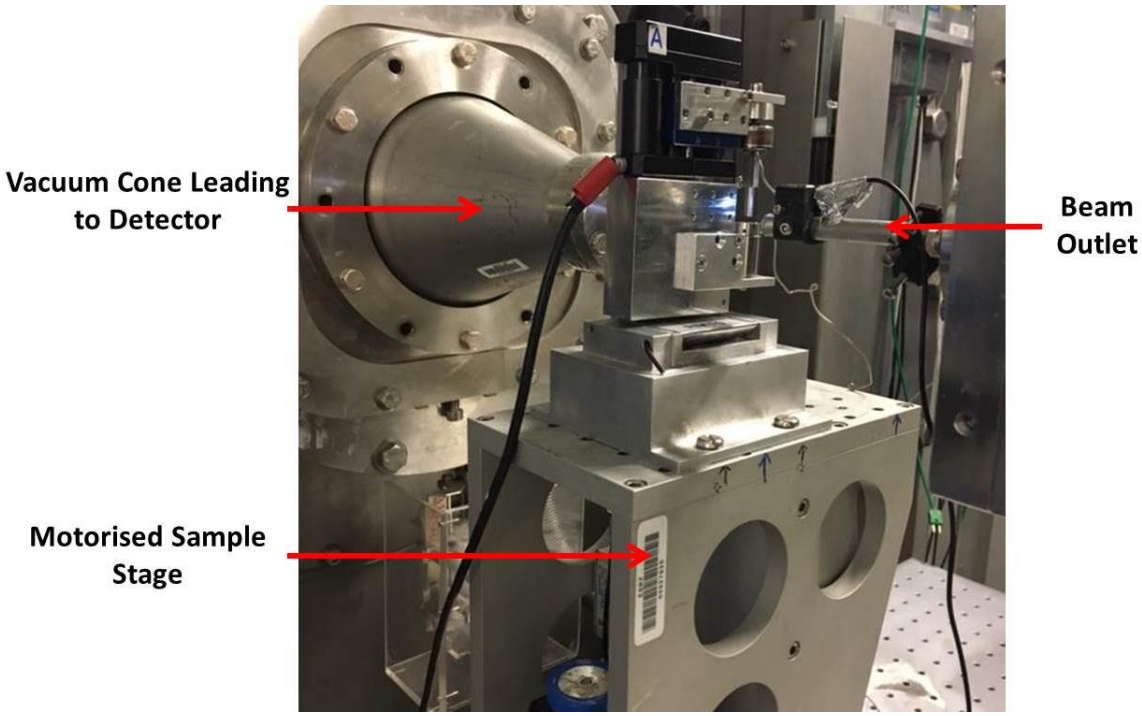

Figure 2.27. Setup of micro-mechanical tester at ID02, ESRF. The tester can be seen mounted on the motorised stage that is adjusted relative to the beam outlet.

As with the stress-relaxation tests, the samples were first scanned in transmission mode to find the centre of the sample where a line scan was performed to find the region of interest. Once located the sample stage was positioned in line with the beam at this particular region and scripting used to both continuously move the sample stage within a 500μm window horizontally (x-direction), and run the SAXS tracking regime. The continuous motion protocol was devised (with the help of Dr. Sylvain Prevost, beamline

scientist at ID02) to minimize radiation damage and repeated exposure of the same point to the beam.

The LabVIEW programme was customised to allow cyclic loading with the ability to vary the rate, strain level and number of cycles applied. To synchronize the acquisition of SAXS patterns with specific points in the loading cycle, a triggering mechanism was introduced, such that a Transistor-Transistor Logic (TTL) pulse was generated at chosen points within a cycle. These TTL pulses were incorporated so that the detector was triggered at pre-defined points within each cycle, specifically at the loaded and unloaded segments of each cycle as indicated by Figure 2.28.

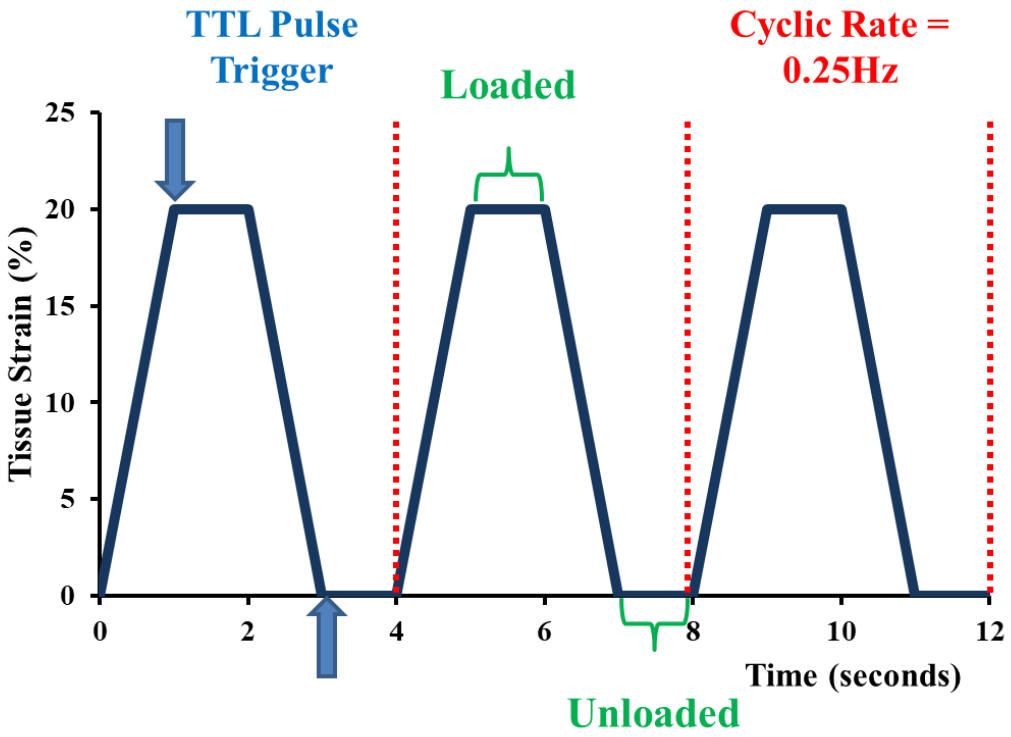

Figure 2.28. Example cyclic loading regime utilised at ESRF with first 3 representative cycles at a cyclic rate of 0.25Hz.

2.7. Analysis of X-ray diffraction

There are a number of parameters that can be extracted from a SAXS pattern. In this project the focus is made on the collagen fibrillar structure and the main factors of interest are fibrillar orientation, degree of orientation, fibrillar D-period and the degree of variability associated with the D-period in both uncompressed and compressed states. Figure 2.29 shows both the coordinate system used as well as a simplistic indication as to how a SAXS pattern can be qualitatively interpreted in terms of angular peak widths.

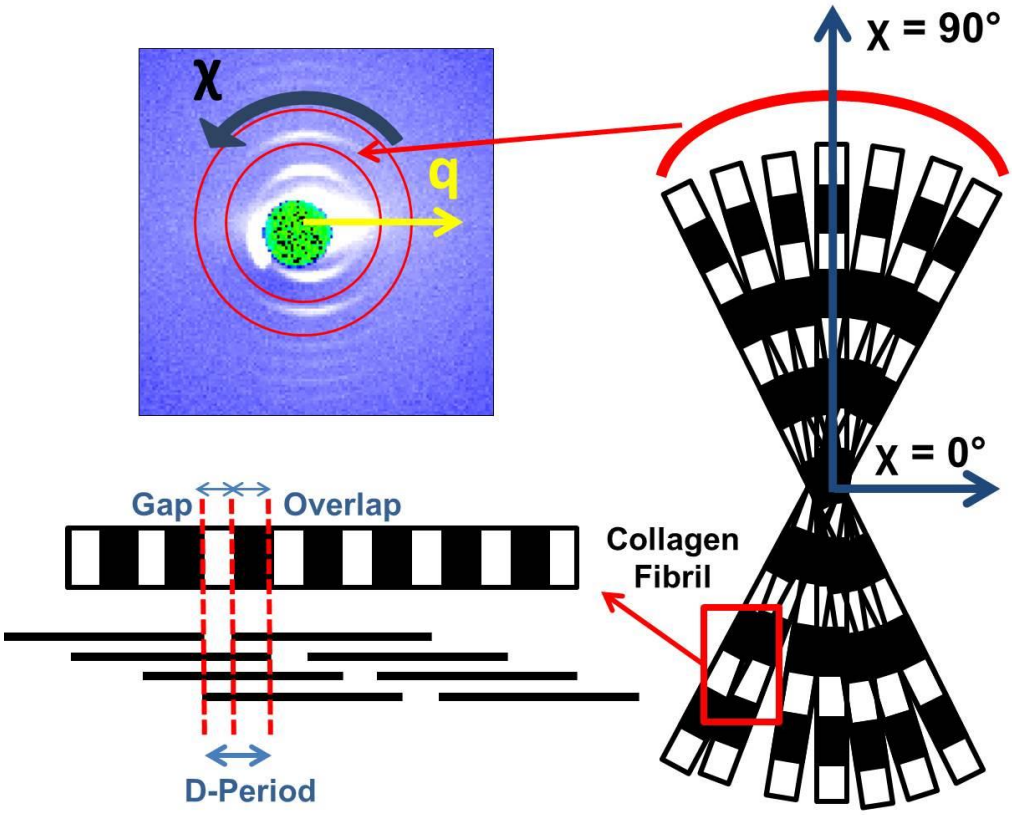

Figure 2.29. Schematic indicated how the SAXS patterns and distribution in reciprocal space translate to fibrillar parameters in real space. The red curve above the fibrillar schematic on the right is representative of the diffraction peak within the red CAKE sector on the left hand SAXS pattern.

Analysis of the SAXS patterns follow a series of steps determining regions of interests, integration, data fitting followed by collation and interpretation of the results. As

indicated by Figure 2.30 below, another level of complexity is contributed by the variation of the key parameters of fibrillar ultrastructure along the thickness of the tissue within each zone, which is reflected in the variable SAXS pattern. Not only is there a change in orientation throughout the thickness, there is also an associated variation in the range of fibrils within a particular orientation indicated by the broader peak fits in the transitional zone when compared to the superficial and deep zones. Furthermore, there is also a depth-dependent variation in D-period and thus associated fibrillar pre-strain as indicated. Extracting this information and interpreting the results are explained as follows.

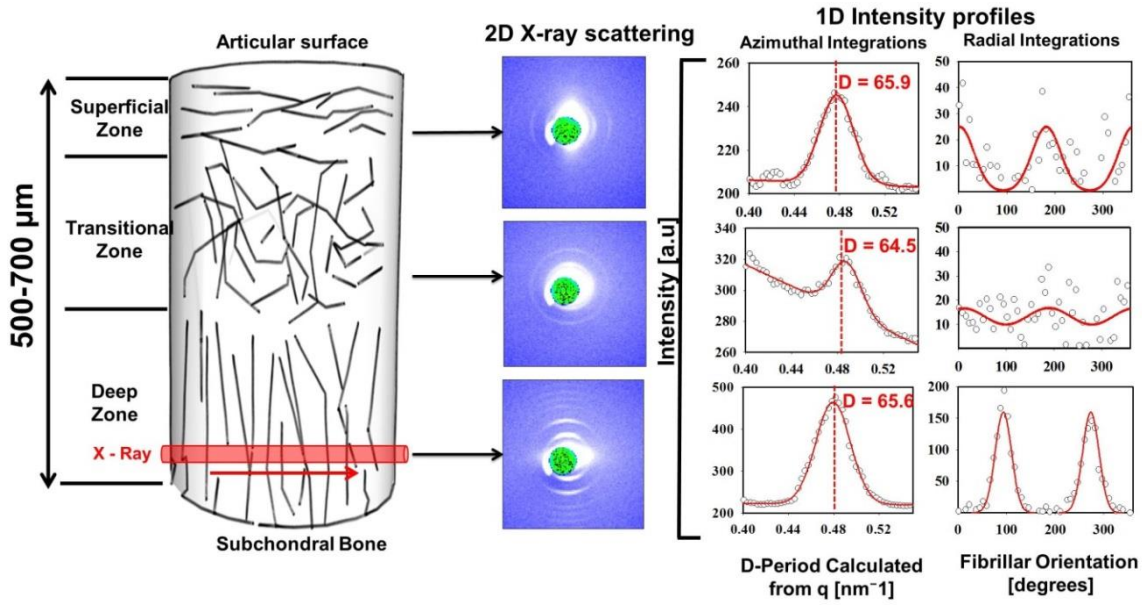

Figure 2.30. Data reduction from SAXS patterns to 1D intensity profiles that are fitted to determine key parameters. To the left is a schematic of the varying collagen distribution with depth into the sample and to the right the associated SAXS patterns from within each zone.

2.7.1. Orientation

The angular width of the peaks are directly correlated to the distribution of the fibrils with the tissue and the predominant direction of the fibrils is determined by the angular position where the majority of the intensity is found. To determine these parameters, the peak intensity is integrated radially around the 5th order Bragg peak (over a wavevector

range of 0 to 360°) to produce a 1D profile of the peak, in each case the data was binned using 100 bins. This is achieved by first determining regions of interests in the form of cake sectors. A 0-360° cake was used to include all the intensity around the beam stop given the regional variation in terms of intensity profiles. First a background subtraction was performed to minimise the influence of background scatter. Regions just inside and just outside of the cake encompassing the peak are used to calculate a ratio that is subtracted from the peak signal using the following equation.

$$I_{Corrected}(\chi) = I_{Original}(\chi) - \frac{1}{2}(I_{Outer}(\chi) + I_{Inner}(\chi)) \qquad \textbf{Equation 6}$$

Once this background subtraction has been completed, the resultant 1D profile is fitted to two Gaussian curves separated by 180° as indicated by Figure 2.31. The fit parameters associated with the Gaussian fit provide the direction of orientation (peak position i.e. χ_0) and degree of orientation (width of the peak fit i.e. w_χ).

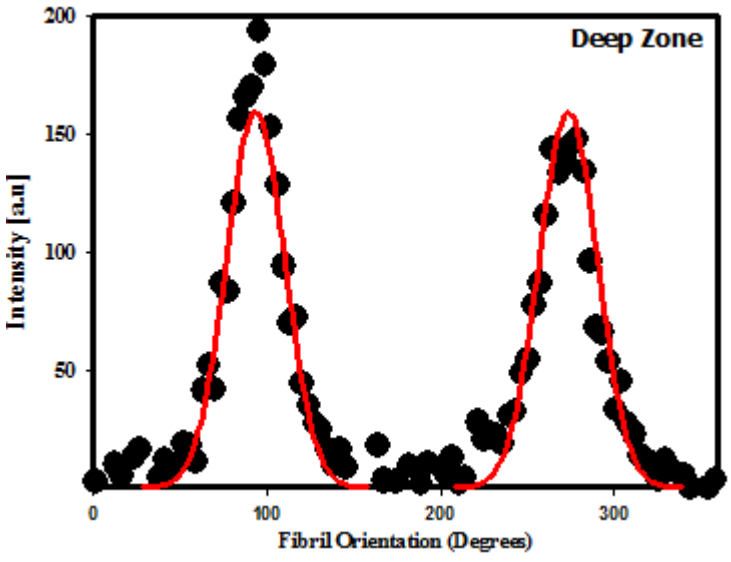

Figure 2.31. Example 1D profile of radially integrated intensity from a deep zone SAXS pattern. The red line indicates the fitting profile of two Gaussians split by 180°.

2.7.2. D-period and Fibril strain

In a complementary manner to the orientation integration, an angular sector (abbreviated CAKE in Fit2D[101] is integrated angularly to determine the 1D profile in the radial direction. Ideally a narrow cake sector is centred at the predominant orientation of the fibrils (χ_0) to ensure that the intensity surrounding the peak is captured, and angular sectors without any meridional Bragg diffraction peaks are not considered. Given that there is a depth-wise variation in the predominant orientation of the fibrils, an automated process was followed for data evaluation. Customized Perl scripts from a pre-existing code base used by the Gupta group to generate Fit2D macros, were updated so that the χ_0 positions were fed into the macro each time so that the CAKE sector was redefined for each new SAXS pattern in the series. In later studies this was simplified to using full 360° cakes as the signal quality was strong enough to generate strong peaks that gave clear 1D profiles for fitting.

The magnitude of the scattering vector **q** (written as q) can be inversely related to the lattice spacing within a crystalline structure, in this case the D-periodicity in the collagen fibrils. Therefore, the peak position relative to the beam centre in q-coordinates can be used to calculate the average local D-period using the earlier Equation 3. To calculate the value of q, first an azimuthal integration is performed to retrieve a 1D radial intensity profile (as shown in Figure 2.32). This profile is then fitted to a peak function that consists of a Gaussian curve and a linear baseline.

$$\boldsymbol{Y_{peak} = Ae^{\left(-\left(\frac{q-q_0}{w}\right)^2\right)} + B1 + B2 \cdot q} \qquad \textbf{Equation 7}$$

where q_0, w and q represent the peak position, meridional peak width and the modulus of the scattering vector respectively[106]. This method has been used extensively before for

bone [69,88,106], mineralized tendon [107], and tendon [70,108]. An example of a fitted $I(q)$ profile from a 3rd order peak integration is indicated below in Figure 2.32.

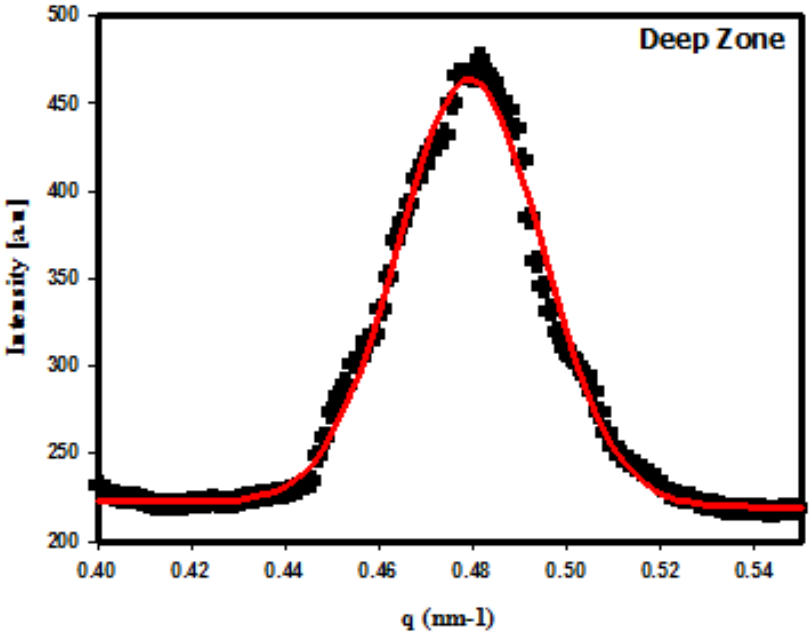

Figure 2.32. Example 1D profile of azimuthally integrated intensity from a deep zone SAXS pattern. The red line indicates the fitting profile of a Gaussian with a linear background.

Using the above as an example, the q_0 value is used to calculate the D-period in nanometres as follows:

$$D = n\frac{2\pi}{q_0} = 3 \cdot \frac{2\pi}{0.298} = 63.25 \text{ nm} \qquad \textbf{Equation 8}$$

Calculation of error associated with fitting

Determining the total error associated with each D-period value obtained is intrinsically difficult to calculate, given that determining the statistical pixel-level error from 2D SAXD pattern captured by the CCD (or other) detector is nontrivial. Therefore, we used the error associated with the fitting of the data to provide some indication of the random variation that may be present. The error in the fitting of the peak position is used to

calculate to the precision to which the D-period should be reported, as shown below using a sample dataset from the deep zone of a bovine specimen based on the 5th order peak.

Given equation 8 then the error associated with the D-period can be quantified with the following relation:

$$\frac{\Delta D}{D} = \frac{\Delta q_0}{q_0} \qquad \textbf{Equation 9}$$

where ΔD is the error in D-period and Δq_0 is the corresponding peak position error.

Equations (8) and (9) lead to:

$$\Delta D = \frac{\Delta q_0 \cdot D^2}{n \cdot 2\pi} \qquad \textbf{Equation 10}$$

Based on equation 10, the D-period error was calculated for a sample data set and tabulated below (Figure 2.33). This shows that on average the error can be estimated at ~0.0166 nm and therefor all values of D-period are reported to 1 decimal place (1 less than the error).

	q_0 (nm^{-1})	Δq_0 (nm^{-1})	D-Period (nm)	ΔD (nm)
Average:	**0.4796**	**0.0002**	**65.5117**	**0.0166**

Figure 2.33: Table indicating the error associated with both the peak fit position as well as the calculated error associated with the D-period. The average error was found to be at 0.0165nm across the sample series and therefore all D-period values are corrected to 1 decimal place.

Percentage change in D-period

The value established from an unstrained state will be referred to as the initial value of D-period, which will also be referred to as the pre-strain value due to the fact that collagen fibrils are believed to exist in a pre-strained state in cartilage. However, when tissue level strain is applied, the associated changes to the D-period can be measured and a mean %

change in D-period, also known as fibril strain ($\mathcal{E}_F$), can be calculated using the following equation:

$$\boldsymbol{\varepsilon_F = \frac{D_{(\varepsilon_T)} - D_{(\varepsilon_{T=0})}}{D_{(\varepsilon_{T=0})}} = \frac{q_0(\varepsilon_{T=0})}{q_0(\varepsilon_T)} - 1} \qquad \textbf{Equation 11}$$

where ε_T represents macroscopic tissue strain [106].

2.7.3. Intra and inter-fibrillar disordering

Intra-fibrillar disordering: Changes to the fibrillar D-Period may be accounted for by changes in the intrafibrillar structure and organisation. This would mean that rather than a change to the gap to overlap ratio that there is an associated 'blurring' of the interfaces such that the molecular arrangement is very slightly shifted and causes a wider range of scattering. This is something that can be qualitatively observed within the SAXS pattern and can be quantified using the $I(q)$ peak fitting by considering multiple Bragg orders in the data.

Inter-fibrillar disordering: The width of the peak radially gives an indication to the level of disordering between the fibrils, whereby, the broader the peak radially the higher the variability in the lattice spacing of the D-period.

2.7.4. Intermolecular d-spacing

Alongside the regularity in the D-period there is also an associated regularity in the lateral spacing between molecules within the fibrils known as the d-spacing. A known value for hydrated collagen fibrils has previously been estimated at ~1.5nm and for dehydrated fibrils at ~1.1nm in type I collagen[109,110]. These values are determined from the equatorial scattering rather than the meridional diffraction peaks. To calculate lateral tropocollagen molecule spacing d_m between the collagen fibrils, a cake-shaped sector is applied within the range from q ~ 1.7 nm^{-1} to ~7.2 nm^{-1} and oriented at 90° to the fibril direction using Fit2D. After azimuthally integrating the intensity, and subtracting the diffuse SAXS

background (Figure 2.34) the equatorial SAXS peak is then fitted to a Gaussian with peak position (q_m). The intermolecular spacing (d_m) is then calculated from Equation 12.

$$d_m = \frac{2\pi}{q_m} \qquad \textbf{Equation 12}$$

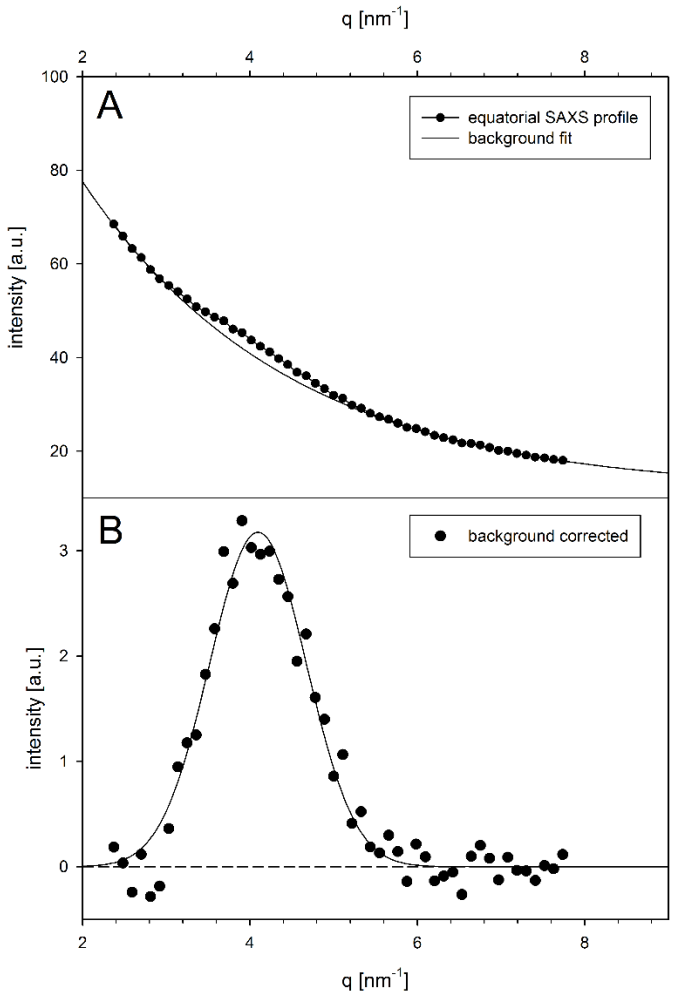

Figure 2.34: Equatorial SAXS intensity profile for cartilage (at zero strain), before (a) and after (b) subtraction of the diffuse SAXS scattering. After subtraction, the equatorial peak is observed at q ~ 4.0 nm^{-1} corresponding to d_m ~ 1.5 nm, characteristic of the lateral intermolecular spacing in hydrated collagen[109].

Chapter 3

Methods: Lab based experimental techniques

3. Methods: Lab based experimental techniques

3.1. Sample preparation

A combination of both bovine and human cartilage was used in experiments both at the beamlines as well as in lab based work. Cylindrical explants were used in all experiments to a) ensure that redistribution of fluid flow within the tissue was consistent laterally within the samples, b) as it was technically most feasible with biopsy punches, and c) also allowed simpler calculations to be made to determine stress levels avoiding stress-concentrations at edges. Furthermore, all explants were 2mm in diameter to ensure that the thickness was enough to generate a good signal at the beamline whilst allowing a relatively simple process of obtaining the explants from the joints.

3.1.1. Bovine articular cartilage

Cartilage samples were harvested from the flattest portion of the proximal surface (Figure 3.1) of bovine metacarpophalangeal joints. Joints were taken from 18-24 month old adult steers that were freshly slaughtered and obtained from a local abattoir. The joints were first washed then immersed in disinfectant (Virkon) for 10 minutes and then immersed in 70% industrial methylated spirit (IMS). The joints were opened in sterile conditions in a tissue culture hood, using sterile scalpel blades.

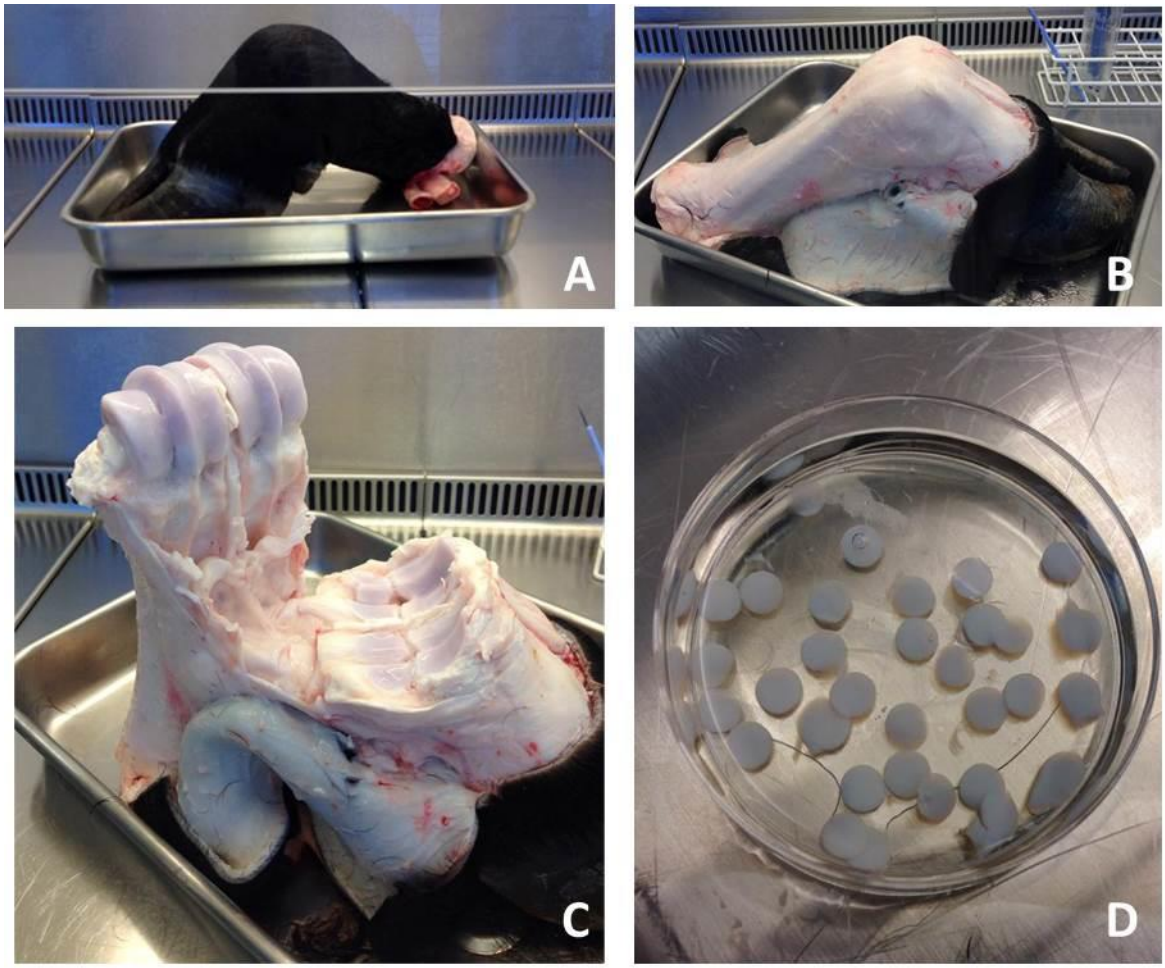

Figure 3.1: Images showing the steps taken in sample extraction, (A) Bovine foot after being washed, (B) Removal of skin, (C) Opening of the joint, (C) Resulting explants following extraction.

Cylindrical explants were directly extracted using biopsy punches and scalpel blades. A 2mm diameter biopsy punch was first used to isolate a region of the joint and was then extracted using the scalpel blades (Figure 3.2). It was assumed that full thickness cartilage was taken through ensuring that the punches hit the subchondral bone and that the deepest possible slice was cut using the scalpel blades. Samples were incubated at 37°C, 5% CO2, in Dulbecco's Modified Eagles Medium (DMEM) supplemented with 10% fetal calf serum (FCS), 1.9mM L-glutamine, 96U/ml penicillin, 96mg/ml streptomycin (Sigma-Aldrich, Poole, UK) for 24 hours when further processing was required. All samples were then transferred to phosphate buffered saline solution before being snap frozen in liquid nitrogen and then stored at -20°C inside Eppendorf tubes till further use.

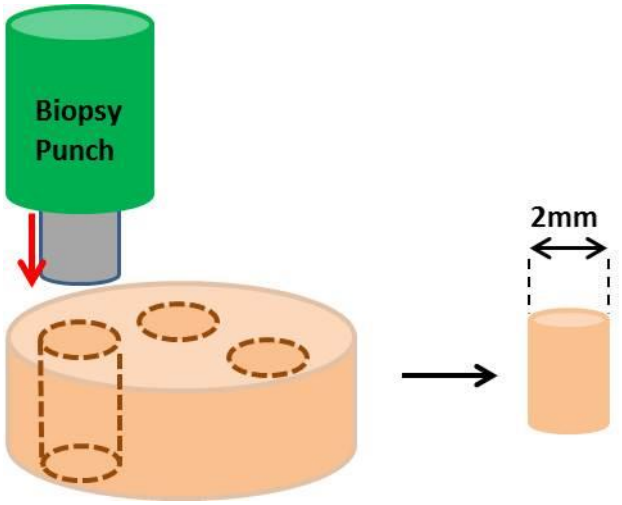

Figure 3.2: Schematic showing the process of cutting 2mm discs directly from the joints using a 2mm biopsy punch followed by a scalpel.

3.1.2. Human articular cartilage

Human explants were sourced from both Imperial College (UK) and Articular Engineering (IL, USA).

Macroscopically normal human explants were isolated from the femoral condyle of a 44 Year old male cadaver supplied by Imperial College, London, UK. All procedures were conducted with full approval from the local ethics committee. Research supported by the National Institute for Health Research (NIHR) Biomedical Research Centre based at Imperial College Healthcare NHS Trust and Imperial College London (project R15046). As with the bovine explants, 2mm explants were extracted using biopsy punches. Explants were rested also in culture medium (DMEM + 10%FCS) for 24 hours, and then snap frozen in liquid nitrogen followed by storage at -80°C.

The 2mm explants that were sourced from Articular Engineering were taken from a 44 year old female cadaver (IL, USA) and were extracted by the company and shipped ready for experimentation. They were again stored in media after removal from the joints and kept chilled until they reached the UK. Once they had been received, they were

transferred into fresh media and incubated at 37°C, 5% CO_2, for 24 hours and then snap frozen in liquid nitrogen followed by storage at -80°C.

3.2. Cartilage degradation

3.2.1. Enzymatic digestion

In order to study the role of the constituent ECM macromolecules, enzymatic digestion was performed on the explants to partially remove either PG's or a combination of both PG's and collagen. Explants were either cultured in normal media, Chondroitinase ABC at 0.1U/ml or Collagenase at 10U/ml for 24 hours (Sigma-Aldrich, Poole, UK). The concentration of each enzyme was tested for viability using mechanical testing to see ensure that the digestion was both a success and adequate to create mechanical instability.

Chondroitinase ABC (0.1U/ml)

A chondroitinase buffer to activate the enzyme was first prepared containing 50mM Tris pH 8.0, 60mM sodium acetate and 0.02% bovine serum albumin. The enzyme is received in powder form and therefore needed to be re-suspended in 0.01% bovine serum albumin (BSA) prior to further dilution. The enzyme solution was then diluted to gain the desired concentration at 0.01U/ml using the prepared buffer solution and 150µl was aliquoted into each well containing a sample. The well plate was then sealed using polyfilm and placed on a plate shaker within an incubator at 37°C, 5% CO_2, for 24 hours. Following this, the media was removed from each well into individual eppendorf tubes for further analysis, and explants transferred into tubes containing PBS prior to snap freezing and storage.

Collagenase (10U/ml)

As with the chondroitinase, a buffer was prepared to for the collagenase containing PBS and Penicillin-Streptomycin (200mM Pen/Strep). Collagenase also was supplied in powder form and was first re-suspended using the buffer. Prior to further dilutions, the stock was filtered using a syringe filter with a pore size of ~0.2µm as it was not sterile at this point. Once filtered, the remaining solution was diluted to the desired concentration of 10U/ml and again 150µl was placed in each well prior to sealing and incubation. The remaining media was also aliquoted for further biochemical analyses.

3.2.2. IL-1β treatment

IL-1β treatment was used in live explants to induce an inflammation response similar to that found in conditions such as OA. IL-1β is an inflammatory cytokine which is upregulated in OA and is involved in causing the chondrocytes to increase the release of inflammatory chemokines, nitric oxide and prostaglandin E2, which all contribute to matrix catabolism[111]. The bovine explants were first extracted using the methods described above. Following incubation the explants were then transferred to 48 well plates. A previously tested dose of IL-1β (Peprotech, UK) at 5ng/ml was used to treat the explants[112]. The IL-1β was reconstituted from solid lyophilized sterile powder in sterile distilled water then used as stock solution to be further diluted to the desired dose level using serum-free supplemented DMEM. 500µl of media was used per sample and retained and replaced every 3 days within the treatment timeline. Samples were treated for 12 days in sterile conditions and retained in an incubator at 37°C, 5% CO_2, for the entire period. Control samples were retained in the same conditions with the media described above.

3.3. Biochemical characterisation

3.3.1. Dimethylmethylene Blue (DMMB) Assay protocol

This assay was used to measure the level of PG release following enzymatic digestion. The dye, 1,9-dimethylmethylene blue (DMMB) complexes with sulphated GAG chains causing a metachromatic shift in the absorbance maximum from 600 to 535nm[113]. The Ascent microplate reader is pre-programmed with a protocol and is able to detect such shifts. To begin with the reagent was prepared using DMMB, ethanol, sodium formate and formic acid (98/100%). Alongside this, a set of standards of chondroitin sulphate with fixed concentrations were prepared to act as reference values in determining sGAG levels using the same buffers as those used in the degradation protocols. A dilution series was used to form standard curves from which media concentrations could be back calculated from. The standard series used can be found in the following table:

Standard	Standard concentration (µg/ml)	Volume 100 µg/mL sGAG(µl)	Buffer Volume (µl)
STD0	0	0	1000
STD1	5	50	950
STD2	10	100	900
STD3	20	200	800
STD4	30	300	700
STD5	40	400	600
STD6	50	500	500
STD7	60	600	400

Figure 3.3: Table indicating standard concentrations and volume of both chondroitin sulphate and buffer used at each level.

A pipetted volume of 40µl of the standards were placed into a 96 well plate with 3 repeats. The media to be analysed were first vortexed and then 40µl transferred into each well (with 3 repeats per sample). These were then topped with 250µl of the DMMB reagent using a multichannel pipette. The plate was then placed into the micro-plate reader and read for absorbance at 595nm. A reduction in the absorbance directly correlates with an

increase in the presence of sGAG. A mean absorbance value was calculated from the triplicates and the sGAG concentrations calculated from the standard curve, where an acceptable standard curve must have an R^2 value above 0.99 as shown in Figure 3.4.

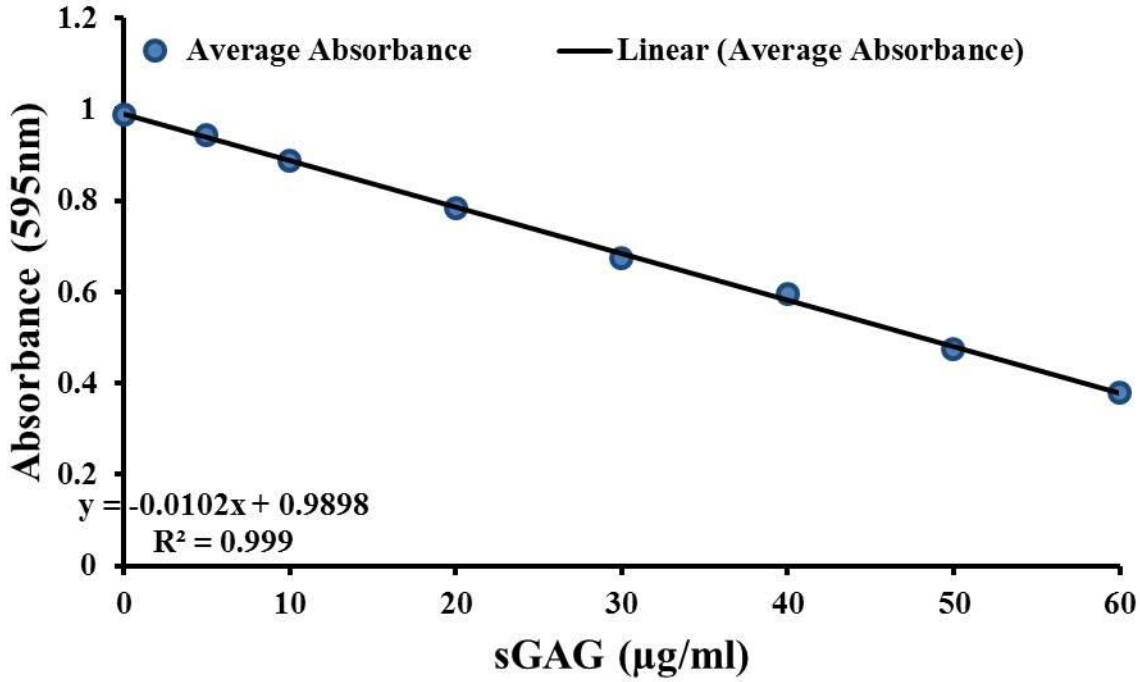

Figure 3.4: Graph showing a sample standard curve fitted with a linear regression with an R^2 value of 0.999.

3.3.2. Results: GAG release

Enzymatic digestion:

Enzymatic digestion resulted in a significant (p<0.001) increase in the release of sGAG from both chondroitinase and collagenase groups when compared to the control group, after 24 hours of treatment, as shown by Figure 3.5. There was also a significant change to the tissue level mechanics, results which can be found in the appendix (Figure A.5.2).

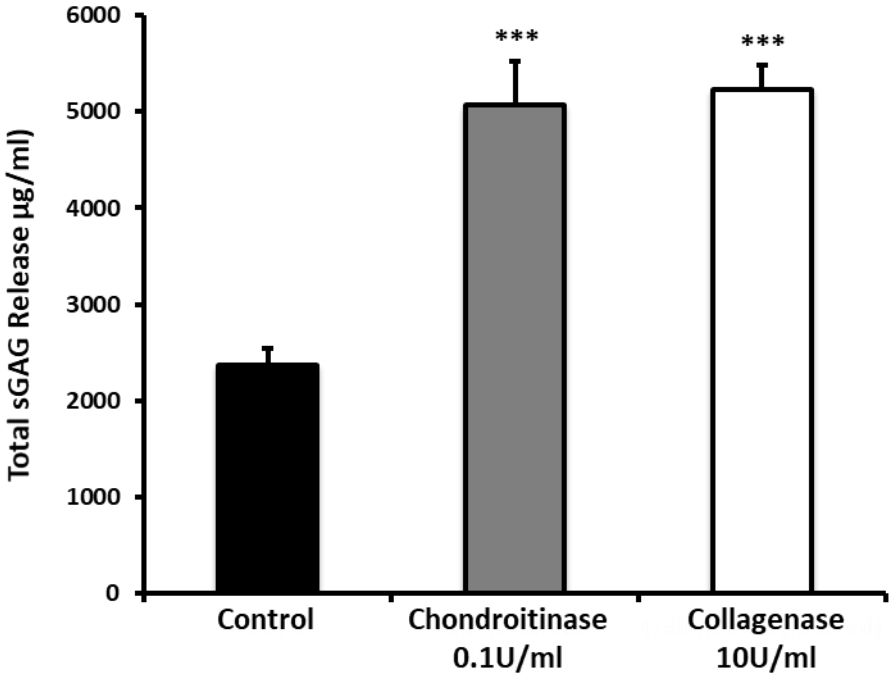

Figure 3.5: During enzymatic digestion the total sGAG release into the treatment media determined using the DMMB assay. Error bars represent standard error of mean and *** refers to significance between the groups (p<0.001).

Il-1β treatment:

The total sGAG release was significantly higher (p<0.001) in the IL-1β treatment group over the first 9 days compared to the control group as shown by Figure 3.6. Cumulatively, there was 29% more sGAG release in the Il-1β group by day 12. This high level of PG disruption caused an overall change in the tissue level mechanics, with the associated mechanics and resultant SAXD data reported in **Chapter 6**.

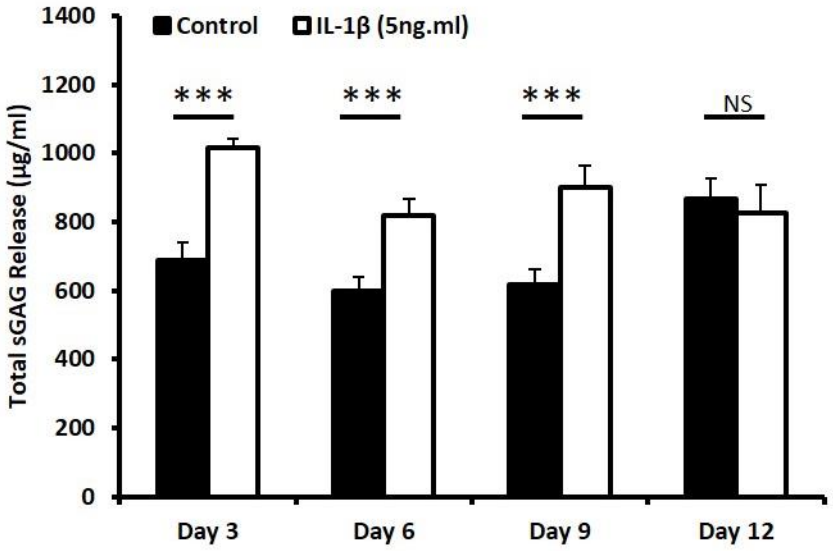

Figure 3.6: During Il-1 β treatment the total sGAG release into the treatment media, determined using the DMMB assay, as a function of time. Error bars represent standard error of mean and *** refers to significance between the groups (p<0.001).

3.4. Mechanical testing

Mechanical tests were conducted both at the beamline and in the QMUL SEMS-labs to characterise the tissue mechanics in all conditions as well as ensuring that digestion and degradation was successful (see Appendix A.5.1). Tests were conducted using the micro-compression tester using specially designed compression platen and base. Samples were either placed through a stress-relaxation or cyclic loading regime. The majority of stress-relaxation tests involved compression at 20%/min up to 20% tissue level strain and then holding for 5-15 minutes to measure the relaxation response as shown in Figure 3.7. In the cyclic regime, the samples were exhibited to fixed number of cycles at varying strain rates but always loaded to 20% strain level.

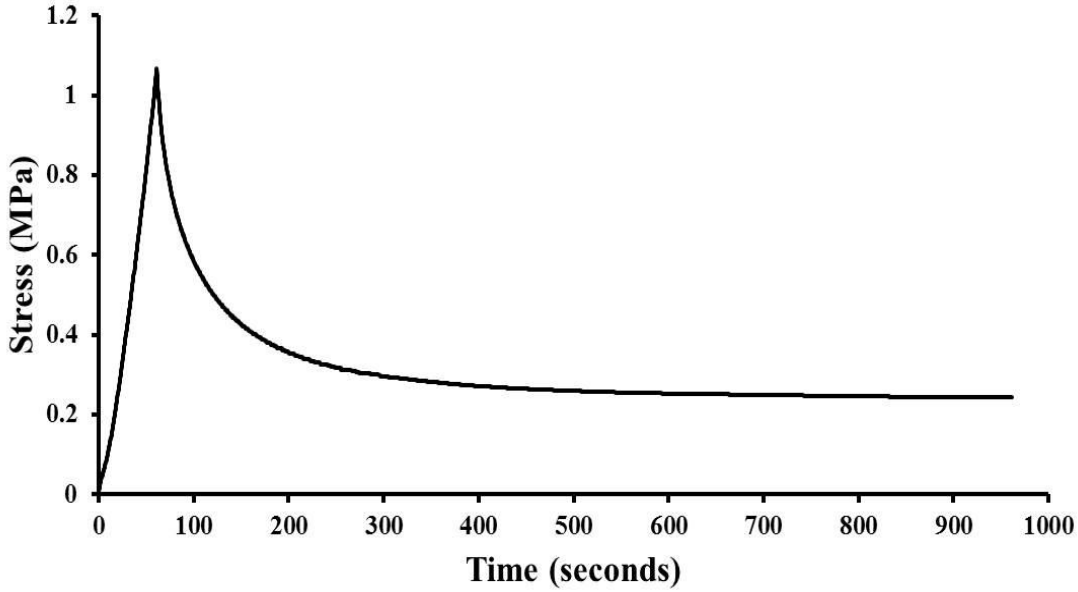

Figure 3.7: Sample plot of a stress versus time curve in a control bovine sample under unconfined compression to 20% strain level at a rate of 20%/min and then held for 15 minutes.

3.4.1. Interpretation of tissue mechanics

The modulus of bovine articular cartilage in the compressed state was investigated through the analysis of the stress strain curve generated by the stress- relaxation tests using the following method.

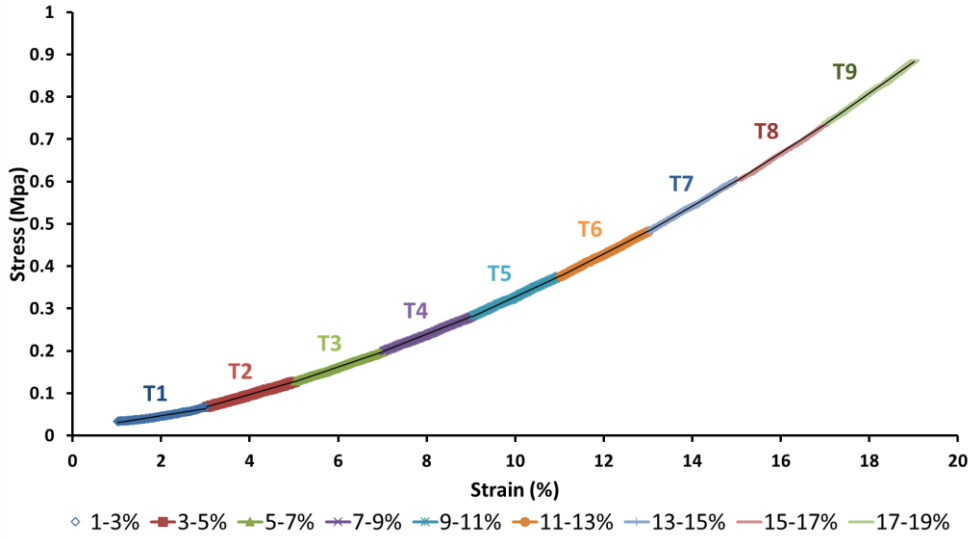

Figure 3.8: Typical ramp up phase of a stress-relaxation test which has been split into 2% tangent intervals across (T1-T9) up to 20% strain level, to which a linear regression was fitted.

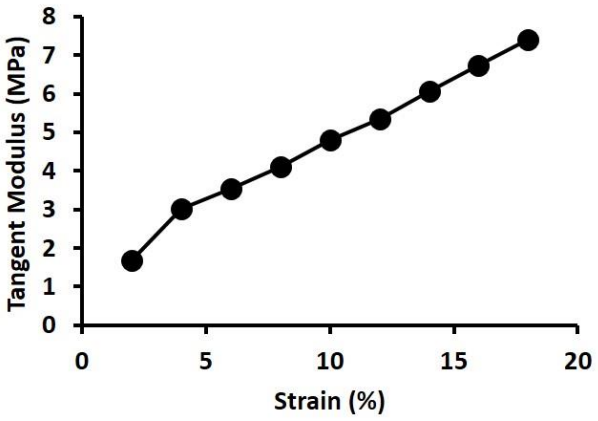

Tangent	Linear Regression Gradient/Modulus	Linear Regression R^2
T1	1.69	0.9769
T2	3.01	0.9993
T3	3.53	0.9992
T4	4.11	0.9994
T5	4.81	0.9993
T6	5.34	0.9995
T7	6.07	0.9992
T8	6.72	0.9992
T9	7.41	0.9991

Figure 3.9: The tangent modulus at each strain increment plotted showing a linear upward trend with the tabulated fit parameters and associated R^2 values.

As determined by a stepwise tangent modulus analysis (Figure 3.8/3.9), it can be shown that there is no unique modulus over the range that has been investigated however given that the majority of the tests are carried out at up to 20% strain level the range chosen should be representative to what is characteristic at this level. As a result, the tangent modulus between 17-19% was chosen as a fixed range to apply across all sample measurements.

The modulus was calculated using the following equation:

$$E_{Tangent} = \frac{\sigma_{n+2} - \sigma_n}{\varepsilon_{n+2} - \varepsilon_n} \qquad \textbf{Equation 13}$$

Where: σ_n is stress value at n % strain
σ_{n+2} is stress value at n+2% strain
ε_n is n % strain
ε_{n+2} is n+2 % strain

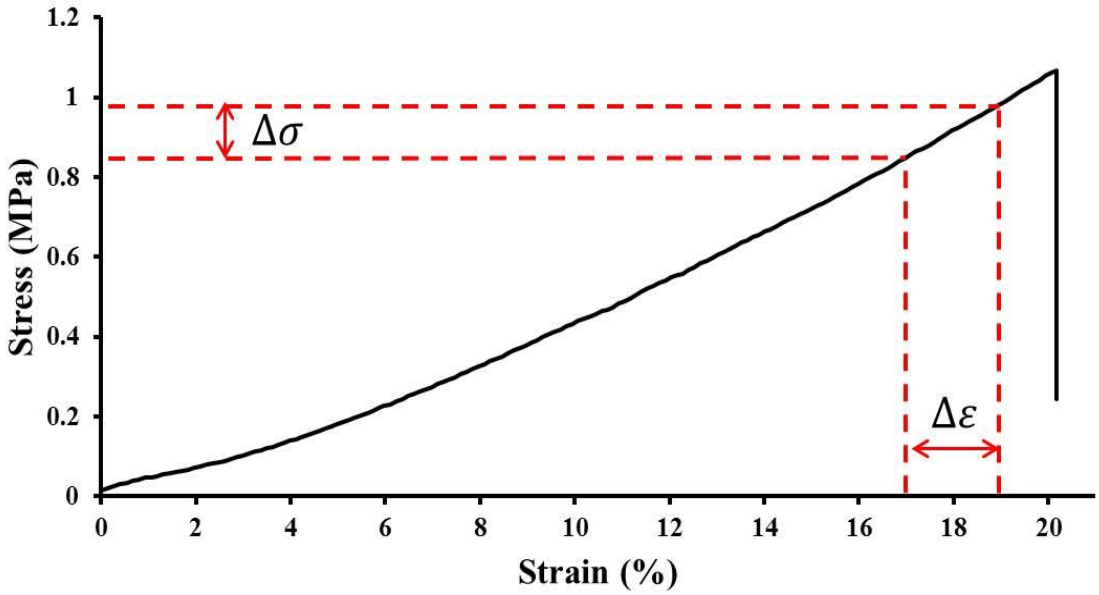

Figure 3.10: Stress strain curve from a control bovine sample where the change in stress and strain is indicated by Δσ and Δε respectively.

The relaxation modulus was calculated using the stress value recorded when the tissue had relaxed for 300 seconds. The following equation was used:

$$E_{Relaxation} = \frac{\sigma_{t=300}}{\varepsilon_{max}} \qquad \textbf{Equation 14}$$

Where: $\sigma_{t=300}$ is stress value at 300 seconds
ε_{max} is maximum strain value (20%)

Percentage relaxation was calculated using the peak stress value alongside the relaxation stress after the relaxation period of 300 seconds in the following equation:

$$\%\, relaxation = \frac{\sigma_{peak} - \sigma_{relaxation}}{\sigma_{peak}} \times 100 \qquad \textbf{Equation 15}$$

Where: σ_{peak} is peak stress value
$\sigma_{relaxation}$ is stress value after 300s relaxation

Chapter 4

Depth-dependent nanoscale structure in articular cartilage

4. Depth-dependent nanoscale structure in articular cartilage

4.1. Synopsis

As summarized in the literature review, the depth-dependent macroscale and microscale structure of cartilage has been characterised in terms of cellular organisation, proteoglycan content and collagen content and architecture (For review see **Chapter 1**). However, very little is known about the nanostructural structure of the collagen fibrils within articular cartilage and how the nanoscale properties are influenced by depth within the tissue.

Given the depth-dependency in terms of organisation and macromolecular content, it is reasonable to hypothesize that there is an associated variation in the nanostructural parameters such as the fibrillar D-period and disorder. The swelling of the proteoglycans, drawing water into the tissue, causes an osmotic swelling pressure which is resisted by the collagen fibrils. Although collagen fibres are relatively stiff with an estimated tensile modulus of ~500 MPa[114], the swelling pressure would be expected to result in a small tensile strain within the fibres. Hence, one would expect to see an increasing fibrillar D-period with depth, positively correlated with proteoglycan content. Further, while the predominant orientation of the fibrils has been established using techniques such as scanning electron microscopy[115], such methods provide limited detail in terms of degree of orientation and disorder at the supramolecular level, which are expected to be functionally important for both biomechanics and cell interactions.

Using small-angle X-ray diffraction, the parameters described in **Chapter 2** can be determined within cartilage, and given the ability to scan through the sample with a micron-sized beam, the depth dependent profile can be determined. Furthermore, in-situ measurements can be conducted to measure changes in the fibrillar architecture in

cartilage explants subjected to physiological compression. This chapter describes a series of experiments aimed at measuring depth-dependant, nanoscale properties of collagen fibrils in unloaded and compressed cartilage explants.

4.2. Materials and methods

Experiments were conducted at Diamond Light Source at beamline I22 using the microfocus setup. The beam size at the sample was measured to be around 12μm with a wavelength of 0.08856nm, beam energy of 14keV and the sample to detector distance at 977.72 mm. Bovine explants were prepared as described in **Chapter 3** producing 2mm diameter, full thickness explants. These samples were placed within the sample holder and pre-strained to 0.1% strain whilst being hydrated with PBS. Each line scan was performed with 20 μm increments in the y-direction (perpendicular to the tissue surface) and an exposure time of 0.5 seconds. A line scan was performed in an uncompressed state prior to any loading. The explant was then compressed to 20% strain and held at this strain for 15 minutes to enable stress relaxation to occur. A further line scan was then performed.

4.3. Results

Individual SAXS patterns, integrated azimuthally over the full 0° - 360° range, and plotted radially over a wide wavevector *q*-range (0.2 – 0.9 nm^{-1}, including the 3^{rd} to the 9^{th} orders) are shown in Figure 4.1 for representative regions within the superficial, transitional and deep zones. What is immediately obvious is that the deep zone has the most visible peaks, as well as a higher number of peak orders when compared to both the superficial and transitional zone, which both provide a much weaker signal.

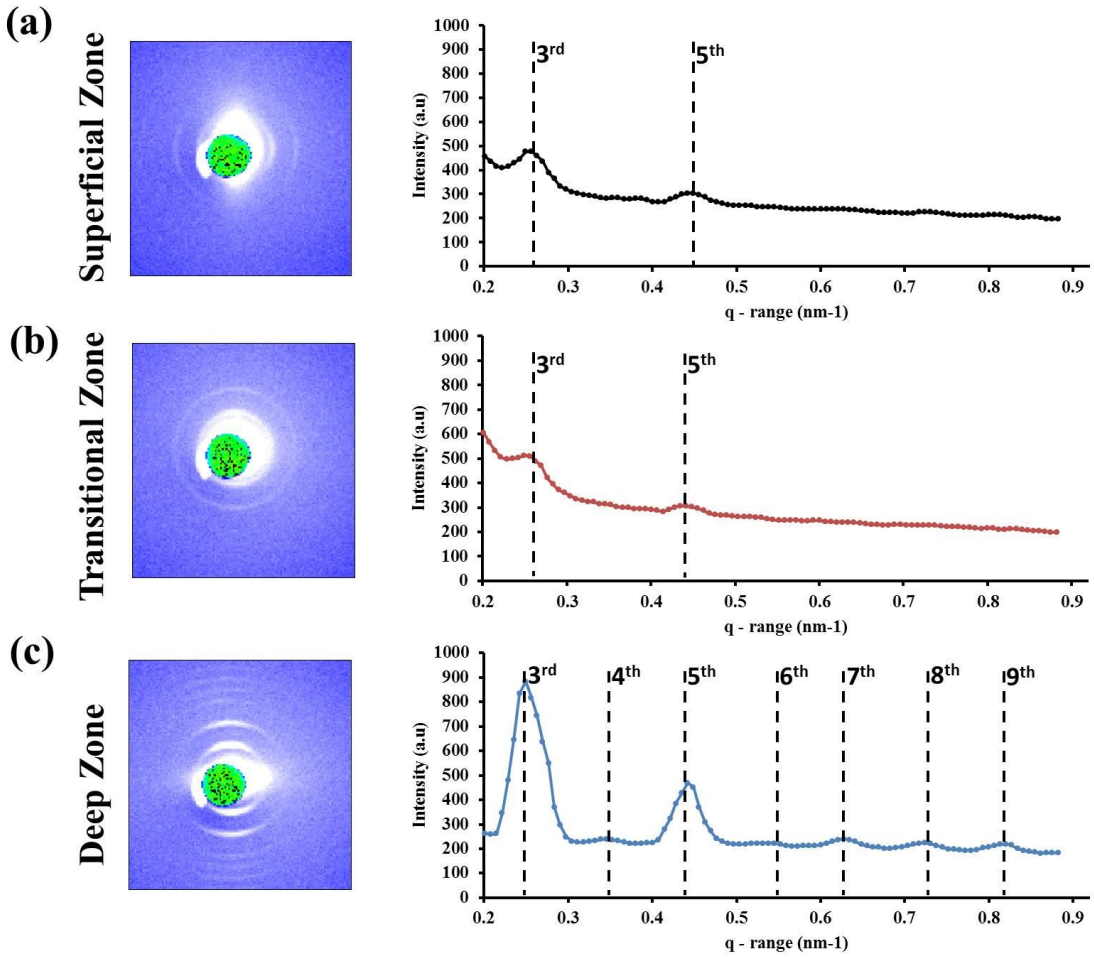

Figure 4. 1: Representative SAXS patterns and associated 1D intensity profiles when integrated azimuthally to show the peak orders in the q range in superficial (a), transitional (b), and deep (c) zones.

4.3.1. Structural variation observed in representative zonal SAXS patterns

Initial integrations confirm the existence of a depth dependence of fibrillar orientation as indicated by Figure 4.2. Within the superficial zone (Figure 4.2a), there is a clear peak in the radially-integrated plot at about 180° indicating that the fibres are predominantly orientated parallel to the surface (w_χ ~ 16 degrees). The width of the peak indicates a relative narrow range of orientations, particularly compared to the transitional zone (Figure 4.2b), where the fibrils are much more randomly orientated (w_χ ~ 57 degrees), resulting in a wider range in the degree of orientation and a flatter $I(\chi)$ profile. The deep zone shows two narrow peaks at approximately 90° and 270° indicating that the collagen

fibrils are perpendicular to the surface with a high degree of orientation. These results agree with previous well-established understanding of collagen orientation within articular cartilage as reviewed in **Chapter 1** (see Figure 1.4).

Interestingly, a new finding visible in Figure 4.2 (middle column) is that there is also a depth-wise variation in fibrillar D-period. Specifically, the example in Figure 4.2 shows that the D-period is larger in superficial zone at 65.9 nm when compared to the transitional zone at 64.9 nm, with an increase back to 65.6 nm in the deep zone. This variation in D-period (relative to the superficial zone, a decrease of 1.5% in the transitional zone and an increase of 1.1% in the deep zone) indicates localised variation in pre-strain of the fibrils.

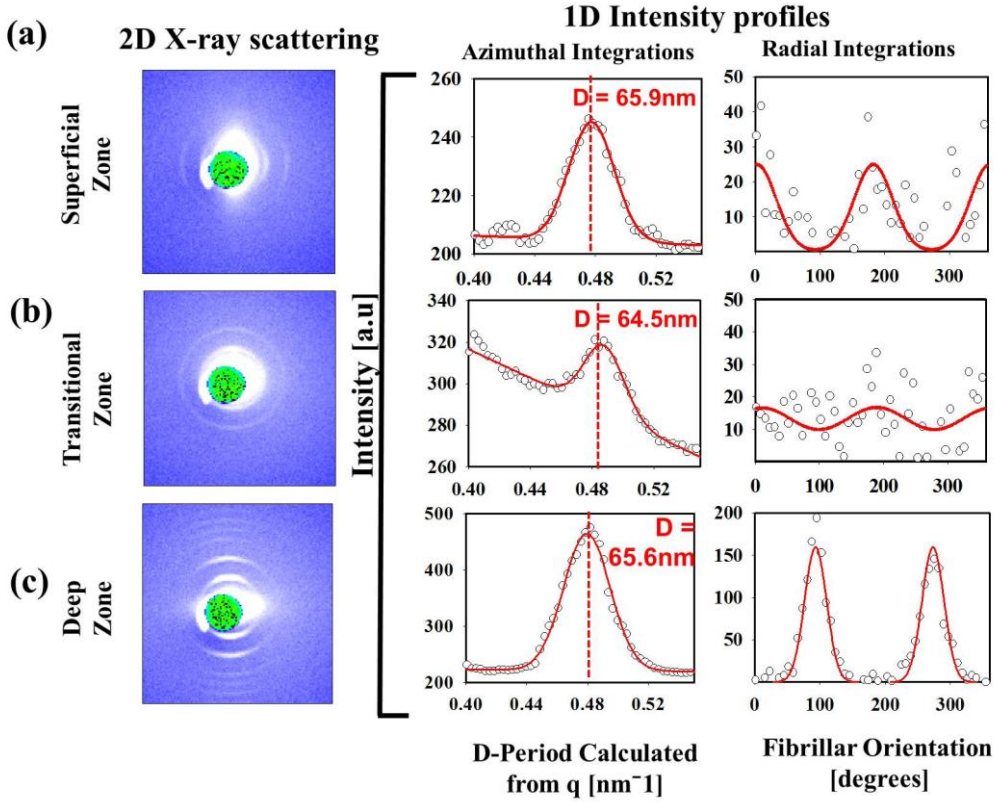

Figure 4.2: Representative SAXS patterns and associate 1D intensity profiles when integrated both azimuthally and radially over the 5th order peak in bovine cartilage. Middle column shows how the 1D profiles are fitted and then the centre of peak used in the calculation for D-period. The right hand column shows the fitted radial profiles to indicate the predominant orientation of the fibrils within each zone in the superficial (a), transitional (b), and deep (c) zones.

4.3.2. Depth-wise variation in static bovine explants

To explore this phenomenon further, a continous SAXS line-scan with high spatial resolution (~10 μm) through the thickness of the tissue was carried out to further investigate the depth-dependent variation. Figure 4.3 shows data from a representative continuous line-scan indicating the depth-wise changes in D-period, w_q (D-period variation), total peak intensity and associated SAXS patterns. Qualitatively from the SAXS patterns one can observes clear differences between each zone. The integrated and fitted data then further defines the depth dependent changes found in the fibrillar structure in terms of the D-period and associated parameters. The D-period shows a clear trend where the superficial zone posseses a value of ~66nm, transtional zone ~64.5nm and an increase to ~66nm in the deep zone.

In contrast, there seems to be no overall change in the variance of fibrillar disorder when comparing the variation of wq across zones. However, the peak intensities vary considerably through the thickness, with an over 500% increase in SAXS peak intensity in the furthest location in the deep zone, compared to the initial point in the superficial zone. The higher peak intensity being observed in the deep zone can be linked to the higher concentration of fibrils in this particular zone and this provides an indication to the collagen content, but it should be emphasized that peak intensity depends on other factors such as degree of fibrillar crystallinity as well, as will be shown in the following chapters.

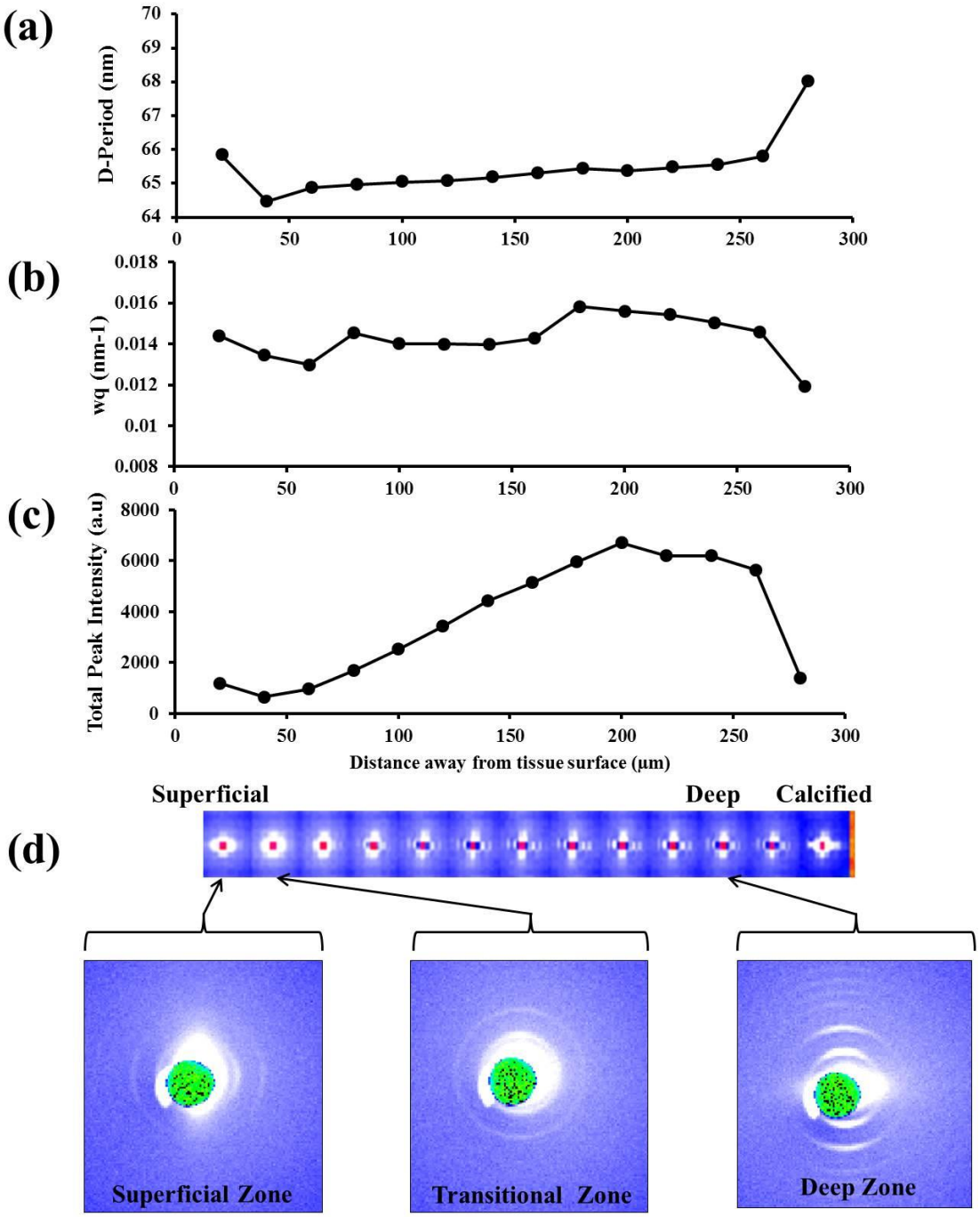

Figure 4.3: Depth-dependent D-period (a), wq (b), total peak intensity (c) and SAXS patterns (d) in an uncompressed sample line scan in a representative sample of bovine articular cartilage.

When analysing the depth-dependency of the orientation, as described earlier, there is a clear continuous shift in orientation between the superficial and deep zone. The transitional zone is the intermediate zone which connects the two opposing orientations

– horizontal in the superficial case and vertical in the deep zone. It is also seen in Figure 4.4b that the degree of misorientation (reflected by the angular width of the I(χ) distribution) also coincides with the transition of predominant orientation, with the highest degree of misorientation corresponding to a wider range of orientation distribution.

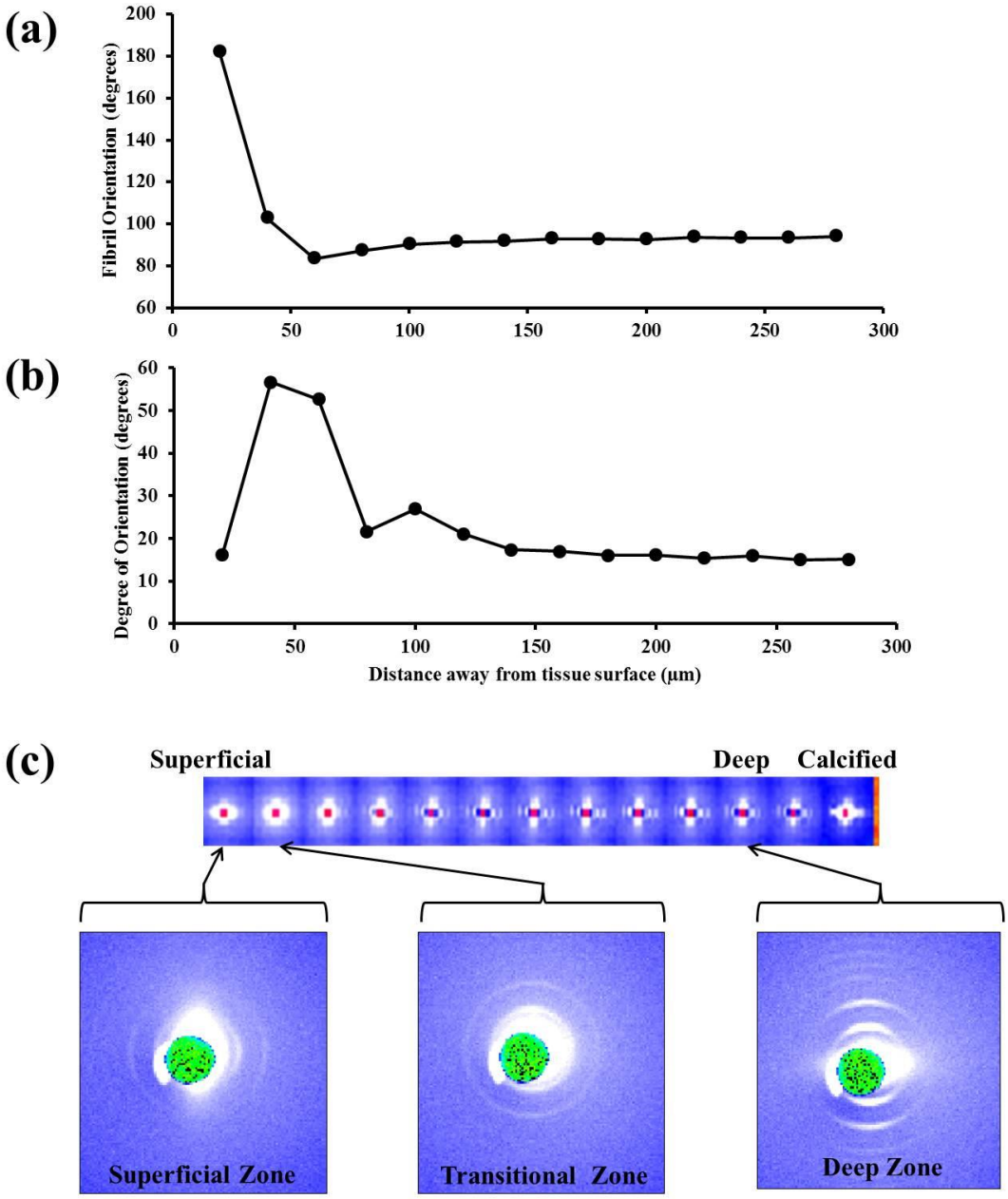

Figure 4.4: Depth-dependent fibrillar orientation (a), degree of orientation (b) and SAXS patterns (c) in an uncompressed sample line scan in a representative sample.

4.3.3. Compression induced changes in the depth-wise fibrillar structure

Following compression and relaxation there are clear residual changes to the fibrillar structure that can be observed. The word "residual" is used as the post-load measurement is (in this chapter) taken after the majority of macroscopic stress relaxation has occurred (by ~300s, as indicated in **Chapter 2**, Figure 2.25), Figure 4.5 shows the changes to the D-period parameters under 20% compression followed by 15 minutes of relaxation time. Given that the same spacing was used in the line scan post relaxation and the fact that the tissue does not possess a linear strain profile through the thickness of the tissue[15,116,117], it is difficult to make point to point comparisons between pre- and post-loading scans. Nevertheless, the overall trend can be compared. Part (a) shows that overall, in the deep zone the fibrillar D-period remains unchanged. The region where there seems to be some non-reversible changes is between the superficial and transitional zone. It is known that the superficial zone fibrils play an important role in resisting compression of the tissue alongside the deep zone[118]. The slight shift and increase in D-period would suggest that the fibrils are in a tensile state, which is likely to be expected when the tissue is placed under compression and the superficial zone fibrils (due to their orthogonal orientation to the loading direction) are placed under tension. There is a shift (14%) in the w_q parameter within the transitional zone (Figure 4.5b); however the significance of this is questionable given the effect of the strain profile and ability to match point to point. The peak intensity (c) however shows a clear drop in intensity on compression. This suggests that there is a clear disordering at the *intra*-fibrillar level, where the loss of regularity in the axial arrangements of tropocollagen molecules leads to a reduction in both peak intensity and visible peak orders. Similar reductions in intensity have been observed for the simpler loading case of tension, in the much more organized tendon tissue[86].

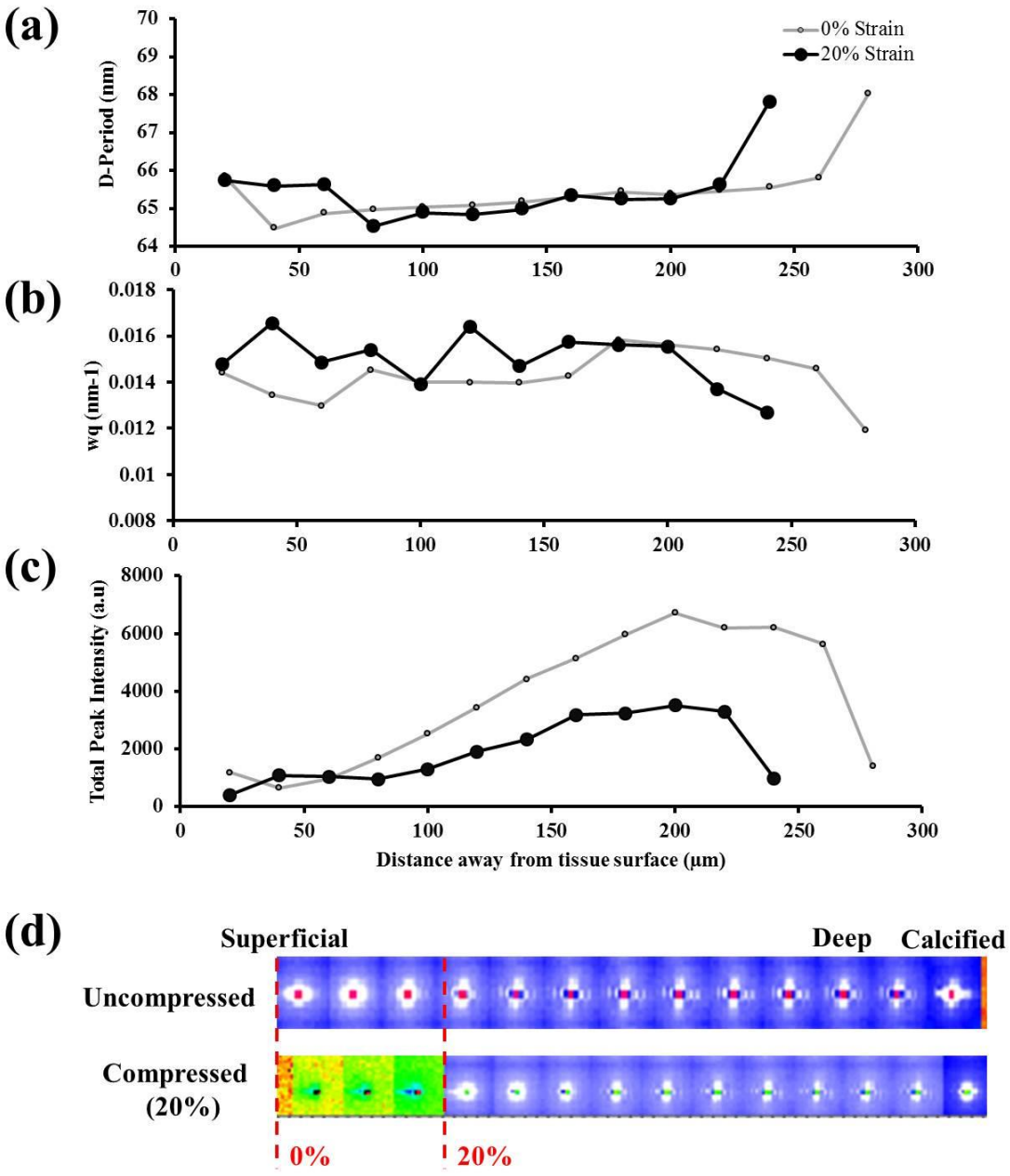

Figure 4.5: Depth-dependent D-period (a), wq (b), total peak intensity (c) and SAXS patterns (d) where the black line denotes the compressed state and grey line denotes the uncompressed state in a representative sample.

Further, in terms of fibrillar orientation Figure 4.6a indicates that there is a change in the orientation in the superficial zone; however when observing the SAXS pattern more carefully it was evident that the superficial zone was not as easily picked up in the second

scan. This was likely due to interference of the upper platen with the signal, and with the zone being significantly thinner than the other regions.

Finally, there appears to be no significant change in the degree of misorientation (Figure 4.6b), which would suggest that at physiological levels of compression in healthy cartilage, the fibrillar network is not dramatically disrupted and the fibrils are able to maintain their orientation and structure – as would be expected, since a fibrillar breakdown would be a pathological occurrence.

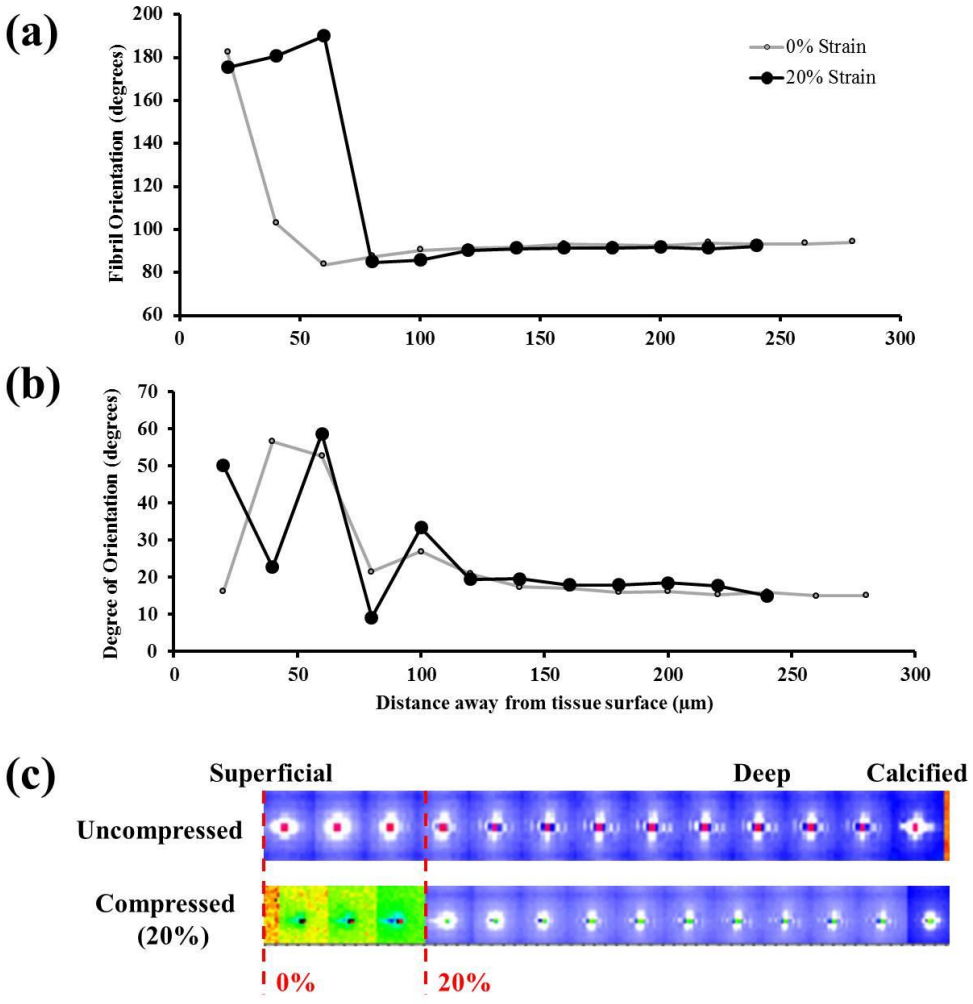

Figure 4.6: Depth-dependent fibrillar orientation (a), degree of orientation (b) and SAXS patterns (c) where the black line denotes the compressed state and grey line denotes the uncompressed state in a representative sample.

4.4. Discussion & Conclusions

The deph-dependent variation in D-period suggests that there is (i) first a higher pre-strain found in the superficial zone when compared to (ii) the transitional zone followed by (iii) a steady, consistent increase in pre-strain on going from the transitional to the deep zone. As described previously, this directly correlates with the depth-wise contribution of each of the constituent macromolecules. The rapid uptick of D at the last point corresponds to the transition to the calcified interface to subchondral bone. These results suggest that the larger pre-strain observed in the deep zone is due to the higher concentration of proteoglycan and hence the greater swelling pressure compared to other zones. The transitional zone fibrils are much more loosely bound and packed (as indicated by the radial integrations with lower peak intensities), which, when combined with a lower proteoglycan content, results in the lower fibrillar pre-strain[119].

We can propose a possible mechanistic reason for this variation in D-period. It is clear that less pre-strained fibrils (lower D) will have a greater degree of "slack" or flexion, and can extend more under load. Therefore, we propose the transitional zone consists of fibrils which are (relative to the superficial and deep zones) relatively slack. Under the kind of lateral sliding loads common in joint articulation, the tissue in the superficial zone will slide, relative to the deep zone, facilitated by the presence of an intermediate, compliant layer (the transitional zone). We suggest that the compliance of the transitional zone is not only from the variation in composition of collagen and PGs and orientation (which is already known[14,119]), but also in the intrinsic slack in the collagen fibrillar restraining meshwork, which allows lateral motion between zones without exceeding the failure strain in the collagen fibrils.

We further suggest that this depth-dependent variation in D-period arises as a result of a combination of factors, including differences in collagen content and levels of intrafibrillar axial disorder. Firstly, the stronger peaks in the deep zone profile are reflective of the higher concentration of collagen fibrils found in this particular zone when compared to the other two zones[119]. Furthermore, the lack of higher orders visible in the superficial and transitional zones is directly linked to the intrinsic disorder within the fibrils. Axial disordering between tropocollagen molecules will result in a blurred, rather than sharp, interface between the overlap- and gap-zones[86]. This phenomenon will suppress the intensity at higher orders, will be quantified in detail in **Chapter 5,** and may reflect reduced pre-strain in superficial and transitional zones. Further, a combination of randomly orientated fibrils as well as disorder to the repeating D-periodic unit can result in a limited number of observed peaks. Thus in the deep zone the 1st to 9th order peaks are all visible whilst in the superficial and transitional zones, only the 3rd and 5th order peaks can be identified (Figure 4. 1). Given these two factors, it was observed that the deep zone provided the best signal quality and thus the future experiments described within this thesis will focus solely on the deep zone for analysis of changes in the SAXD signal in response to cyclic loading. Furthermore, given the clarity and consistency of the 5th order, and its position away from the beam centre and bulk of the equatorial scattering, this order was chosen for the bulk of the analyses.

In summary, we report the first combined microscale maps of nanoscale fibrillar D-period and orientation in articular cartilage, as well as the changes under loading. Our main findings are as follows:

- There is a variation in the fibrillar D-period with depth such that the fibrils are pre-strain more in the superficial and deep zone when compared to the loosely bound transitional zone fibrils.
- The collagen content increases with depth such that the deep zone fibrils provide the strongest SAXD signal as well as multiple peak orders due to the regularity of the fibrillar arrangement in this zone.
- There seems to be no significant difference in the level of fibrillar disorder as observed by the w_q parameter both in the static and compressed states.
- SAXD analysis confirms the depth-wise fibrillar orientation found in articular cartilage and provides a method of quantifying the degree of orientation.
- Compression followed by relaxation shows that there are very minor changes to the fibrillar parameters; however there are some residual changes observed in the superficial/transitional zone.

Based on these results, we suggest that future research needs to follow changes immediately after dynamic loading, or during dynamic repetitive cyclic loading (as occurs in gait[104,105]) - rather than after equilibration following application of tissue-level strain – as much of the changes in the fibrillar network must occur during and immediately after macroscopic compression. The following research chapters will develop these themes.

Chapter 5

The secret life of collagen temporal changes in nanoscale fibrillar pre-strain and molecular organization during physiological loading of cartilage

The content of this chapter has been published in ACS Nano[120].

5. The secret life of collagen: temporal changes in nanoscale fibrillar pre-strain and molecular organization during physiological loading of cartilage.

5.1. Synopsis

The existence of pre-tensed, extensible fibrils in a hydrated, amorphous gel is a widespread characteristic of both natural and synthetic nanostructured soft matter systems[121–125]. The mechanical functions of these composites are dependent on the interactions between the fibril phase, the surrounding gel phase and free- and bound water. However, the critical nanoscale mechanics, in particular the extension, reorientation and strain of the nanofibrous phase, are challenging to determine experimentally. Articular cartilage is a biological example where such a nanofibrous architecture is believed to be essential in providing the tissue with its mechanical functionality. Collagen fibrils play a crucial role in the mechanical functionality of articular cartilage, through interactions with the other main extracellular matrix (ECM) component, hydrated proteoglycans[10,37,126]. The negatively charged entangled proteoglycans create an osmotic swelling pressure which is resisted by the collagen fibrils in order to maintain equilibrium[127]. This mechanism requires the collagen fibres to be permanently under a state of tensile pre-strain[42,128]. The magnitude of this pre-strain, however, has never been quantified experimentally. Indeed, little is known about the collagen fibril nano-mechanics *in situ* within the cartilage extracellular matrix.

While many investigations have used ultrastructural and microscopic imaging methods to help to understand collagen structure-function relations in cartilage, these studies have largely ignored temporal changes during loading and unloading and do not provide quantitative information on the mechanics at the fibrillar level. These investigations

primarily include electron microscopy and vibrational spectroscopy to image collagen fibril orientation and content in static conditions, alongside estimates of increasing fibre diameter with depth from the articular surface [129–131]. The present study uses time-resolved SAXS combined with *in situ* mechanics to directly quantify the kinetic response of collagen fibrils in cartilage. Here we use SAXS to measure the collagen fibril strain and the temporal dynamics during stress relaxation using a microfocus X-ray beam to spatially resolve fibril ultrastructure in the deep and transitional zones separately. We investigate collagen nanomechanics in healthy bovine and human cartilage explants and how this behaviour is affected by removal of the hydrated proteoglycans by enzymatic digestion. Such fundamental collagen nano-mechanics behaviour has never before been investigated in cartilage and will provide new insight into its mechanical behaviour and functionality.

5.2.Materials and methods

5.2.1. Bovine explant preparation

Bovine explants were extracted and prepared as described in **Chapter 2**. Full depth cartilage explants were isolated using 2mm biopsy punches from the normal load bearing areas of the proximal surface of the joint. Explants were cultured for 24 hours either in normal media, Chondroitinase ABC at 0.1U/ml or Collagenase at 10U/ml (Sigma-Aldrich, Poole, UK). Samples were snap frozen in liquid nitrogen followed by storage at -20°C for subsequent mechanical testing and SAXD analysis.

5.2.2. Human explant preparation

Macroscopically normal human explants were isolated from the femoral condyle of a 44 Year old male cadaver supplied by Imperial College, London, UK. All procedures were conducted with full approval from the local ethics committee. As with the bovine

explants, 2mm explants were extracted using biopsy punches. Explants were maintained also in culture medium (DMEM + 10%FCS) for 24 hours, and then snap frozen in liquid nitrogen followed by storage at -80°C.

5.2.3. Mechanical Testing

Mechanical tests were conducted on a subset of explants to determine efficacy of digestion as well as to pre-characterise the mechanics, prior to *in situ* SAXD measurements on the remaining samples. The same mechanical testing protocol was also used for testing during synchrotron SAXD measurements. The explant thickness was measured using calibrated Vernier callipers to within 10 μm. Explants were then compressed in unconfined conditions in a custom made micro-compression tester with a 22N load cell (RDP Electronics, UK), and a LabVIEW control interface (National Instruments, UK). Explants were hydrated using phosphate buffered saline (PBS). A 0.1N tare load was initially applied prior to uniaxial compression at a strain rate of 20%/min to a maximum strain of 20%. After compression, the tissue was held at 20% strain for a stress relaxation period of 900s. Tissue stiffness was quantified by the tangent modulus calculated from the linear portion of the stress-strain curve during the ramp-up compression phase of the test. A total of 9 samples were tested in each group.

5.2.4. *In situ* small-angle X-ray diffraction (SAXD)

SAXD measurements were carried out on the microfocus endstation at the I22 beamline at Diamond Light Source (DLS, Harwell, UK). The beam size was 15μm and the photon energy 14keV. The micro-compression tester was mounted onto the microfocus platform to allow simultaneous compression of the tissue during X-ray measurements (Figure 5.1a). SAXD patterns were recorded with a Pilatus P3-2M detector (Dectris, Villingen, CH) with a pixel size of 172μm and a resolution of 1475 × 1679 pixels (horizontal x

vertical)) The sample to detector distance of 841.7±1.0mm was calibrated using silver behenate (AgBe).

SAXD measurements were carried out during relaxation of the tissue (either in the deep or transitional zone), in an automated manner using Python scripts integrated into GDA, the open source framework for data collection at DLS (http://www.opengda.org/). As the majority of the relaxation in stress occurs over the first ~150 seconds, the time-interval between SAXD acquisitions was shorter (10 seconds) in this period and longer (60 seconds) afterward. The superficial zone was not measured when performing time-dependent tracking using the X-ray beam, due to the limited thickness of the superficial zone in cartilage as well as its relatively large deformation.

When calculating fibrillar pre-strain (% change in D-period) the reference D-period value was taken as the value in the uncompressed state. To calculate peak intensities of different meridional orders in the SAXD pattern (e.g. I_5 for the 5th order peak), the peak area was estimated (up to a multiplicative constant $\sqrt{2\pi}$) from the product of the fitted amplitude and width.

To calculate lateral tropocollagen molecule spacing d_m between the collagen fibrils, a cake-shaped sector from q ~ 1.7 nm^{-1} to ~7.2 nm^{-1} and oriented at 90° to the (vertical) fibril direction was defined in Fit2D. After azimuthally averaging the intensity, and subtracting the diffuse SAXS background (Appendix Fig. A.5.6A), the equatorial SAXS peak was fitted to a Gaussian (Appendix Fig. A.5.6B) with peak position q_m, and d_m was calculated from $d_m = 2\pi/q_m$.

To determine the ratio of the overlap zone (O) in the fibril to the D-period (O/D here and elsewhere) from the SAXD pattern, in the presence of intrafibrillar disorder, an analysis

approach combining elements of prior analysis[84,86] is used. Specifically, in the absence of disorder, the ratio of the m^{th} to n^{th} order meridional Bragg peak intensities in the SAXD pattern is $\frac{I_m}{I_n} = \left(\frac{n}{m}\right)^2 \left(\frac{\sin(m\pi(O/D))}{\sin(n\pi(O/D))}\right)^2$ [84,132]. If a degree of disordering of the sharp gap/overlap interface is present, the peak intensities are reduced by a Debye-Waller type factor $\exp\left(-\kappa q^2\right)$ where κ is a term proportional to the disordering, and q is the wavevector of the specific SAXD peak[86]. Higher order peaks (with larger q) are thus reduced in intensity by a larger amount than lower order peaks. Combining these effects and using $q_n = \frac{2\pi n}{D}$, we have Equations (14) and (15):

$$\frac{I_7}{I_5} = \left(\frac{5}{7}\right)^2 \left(\frac{\sin(7\pi(O/D))}{\sin(5\pi(O/D))}\right)^2 \exp\left(-24\kappa\left(\frac{2\pi}{D}\right)^2\right) \quad \textbf{Equation 16}$$

and

$$\frac{I_8}{I_5} = \left(\frac{5}{8}\right)^2 \left(\frac{\sin(8\pi(O/D))}{\sin(5\pi(O/D))}\right)^2 \exp\left(-39\kappa\left(\frac{2\pi}{D}\right)^2\right) \quad \textbf{Equation 17}$$

In the Appendix, the variation of $\frac{I_7}{I_5}$ and $\frac{I_8}{I_5}$ is plotted for different levels of disorder (Fig. A.5.4), and the calculation of O/D and κ from known values of $\frac{I_7}{I_5}$ and $\frac{I_8}{I_5}$ is described in Appendix A.5.2.

5.2.5. Statistical Analysis

The representative trace refers to a single sample whereas the grouped data are mean values with standard error of mean (SEM) (where n=5-9). Statistical analyses were performed using Microsoft Excel. Data was analysed and significance measured using either paired (within-group) or un-paired (between-groups) t-test. Within-group tests refer

to statistical significance relative to the corresponding uncompressed fibrillar state (prior to mechanical loading) within a sample group and are indicated at $p<0.05$ (#), $p<0.01$ (##) and $p<0.001$(###). Between-group tests refer to the statistical significance of the enzymatic group relative to the control groups within each fibrillar state and are indicated at $p<0.05$ (*), $p<0.01$ (**) and $p<0.001$(***).

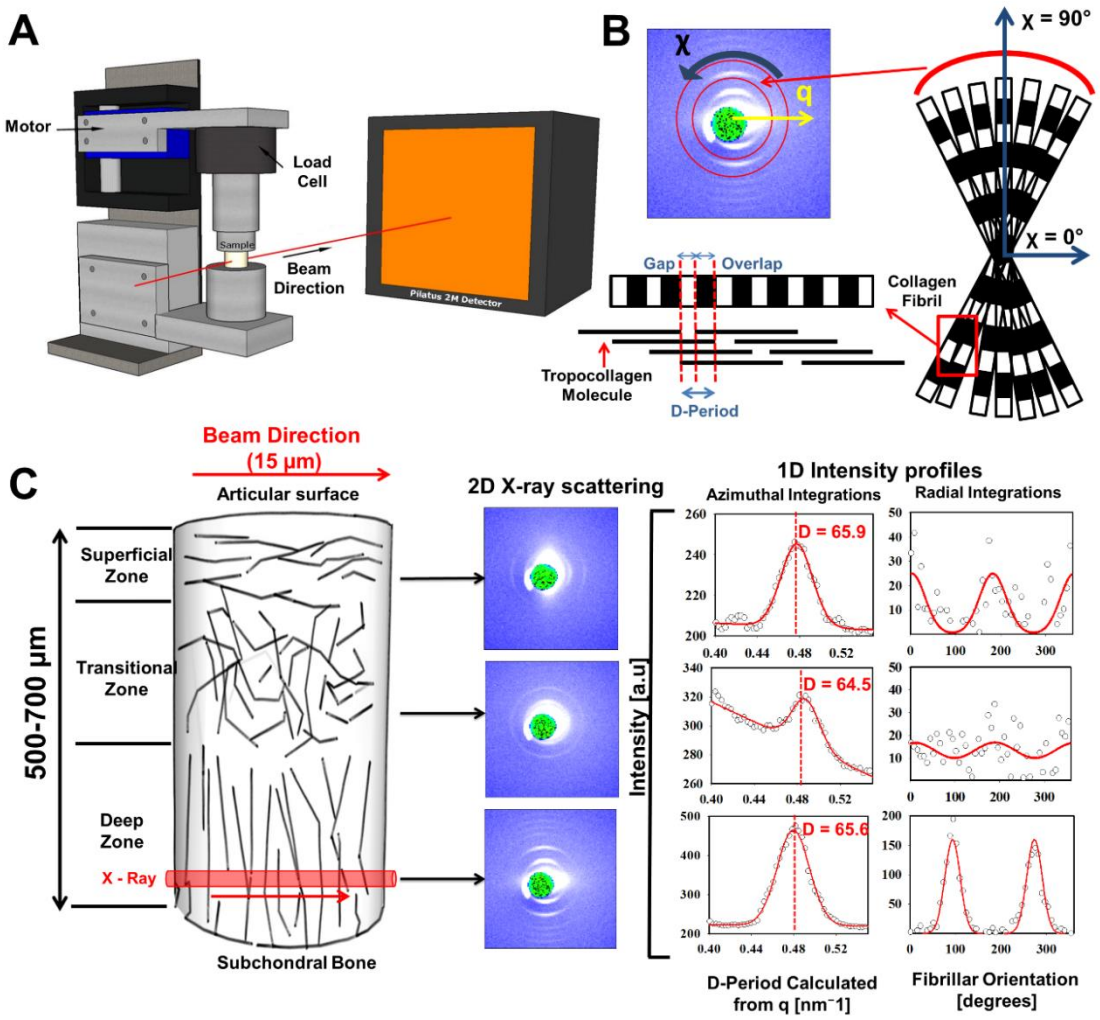

Figure 5.1: Experimental setup for in situ structural analysis of collagen fibrils in cartilage. (A) schematic of the micro-compression tester setup(B) Representative SAXD pattern from the deep zone of bovine articular cartilage alongside a schematic of the fibrillar structure and distribution. (C) The depth-dependent collagen architecture in articular cartilage can be observed in the associated diffraction patterns, with fibrillar D-period and orientation determined from the peak positions in the azimuthally and radially integrated intensity profiles, respectively.

5.3. Results & Discussion

5.3.1. Zonal variation in collagen fibre orientation

Using SAXD in conjunction with a specially built mechanical testing system[133] (adapted from Karunaratne *et al.* (2012)) (Figure 5.1a) we have produced diffraction data which we have used to quantify the collagen orientation and D-period in unstrained and compressed articular cartilage, as shown schematically in Figure 5.1b. Our SAXD patterns show that the collagen fibres are parallel to the articular surface in the superficial zone and perpendicular to the surface in the deep zone, while they have a more isotropic distribution in the transitional zone (Figure 5.1c) confirming the well-established spatial pattern of collagen orientation in articular cartilage[14,26,90].

5.3.2. Sudden transient reduction in collagen fibril pre-strain during stress relaxation

We reveal a completely new time-dependent phenomenon observed in collagen fibrils during compression of articular cartilage. During the stress relaxation phase at constant applied tissue strain (Figure 5.2a), there is a sudden transient reduction in collagen D-period (Figure 5.2b). This indicates a reduction in the level of fibril tensile pre-strain. This behaviour occurs approximately 60-100 s after the peak stress and is followed by a rapid return to the original loaded D-period. The whole event lasts approximately 50-80 s and occurs without any perceptible fluctuation in the macroscopic stress relaxation response (Figure 5.2a inset). This transient reduction in pre-strain indicated by change in the collagen D-period was observed in both bovine (Figure 5.2) and human articular cartilage (Figure 5.3). There was no statistically significant difference between the transitional and deep zones in terms of the timing of the sudden reduction in D-period after the onset of the application of compression, with mean values (±standard error of the mean or ±SEM) of 60.0 (±11.4) and 82.5 (±11.1) seconds respectively (Figure 5.3c). Immediately after compression of human articular cartilage, there was a slight reduction in D-period of

approximately 0.5%. This was statistically significant in the deep zone with a change in D-period from 65.6 (±0.07, n=4) nm to 65.3 (±0.11, n=4) nm (mean ± SEM, $p<0.05$, Figure 5.3d).

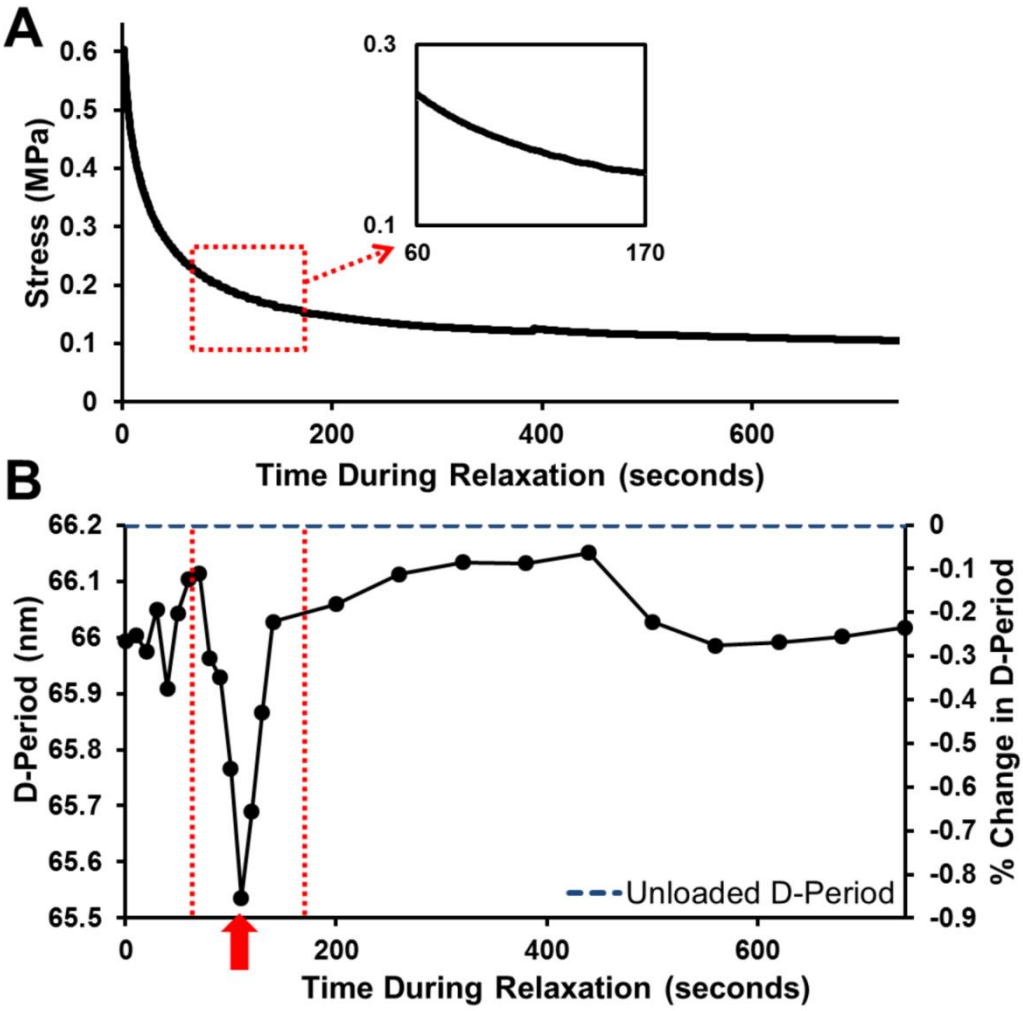

Figure 5.2: Collagen fibrils experience a delayed reduction and recovery in fibrillar pre-strain in response to stress-relaxation. (a) Representative, macro-scale stress response in compressed bovine cartilage during relaxation (20% strain level loaded at a rate of 20%/min). (b) Corresponding absolute and percentage change in D-period, relative to the unloaded local D-period. Red arrow highlights the time at minimum D-period. The onset of the event starts at ~50 seconds after peak load, and the subsequent D-period recovery is complete by ~150 seconds (Figure 5.2b), during which period no visible changes in tissue stress is visible (Figure 5.2a, inset).

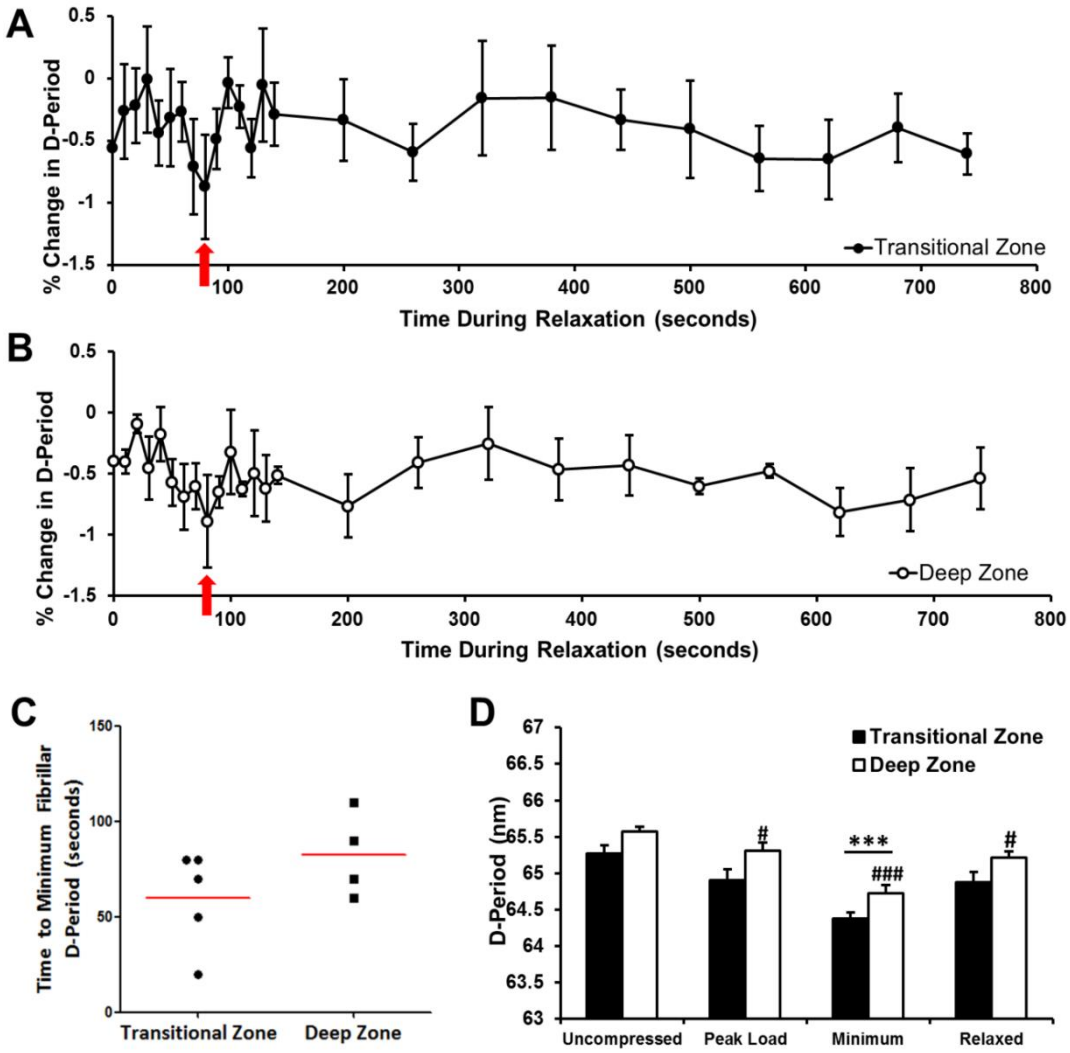

Figure 5.3: Delayed fibrillar response to loading observed in human femoral cartilage. Percentage change in fibrillar D-period during macroscale tissue relaxation found in both the transitional (a) and deep (b) zones, averaged over multiple samples (Transitional n=5, Deep n=4). A delayed rapid reduction to a minimum D-period (red arrow), followed by a recovery is observed ~50-100 seconds after peak load in both cases. (c) The time from the start of tissue-level relaxation until the minimum D-period value; no significant differences were observed between the two zones (p>0.05). (d) Variation in absolute D-period at different time points (uncompressed, at peak load, at the point of minimum D and relaxed) for both transitional and deep zones. Error bars represent standard error of mean throughout, * indicate significance between groups, # indicate significance within groups.

5.3.3. Calculation of collagen pre-strain and the effect of swelling pressure

To examine the mechanism regulating the observed transient changes in collagen pre-strain and D period, we next investigated the effect of proteoglycan swelling pressure. For these studies, bovine articular cartilage explants were examined with and without pre-treatment with chondroitinase ABC (Sigma-Aldrich, Poole, UK). Treatment resulted in loss of sulphated glycosaminoglycan chains (sGAG) into the media (Appendix, Fig. A.5.1) and changes in macroscopic tissue mechanics with a reduction in mean (±SEM) tangent modulus from 5.9MPa (±0.52) in the untreated group to 3.4MPa (±0.37) in the 0.1U/ml treatment group (Appendix, $p<0.001$; Fig. A.5.2 and A.5.3). In the untreated bovine cartilage samples, compression induced the sudden transient reduction in collagen D-period in both transitional and deep zones (Figure 5.4a,b) as seen in human cartilage (Figure 5.3) indicative of a reduction in fibril tensile strain. In the unloaded cartilage, enzymatic degradation of the proteoglycan produced a significant reduction in D-period in both the transitional (Figure 5.4e) and deep zones (Figure 5.4f). This reduction is accompanied by an increased scatter in the D-period variation for the chondroitinase-treated samples (Figure 5.4a and b, lower rows), especially in the transitional zone, suggesting mechanical disruption of the fibrillar network, as well as a reduction in pre-strain. These findings demonstrate the relationship between proteoglycan/water content and collagen fibrillar pre-strain. Specifically, the swelling pressure, exerted by the hydrated proteoglycan, causes tensile strain of the collagen fibres as predicted by established models of cartilage biomechanics[134–136]. Without knowledge of the collagen D-period in the complete absence of any swelling pressure it is not possible to calculate the exact level of collagen pre-strain. However, assuming that the chondroitinase treatment removes all the intrinsic swelling pressure, the collagen fibres would experience a tensile pre-strain of approximately 1.5%. Based on previous estimates of a single

collagen fibril stiffness of ~500 MPa[114], this level of pre-strain is equivalent to a tensile force resisting the swelling pressure of ~0.3 μN / fibril for a fibril radius of ~100 nm (corresponding to a stress of ~7.5 MPa). Furthermore, the results suggest that the sudden transient reduction in D-period is equivalent to a 60% reduction in total collagen pre-strain (Figure 5.2).

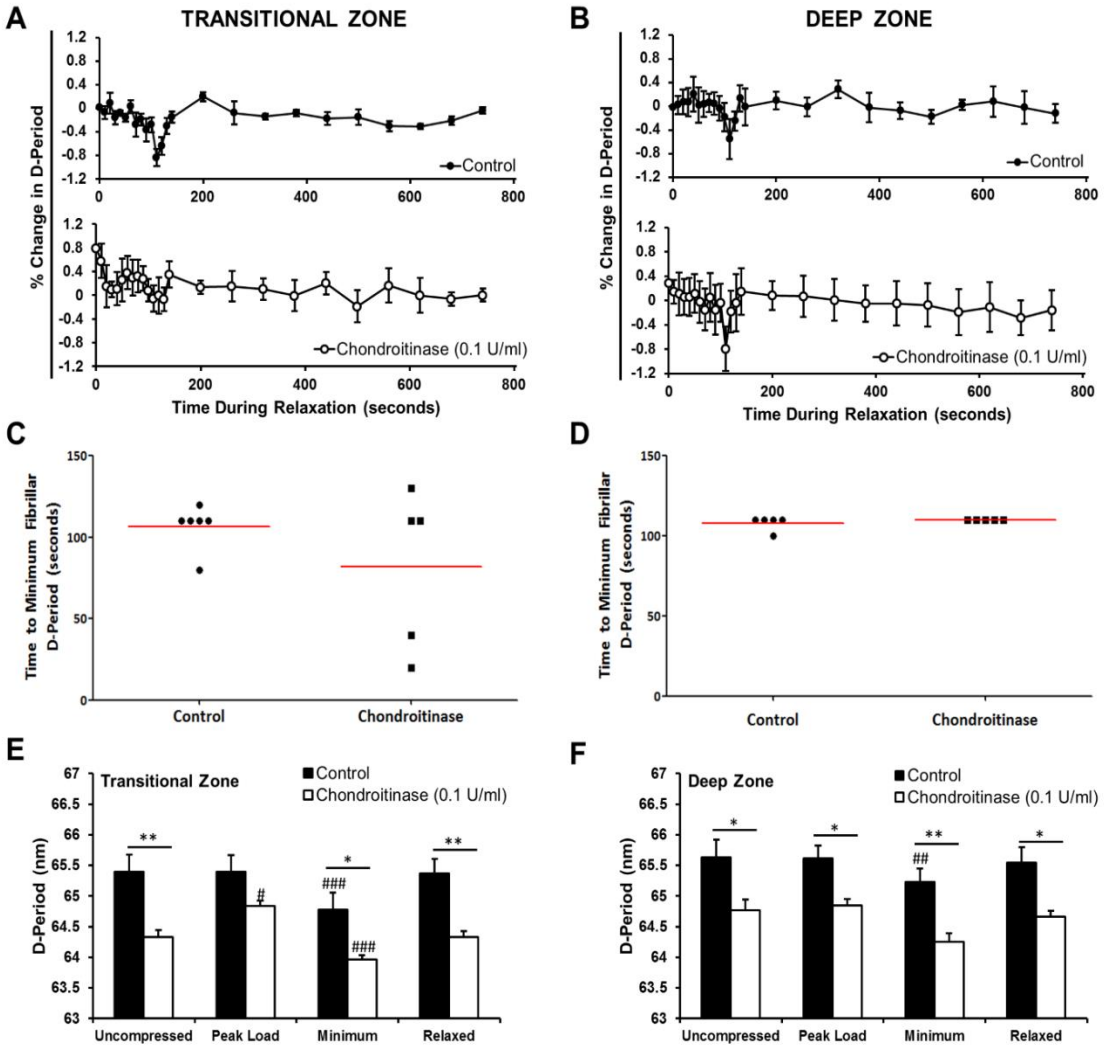

Figure 5.4: Enzymatic degradation leads to an altered fibrillar pre-strain alongside changes to fibrillar response directly after loading in bovine cartilage. Data shown separately for transitional (a,c,e) and deep (b,d,f) zones. (a,b) Time-dependent variation in percentage change of D-period, showing delayed fibrillar response within both the transitional and deep zones in the control group and a loss of response in the transitional zone of the enzymatic group (a, lower plot). (c,d) Time from the start of macro-scale relaxation to minimum D-period. (e,f) Variations in absolute values of D-period (at the different stages of stress relaxation) in both the transitional and deep zones. These values show reduced fibrillar pre-strain as a result of enzymatic digestion. Error bars represent standard error of mean (n=5), * indicate significance between groups, # indicate significance within groups.

Interestingly, in the transitional zone of bovine cartilage digested with chondroitinase to remove proteoglycan, compression resulted in a significant increase in D-period at peak load (Figure 5.4e), in contrast to the lack of change seen in both zones of untreated control samples (Figure 5.3d and Figure 5.4e,f). Further, it is seen that the sudden decrease in collagen D-period is much less clear in the transitional zone of the enzymatically digested tissue, compared to controls in the same region (Figure 5.4a) and both groups in the deep zone (Figure 5.4b). It is possible that these effects are related to fibril-fibril interaction between zones. Horizontally oriented superficial zone collagen fibrils are continuously connected to the transitional zone fibrils *via* the well-known arcade-like collagen fibril structure[30,43]. On vertical compression, the superficial zone fibrils (at 90° to the loading direction) will extend in tension, and (due to their interconnection to the transitional zone) exert a tensile force on the transitional zone fibrils. We suggest that in native cartilage, fibrils are pre-strained by the proteoglycans almost to their maximum limit, while on enzymatic digestion, this pre-strain is lost. Therefore, in the chondroitinase digested tissue, the fibrils are more flexible due to the loss of pre-strain and have a greater range to extend (increase) in D when tension is applied. We can speculate, therefore, that the tensile force from the superficial zone fibrils will not have any effect on the transitional zone fibrils in native cartilage (as the fibrils can't extend further) but in chondroitinase-digested cartilage, leads to an increase in D-period for the transitional zone fibrils.

5.3.4. Intra-fibrillar reordering correlating to a reduction in D-period

In order to understand the origins of the transient reduction in fibrillar pre-strain (in terms of the D-period), the structural mechanisms enabling mechanical homeostasis between fibrils and the hydrated proteoglycans first much be considered. The resultant loss of pre-strain is most likely due to the reduction of the localised proteoglycan-induced swelling pressure and will arise if the hydration of the proteoglycans is lowered. The osmotic and

swelling pressures inside cartilage are determined by a combination of water content in both the proteoglycan and collagen components, as well as ionic strength and pH of the immersing medium, and it has been shown that ionic strength variations can alter intrafibrillar spacing[137]. Here we have applied controlled compression, whereby some of the water associated with the proteoglycans will undergo stress induced movement, thus expelling water from the interstitial space within the tissue. This effect, and the associated reduction in the fibrillar pre-strain, will also lead to further structural changes within the fibrillar network.

Three hypothetical scenarios to accommodate such local changes are (i) intrafibrillar rearrangement and disordering, (ii) flow of water from the intrafibrillar space to the interfibrillar compartment, and (iii) fibrillar reorientation. Intrafibrillar rearrangement of tropocollagen molecules, specifically leading to changes in the gap to overlap ratio, have a characteristic and quantifiable effect on the Bragg peak intensities in the meridional SAXD pattern. If mechanism (i) is correct then we would expect either changes in the relative intensity ratios of different Bragg peaks in the SAXD pattern due to a change in the ratio of overlap zone in the fibril to the fibrillar D-stagger (O/D)[84,86], and/or a disorder-induced reduction of peak intensities, with higher orders (larger wave vector) reducing more than lower orders, via a Debye-Waller term[86]. In this scenario, assuming a step-function line-shape for the electron density variation across the gap and overlap zones in the fibril, it is possible to derive analytical expressions for the ratios of the intensities of different orders of Bragg peaks (Equations (14)-(15), ***Materials and Methods***), as functions of D, the overlap/D-period ratio (O/D) and a Debye-Waller term (κ) proportional to the axial disorder at the gap/overlap interface[84,86] Peak intensities are denoted as I_n with n the peak order (e.g. I_5 for the 5th order peak), and are measured from the total area under each Bragg peak (***Materials and Methods***). For mechanism (ii), the

lateral intermolecular spacing of the tropocollagen molecules would reduce from the known value for hydrated type I collagen fibrils (d_m~1.5 nm) towards the value for dehydrated fibrils (d_m~1.1nm)[109,110]. Lastly, for mechanism (iii), changes to predominant fibrillar orientation (from the SAXD I(χ) position) would occur transiently at the point of minimum D. To obtain an initial indication as to which one of these mechanisms is predominant, we analyse in more detail the SAXD patterns in a representative example (sample shown in Figure 5.2).

Figure 5.5A) and B) show the variation of I_7/I_5 and I_8/I_5 with time, overlaid with a trace of the D-period variation to observe any correlated change. It is seen that near the minimum of D, the peak intensity ratios likewise exhibit a minimum. Viewing just the time-zone of the reduction of D (Figure 5.5C)) it is observed that the ratios first decrease (zone 1), then vary in opposite directions, with I_8/I_5 increasing and I_7/I_5 decreasing, in zone 2, which contains the minimum of D. In the subsequent zone 3, there is a recovery of intensity ratios to near original values. From the disordered step-function model of the gap/overlap zone of the collagen fibril, a "phase-diagram" of intensity ratios for varying levels of disorder can be constructed, and is shown in Figure 5.5D. By varying the disorder term κ until a mutually consistent solution for O/D is obtained (κ~1.75 nm^2; see Appendix A.5.2) for the initial values of I_7/I_5~0.25 and I_8/I_5~0.15, an initial value for O/D ~0.466 is found. This value is very close to previous O/D values of 0.46-0.47 reported in vertebrate tissues like tendon[132]. The concurrent decrease in intensity in zone 1 (Oa → Ob in Figure 5.5D; concurrently Ea →Eb) can be modelled by a further increase in the disorder term κ from 1.75 nm^2 to 4.00 nm^2. The next stage (zone 2; Ob → Oc in Figure 5.5D) can be reproduced by keeping κ fixed and reducing O/D from 0.466 to 0.458 (leftward arrows Figure 5.5D), as I_7/I_5 and I_8/I_5 vary in opposite directions near O/D ~

0.466. The last stage Oc → Od, involving a combined reduction in disorder and increase in O/D, returns intensity ratios and D to near initial values, as observed. A reduction from the initial values exists (κ = 2.8 nm^2 at the end vs 1.75 nm^2 at the start), indicating residual disorder. Line-plots of these variations in intensity ratios are shown, together with the experimental data from Figure 5.5C, in Appendix Fig. A.5.4. Because of the high observed sensitivity of the intensity ratio changes to small variations in O/D and disorder, it is possible that across different samples, precise details of the time-sequence of intensity ratio variations may differ somewhat.

These findings support the idea that change of intrafibrillar disorder and axial arrangement of tropocollagen molecules (changes in O/D ratios) as relevant mechanisms operating during the transient reduction in D-period, and are schematically shown at the intrafibrillar/molecular level in Figure 5.5E. Here each vertical dark blue rod corresponds to a single tropocollagen molecule, which are aggregated to form a fibril. D-period, overlap (O) and gap (G) regions indicated on the leftmost schematic. As above, a, b, c and d correspond to points in Figure 5.5D. Left to right: ordered arrangement of tropocollagen molecules with well-defined gap/overlap interface, followed by an increase in intrafibrillar disorder leading to a blurred interface, then a reduction in overlap zone and finally ordered intrafibrillar arrangement after recovery of pre-strain – for schematic clarity, the residual disorder at the last stage is not depicted. In contrast, analysis of the equatorial intermolecular spacing between tropocollagen molecules inside the fibrils shows no change during the D-period reduction (Appendix Fig. A.5.7A), indicating intrafibrillar loss of water to the extrafibrillar compartment is not a major factor. Further, analysis of the azimuthal distribution of SAXD intensity show that the fibril orientation distribution does not change during the transient reduction in D-period (Appendix Fig. A.5.7B). The data presented are thus supportive of mechanism (i) rather than mechanisms

(ii)-(iii), where under compression, as a result of localised changes in swelling pressure, there is a transient reduction in fibrillar D-period accompanied by intrafibrillar disordering and changes in O/D ratio, followed by a reordering as the tissue equilibrates. A schematic of these mechanisms at the fibrillar level (one level higher than the intrafibrillar scale) is given in Figure 5.6.

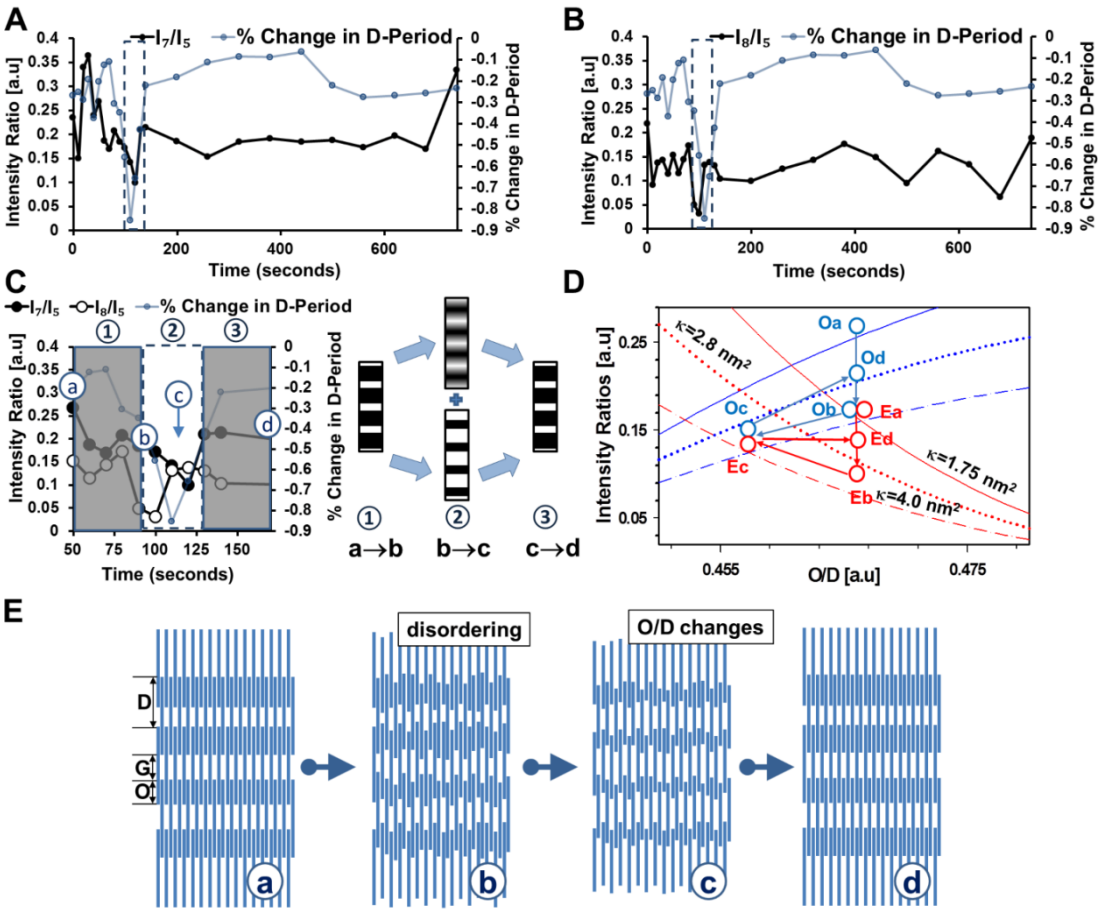

Figure 5.5: Intra- and interfibrillar structural alterations during transient reduction of pre-strain: A) The time-variation of the 7th to the 5th order peak intensity ratio I_7/I_5 (solid black line) shows a characteristic dip (highlighted in dashed box) near the minimum in D (grey line) B) Similar to A), but for the 8th to the 5th order peak intensity ratio I_8/I_5. C) Left: A temporally magnified overlay of the D-period variation, I_7/I_5 and I_8/I_5 near the minimum in D. The symbols (a, b, c, d) denote specific time-points in the schematic of the fibrillar level changes. D) Modelling of the observed behavior in C), in terms of changes in overlap/D ratio and changes in the intrafibrillar disorder parameter κ. E) Schematics of the intrafibrillar-level mechanisms corresponding to the transient changes in D.

The time delay (Figures. 2-4), from the start of relaxation to the time at which the transient changes in the D-period occurs, may be explained by the graded structure within cartilage. The depth-dependent poroelastic variation in extracellular matrix composition and organisation leads to a reduction in the compression induced deformation of the deeper zones compared to the superficial zone[117,55]. Simulations to determine the localised mechanical environment within this inhomogeneous tissue have shown that drag forces between solid and fluid, fluid pressure and velocities, are zone-dependent, such that there are time-delayed peaks in the transitional and deep zone under time-dependent loading[138,139]. These increases in force and pressure will likely induce fluid flow out of the proteoglycan gel around the fibrils in a time-dependent manner such that there is a wave propagation of localised strain transfer[140].

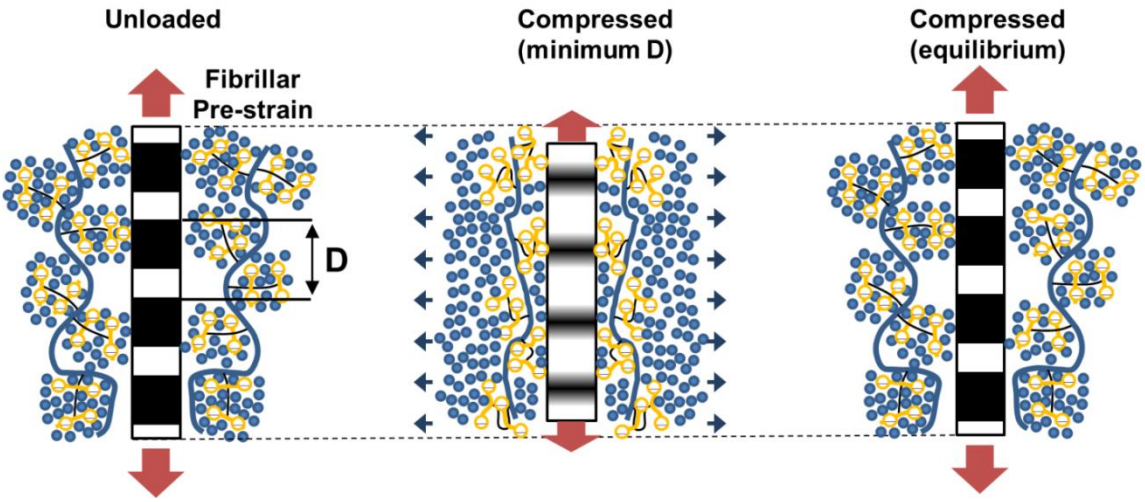

Figure 5.6: Fibrillar level mechanisms underlying transient change in pre-strain in cartilage: Schematic of the cartilage ECM nanostructure at the fibrillar (~10-100 nm) scale, with ordered Type II collagen fibrils (banded rods) surrounded by swollen, amorphous aggregates of negatively charged proteoglycans (orange circles) with a large number of loosely bound water molecules (blue circles)). Orange arrows indicated direction and relative magnitude of tensile pre-strain exerted by the proteoglycan aggregates on the collagen fibril. Left: Unloaded cartilage. Middle: Static compression of tissue is followed by a transient reduction of pre-strain in the collagen fibrils. Right: As water molecules return to the proteoglycan aggregates there is a restoration of collagen fibril pre-strain and ordering/crystallinity.

Our findings on the nanoscale mechanics of cartilage, including the reductions of fibrillar D-period due to removal of proteoglycan and associated water content, as well as the alterations in intrafibrillar ordering and molecular packing, can be linked to recent findings of hydration-induced alterations in fibrillar and intrafibrillar structure in tendon[123]. Masic *et al*. found, in tendon collagen, that removal of water induced shifts in fibril D-period comparable to the pre-strains observed here (2.5% vs 1.5% in our case), and osmotic pressure changes had similar (but smaller) effects[123]. Although the studies cannot be directly compared as Masic *et al.*[123] studied complete dehydration of tendon collagen, while in our case we investigate partial loss of proteoglycans and associated water in cartilage collagen, the fibrillar-level structural changes in strain and molecular ordering may be related. Under a compositional change of the ECM (removal of 30-50% of proteoglycan[64,141]) that can be considered a disruptive change similar to but somewhat less severe than that induced by dehydration[123], stress relaxation in the fibrils is larger in articular cartilage than in tendon. This potentially reflects the greater volume fraction (and thus influence) of the non-fibrillar matrix in cartilage, as well as the difference in ECM architecture. Further, even during application of strains that are physiological in level (during stress-relaxation), the pre-strain reduction at the point of minimum D-period was ~0.5%, corresponding to a 2.5 MPa stress off-loaded from the fibrils. Interestingly, the level of stress removed from the collagen fibrils in cartilage on enzymatic digestion (~7.5 MPa) is considerably larger than the osmotic pressures of proteoglycans of ~0.1-0.4 MPa reported in Chahine *et al.*[142] across solutions of varying ionic strength, with similar values reported by Maroudas and co-workers[137,143]. Experiments where both PG content and ionic concentration are varied, together with the alteration of fibrillar pre-strain and structure, may in future shed light on these differences, as would selective removal of specific PG components like hyaluronan. We lastly note that these stress-values (such as

the value of 7.5 MPa reported earlier) are of the order of the maximum macroscopic compressive stresses in cartilage. For example, the maximum stress during stress relaxation in bovine cartilage, over similar percentage strains as in this study, can range from less than 1 MPa (Appendix A.5.2) to ~6-8 MPa[57,128]. Such large internal pre-stresses have been found in tendon collagen as well[123]. In this context, our results show clear evidence for the highly pre-stressed environment of the collagen fibrils *in situ* and in physiological conditions in cartilage, which may be related to recent suggestions concerning the active role of collagen fibrils in connective tissue[86,123].

5.4. Conclusion

To conclude, we have quantified the presence of pre-strain in cartilage collagen prior to compression. We also find that under physiological levels of compressive strain, the stress-relaxation dynamics of the collagen fibrils in articular cartilage shows an unusual and hitherto unknown behaviour which is not detected in the macroscopic mechanical response. This phenomenon appears as a delayed but very rapid reduction in collagen pre-strain followed by an equally rapid recovery. We suggest that the temporal changes in collagen strain and diffraction intensity are related to compression induced changes in water content in the extrafibrillar proteoglycan phase. These changes in the interfibrillar phase, which controls swelling pressure, lead to alterations in the intrafibrillar structure, specifically an increase in fibrillar disordering and a decrease in the overlap of adjacent axially staggered tropocollagen molecules. These mechanisms have implications for cartilage biomechanics and are likely to prove valuable for computational modelling, particularly in incorporating collagen fibrillar network mechanics (as per Figure 5.6) in fibril-reinforced poroelastic models of cartilage, where up to now the mechanical behaviour of collagen has had to be assumed[134]. Future studies may investigate the influence of different loading, disease and ageing conditions, which are all associated

with changes in cartilage proteoglycan and water content[20,140]. These factors are expected to regulate swelling and osmotic pressures as well as collagen D-period and microfibril packing, and significantly alter biomechanical performance, with biomedical and clinical implications in joint degeneration. While the details of the mechanism behind the delayed transient reduction in fibril strain are, as yet, not fully understood, we suggest that this interesting new phenomenon may provide a step change in understanding collagen nano-mechanics, which is of fundamental importance in cartilage and other hydrated collagenous soft tissues.

Chapter 6

IL-1β effects the fibrillar response in cyclic loading

6. Il-1β effects the fibrillar response in cyclic loading

6.1. Synopsis

Although it is unlikely that osteoarthritis can be characterised as a single disease, in many cases it is thought to involve an inflammatory response[144,145]. Pro-inflammatory cytokines such as interleukin-1β (IL-1β), are secreted by both the chondrocytes and the synoviocytes found in the synovial sublining layer[20,111]. Elevated levels of IL-1β in the synovial fluid have been reported in humans with osteoarthritis at concentrations between 0.021 to 0.146 ng/ml compared to levels up to 0.020 ng/ml in healthy cartilage[146]. IL-1β leads to increased production of nitric oxide (NO) and prostaglandin E_2 (PGE_2) both of which are inflammatory mediators leading to the upregulation of matrix metalloproteases (MMPs), such as MMP-13 which primarily drives collagen type II cleavage[147], which in turn drives cartilage degradation. In the longer term IL-1β causes suppression in collagen synthesis[148].

In osteoarthritic cartilage, the changes to the normal biomechanical and biochemical factors lead to alterations in the normal functional activities of the chondrocytes leading to an inflammatory response within the tissue[23]. As a result, the chondrocytes are driven to both synthesize and secrete more catabolic molecules such as proteases, cytokines and other inflammatory mediators[24]. The inflammatory cytokines help to direct and progress the MMP-mediated degradation of the matrix whilst disrupting homeostasis[20].

As a result of these molecular changes, there is a direct impact on the tissues mechanical integrity, reducing the stiffness of cartilage, and the load bearing capacity[149]. In OA, this further leads to surface fibrillations and osteoarthritic lesions which over time develop to complete tissue breakdown, when combined with continued physiological loading[112]. A study by Thompson *et al.* (2015) found that IL-1β treatment led to approximately a 60%

reduction in the tangent modulus from 2.42 MPa in the control to 0.88 MPa in the IL-1β group. Alongside this, the relaxation modulus was also reduced by approximately 75% whilst the relaxation half-life was also significantly shorter in the IL-1β group indicating alterations in both the solid elastic and viscoelastic behaviour of fluid movement[112]. Here we study the effects of IL-1β treatment on the mechanical response of the collagen fibrils in articular cartilage during cyclic loading. Cyclic loading was chosen to simulate, as far as possible, a more physiological loading condition within the tissue compared to static loading as examined in the previous **Chapter 5**.

6.2. Materials and methods

6.2.1. Sample preparation and IL-1B treatment

Bovine explants were prepared as described in **Chapter 3**, producing 2 mm diameter full thickness explants. Explants were treated for 12 days in 5ng/ml of IL-1β (Peprotech, UK) prepared in serum-free supplemented DMEM. Control samples were maintained in media without IL-1β. Following treatment samples were transferred to PBS, snap frozen using liquid nitrogen and stored at -20°C prior to shipment to ESRF.

6.2.2. Mechanical Loading and SAXD procedure

Experiments were conducted at the European Synchrotron Radiation Facility (ESRF) at beamline ID02 using the SAXD setup with the beam size reduced to as small as technically feasible (as ID02 is not a dedicated microfocus line). The beam size at the sample was measured to be approximately 50μm and the sample to detector distance at approximately 1m as determined using a chicken collagen standard.

During each experiment, samples were placed within the sample holder and pre-strained to 0.1% compressive strain whilst being hydrated with PBS prior to any loading. Figure 6.1 shows an image of the micro-compression tester setup at the ID02 beamline. An initial

line scan with 50 μm increments in the y-direction (perpendicular to the tissue surface) was performed to determine a zone of interest based on the qualitative differences in the SAXD patterns. Once a region was determined a specialised script produced by the beamline scientists was run to continuously move the sample-stage motors both in horizontal (x-) and vertical (y-) directions within a fixed window 500 mm wide (in x-direction) by 200mm wide (in y-direction). The continuous scanning motion was to reduce the amount of time any particular part of the tissue was exposed to the beam, thus minimising radiation-damage effects. Given the high flux of the beam at ID02 of 1 x 10^{14} versus 3.57 x 10^{9} at beamline I22 at DLS respectively, and therefore higher potential for radiation damage, an exposure-time test (similar to that conducted at DLS in **Chapter 2**) was conducted to determine the minimum exposure time required to obtain a quantifiable pattern. This was determined to be at 0.03 seconds.

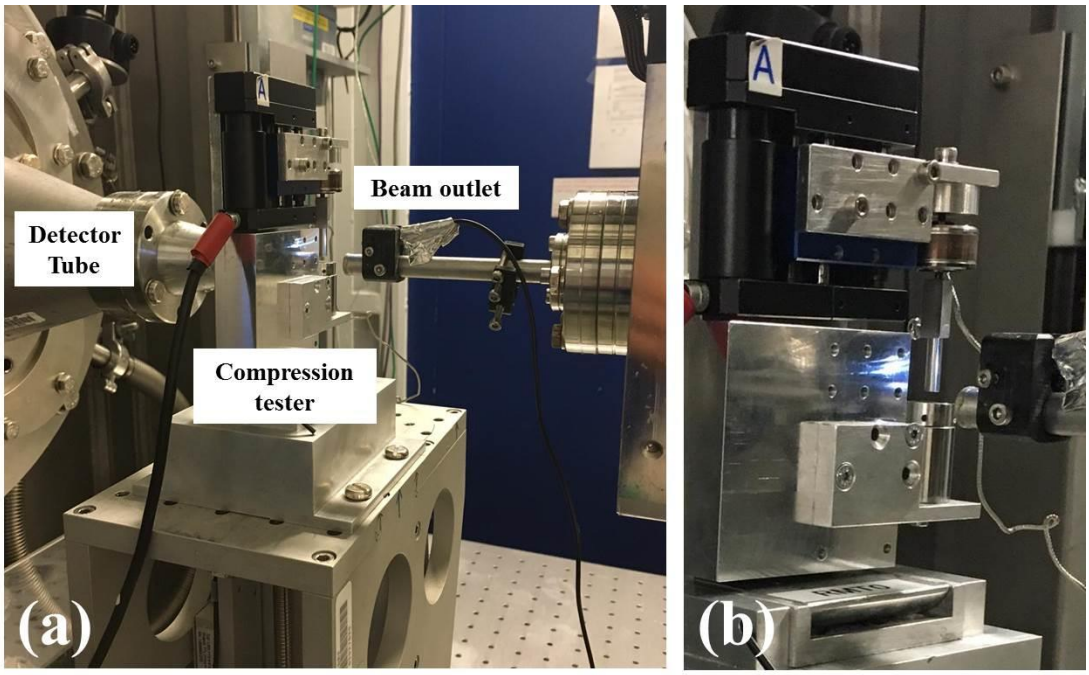

Figure 6.1: Images of micro-mechanical tester setup at beamline ID02 at ESRF. (a) Sample stage with mounted tester, (b) View of sample base and compression platen in line with the beam outlet.

The loading regime, and subsequent parameters that were obtained from the cyclic loading experiments, are indicated in Figure 6.2. Each sample was subjected to 150 cycles at 0.25Hz which included a ramp-up to 20% strain level, hold-period for 1 second to allow SAXS acquisition (loaded state), followed by a release back down to 0% strain level, where the strain is again held fixed for 1 second to allow a second acquisition (unloaded state). A TTL pulse trigger, initiated by a customization of the LabVIEW programme, was used to remotely control when the detector was activated. Detector acquisition was set to occur every 5 cycles both in the ramp up and ramp down holding phases. The integration of the micromechanical control software with the beamline and detector control was accomplished via the expert technical assistance of the beamline scientists at ID02, in particular Dr Sylvain Prevost (currently at ILL, Grenoble).

6.2.3. SAXD Analysis

From the SAXS patterns a combination of parameters were measured, reflecting the changes along the fibril axis (from azimuthally integrated radial profiles $I(q)$) and perpendicular to it (from radially integrated azimuthal profiles $I(\chi)$). Figure 6.2a indicates both the amplitude and width of the azimuthally integrated peak $I(q)$. The width parameter w_q provides an indication into the level of *inter*fibrillar disorder in terms of the D-period structure and regularity (the *intra*fibrillar disorder is more accurately measured via the model described in the previous **Chapter 5**). A similar principle is applied in Figure 6.2b, where the width of the radially integrated profile $I(\chi)$ provides an indication into the degree of angular orientation i.e. the wider the peak, the larger range of possible fibrillar orientation. Figure 6.2d indicates the peak intensity, which is calculated as the area under the azimuthally integrated peak, which provides insight into the collagen content within the particular zone i.e. the larger the peak intensity the more collagen present within the region. However, the ratio of peak intensities of different orders is also a marker

indicating disordering within the tissue (as described in the previous **Chapter 5**). The peak position in the azimuthally integrated profile (Figure 6.2d) is used to calculate the D-period, whilst the angular intensity maximum in the radially integrated profile provides the predominant orientation of the fibrils (Figure 6.2e).

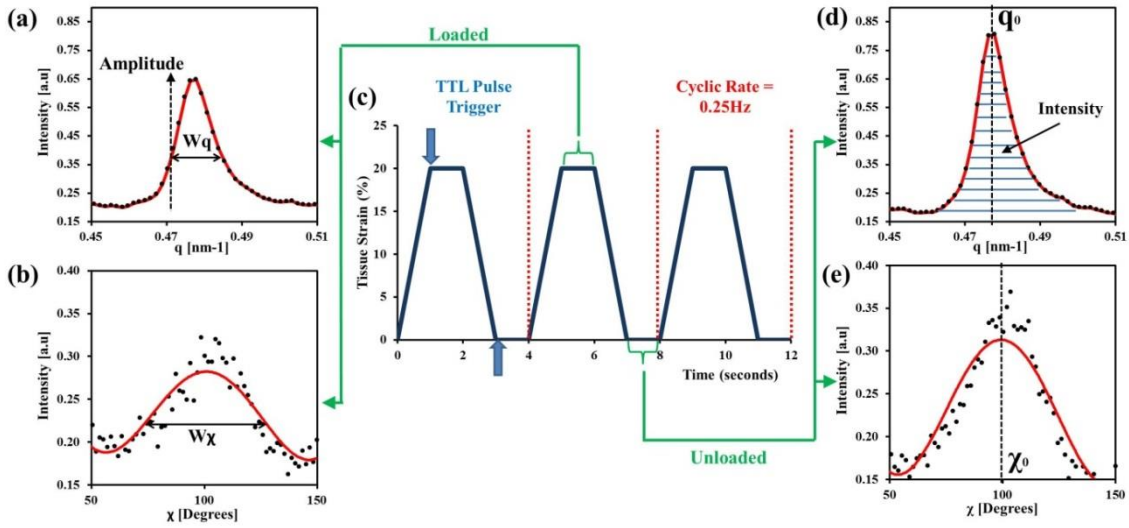

Figure 6.2: Schematic of loading/scanning protocol. (a) Plot of I(q) integrated from a SAXD pattern taken under load application with the associated I(χ) in (b), and unloaded plots in (d)-(e) respectively. (c) Indicates the loading profile utilised over 150 cycles with maximum tissue strain at 20% at a rate of 0.25Hz.

6.3. Results

6.3.1. Short-term changes in fibrillar D-period and related parameters

When observing the short-term trends (16 loading cycles) within cyclically loaded cartilage, the fibrillar structural parameters undergo time-resolved, reproducible changes. Figure 6.3 shows, in a control sample, that during each cycle there is a compression-induced change in the D-period, w_q and intensity alongside tissue level stress. In regard to temporal changes over multiple cycles, tissue stress shows a gradual decrease in peak stress from ~1.7MPa down to approximately 1MPa within the first 16 cycles of loading and thereafter a near-equilibrium level is reached as indicated by Figure 6.3a. Conversely,

each of the measured fibrillar parameters do not show such a trend over this short period of loading.

In more detail, when observing the first cycle alone in Figure 6.3b, the D-period is reduced at 20% strain level, followed by recovery of the D-period when the tissue strain is released as indicated by the point above at cycle number 1. This same trend continues with subsequent cycles where the D-period has a value of ~65.9nm and under compression a reduced value ~65.8nm. Inter-fibrillar variations of the D-period distribution between the fibrils are indicated in Figure 6.3c. This shows a pattern via the width w_q of the $I(q)$ peak, where on compression there is an increase in w_q at ~0.006nm^{-1} followed by a reduction to ~0.005nm^{-1} following the removal of strain. This behaviour is linear throughout the first 16 cycles and the shifts observed are relatively maintained at the same level throughout. Lastly, the same periodic response is observed when observing the peak intensity, where a ~33% change is observed between the compressed and uncompressed state (Figure 6.3d). Upon compression there is a reduction in intensity to ~0.002 which is followed by a recovery/increase in intensity to ~0.003 on removal of the tissue level strain.

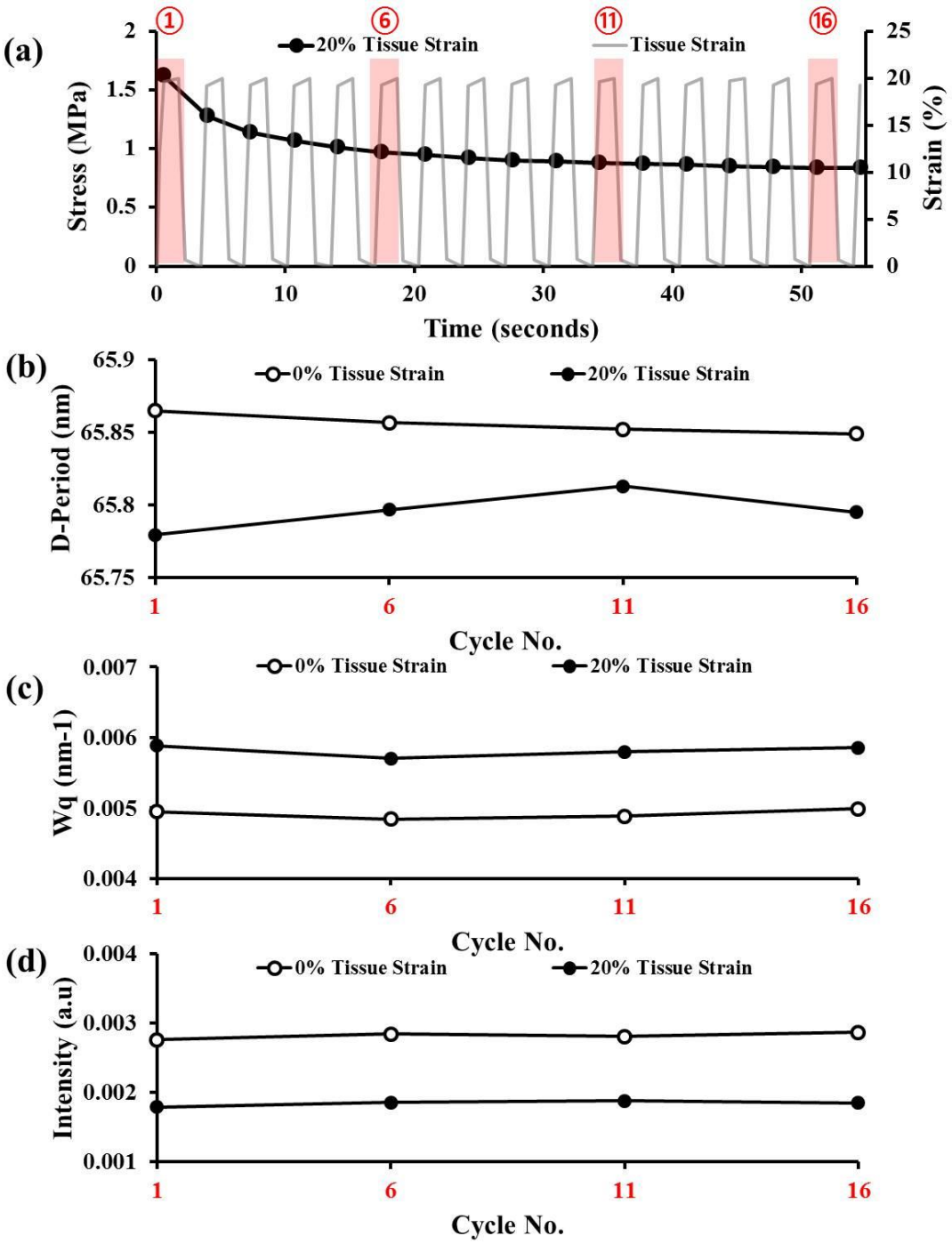

Figure 6.3: Changes in fibrillar structure and mechanics found as a result of cyclic loading in the deep zone. (a) Peak stress measured over 16 cycles at 0.25Hz alongside strain levels at each cycle, (b-d) shifts in D-period, w_q and I(q) peak intensity found at 0 and 20% tissue strain where n=7. The cycles where SAXD spectra were obtained are indicated in red.

6.3.2. Short-term changes in fibrillar orientation and related parameters

Alongside measurable changes to the axial parameters like the D-period, there are observable shifts under cyclic loading in both the predominant orientation of the fibrils χ_0 as well as the degree of orientation w_χ. Whilst the angular shifts are small (~ a couple of degrees), the most noticeable change is observed in the w_χ. In terms of the measured χ_0 positions, Figure 6.4b shows that there are shifts in orientation that can be either way in relation to the predominant direction, such that in the first cycle there is a shift from approximately 89° in the compressed state to 88° when uncompressed, whereas at cycle 6 the direction reverses, although minimally, from approximately 86° to 87°. When looking at Figure 6.4c, within the first cycle there is an increase in w_χ to 28° upon 20% strain followed by an immediate reduction to 18° at 0% strain.

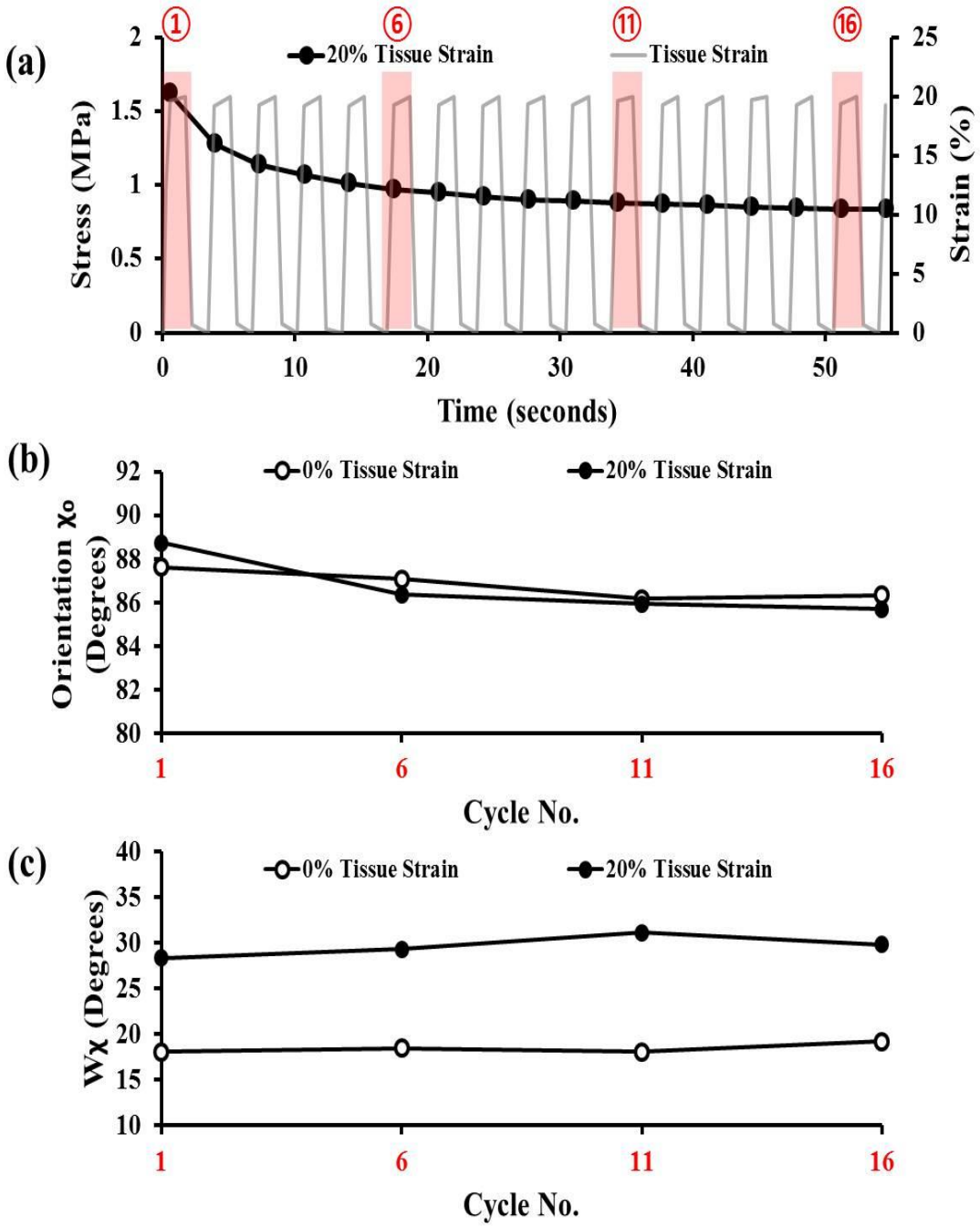

Figure 6.4: Changes in fibrillar structure and mechanics found as a result of cyclic loading. (a) Peak stress measured over 16 cycles at 0.25Hz alongside strain levels at each cycle, (b,c) χ_0 and w_χ peak found at 0 and 20% tissue strain where n=7. The cycles where SAXD spectra were obtained are indicated in red.

6.3.3. Effects of IL-1β treatment on tissue level mechanics

Figure 6.5a shows that treatment with IL-1β leads to a reduction in the measured peak stress during cyclic loading. Taking the first cycle alone, there is a 22% reduction in peak stress between the control and IL-1β groups where the stress values are 1.8MPa and 1.4MPa respectively. This difference in peak stress increases over time whereby at the 16th cycle there is a 38% difference between the two groups. Furthermore, Figure 6.5b shows that there is a significant difference in the mean peak stresses within the first 16 cycles where $p<0.01$. This confirms the efficacy of the treatment with IL-1β in creating mechanical instability leading to changes in the tissue level mechanics.

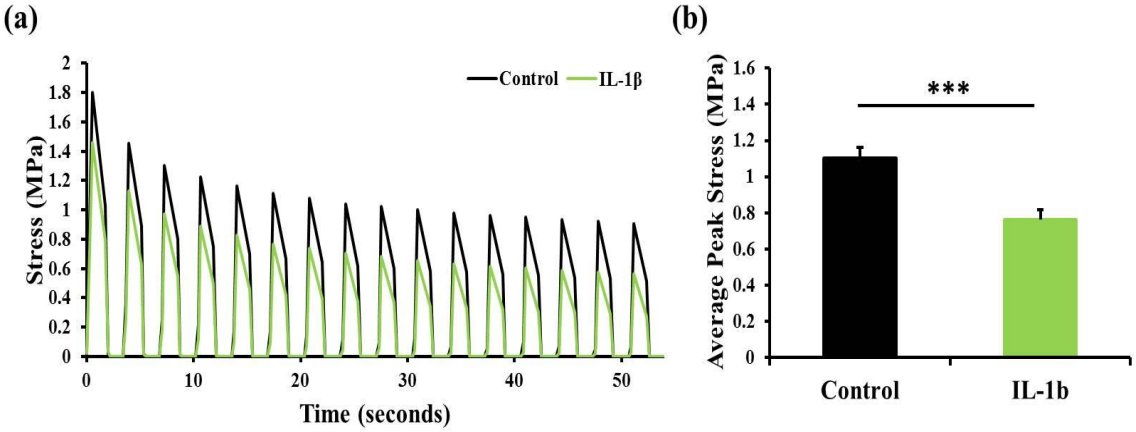

Figure 6.5: Reduction in tissue level stress under 20% strain in cyclic loading as a result of IL-1β treatment in bovine explants. (a) Stress measured over the first 16 cycles, Black line indicates the control that were kept in media whilst the green line indicates the treatment group with 5ng/ml of IL-1β in media (representative traces) (b) average peak stress from first 16 cycles. Error bars represent standard error of mean and * refers to significance between the groups (p<0.01).

6.3.4. Long-term changes in fibrillar D-period and related parameters

We will use a slightly different method (relative to the previous section) of presenting the data over longer timescales, to more coherently discuss the changes in unloaded and loaded states separately, and to show both absolute and fractional-level changes.

Figure 6.6 shows the various azimuthally integrated parameters at the 0% strain level from every 5 cycles over a longer period than the short 16 cycles previously considered – 150 cycles in total. When observing the long-term trends, there are some clear differences in fibrillar parameters between the control versus the IL-1β treatment groups in the unloaded state. To begin with, when considering the two treatment groups Figure 6.6a shows overall that there is a reduction of approximately 0.1% in D-period in the IL-1β treated cartilage as highlighted by the red box. This difference in D-period is maintained throughout the 150 cycles. The reduction in D-period in the IL-1β . Indeed, in both groups the fibrils consistently return close to their pre-loaded state within each cycle. Figure 6.6b shows the w_q parameter, which indicates the interfibrillar disorder between the fibrils. There is an overall reduction in the level of interfibrillar heterogeneity observed within the IL-1β group when compared to the control, as indicated by Figure 6.6b. Here, in the most extreme cases the difference in the two groups can be approximately 64% - calculated at cycle 46. The reduction of the intensity parameter shown in Figure 6.6c further supports the fact that IL-1β leads to degradation of collagen and overall loss in concentration, therefore leading to lowered peak intensity. Specifically, there is a difference of ~15% in the base level of intensity at ~0.0028 in the control versus -0.0024 in the IL-1β group between the two groups which is maintained

throughout the 150 cycles. Furthermore, the long term level of intensity is retained after each cycle in both groups.

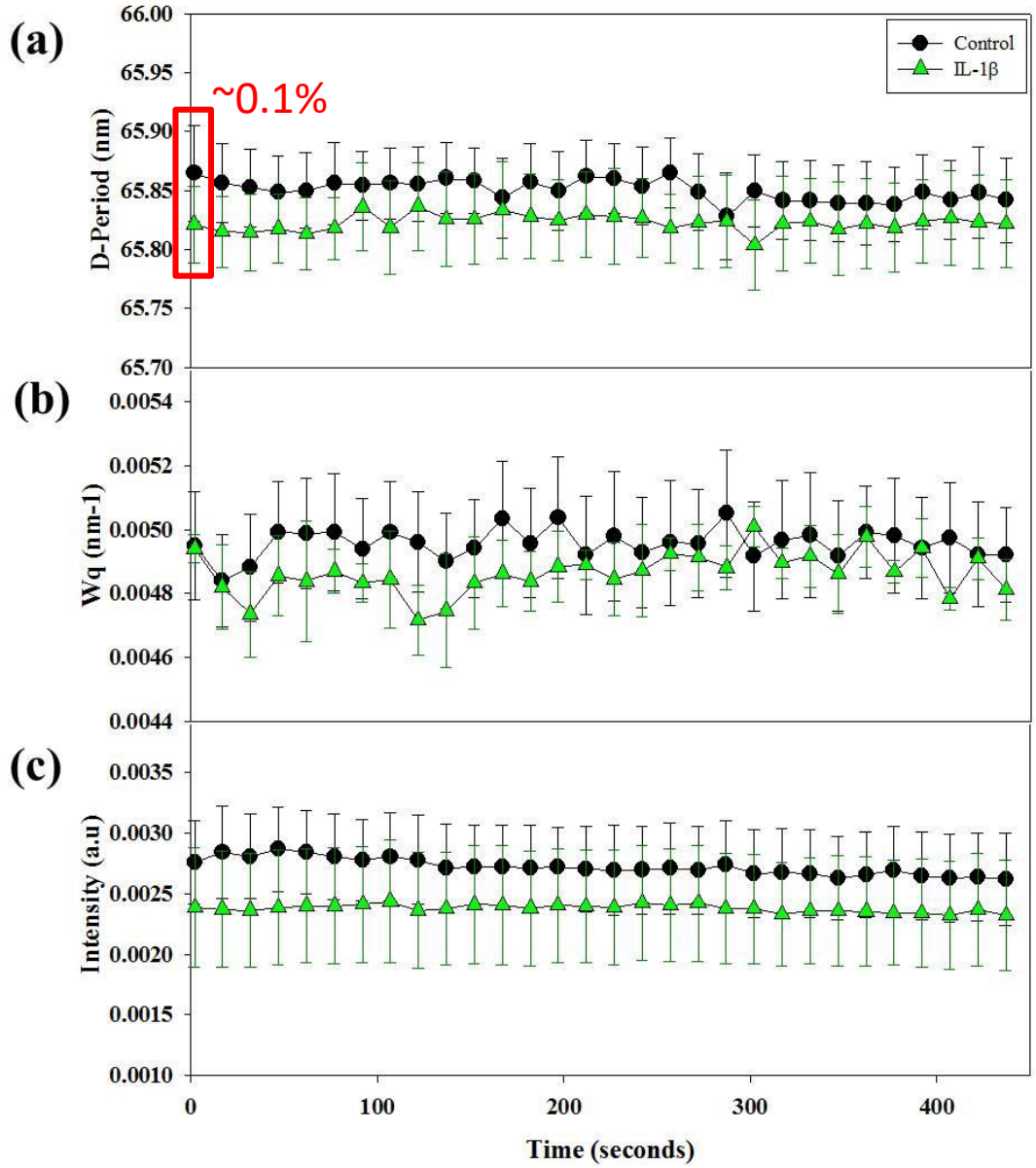

Figure 6.6: 0% Tissue strain (second trigger) segment of cycle: Fibrillar dynamics over 150 cycles at 0.25Hz. Comparison of absolute D-Period (a), w_q (b), I(q) Peak Intensity (c) in the control (n=7) versus IL-1β (n=6) treatment group.

When considering the tissue at the compressed state of 20% strain (Figure 6.7), the parameters do not differ, between control and IL-1β, as much as in the 0% case. Firstly,

the compressed D-period in both groups is similar at ~65.8nm. In other words, whilst the initial (uncompressed) values of D-period (and consequently fibrillar pre-strain) are different between IL-1β and the control group (Figure 6.6), the values under compression are similar (Figure 6.7). Secondly, considering w_q, we note that - as with the unloaded case - the w_q parameter is lower in IL-1β, which suggests that there is less disorder between the fibrils in the IL-1β group even under compression, when compared to control. Thirdly, under compression there is no observable difference in the peak intensity between the two groups and therefore no major differences in the intrafibrillar disordering level. We note that while in the unloaded case there was a visible difference in intensity (Figure 6.6c) from the loss of collagen in the IL-1β group, under compression (Figure 6.7c) the difference is minimal.

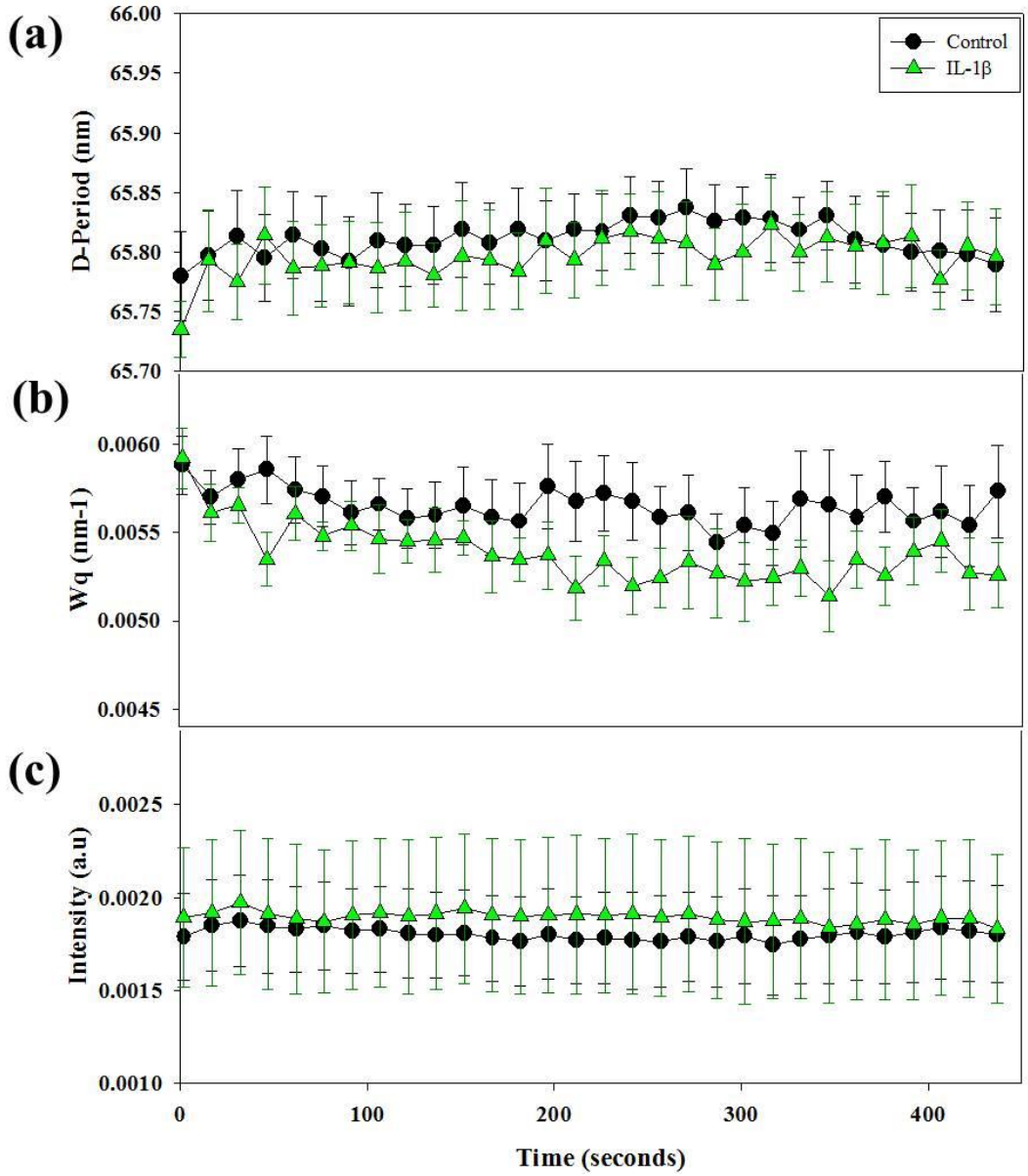

Figure 6.7: 20% Tissue strain (first trigger) segment of cycle: Fibrillar dynamics over 150 cycles at 0.25Hz. Comparison of absolute D-Period (a), w_q (b), I(q) Peak Intensity (c) in the control (n=7) versus IL-1β (n=6) treatment group.

Regarding the orientation of the fibrils at 0% strain level, the direction of orientation is similar between groups (Figure ***6.8***a) with χ_0 ~ 84° in the control and ~ 82° in the IL-1β group. The degree of orientation is also similar (Figure ***6.8***b) where the average values across the long term are ~19° for IL-1β and ~ 20° for control.

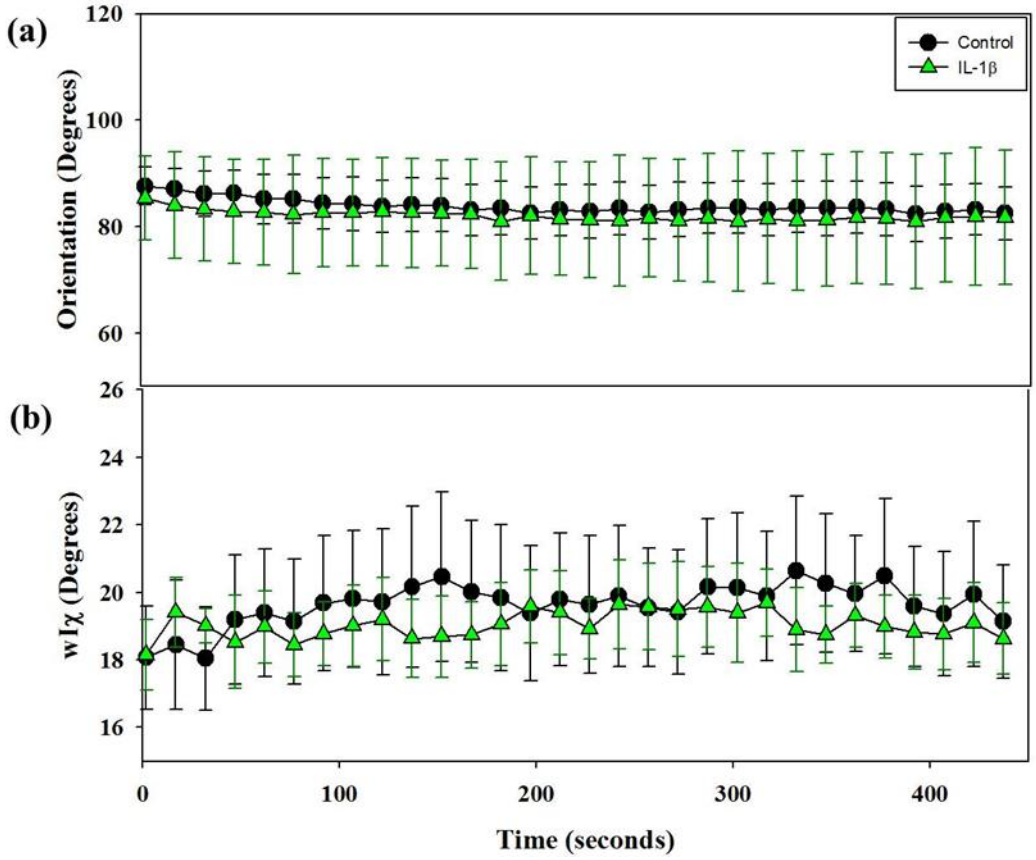

Figure 6.8: 0% Tissue strain (first trigger) segment of cycle: Fibrillar dynamics over 150 cycles at 0.25Hz. χ_0 (a) and w_χ (b) in the control (n=7) versus IL-1β (n=6) treatment group.

In contrast, under 20% compression a downward linear trend in χ_0 in both groups is visible (Figure 6.9), where the initial direction shifts from ~86° to ~77° at 150 cycles. As the direction of loading is at 90°, a downward trend implies a shift of fibrils away from the loading axis. Further, there is a reduction in the degree of angular orientation in both groups, as w_χ increases to ~30°, which is 50% more than the uncompressed level (Figure 6.8).

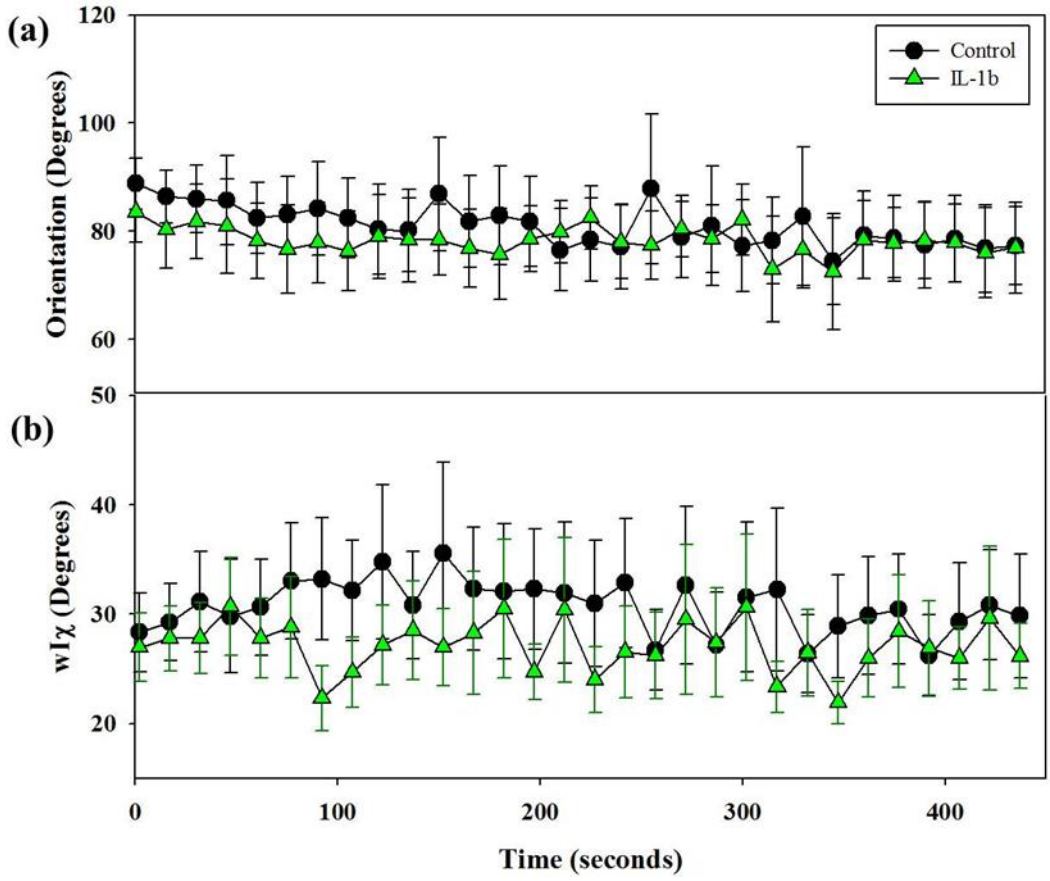

Figure 6.9: 20% Tissue strain (first trigger) segment of cycle: Fibrillar dynamics over 150 cycles at 0.25Hz. χ_0 (a) and w_χ (b) in the control (n=7) versus IL-1β (n=6) treatment group.

6.3.5. Percentage change of axial fibrillar parameters during cyclic loading

Figure 6.10 shows the averaged % changes in D-period for all the samples, where the reference state is the initial SAXD pattern before loading, for each sample. Here, while the pre-strain is reduced on compression, the long-term trend-lines show an upward trend (i.e. reduction of the extent of pre-strain loss) in both groups during the 20% compression phase of each cycle. In contrast, the 0% unloaded case for both groups is largely constant over time, with no long term changes. Looking at the trend-lines alone, under compression the % change in D-period shifts from ~ -0.12% to ~ -0.06% in the control and -0.03% in the IL-1β group. It is noted that the initial % change (i.e. leftmost set of

points in Figure 6.10) does appear similar between control and IL-1β. In the cycles that follow, the level of change in the compressed state is greater in the control group overall at approximately -0.1% compared to the IL-1β case at approximately -0.05%.

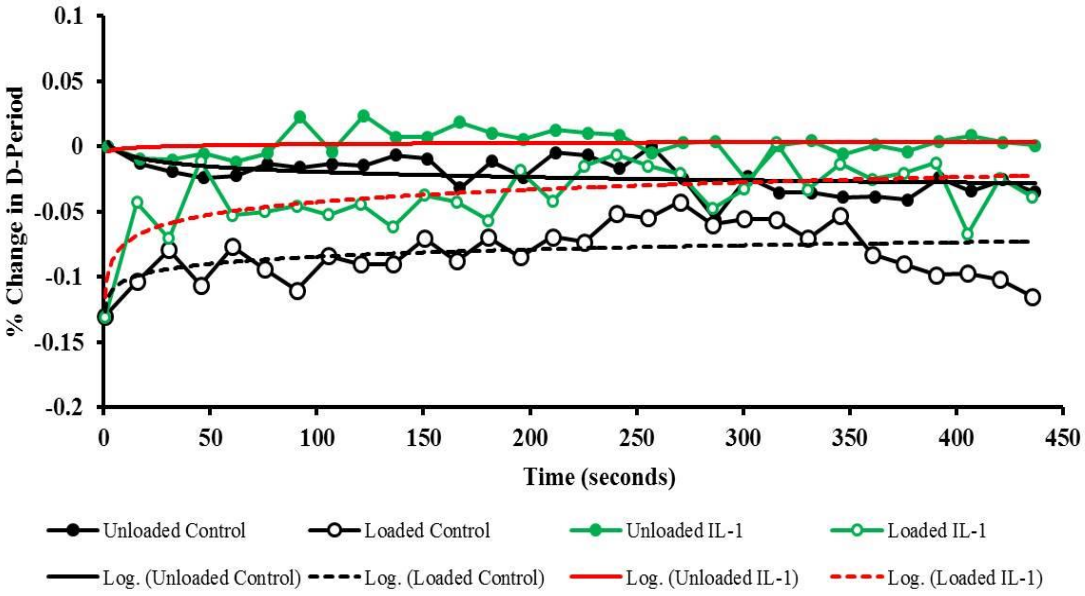

Figure 6.10: Averaged % Change in D-Period in the long term trends in both the control (n=7) and IL-1β (n=6) treatment groups during the loaded and unloaded phase of the cyclic loading. A logarithmic trend line has been fitted as a guide to the eye.

This difference in % D-period between the two groups is supported by the trend in the heterogeneity of the fibrillar d-period (w_q) shown in Figure 6.11. The unloaded state (at 0% strain levels within each cycle) show no long term trend (in either group) associated with disordering. However, as with the % change in D-period, there is a trend under the compressed state whereby there is an overall reduction in w_q in both groups. Further, the reduction of intrafibrillar D-variance is more in the IL-1β group decreasing from ~15% to ~5% than in control group where the final level is around ~13% at 150 cycles, resulting in lower values of w_q IL-1β case.

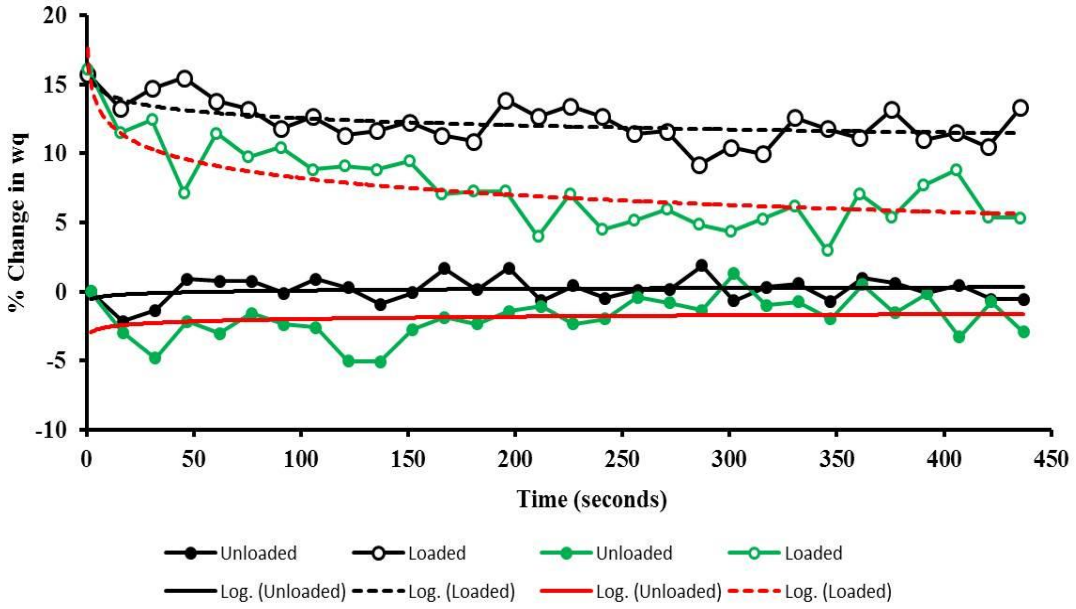

Figure 6.11: Averaged % Change in radial peak width (w_q) over the long term trends in both the control (n=7) and IL-1β (n=6) treatment groups during the loaded and unloaded phase of the cyclic loading. A logarithmic trend line has been fitted as a guide to the eye.

From Figure 6.12, it is seen that the control group undergoes a larger reduction in intensity on compression to 20% strain, when compared to the IL-1β group. The level of % change in intensity remains constant with time in both groups, however there is a difference in the level of intensity with the control-group at approximately -55% with the IL-1β at -25%. Because % intensity reduction is linked to intra-fibrillar disordering, these data suggest there is more disorder under compression in control than in IL-1β. This finding complements the increased inter-fibrillar heterogeneity of control from w_q in Figure 6.11.

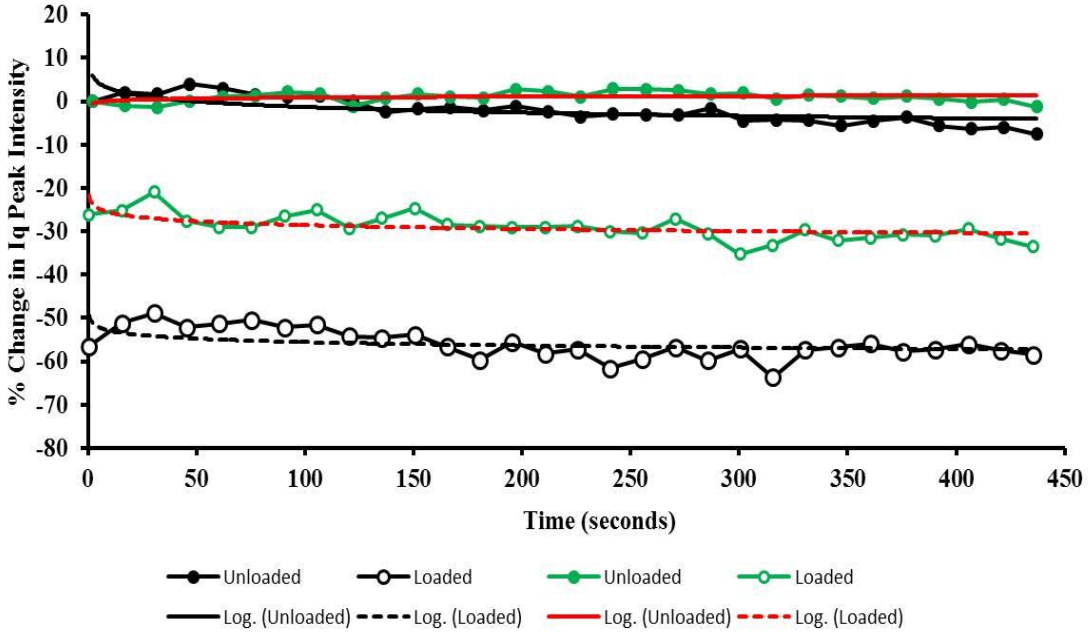

Figure 6.12: Averaged % Change in radial peak intensity I(q) over the long term trends in both the control (n=7) and IL-1β (n=6) treatment groups during the loaded and unloaded phase of the cyclic loading. A logarithmic trend line has been fitted as a guide to the eye.

There is little difference in predominant orientation in the unloaded % case between groups and with time (Figure 6.13; solid lines). As mentioned previously, there are certainly shifts in the direction of orientation under compression which are reversible and there is an overall long term trend leading to ~20% change in χ_0. The two groups behave relatively the same over time, apart from the larger dips between 300-350 seconds; these are likely due to fitting error associated with noisy data.

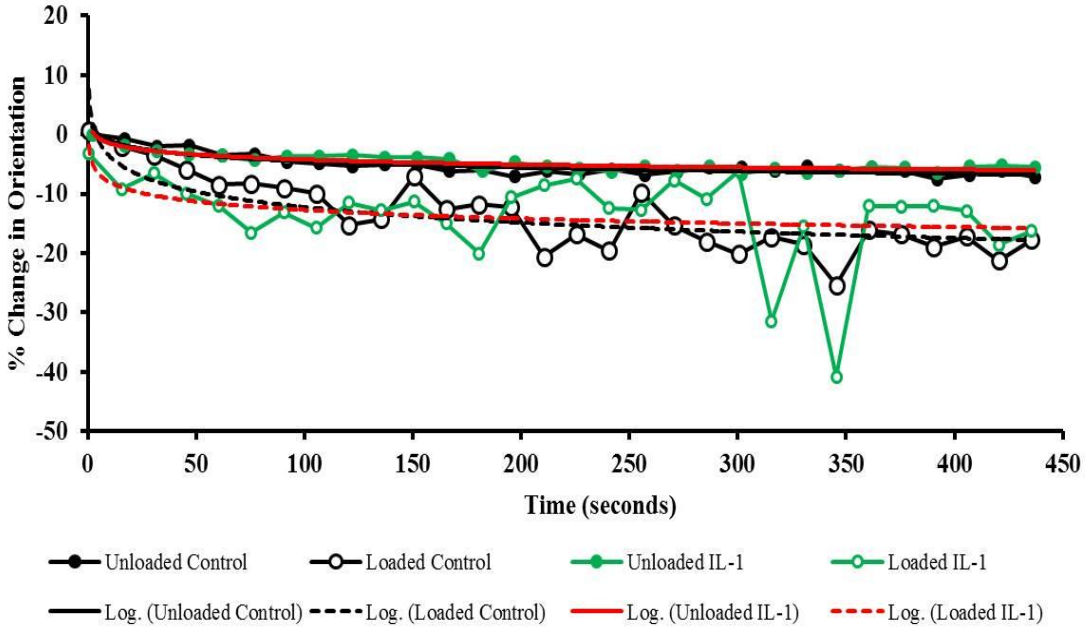

Figure 6.13: Averaged % Change in the predominant fibril orientation over the long term trend in both the control (n=7) and IL-1β (n=6) treatment groups during the loaded and unloaded phase of the cyclic loading. A logarithmic trend line has been fitted as a guide to the eye.

Finally, the % change in w_χ is indicated in Figure 6.14 and as with χ_0 there is only a marginal difference between the groups in the uncompressed state (solid lines). A greater difference is observed under compression, where the % change is much higher in the control group at ~40% compared to the IL-1β at ~30%, with an average long term difference of ~10% between the groups. Observing the trend-lines only, the level of change across 150 cycles shows a small upward trend in the uncompressed state and a downward trend in the compressed state for both groups.

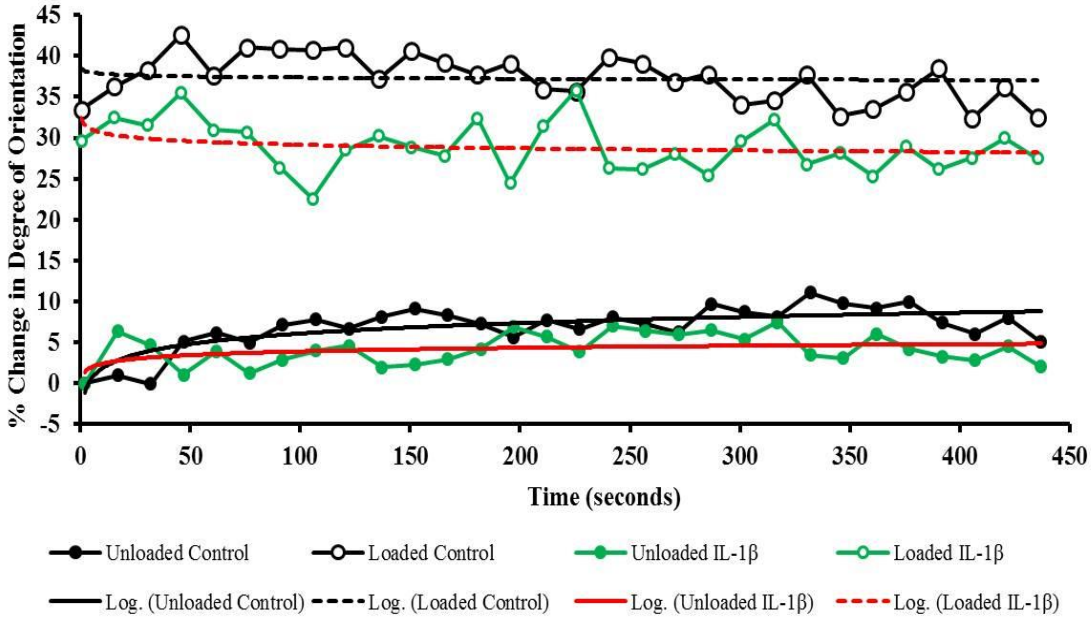

Figure 6.14: Averaged % Change in the degree of fibril orientation over the long term trend in both the control (n=7) and IL-1β (n=6) treatment groups during the loaded and unloaded phase of the cyclic loading. A logarithmic trend line has been fitted as a guide to the eye.

6.4. Discussion & Conclusions

Taken together, these findings would suggest that as the tissue is cyclically compressed, the fibrils dynamically respond through a combination of a reduction in D-period alongside inter- and intrafibrillar disordering to the internal structure of the fibrils. Furthermore, these effects are reversible when the compression is removed, therefore showing that the network of fibrils are flexible and undamaged under physiological (non-injurious) loading.

To begin with, the results demonstrate an overall reduction in D-period as a result of IL-1β induced inflammation within the tissue (Figure 6.3). This is supported by us in a previous study[120] (and reported in **Chapter 5**), where degradation and loss of ECM components lead to a reduction in the fibrillar pre-strain observed in cartilage. We suggest

that as a result of the inflammation response produced by IL-1β, and the subsequent release of both proteoglycan and collagen, the resultant reduction in fibrillar pre-strain is observed.

Under compression both control and IL-1β groups reached a similar absolute value of D-period (Figure 6.7). This would suggest that there is a minimum level that the fibrils are able to 'compress' to, whereby compression of the fibril refers to a loss in the fibrillar pre-strain. Regardless of the initial pre-strain level, it seems that the fibrils can only 'compress' so far – possibly till a pre-tensed fibril reaches the minimum "slack" length - suggesting that the range of flexibility within the fibrils is fixed. In the IL-1β group, this range is significantly reduced due to the reduction in pre-strain following ECM degradation. This is likely to have an effect on the tissue's mechanical properties overall as the fibrils are no longer fulfilling their role as a fully pre-tensed network which can change pre-strain levels substantially under loading. One possible mechanism behind this reduction in flexibility may be a change in the level of cross-linking amongst the collagen fibrils when placed in an inflammatory state.

The results also show that over time the overall reduction in D-period under compression becomes less severe (Figure 6.10), suggesting that the fibrils have the capacity to adapt to loading over longer periods. We suggest that this reduction in pre-strain may be due to both localised reorganisation (and exudation) of PG-molecules and water alongside the internal organisation of the fibrils. This is supported by the trend in the disorder factor w_q (Figure 6.11) where a disordering reduces over time, suggesting that the internal disordering of the fibrils play a role in how the fibrils adapt to compression.

When observing the *inter*-fibrillar disorder there was a marked difference between the groups, such that a reduction in disorder was observed in the IL-1β group (Figure 6.11).

While the physical reasons behind this are unclear to us at the moment, a possibility could be that due to reduced swelling pressure on the fibrils (from the PG-matrix) in the IL-1β case, some fibrils which would be excessively pre-strained (larger D) in normal tissue have relaxed back closer to the overall mean D-value in IL-1β samples, thus reducing the variance in D.

Combined with the D-period and w_q reductions under compression, there was also a reduction in the I(q) peak intensity (Figure 6.12). This further highlights what we have discussed earlier – that there is a degree of flexibility or springiness within the fibrillar network, and that compression disorders the fibrils internally. Additionally, partial removal of extrafibrillar ECM components like the PGs can somewhat suppress such changes in the internal reorganization of the fibrils under compression.

In the short term, we suggest the increase in $w_{\chi,}$, and thus the associated spreading out of the fibrils, may be an attempt to resist compression. Another factor to note is that the degree of change and subsequent return is almost always the same through all the displayed cycles over these first 20 cycles (Figure 6.4). This means that when placed under compression some fibrils found along the loading direction dynamically change their angular orientation to a more inclined direction to the load and this behaviour is reversed when the load is removed.

Given the limited difference between the groups in terms of overall direction of orientation (Figure 6.8/Figure 6.9a) we suggest that this level of degradation does not start to impact the orientation of fibrils but more so the flexibility in terms of the angular dispersion of the distribution (Figure 6.9b), as determined by the % change in w_{χ}. The significant changes are more observable at the intrafibrillar (molecular) level within the

fibrils, as indicated by the previous figures that report changes in parameters extracted from the radial profiles $I(q)$.

Combining these findings, we make the following conclusions:

- IL-1β treatment leads to a reduction in the fibrillar pre-strain as a result of inflammation-induced ECM break down.
- The fibrils have the capacity to dynamically change their internal structure to adapt to loading via change to the D-period through internal disordering.
- Collagen fibrils possess limited level of flexibility in terms of how much the D-period can reduce. This level of flexibility is dramatically reduced in IL-1β treated cartilage, likely due to pre-strain reduction.
- Under compression the fibrils considerably broaden the range of orientations while shifting slightly in orientation, which is a mechanism to accommodate compression; this is observed even when the tissue is degraded.
- There are no long term effects on the orientation of fibrils in either group and there is also a reversible shift in orientation that is unaffected by changes to the ECM.
- IL-1β induced inflammation also affects the fibril response under compression such that the % change w_χ in is reduced, again limiting the flexibility of the fibrils.
- The main fibrillar changes observed are long term effects in the intrafibrillar structure, whereby there is over time a reduced % change in D-period and reduced disorder observed in both groups.

Chapter 7

Cyclic rate effects on the fibrillar response in human cartilage

7. Cyclic rate effects on the fibrillar response in human cartilage

7.1. Synopsis

The loading rate to which cartilage is subjected affects the time-dependent mechanical changes under loading, but the response of the nanostructure as a function of loading rate is little studied. Previous studies have shown that under physiological loading, whereby levels of tissue stress range from 2-12MPa[150], there is an effect on both the thickness of the tissue as well as successive changes in the interstitial fluid pressurisation and thus changes to the tissue stiffness under dynamic loading until an equilibrium response is reached[103,150–152]. The viscoelastic nature of cartilage in compression is highlighted during cyclic loading, as the dynamic modulus of the tissue can increase by a factor of 2 when transitioning within the range of physiological frequencies from 0.01 to 2Hz[103]. Based on the mechanical response, a differentiation between the fluid flow-dependent and flow-independent mechanisms within cartilage can be made through varying the rate of loading. Specifically, at higher rates the flow-dependent viscoelasticity becomes less significant and the tissue begins to behave more as an elastic solid, accompanied by an increase in hydrostatic pressure within the tissue[151]. Sah *et al.* (1989) theorised around the observed frequency dependence on the dynamic stiffness of cartilage. They suggested that at low frequencies smaller than or equal to 0.001Hz, fluid exudation was at a slower rate combined with reduced intra-tissue pressurisation, however, at higher frequencies between 0.01-1Hz there would be an associated increase in the tissue pressurization and as a result, an increase in the resistance to fluid motion via the solid matrix, leading to a more elastic response would be observed[151].

Several efforts have been made to further explain the mechanisms behind the behaviour described above, specifically the role of each tissue constituent in determining these

properties. Many of these attempts involve computational models in the form of fibril-reinforced poroelastic models that have the capacity to reproduce cartilage behaviour[53,64,135,153]. These models attempt to predict the role of the collagen fibrils during typical cyclic loading during activities such as walking. For example, a model derived by Ateshian *et al.* (2009) to determine the tissue equilibrium response assumes the fibrils to be in a continuous arrangement with the capacity to only sustain tension[136]. However work within this thesis, as well as a previous study[120] have shown that the fibrils are able to dynamically reorganise their internal structure in order to respond to localized changes during compression and relaxation. The study in **Chapter 6** determined that the fibrils also respond during cyclic loading, where there is an immediate reduction in D-period under compression followed by a recovery on removal of strain. What is yet to be determined is how the fibrils respond during different rates of macroscopic loading across the physiological loading range – and whether the rate-dependent alterations in macroscale mechanical response is represented by changes within the fibrillar network.

7.2. Materials and methods

7.2.1. Sample preparation

Experiments were conducted at the European Synchrotron Radiation Facility (ESRF) at beamline ID02 using the SAXS setup described in **Chapter 6**. The beam size at the sample was measured to be approximately 50μm and the sample to detector distance at 1000.71mm. Human explants were prepared as described in **Chapter 3** whereby 2mm full thickness explants were used. Samples were placed into the micro-compression tester and a region of interest determined in the same manner as of that described in **Chapter 6**.

7.2.2. Mechanical loading and SAXD procedure

The varying cyclic rates used to load the sample are indicated in Figure 7.1**,** and the rates include a 'slow' rate at 0.08Hz, a 'medium' rate at 0.25Hz and a 'fast' rate at 0.33Hz. All samples were loaded to 20% strain level. It is noted that these rates are slower than that of walking, but are within the physiological range stated above. These rates were also chosen given the necessity to acquire SAXS acquisitions – with finite exposure times – at both the ramp-up and ramp-down phase. The cyclic loading alongside the detector triggering mechanisms used are described in **Chapter 6**. The same parameters as those described in **Chapter 6** were determined from the SAXS patterns including D-period, w_q and the peak intensity $I(q)$.

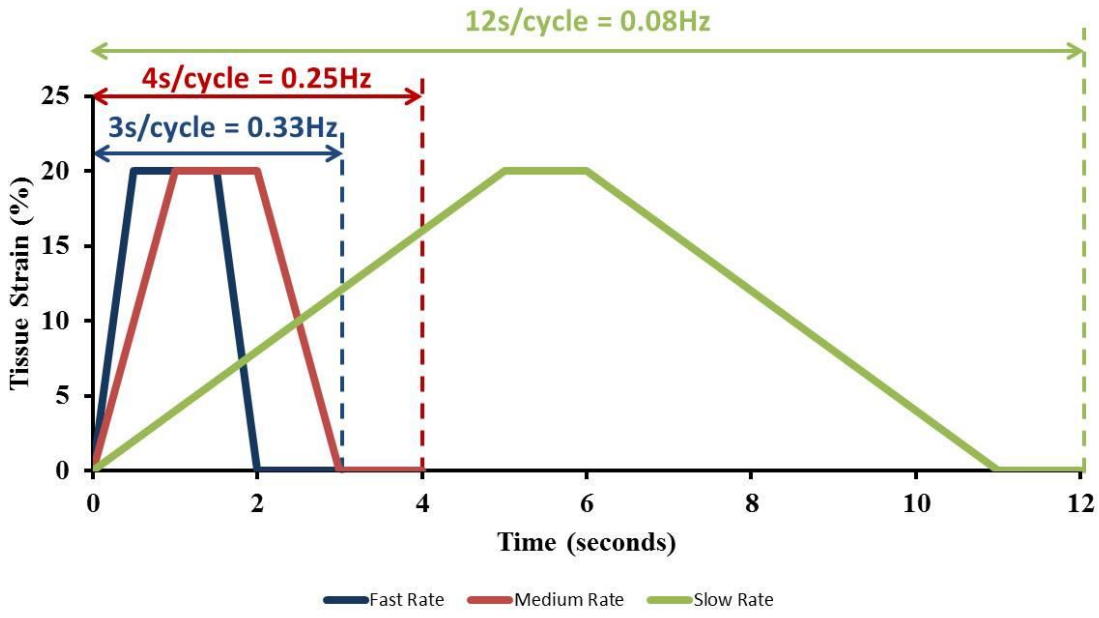

Figure 7.1: Schematic of 3 different frequencies used in cyclic loading including 0.08Hz, 0.25Hz and 0.33Hz with a 1 second hold time at both the ramp-up and ramp-down phase.

7.3.Results

7.3.1. Short term effects of cyclic loading rates

In this section the short term responses are plotted in order to highlight the shifts in the parameters that occur under cyclic loading.

The 3 different cyclic rates have an effect on the tissue level mechanics as shown in Figure 7.2. The peak stress values within the first 21 cycles are indicated whereby at the first cycle the peak stress is significantly high at 2.86MPa in the fast rate when compared to both the medium at 1.94MPa and slow 1.28MPa rates. Furthermore, over the following cycles there is a continued difference in peak stress even as the tissue approaches an equilibrium stress level where the fast rate is at 0.71MPa, medium rate is at 0.63MPa and slow rate is at 0.3MPa by cycle 21.

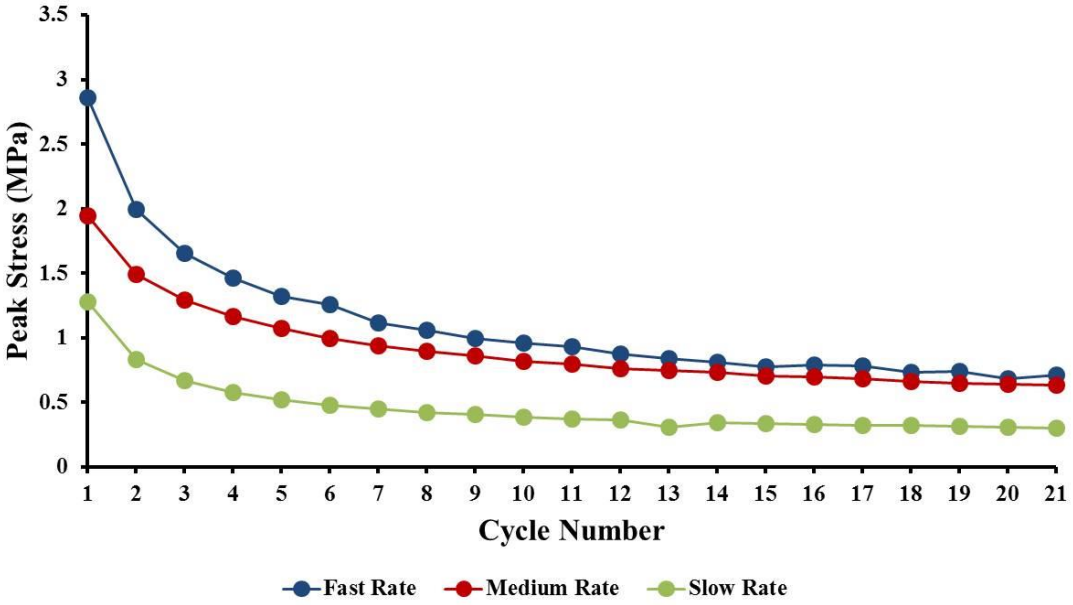

Figure 7.2: Peak stress values at each cycle over the first 21 cycles at all 3 loading rates of 0.33Hz (blue), 0.25Hz (red) and 0.08Hz (green).

When considering the % change in D-period in Figure 7.3, by comparing uncompressed (open circles) versus compressed states (filled circles), we see that there is a reduction in

D-period upon compression in all 3 frequencies. The triangular points indicate the averaged pre-compression static D-period in all 3 groups where the values vary by ~0.04% which would be expected given the small variability between the samples. There is no monotonic change with loading-rate when comparing either compressed (20% tissue strain) or uncompressed (0% tissue strain) states, as indicated in Figure 7.3a. There are statistically significant shifts in D-period between the loaded (20%) and unloaded (0%) states in all 3 groups, as shown by the averaged values across the first 21 cycles in Figure 7.3b. Figure 7.3c indicates that the % change in D-period between the compressed and uncompressed increases with increasing loading rate, such that on average the difference is ~0.06% in the slow rate, 0.08% in the medium rate and 0.10% in the fast rate, and the difference between the slow and the fast rate is significant.

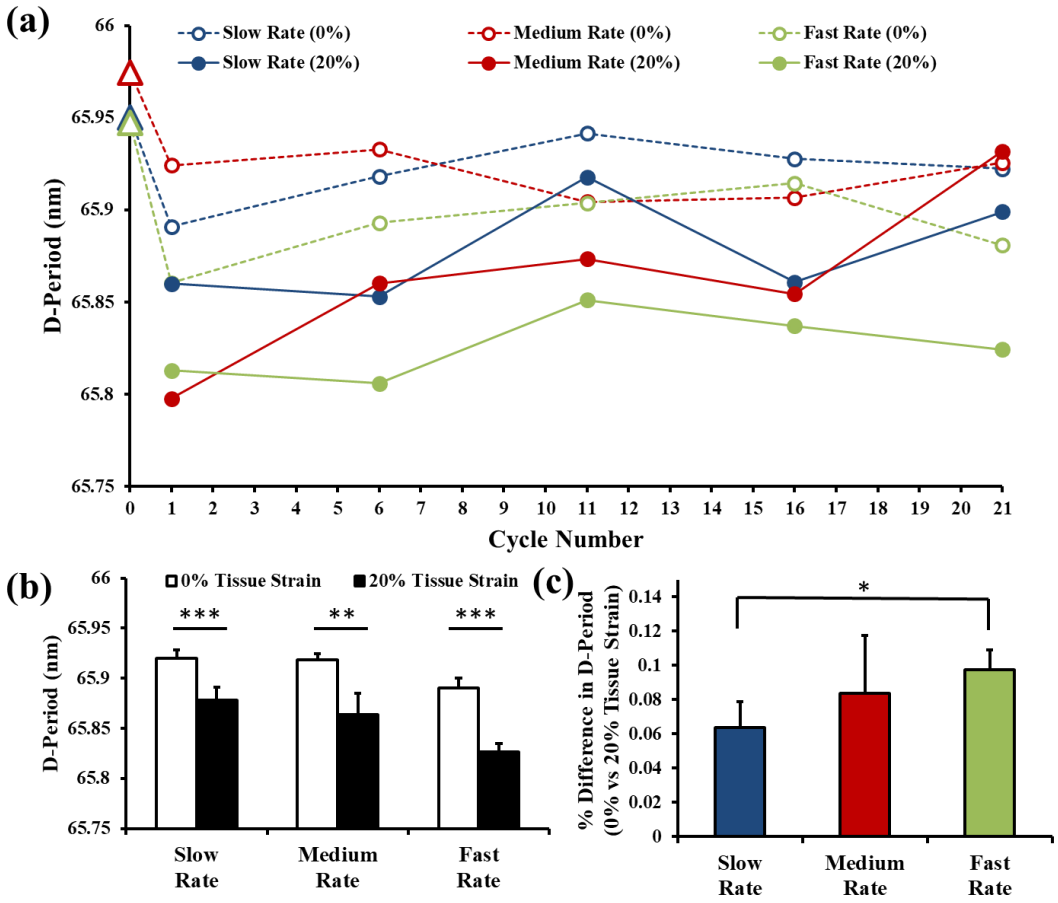

Figure 7.3: (a) Averaged D-period at all 3 cyclic rates where the slow rate at 0.08Hz is indicated in blue, medium rate at 0.25Hz is indicated in red and fast rate at 0.33Hz is indicated in green. The static uncompressed averaged values are shown in triangular symbols, n=4 in all groups. (b) Comparison of the averaged D-period in the first 21 cycles at 0% and 20% tissue strain at all 3 rates (n=5). (c) Indicates the % difference in average D-period values calculated in part (b). Significance is indicated in terms of p<0.05 (*), p<0.01 (**) and p<0.001 (***).

Similarly, it is seen that the level of inter-fibrillar disorder – as represented by w_q – increases in all groups under tissue compression (filled circles) compared to the unloaded case (open circles), as shown in Figure 7.4a. This is further indicated in Figure 7.4b where again there is a significant difference in the average level of interfibrillar disorder over the first 21 cycles. Interestingly, there is a rate-dependent level of disorder, such that when considering the % difference in w_q the value is 29.53% in the slow rate, 24.36% in the medium rate and 18.29% in the fast rate (Figure 7.4c). The uncompressed values of w_q,

prior to any loading (triangular symbols, Figure 7.4a) also highlight that there is inter-fibrillar disorder present in fully relaxed tissue. The increase of interfibrillar disorder is larger with with higher loading rate as seen by the difference between cycle 0 and cycle 1. Another observable effect is that in the compressed state in all groups, the first cycle undergoes a higher level of inter-fibrillar disorder followed by a downward trend in the later cycles. Further, the dashed lines in the uncompressed state would suggest a constant level of disorder along all three groups.

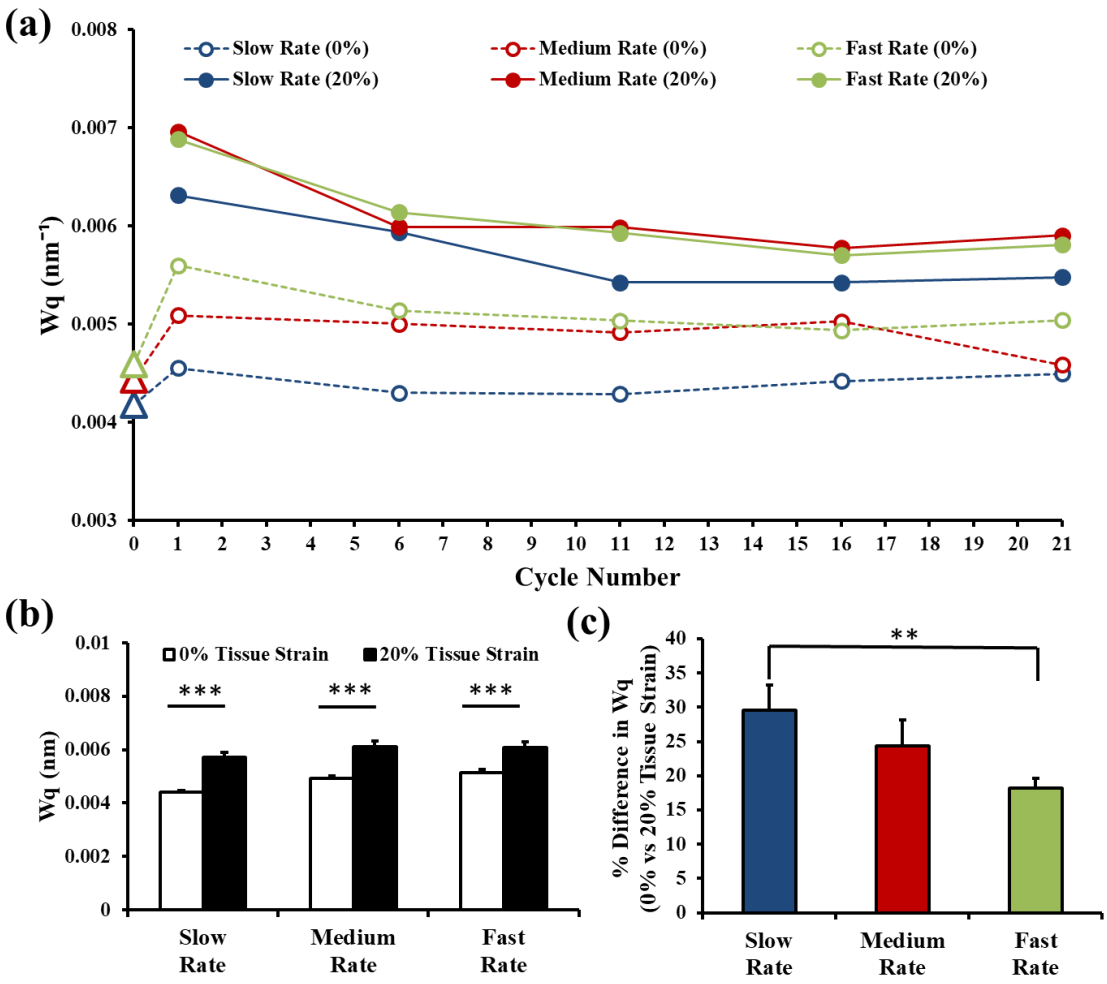

Figure 7.4: (a) Averaged w_q at all 3 cyclic rates where the slow rate at 0.08Hz is indicated in blue, medium rate at 0.25Hz is indicated in red and fast rate at 0.33Hz is indicated in green. The static uncompressed averaged values are shown in triangular symbols, n=4 in all groups. (b) Comparison of the averaged w_q in the first 21 cycles at 0% and 20% tissue strain at all 3 rates (n=5). (c) Indicates the % difference in average w_q values calculated in part (b). Significance is indicated in terms of p<0.05 (*), p<0.01 (**) and p<0.001 (***).

The *I(q)* peak intensity changes show, in the short term, that there is a decrease in intensity under compression followed by an increase on unloading (Figure 7.5a, dashed versus solid lines). The level of change also follows a similar trend as w_q between each rate as shown in Figure 7.5c, with an increasing % change in intensity with increasing loading rate over the first 21 cycles; 34.40% in the slow rate, 30.65% in the medium rate and

21.62% in the fast rate. There is a significant difference between the slow to fast and medium to fast rate (Figure 7.5c). Furthermore, across the short term the absolute levels of average *I(q)* show no monotonic increasing or decreasing behaviour with loading rate (Figure 7.5b) but rather a difference as a result of loading alone.

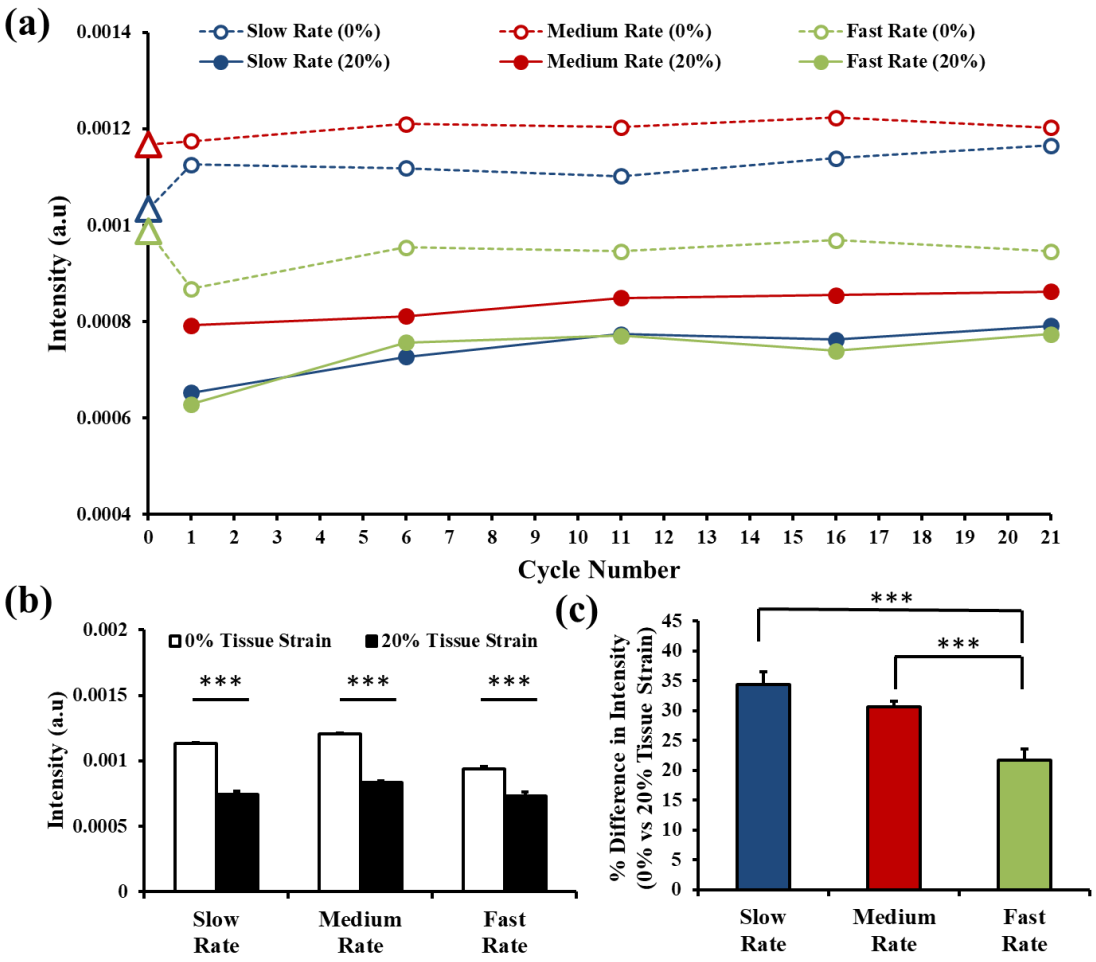

***Figure 7.5**: (a) Averaged I(q) at all 3 cyclic rates where the slow rate at 0.08Hz is indicated in blue, medium rate at 0.25Hz is indicated in red and fast rate at 0.33Hz is indicated in green. The static uncompressed averaged values are shown in triangular symbols, n=4 in all groups. (b) Comparison of the averaged I(q) in the first 21 cycles at 0% and 20% tissue strain at all 3 rates (n=5) (c) Indicates the % difference in average I(q) values calculated in part (b). Significance is indicated in terms of p<0.05 (*), p<0.01 (**) and p<0.001 (***).*

7.3.2. Long term effects of cyclic loading rates

In this section the % change in each parameter is plotted to highlight the long term trends in relation to the static uncompressed state.

When investigating the longer term % changes in D-period, with respect to the initial static D-period (for each loading rate), as shown in Figure 7.6, the main difference between the 3 rates is observed in the initial cycles followed by a convergence to a similar level of % change towards the longer term in the both load phases. Interestingly, under compression there seems to be less temporal variation in the % change of the fibrillar D-period in the slow rate (0.08 Hz; black circles Figure 7.6a) whereas there is an initial rapid relaxation-type behaviour on the medium and fast rates followed by a convergence to the same level of % change of ~ 0.1% as the slow rate. Quantitatively, Figure 7.6 shows that in the initial cycles there is a % change of between -0.25 and -0.2% in the two faster rates followed by a reduction in change to approximately -0.1% by cycle 80.

Overall there seems to be no complete recovery in human cartilage in the uncompressed state, as evidenced by the curves in Figure 7.6b lying below zero. Further, at 0% tissue strain during the first cycle there seems to be a larger % difference in the fastest rate at approximately -0.13% compared to the medium and slow rate at -0.08% and -0.09% respectively. Over successive cycles, there seems to be continual shifts in % change in all groups, none of which recover to 0%.

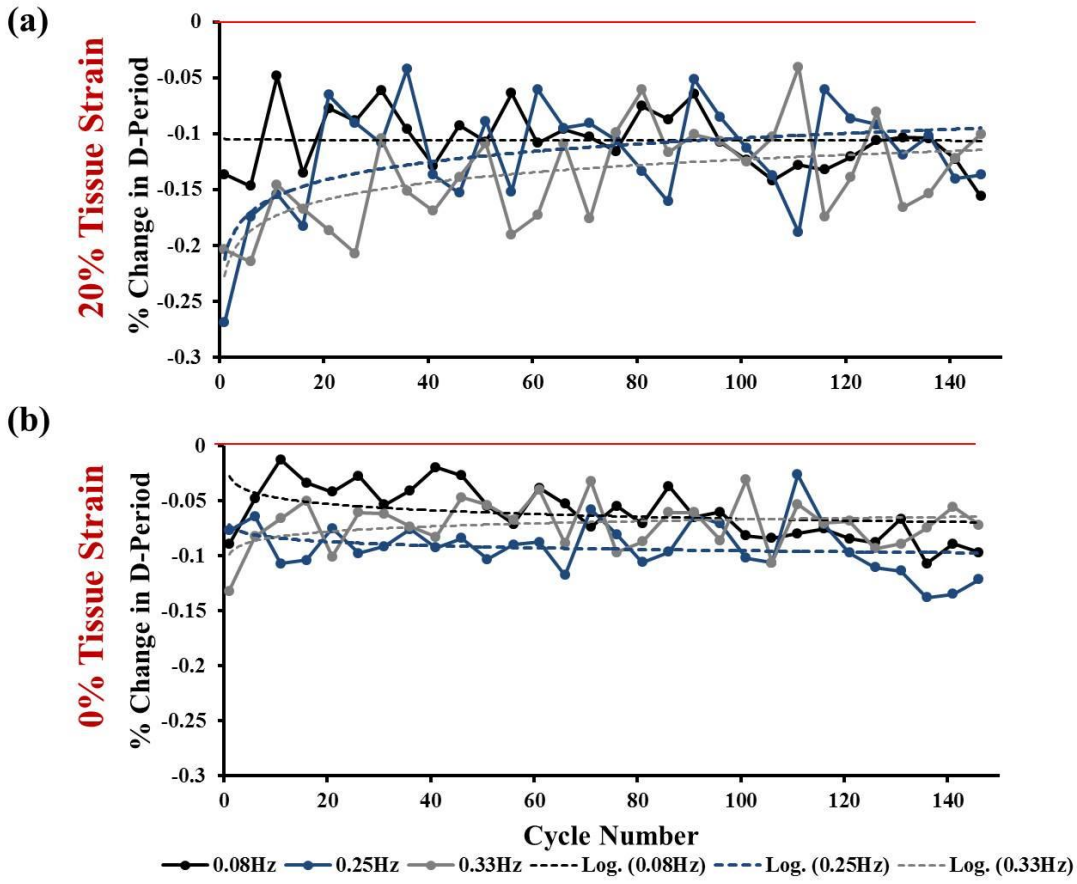

Figure 7.6: Long term averaged % change in D-Period in the both the (a) loaded (20% tissue strain) and (b) unloaded (0% tissue strain) is indicated in all 3 cyclic rates. A logarithmic trend line has been fitted as a guide to the eye. Red lines indicate 0% change, and n=4 in all groups.

In terms of inter-fibrillar disorder parametrized by w_q, under compression (Figure 7.7a) there is initially an increase in the inter-fibrillar disorder at a % change between 50-60% in all 3 groups in the first cycle. Following successive cycles over the longer term, there is a reduction in the level of inter-fibrillar disorder to ~25% in the slow and medium rates and to ~ 15% in the fast rate. There is a residual level of % change in w_q in all cyclic rates in the unloaded state, as indicated by Figure 7.7b, which is approximately 5-25%. However, this level of disorder remains constant throughout the full range of cycles at all rates, barring an initial transient decrease. Concerning this initial transient phase in both loaded and unloaded states, in the 0% tissue level strain group there seems to be no clear

rate dependent effect on the response as all 3 groups follow a similar trend throughout, however at 20% tissue level strain the disorder overall is lower in the fast rate.

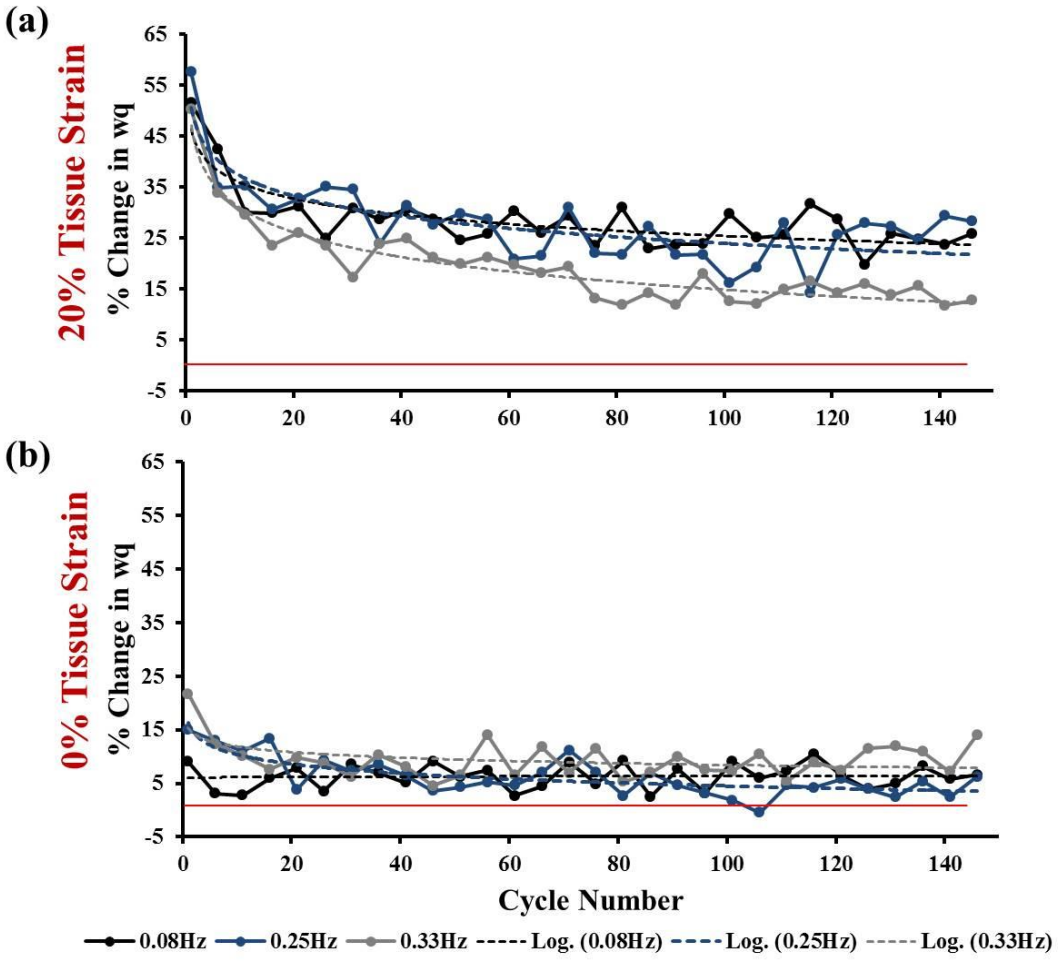

Figure 7.7: Long term averaged % change in w_q in the both the (a) loaded (20% tissue strain) and (b) unloaded (0% tissue strain) is indicated in all 3 cyclic rates. A logarithmic trend line has been fitted as a guide to the eye. Red lines indicate 0% change, and n=4 in all groups.

Concerning SAXD peak intensities (Figure 7.8), under compression, there is a steady level in the % change of intensity suggesting that the level of fibrillar level disorder is approximately the same across all cyclic rates, as indicated by the dashed lines in Figure 7.8a. This ranges between -20 to -35% more than the pre-strained state. At 0% tissue strain level all 3 rates behave in a similar manner such that there is an initial increase in the % change of intensity followed by a reduction over successive cycles suggesting an increase in the intra-fibrillar order. For example the level of % change in intensity reduced

from approximately 10% in the first cycle back down to 0% change by cycle 140 in the slow rate. In all groups the initial increase in intra-fibrillar order is lost over sucessive cycles. It is noteworthy that there is a monotonic trend in intensity across loading rates in the unloaded state (Figure 7.8b), with the slowest loading rate exhibiting a positive change in SAXD peak intensity initially (increased intrafibrillar ordering), the intermediate state with almost no change, and the fastest rate with a negative % change (corresponding to a decrease in intrafibrillar order). What is also interesting to observe is that in both the medium and fast rates towards cycle 60+ there are negative values in the % change of between -10% and -30%, indicating a transition into intra-fibrillar disorder at a similar level as to that under compression.

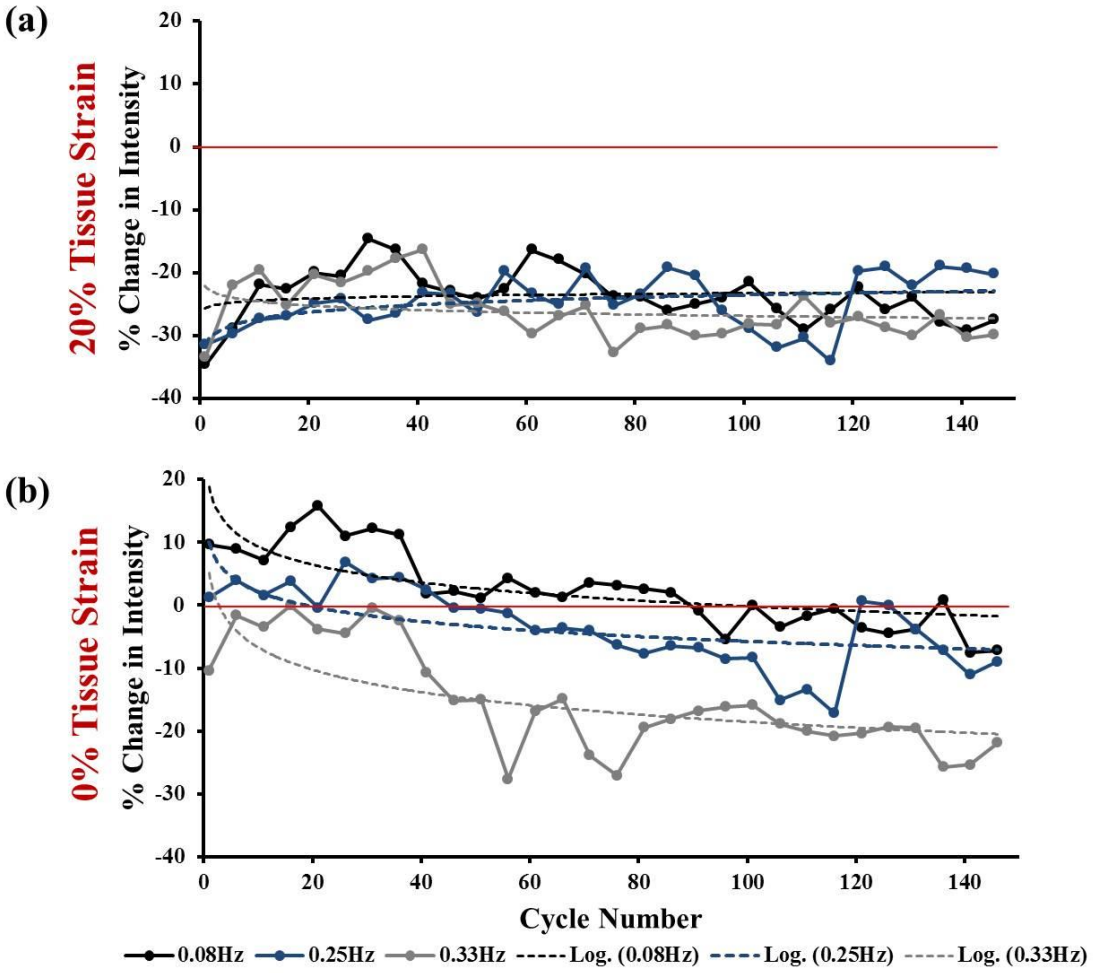

***Figure 7.8**: Long term averaged % change in I(q) in the both the (a) loaded (20% tissue strain) and (b) unloaded (0% tissue strain) is indicated in all 3 cyclic rates. A logarithmic trend line has been fitted as a guide to the eye. Red lines indicate 0% change, and n=4 in all groups.*

7.4. Discussion & Conclusions

These findings suggest that, at the chosen rates, there are both short and long term effects on the way the fibrils are able to respond to the loading. Over the short term, the fibrils dynamically respond to each loading rate through a reduction in D-period consistent with the results in the previous **Chapter 6**. Furthermore, there is a rate-related trend in the response observed under compression or release where the difference in absolute D-period values increase with increasing loading rates (Figure 7.3c). There is also a similar trend observed in terms of peak intensity and thus intra-fibrillar disorder such that on compression there is an increase in disorder (Figure 7.5a). This is matched with an increase in w_q and therefore an increase in inter-fibrillar heterogeneity (Figure 7.4). Notably, the % change of inter- and intra-fibrillar disorder is significantly lower in the fastest rate (Figure 7.4/Figure 7.5c). This would suggest that under faster rates of compression, given the transition to a more elastic tissue response, the fibrils resist compression via their ability to control the level of structural reorganisation. The changes in the fibrillar network response may also be due to the associated changes in local hydrostatic pressure as a result the loading-influenced change in the intra-fibrillar structure.

When investigating the % changes in Figure 7.6-Figure 7.8, an interesting finding is that the rate dependent intra-fibrillar disorder does not correlate with an associated change in inter-fibrillar disorder. Here we show that with increasing loading rate there is actually a reduction in the level of inter-fibrillar disorder as indicated by w_q. This would suggest that while there is an initial broad distribution of D-periods in the native tissue, under faster loading rates the reduction of fibrillar pre-strain reduces also the variation in D-period. Possibly, the change in peak intensity (Figure 7.8) shows that the initial response is by intra-fibrillar changes, leading to a ‘fuzziness’ in repeating D-period rather than a

structural change in terms of the gap to overlap ratio. Further, the rate dependency of w_q, initially, in all three groups experience a high % change of approximately 60%, but over successive cycles this is dramatically reduced which suggests that regardless of cyclic rate the fibrils are able to equilibrate in terms of the D-period regularity. It also appears that the faster rate reaches this level of fibrillar equilibrium faster than in the other two loading rates.

Alongside this, it appears that the fibrils have the dynamic capacity to reorganise their internal structure in response to a range of cyclic loading rates. Initially, when compression is removed, the intensity actually increases which would indicate a reduction in the intra-fibrillar disorder compared to the static state. Then following 150 cycles the level of intra-fibrillar disorder in the uncompressed state is comparable to the associated compressed state. This further highlights the capacity of the fibrils to dynamically respond and the observed rate dependent changes are likely linked to the changes in the level of macroscopic hydration and thus the associated interfibrillar hydration over successive cycles. Initially, there is likely an immediate increase in interstitial fluid pressurisation, which is elevated in the faster rate, followed by a reduction over successive cycles as the tissue equilibrates. In the same manner, the fibrils internally respond with an initial increase in intra-fibrillar order with an associated reduction in inter-fibrillar disorder, and as the tissue reaches equilibrium. At all 3 rates and more so in the fast rate, the fibrils respond through a disordering in the internal structure whereas the inter-fibrillar disorder in terms of D-period is dramatically reduced.

Based on these findings we make the following conclusions:

- At all three cyclic rates, the fibrils initially experience a reduction in D-period, increase in inter-fibrillar disorder and a reduction in intra-fibrillar disorder, all of which are recovered during successive cycles.
- In the short term, there is a clear rate dependent difference in the level of change in all 3 parameters such that there is higher change in D-period, lower level of inter-fibrillar disorder alongside a lower level of intra-fibrillar disorder in the fast rate compared to the medium and slow rates.
- When considering the longer term % changes (in Figure 7.6-Figure 7.8), there is a rate dependent effect on all three parameters such that at fast and medium rates the D-period takes longer to converge under compression that the slow rate.
- The converse is true when considering w_q in the long term, whereby the fast rate reaches a lower level of disorder under compression when compared to the other two rates.
- The level of inter-fibrillar disorder is reduced over repeated cycles whilst the intra-fibrillar disorder is increased in response to dynamic loading, thus, the fibrils have the capacity to dynamically change their structure in response to localised changes in tissue stress.

Chapter 8

Final discussion and outlook

8. Final discussion and outlook

8.1. Discussion

It is widely believed that collagen fibrils play an important role in cartilage mechanics through their ability to restrain swelling induced by the proteoglycans[42,128]. Although attempts have been made to understand the contribution of the collagen fibrils in tissue mechanics[68], relatively few studies have investigated their role at the nanoscale and more importantly their dynamic mechanical response during cartilage deformation. Here we utilised *in situ* small angle X-ray diffraction to measure the nanostructural parameters associated with the fibrillar architecture whilst performing time-resolved measurements during compression of bovine and human cartilage explants (**Chapters 5-7**). Furthermore, we were able to demonstrate fibrillar-level mechanical changes associated with enzymatic tissue degradation (**Chapter 5**), alongside the response to IL-1β induced inflammation (**Chapter 6**).

A sample holder was successfully designed and produced for the micromechanical tester used for *in situ* measurements, and experimental protocols were developed at the two beam lines (DLS and ESRF) that allowed both static and dynamic measurements of the fibrillar network in bovine and human cartilage. In **Chapter 4** we report the first combined microscale maps of nanoscale fibrillar D-period and orientation in articular cartilage, as well as the changes under loading. We found that there was a depth-dependent variation in the D-period which was consistent with the associated depth-wise concentrations in the constituent macromolecules that influence the fibrillar D-period through the swelling pressure imposed by the proteoglycans. We also suggest that the observed variation is also likely a result of the differences in collagen content and levels of fibrillar disorder. A possible mechanistic role of this gradient may be due to the way

in which load is propagated through the tissue such that the apparent ‘slack’ in the transitional zone fibrils allows lateral motion between zones without exceeding the failure strain in the collagen fibrils.

Results in **Chapter 5** also showed that applications of structural manipulation led to a disruption to both the collagen fibril pre-strain and the transient response during stress relaxation. Specifically, we have quantified the presence of pre-strain in cartilage collagen prior to any compression, estimated at approximately 1-2%, due to osmotic swelling pressure from the proteoglycans. Furthermore, we revealed that under physiological levels of compression, a rapid reduction and recovery of this pre-strain occurs during stress relaxation, approximately 60 seconds after the onset of peak load which is not observable in the macroscopic tissue mechanics. The mechanisms behind these dynamic changes are likely linked to the compression induced changes in water content within the extrafibrillar proteoglycans.

When the tissue was placed under cyclic compression (**Chapter 6 & 7**), the fibrils dynamically respond through a combination of a reduction in D-period alongside inter- and intrafibrillar disordering in the internal structure. Furthermore, these effects are reversible when the compression is removed, therefore showing that the network of fibrils are flexible and undamaged. Over longer term loading it was observed that the overall change in D-period under compression reduced over successive cycles, suggesting that the fibrils have the capacity to adapt to loading, which may be as a result of localised reorganisation of the ECM macromolecules and associated water content.

Alongside the direct enzymatic digestions performed in **Chapter 5**, we also show in **Chapter 6** that IL-1β induced tissue inflammation also results in a reduction in fibrillar pre-strain and altered fibrillar mechanics. The range, in terms of D-period, at which the

fibrils were able to respond were significantly reduced due to the associated release in pre-strain. We would suggest that this has a knock-on effect on the way that the tissue is able to resist compression at the macroscale. However, we also found that the level of D-period reached under compression in either control or treatment group remained the same which would suggest that there is a minimum level the fibrils are able to compress. Lastly, the direction of orientation did not vary between the groups, but a greater difference was observed in the level of angular dispersion the fibrils underwent during tissue level compression.

Cartilage is a material with time-dependent mechanical properties, and understanding the nanoscale behaviour as a function of variable macroscopic strain rate will help understand the structure-function relations enabling function. In this regard, the results in **Chapter 7** showed that there is a rate dependent fibrillar response observed in human cartilage under cyclic compression. All three parameters - D-period, w_q, and $I(q)$ – are dependent on the cyclic rate and increase significantly with faster cyclic loading. Over successive cycles all 3 rates showed a similar trend whereby the level of inter-fibrillar disorder was reduced, while the intra-fibrillar disorder is increased, suggesting a new mechanism by which the fibrils response to longer term loading.

The findings in this thesis suggest that the fibrils have the capacity to respond to loading via *intra*- and *inter*-fibrillar disordering alongside a transient response that is mediated by changes in hydration. These are the first studies to highlight previously unknown transient responses and are likely to transform our understanding of the role of collagen fibril nano-mechanics in cartilage and other hydrated soft tissues. Furthermore, the proposed fibrillar mechanisms have implications for cartilage biomechanics and are likely to prove valuable

for computational modelling, particularly in incorporating collagen fibrillar network mechanics in fibril-reinforced poroelastic models of cartilage

8.2. Future work

As a result of the findings within this project a 3 year project grant "*The mechanics of the collagen fibrillar network in ageing cartilage*" has been successfully awarded to the Gupta/Knight team through the Biotechnology and Biological Sciences Research Council (BBSRC) in which the following studies will be conducted by the named PDRA (Sheetal Inamdar, the author of the present thesis) to advance the existing knowledge.

8.2.1. Collagen fibril ultrastructural changes with ageing

Ageing and diseases such as osteoarthritis causes the collagen fibrillar ultrastructure to undergo alterations, with electron microscopy showing splitting of rope-like fibre-bundles into fibrils at the nanoscale[154]. We propose that these changes are linked to changes in local mechanical homeostasis at the nanoscale. A disruption is expected due to changes in proteoglycan content, structure and tissue hydration (altering osmotic and swelling pressures), and increased non-enzymatic cross-linking increasing fibrillar stiffness (and reducing pre-strain in the network). Data in this thesis involving SAXD data on bovine cartilage (**Chapter 5**) supports this, showing that chondroitinase digestion of cartilage leads to a reduction of fibrillar pre-strain, which we believe is due to a reduction of swelling pressure on the collagen fibrils by the partial removal of chondroitin sulphate. SAXD is a promising approach to measure fibrillar structure in young and old human cartilage, focusing on structural parameters which will be affected by a change in local mechanical equilibrium, such as the D-period, lateral molecular spacing, or fibril radius. Using microfocus synchrotron X-ray beams to scan across the cross sections of cartilage (from articular surface to the deep zone), the spatial variation of these ultrastructural fibrillar parameters will be determined in ageing human cartilage as was

done in **Chapter 4**. To understand how healthy ageing of cartilage relates to changes in collagen in greater detail, we will compare the age-related changes of fibrillar collagen ultrastructure in regions of cartilage subjected to high versus low mechanical loading. We hypothesize that tissue in regions susceptible to high loading will be more prone to damage and degeneration, which will be reflected in nanoscale SAXD parameters, such as lowered pre-strain, more random fibril orientation, and greater interfacial separation between fibrils and interfibrillar matrix.

8.2.2. Investigation of how age-related changes in matrix composition/hydration influence collagen ultrastructure and pre-strain/tension

In naturally aged cartilage, the ultrastructure and composition of the ECM will depend on multiple independent factors, including collagen crosslinking, hydration, and tissue turnover, and may also be associated with structural degradation in the joint. The ultrastructural changes and nanomechanics of human cartilage in the study stated above are therefore a complex function of a number of interacting variables. To understand how two key age-related mechanisms – collagen crosslinking and hydration – control collagen fibrillar ultrastructural changes in cartilage, we will vary them independently. To do this, bovine cartilage modified to increase crosslinking or to reduce water content will be used. The covalent crosslinking and hydration level of bovine cartilage tissue samples will be altered in a controlled manner using physicochemical methods and measured with synchrotron microfocus SAXD.

8.2.3. Influence of ageing on collagen fibril response to gross mechanical loading

Due to the interactions between fibrils, GAGs and water components, age related changes in individual component properties may lead to significant changes in the nanomechanical behaviour of the cartilage ECM composite, analogous to how small changes in non-collagenous protein fraction or interfibrillar mineralization may

significantly change tissue mechanics of bone[155]. Data in **Chapter 5** on the fibrillar deformation during stress relaxation of bovine cartilage shows a novel transient reduction of ~1.0% in fibril strain followed by a rapid recovery[120]. We propose that pressure-induced fluid flow of water between fibrillar and extrafibrillar compartments is a key driver of this process, which is concurrent with a transient intrafibrillar disordering. We hypothesize that in ageing cartilage, these dynamics of fibrillar-level deformation under time-varying external loads will qualitatively and quantitatively change due to the increased fibrillar stiffness (due to increased crosslinking), and reduced osmotic and swelling pressures (due to changes in the proteoglycan phase and lowered hydration).

8.2.4. Influence of ageing on collagen fibril nanomechanics/ultrastructural response to repetitive loading

We will determine if the ageing process affects the ECM of cartilage in ways that reduce the fatigue resistance of the collagen fibrillar network. Excess fatigue damage at the macroscale has been suggested as a cause of OA[156,157], and we hypothesize that age-related changes in the fibrillar network will affect the response to cyclic load. Results in **Chapter 6 & 7** shows that cyclic loading on bovine and human cartilage combined with SAXD leads to a clear, cyclic oscillation in D-period, w_q and total SAXD intensity. These indicate that under repetitive loading, fibril D-period reduces, higher variability in D-period and the fibril is disordered internally.

8.2.5. Influence of ageing on fibrillar response to injurious mechanical loading

We hypothesize that the age-related changes in ECM structure in cartilage lead to microscopic zones of damaged tissue when subjected to localized loading, which are both larger and with more severe nanoscale disruption in aged cartilage compared to young tissue. To test the hypothesis, we will create sites of localized deformation and fibrillation by point-loading of the surface of cartilage samples (both bovine and human) with an

indenter. Microfocus synchrotron scanning SAXD will be used to measure – around the loading site –two dimensional cross-sectional maps of collagen fibrillar parameters, including fibril pre-strain, intrafibrillar ordering and orientation. We anticipate that the extent of local pre-strain alterations, intrafibrillar disordering, transverse fibrillar expansion and other nanomechanical parameters will be larger in ageing tissue. Such changes will help understand how focal damage spreads (or not) in ageing cartilage, leading to large scale fibrillation and osteoarthritis. Quantifying the extent and nature of the mechanical changes in the fibrillar network in the ECM may lead to new approaches for treating local damage.

8.3. Future work: Broader applications

Alongside the above planned studies, the findings in this thesis can be applied to a range of other applications to further knowledge into cartilage biomechanics. The contributions of the collagen fibrillar network, through the measured and quantified response, can be integrated into existing models[55,158] to further develop the understanding of the unique role played by the constituent macromolecules. These fundamental findings can further be incorporated into multi-scale experimental schemes and modelling to understand the importance and role of each building block in the overall structure and function of cartilage, analogous to other work in examples such as cuticle[159].

Bibliography

1. Bhosale, A. M. & Richardson, J. B. Articular cartilage: structure, injuries and review of management. *Br. Med. Bull.* **87,** 77–95 (2008).

2. Boschetti, F., Pennati, G., Gervaso, F., Peretti, G. M. & Dubini, G. Biomechanical properties of human articular cartilage under compressive loads. *Biorheology* **41,** 159–66 (2004).

3. Kiviranta, P. *et al.* Collagen network primarily controls Poisson's ratio of bovine articular cartilage in compression. *J. Orthop. Res.* **24,** 690–699 (2006).

4. Wenger, M. P. E., Bozec, L., Horton, M. a & Mesquida, P. Mechanical properties of collagen fibrils. *Biophys. J.* **93,** 1255–63 (2007).

5. Wess, T. J. in *Collagen: Structure and Mechanics* (ed. Fratzl, P.) 49–80 (Springer, 2008).

6. Cameron, G. J., Alberts, I. L., Laing, J. H. & Wess, T. J. Structure of type I and type III heterotypic collagen fibrils: an X-ray diffraction study. *J. Struct. Biol.* **137,** 15–22 (2002).

7. Aigner, T. Collagens—major component of the physiological cartilage matrix, major target of cartilage degeneration, major tool in cartilage repair. *Adv. Drug Deliv. Rev.* **55,** 1569–1593 (2003).

8. JPK Instruments. Observing the Levels of Alignment and Organisation in Collagen Structures Using Atomic Force Microscopy by JPK Instruments. (2009). Available at: http://www.azonano.com/article.aspx?ArticleID=2267. (Accessed: 8th February 2017)

9. Hulmes, D. J. S. in *Collagen: Structure and Mechanics* (ed. Fratzl, P.) 15–47 (Springer, 2008).

10. Responte, D. J., Natoli, R. M. & Athanasiou, K. A. Collagens of articular cartilage. *Crit. Rev. Biomed. Eng.* **35,** 363–411 (2007).

11. Roughley, P. J. The structure and function of cartilage proteoglycans. *Eur. Cell. Mater.* **12,** 92–101 (2006).

12. Athanasiou, K. A., Darling, E. M. & Hu, J. C. Articular Cartilage Tissue Engineering. *Synth. Lect. Tissue Eng.* **1,** 1–182 (2009).

13. Sophia Fox, A. J., Bedi, A. & Rodeo, S. A. The basic science of articular cartilage: structure, composition, and function. *Sports Health* **1,** 461–8 (2009).

14. Mansour, J. M. Biomechanics of Cartilage. *Kinesiol. Mech. pathomechanics Hum. Mov.* 66–79 (2003).

15. Thambyah, A. & Broom, N. D. Further insight into the depth-dependent microstructural response of cartilage to compression using a channel indentation technique. *Comput. Math. Methods Med.* **2013,** (2013).

16. Below, S., Arnoczky, S. P., Dodds, J., Kooima, C. & Walter, N. The split-line pattern of the distal femur. *Arthrosc. J. Arthrosc. Relat. Surg.* **18,** 613–617 (2002).

17. Klein, T. J., Chaudhry, M., Bae, W. C. & Sah, R. L. Depth-dependent biomechanical and biochemical properties of fetal, newborn, and tissue-engineered articular cartilage. *J. Biomech.* **40,** 182–190 (2007).

18. Wilson, W., Huyghe, J. M. & Van Donkelaar, C. C. Depth-dependent compressive equilibrium properties of articular cartilage explained by its composition. *Biomech. Model. Mechanobiol.* **6,** 43–53 (2007).

19. Lu, X. L. & Mow, V. C. Biomechanics of articular cartilage and determination of material properties. *Med. Sci. Sports Exerc.* **40,** 193–9 (2008).

20. Pearle, A. D., Warren, R. F. & Rodeo, S. a. Basic science of articular cartilage and osteoarthritis. *Clin. Sports Med.* **24,** 1–12 (2005).

21. Sandell, L. J. & Aigner, T. Articular cartilage and changes in arthritis. An introduction: cell biology of osteoarthritis. *Arthritis Res.* **3,** 107–13 (2001).

22. Setton, L. A., Elliott, D. M. & Mow, V. C. Altered mechanics of cartilage with osteoarthritis: Human osteoarthritis and an experimental model of joint degeneration. *Osteoarthr. Cartil.* **7,** 2–14 (1999).

23. Guilak, F. Biomechanical factors in osteoarthritis. *Best Pract. Res. Clin. Rheumatol.* **25,** 815–823 (2011).

24. Goldring, M. B. The role of the chondrocyte in osteoarthritis. *Arthritis Rheum.* **43,** 1916–1926 (2000).

25. Poole, A. R. *et al.* Type II collagen degradation and its regulation in articular cartilage in osteoarthritis. *Ann Rheum Dis* **61,** 78–81 (2002).

26. Moger, C. J. *et al.* Regional variations of collagen orientation in normal and diseased articular cartilage and subchondral bone determined using small angle X-ray scattering (SAXS). *Osteoarthritis Cartilage* **15,** 682–7 (2007).

27. Saarakkala, S. *et al.* Depth-wise progression of osteoarthritis in human articular cartilage: investigation of composition, structure and biomechanics. *Osteoarthr. Cartil.* **18,** 73–81 (2010).

28. Bank, R. A., Bayliss, M. T., Lafeber, F. P. J. G., Maroudas, A. & Tekoppele, J. M. Ageing and zonal variation in post-translational modification of collagen in normal human articular cartilage. The age-related increase in non-enzymatic glycation affects biomechanical properties of cartilage. *Biochem. J.* **330,** 345–351 (1998).

29. Swann, A. C. & Seedhom, B. B. The Stiffness of Normal Articular-cartilage and the Predominant Acting Stress Levels - Implications For the Etiology of Osteoarthrosis. *Br. J. Rheumatol.* **32,** 16–25 (1993).

30. Mow, V. C. & Hung, C. T. in *Basic Biomechanics of the Musculoskeletal System* (eds. Nordin, M. & Frankel, V.) 60–102 (Lippincott Williams & Wilkins, 2001).

31. Young, J. A. E., Ashman, R. B. & Turner, C. H. Young's modulus of trabecular and cortical bone material : ultrasonic and microtensile measurements. *J. Biomech.* **26,** 111–119 (1993).

32. Cox, T. R. & Erler, J. T. Remodeling and homeostasis of the extracellular matrix: implications for fibrotic diseases and cancer. *Dis. Model. Mech.* **4,** 165–78 (2011).

33. Kempson, G. E. in *The Joints and Synovial Fluid II* 177–235 (Academic Press, 1980).

34. Mow, V. C., Kuei, S. C., Lai, W. M. & Armstrong, C. G. Biphasic Creep and Stress Relaxation of Articular Cartilage in Compression: Theory and Experiments. *J. Biomech. Eng.* **102,** 73 (1980).

35. Kempson, G. E., Freemas, M. A. R. & Swanson, S. A. V. The determination of a creep modulus for articular cartilage from indenta- tion tests on the human femoral head. *J. Biomech.* **4,** 239–250 (1971).

36. Halloran, J. P. *et al.* Multiscale mechanics of articular cartilage: potentials and challenges of coupling musculoskeletal, joint, and microscale computational models. *Ann. Biomed. Eng.* **40,** 2456–74 (2012).

37. Kleeman, R. U., Krocker, D., Cedrano, A., Tuischer, J. & Duda, G. N. Altered cartilage mechanics and histology in knee osteoarthritis: Relation to clinical assessment (ICRS Grade). *Osteoarthr. Cartil.* **13,** 958–963 (2005).

38. Varady, N. H. & Grodzinsky, A. J. Osteoarthritis year in review 2015: Mechanics. *Osteoarthr. Cartil.* **24,** 27–35 (2016).

39. Myers, E. R. & Mow, V. C. in *Cartilage* (ed. Hall, B. K.) 313–341 (Academic Press, 1983).

40. Thambyah, A., van Heeswijk, V. M., van Donkelaar, C. C. & Broom, N. A Microstructural Study of Load Distribution in Cartilage: A Comparison of Stress Relaxation versus Creep Loading. *Adv. Mater. Sci. Eng.* **2015,** 1–11 (2015).

41. Martin, R. B., Burr, D. B., Sharkey, N. A. & Fyhrie, D. P. *Skeletal Tissue Mechanics*. (Springer, 2015).

42. Han, E., Chen, S. S., Klisch, S. M. & Sah, R. L. Contribution of proteoglycan osmotic swelling pressure to the compressive properties of articular cartilage. *Biophys. J.* **101,** 916–24 (2011).

43. Xia, Y. *et al.* in *Biophysics and Biochemistry of Cartilage by NMR and MRI* (eds. Xia, Y. & Momot, K.) 3–35 (The Royal Society of Chemistry, 2017).

44. Kim, Y., Bonassar, J. & Grodzinsky, A. J. The Role of Cartilage Streaming Potential , Fluid Flow and Pressure in the Stimulation of During Dynamic Compression. *J. Biomech.* **28,** 1055–66 (1995).

45. Hauser, R. The Acceleration of Articular Cartilage Degeneration in Osteoarthritis by Nonsteroidal Anti-inflammatory Drugs. *J. Prolotherapy* 305–322 (2010).

46. Bader, D. L., Kempson, G. E., Egan, J., Gilbey, W. & Barrett, A. J. The effects of selective matrix degradation on the short-term compressive properties of adult human articular cartilage. *Biochim. Biophys. Acta - Gen. Subj.* **1116,** 147–154 (1992).

47. Setton, L. A., Tohyama, H. & Mow, V. C. Swelling and curling behaviors of articular cartilage. *J. Biomech. Eng.* **120,** 355–61 (1998).

48. Hardingham, T. E. Cartilage: Aggrecan - Link Protein - Hyaluronan Aggregates. (1998). Available at: http://glycoforum.gr.jp/science/hyaluronan/HA05/HA05E.html. (Accessed: 4th November 2016)

49. Hayes, W. C. & Bodine, A. J. Flow-independent viscoelastic properties of articular cartilage matrix. *J. Biomech.* **11,** 407–19 (1978).

50. Lai, W. M., Hou, J. S. & Mow, V. C. A Triphasic Theory for the Swelling and Deformation Behaviours of Articular Cartilage. *J. Biomech. Eng.* **113,** 245–258 (1991).

51. Julkunen, P. *et al.* A review of the combination of experimental measurements and fibril-reinforced modeling for investigation of articular cartilage and chondrocyte response to loading. *Comput. Math. Methods Med.* **2013,** (2013).

52. Li, L. P., Buschmann, M. D. & Shirazi-Adl, A. A fibril reinforced nonhomogeneous poroelastic model for articular cartilage : inhomogeneous response in unconfined compression. *J. Biomech.* **33,** 1533–1541 (2000).

53. Wilson, W., Van Donkelaar, C. C., Van Rietbergen, B. & Huiskes, R. A fibril-reinforced poroviscoelastic swelling model for articular cartilage. *J. Biomech.* **38,** 1195–1204 (2005).

54. Hosseini, S. M., Wu, Y., Ito, K. & van Donkelaar, C. C. The importance of superficial collagen fibrils for the function of articular cartilage. *Biomech. Model. Mechanobiol.* **13,** 41–51 (2014).

55. Halonen, K. S., Mononen, M. E., Jurvelin, J. S., Töyräs, J. & Korhonen, R. K. Importance of depth-wise distribution of collagen and proteoglycans in articular cartilage-A 3D finite element study of stresses and strains in human knee joint. *J. Biomech.* **46,** 1184–1192 (2013).

56. Szarko, M. & Xia, Y. Direct Visualisation of the Depth-Dependent Mechanical Properties of Full-Thickness Articular Cartilage. *Open J. Orthop.* **2,** (2012).

57. Mow, V. C. & Guo, X. E. Mechano-Electrochemical Properties Of Articular Cartilage: Their Inhomogeneities and Anisotropies. *Annu. Rev. Biomed. Eng.* **4,** 175–209 (2002).

58. Schinagl, R. M., Gurskis, D., Chen, a C. & Sah, R. L. Depth-dependent confined compression modulus of full-thickness bovine articular cartilage. *J. Orthop. Res.* **15,** 499–506 (1997).

59. Tomkoria, S., Patel, R. V. & Mao, J. J. Heterogeneous nanomechanical properties of superficial and zonal regions of articular cartilage of the rabbit

proximal radius condyle by atomic force microscopy. *Med. Eng. Phys.* **26,** 815–822 (2004).

60. Grenier, S., Bhargava, M. M. & Torzilli, P. A. An in vitro model for the pathological degradation of articular cartilage in osteoarthritis. *J. Biomech.* **47,** 645–652 (2014).

61. Griffin, D. J. *et al.* Effects of enzymatic treatments on the depth-dependent viscoelastic shear properties of articular cartilage. *J. Orthop. Res.* **32,** 1652–1657 (2014).

62. Han, L. *et al.* Time-Dependent Nanomechanics of Cartilage. *Biophys. J.* **100,** 1846–1854 (2011).

63. Han, L., Grodzinsky, A. J. & Ortiz, C. Nanomechanics of the Cartilage Extracellular Matrix. *Annu. Rev. Mater. Res.* **41,** 133–168 (2011).

64. Korhonen, R. K. *et al.* Fibril reinforced poroelastic model predicts specifically mechanical behavior of normal, proteoglycan depleted and collagen degraded articular cartilage. *J. Biomech.* **36,** 1373–1379 (2003).

65. Julkunen, P., Jurvelin, J. S. & Isaksson, H. Contribution of tissue composition and structure to mechanical response of articular cartilage under different loading geometries and strain rates. *Biomech. Model. Mechanobiol.* **9,** 237–245 (2010).

66. Aspden, R. M. & Hukins, D. W. L. Determination of the direction of preferred orientation and the orientation distribution function of collagen fibrils in connective tissues from high-angle X-ray diffraction patterns. *J. Appl. Crystallogr.* **12,** 306–311 (1979).

67. Aspden, R. M. & Hukins, D. W. L. Collagen organization in articular cartilage, determined by X-ray diffraction, and its relationship to tissue function. *Proc. R. Soc. Lond.* **212,** 299–304 (1981).

68. Moger, C. J. *et al.* Cartilage collagen matrix reorientation and displacement in response to surface loading. *J. Biomech. Eng.* **131,** 1–9 (2009).

69. Gupta, H. S. *et al.* Nanoscale deformation mechanisms in bone. *Nano Lett.* **5,** 2108–11 (2005).

70. Screen, H. R. C., Seto, J., Krauss, S., Boesecke, P. & Gupta, H. S. Extrafibrillar diffusion and intrafibrillar swelling at the nanoscale are associated with stress relaxation in the soft collagenous matrix tissue of tendons. *Soft Matter* **7,** 11243–11251 (2011).

71. Assmus, A. Early History of X Rays. *SLAC Beam Line 25N2* **10,** 10–24 (1995).

72. Attwood, D. & Sakdinawat, A. *X-Rays and Extreme Ultraviolet Radiation*. (Cambridge University Press, 2016).

73. Drenth, J. *Principles of Protein X-ray Crystallography*. (Springer New York, 1999).

74. Wess, T. J. *et al.* The use of small-angle x-ray diffraction studies for the analysis

of structural features in archaeological samples. *Archaeometry* **43,** 117–129 (2001).

75. Guinier, A. *X-ray Diffraction In Crystals, Imperfect Crystals, and Amorphous Bodies*. (Dover Publications INC, 1994).

76. Petruska, J. A. & Hodge, A. J. A subunit model for the tropocollagen macromolecule. *Biochemistry* **51,** 871–876 (1964).

77. Suryanarayana, C. & Norton, M. G. *X-Ray Diffraction: A Practical Approach*. (Springer, 1998).

78. Fratzl, P., Paris, O., Klaushofer, K. & Landis, W. J. Bone mineralization in an osteogenesis imperfecta mouse model studied by small-angle x-ray scattering. *J. Clin. Invest.* **97,** 396–402 (1996).

79. Bear, R. S. Long x-ray diffraction spacings of collagen. *J. Am. Chem. Soc.* **64,** 727–727 (1942).

80. Meek, K. M. & Quantock, A. J. The Use of X-ray Scattering Techniques to Determine Corneal Ultrastructure. *Prog. Retin. Eye Res.* **20,** 99/137 (2001).

81. North, A. C. T., Cowen, P. M. & Randall, J. T. Structural Units in Collagen Fibrils. *Nature* **174,** 1142–1143 (1954).

82. Orgel, J. P. R. O. *et al.* Structure of Type I Collagen. *Structure* **9,** 1061–1069 (2001).

83. Orgel, J. P. R. O., Irving, T. C., Miller, A. & Wess, T. J. Microfibrillar structure of type I collagen in situ. *Proc. Natl. Acad. Sci. U. S. A.* **103,** 9001–5 (2006).

84. Mosler, E. *et al.* Stress-induced molecular rearrangement in tendon collagen. *J. Mol. Biol.* **182,** 589–96 (1985).

85. Folkhard, W. *et al.* Structural dynamic of native tendon collagen. *J. Mol. Biol.* **193,** 405–407 (1987).

86. Fratzl, P. *et al.* Fibrillar structure and mechanical properties of collagen. *J. Struct. Biol.* **122,** 119–22 (1997).

87. Gupta, H. S. *et al.* Intrafibrillar plasticity through mineral/collagen sliding is the dominant mechanism for the extreme toughness of antler bone. *J. Mech. Behav. Biomed. Mater.* **28,** 366–82 (2013).

88. Gupta, H. S. *et al.* Fibrillar level fracture in bone beyond the yield point. *Int. J. Fract.* **139,** 425–436 (2006).

89. Tadimalla, S., Tourell, M. C., Knott, K. I. & Momot, K. Quantifying collagen fibre architecture in articular cartilage using small-angle X-ray scattering. *Biomed. Spectrosc. Imaging* **6,** 37–57 (2017).

90. Mollenhauer, J., Aurich, M., Muehleman, C., Khelashvilli, G. & Irving, T. C. X-ray diffraction of the molecular substructure of human articular cartilage. *Connect. Tissue Res.* **44,** 201–7 (2003).

91. Duke, P. J. *Synchrotron Radiation: Production and Properties*. (Oxford University Press, 2000).

92. Diamond Light Source Ltd. How Diamond Works. (2017). Available at: http://www.diamond.ac.uk/Home/About/How-Diamond-Works.html#. (Accessed: 26th May 2017)

93. European Synchrotron Radiation Facility. What is a synchrotron? (2017). Available at: http://www.esrf.eu/about/synchrotron-science/synchrotron. (Accessed: 26th May 2017)

94. Barth, H. D., Launey, M. E., Macdowell, A. a, Ager, J. W. & Ritchie, R. O. On the effect of X-ray irradiation on the deformation and fracture behavior of human cortical bone. *Bone* **46,** 1475–85 (2010).

95. Barth, H. D. *et al.* Characterization of the effects of x-ray irradiation on the hierarchical structure and mechanical properties of human cortical bone. *Biomaterials* **32,** 8892–904 (2011).

96. Gallagher-Jones, M. *et al.* Macromolecular structures probed by combining single-shot free-electron laser diffraction with synchrotron coherent X-ray imaging. *Nat. Commun.* **5,** 3798 (2014).

97. Hammersley, A. P. Fit2D: An Introduction and Overview. *ESRF Intern. Rep.* (1997).

98. Paris, O. From diffraction to imaging: New avenues in studying hierarchical biological tissues with x-ray microbeams (Review). *Biointerphases* **3,** FB16-FB26 (2008).

99. Rinnerthaler, S. *et al.* Scanning Small Angle X-ray Scattering Analysis of Human Bone Sections. *Calcif. Tissue Int* **64,** 422–429 (1999).

100. Fratzl, P., Jakob, H. F., Rinnerthaler, S., Roschger, P. & Klaushofer, K. Position-Resolved Small-Angle X-ray Scattering of Complex Biological Materials. *J. Appl. Crystallogr.* **30,** 765–769 (1997).

101. Hammersley, A. P. FIT2D: a multi-purpose data reduction, analysis and visualization program. *J. Appl. Crystallogr.* **49,** 646–652 (2016).

102. Karunaratne, A. Analysis of Alterations in Matrix Quality at Nanoscale in Metabolic Bone Diseases using Synchrotron X-ray Diffraction. (Queen Mary University of London, 2013).

103. Park, S. M. S., Hung, C. T. & Ateshian, G. A. Mechanical response of bovine articular cartilage under dynamic unconfined compression loading at physiological stress levels. *Osteoarthr. Cartil.* **12,** 65–73 (2004).

104. Palmoski, M. J. & Brandt, K. D. Effects of static and cyclic compressive loading on articular cartilage plugs in vitro. *Arthritis Rheum.* **27,** 675–681 (1984).

105. Barker, M. K. & Seedhom, B. B. Articular cartilage deformation under physiological cyclic loading - Apparatus and measurement technique. *J. Biomech.* **30,** 377–381 (1997).

106. Krauss, S. *et al.* Inhomogeneous fibril stretching in antler starts after macroscopic yielding: indication for a nanoscale toughening mechanism. *Bone* **44,** 1105–10 (2009).

107. Gupta, H. *et al.* Synchrotron diffraction study of deformation mechanisms in mineralized tendon. *Phys. Rev. Lett.* **93,** 158101-1-158101–4 (2004).

108. Gupta, H. S., Seto, J., Krauss, S., Boesecke, P. & Screen, H. R. C. In situ multi-level analysis of viscoelastic deformation mechanisms in tendon collagen. *J. Struct. Biol.* **169,** 183–91 (2009).

109. Fratzl, P. Collagen packing and mineralization: An x-ray scattering investigation of turkey leg tendon. *Biophys. J.* **64,** 260–266 (1993).

110. Lees, S., Bonar, L. C. & Mook, H. A. A study of dense mineralized tissue by neutron diffraction. *Int. J. Biol. Macromol.* **6,** 321–326 (1984).

111. Wann, A. K. T. & Knight, M. M. Primary cilia elongation in response to interleukin-1 mediates the inflammatory response. *Cell. Mol. Life Sci.* **69,** 2967–77 (2012).

112. Thompson, C. L. *et al.* Lithium Chloride Prevents Interleukin-1 b Induced Cartilage Degradation and Loss of Mechanical Properties. *J. Orthop. Res.* **33,** 1552–1559 (2015).

113. Farndale, R. W., Sayers, C. A. & Barrett, A. J. A direct spectrophotometric microassay for sulfated glycosaminoglycans in cartilage cultures. *Connect. Tissue Res.* **9,** 247–8 (1982).

114. Eppell, S. J., Smith, B. N., Kahn, H. & Ballarini, R. Nano measurements with micro-devices: mechanical properties of hydrated collagen fibrils. *J. R. Soc. Interface* **3,** 117–121 (2006).

115. Kaab, M. ., Gwynn, I. A. & Notzli, H. . Collagen fibre arrangement in the tibial plateau articular cartilage of man and other mammalian species. *J. Anat* **193,** 23–34 (1998).

116. McLeod, M. a, Wilusz, R. E. & Guilak, F. Depth-dependent anisotropy of the micromechanical properties of the extracellular and pericellular matrices of articular cartilage evaluated via atomic force microscopy. *J. Biomech.* **46,** 586–92 (2013).

117. Erne, O. K. *et al.* Depth-dependent strain of patellofemoral articular cartilage in unconfined compression. *J. Biomech.* **38,** 667–72 (2005).

118. Bevill, S. L., Thambyah, A. & Broom, N. D. New insights into the role of the superficial tangential zone in influencing the microstructural response of articular cartilage to compression. *Osteoarthr. Cartil.* **18,** 1310–1318 (2010).

119. Kempson, G. E., Muir, H., Pollard, C. & Tuke, M. The tensile properties of the cartilage of human femoral condyles related to the content of collagen and glycosaminoglycans. *Biochim. Biophys. Acta* **297,** 456–472 (1973).

120. Inamdar, S. R. *et al.* The Secret Life of Collagen : Temporal Changes in

Nanoscale Fibrillar Pre-Strain and Molecular Cartilage. *ACS Nano* **11,** 9728–9737 (2017).

121. Bakarich, S. E., Gorkin, R., in het Panhuis, M. & Spinks, G. M. Three-Dimensional Printing Fiber Reinforced Hydrogel Composites. *ACS Appl. Mater. Interfaces* **6,** 15998–16006 (2014).

122. Wu, Z. L. *et al.* Three-dimensional shape transformations of hydrogel sheets induced by small-scale modulation of internal stresses. *Nat. Commun.* **4,** 1586 (2013).

123. Masic, A. *et al.* Osmotic Pressure Induced Tensile Forces in Tendon Collagen. *Nat. Commun.* **6,** 5942 (2015).

124. Stamenovic, D. & Ingber, D. E. Tensegrity-guided self assembly: from molecules to living cells. *Soft Matter* **5,** 1137–1145 (2009).

125. Gardel, M. L. *et al.* Scaling of F-actin network rheology to probe single filament elasticity and dynamics. *Phys. Rev. Lett.* **93,** (2004).

126. Broom, N. D. & Silyn-Roberts, H. Collagen-collagen versus collagen-proteoglycan interactions in the determination of cartilage strength. *Arthritis Rheum* **33,** 1512–1517 (1990).

127. Han, L., Grodzinsky, A. J. & Ortiz, C. Nanomechanics of the Cartilage Extracellular Matrix. *Annu Rev Mater Res.* **41,** 133–168 (2011).

128. Korhonen, R. K. & Jurvelin, J. S. Compressive and tensile properties of articular cartilage in axial loading are modulated differently by osmotic environment. *Med. Eng. Phys.* **32,** 155–60 (2010).

129. Potter, K., Kidder, L. H., Levin, I. W., Lewis, E. N. & Spencer, R. G. S. Imaging of collagen and proteoglycan in cartilage sections using fourier transform infrared spectral imaging. *Arthritis.Rheum.* **44,** 846–855 (2001).

130. Bi, X., Li, G., Doty, S. B. & Camacho, N. P. A novel method for determination of collagen orientation in cartilage by Fourier transform infrared imaging spectroscopy (FT-IRIS). *Osteoarthritis Cartilage* **13,** 1050–8 (2005).

131. Changoor, A. *et al.* Structural characteristics of the collagen network in human normal, degraded and repair articular cartilages observed in polarized light and scanning electron microscopies. *Osteoarthr. Cartil.* **19,** 1458–1468 (2011).

132. Sasaki, N. & Odajima, S. Elongation mechanisms of collagen fibrils and force-strain relations of tendons at each level of structural hierarchy. *J. Biomech.* **29,** 1131–1136 (1996).

133. Karunaratne, A. *et al.* Significant deterioration in nanomechanical quality occurs through incomplete extrafibrillar mineralization in rachitic bone: evidence from in-situ synchrotron X-ray scattering and backscattered electron imaging. *J. Bone Miner. Res.* **27,** 876–90 (2012).

134. Julkunen, P. *et al.* A review of the combination of experimental measurements and fibril-reinforced modeling for investigation of articular cartilage and

chondrocyte response to loading. *Comput. Math. Methods Med.* **2013,** 326150 (2013).

135. Shirazi, R., Shirazi-Adl, a & Hurtig, M. Role of cartilage collagen fibrils networks in knee joint biomechanics under compression. *J. Biomech.* **41,** 3340–8 (2008).

136. Ateshian, G. A., Rajan, V., Chahine, N. O., Canal, C. E. & Hung, C. T. Modeling the matrix of articular cartilage using a continuous fiber angular distribution predicts many observed phenomena. *J. Biomech. Eng.* **131,** 61003 (2009).

137. Wachtel, E. & Maroudas, A. The effects of pH and ionic strength on intrafibrillar hydration in articular cartilage. *Biochim. Biophys. Acta* **1381,** 37–48 (1998).

138. Wang, C. C. B., Hung, C. T. & Mow, V. C. An analysis of the effects of depth-dependent aggregate modulus on articular cartilage stress-relaxation behavior in compression. *J. Biomech.* **34,** 75–84 (2001).

139. Setton, L. A., Zhu, W. & Mow, V. C. The biphasic poroviscoelastic behavior of articular cartilage: Role of the surface zone in governing the compressive behavior. *J. Biomech.* **26,** 581–592 (1993).

140. Tavakoli Nia, H. *et al.* Aggrecan nanoscale solid-fluid interactions are a primary determinant of cartilage dynamic mechanical properties. *ACS Nano* **9,** 2614–2625 (2015).

141. Roman, N. M., Christopher, R. M. & Athanasiou, K. A. Chondroitinase ABC Treatment Results in Greater Tensile Properties of Self-Assembled Tissue-Engineered Articular Cartilage. *Tissue Eng.* **15,** (2009).

142. Chahine, N. O., Chen, F. H., Hung, C. T. & Ateshian, G. A. Direct Measurement of Osmotic Pressure of Glycosaminoglycan Solutions by Membrane Osmometry at Room Temperature. *Biophys. J.* **89,** 1543–1550 (2005).

143. Basser, P. J., Schneiderman, R., Bank, R. A., Wachtel, E. & Maroudas, A. Mechanical Properties of the Collagen Network in Human Articular Cartilage as Measured by Osmotic Stress Technique. *Arch. Biochem. Biophys.* **351,** 207–219 (1998).

144. Goldring, M. B. & Otero, M. Inflammation in osteoarthritis. **23,** 471–478 (2014).

145. Sokolove, J. & Lepus, C. M. Role of inflammation in the pathogenesis of osteoarthritis : latest findings and interpretations. *Ther. Adv. Muscoskeletal Dis.* **5,** 77–94 (2013).

146. Mcnulty, A. L., Rothfusz, N. E., Leddy, H. A. & Guilak, F. Synovial Fluid Concentrations and Relative Potency of Interleukin-1 Alpha and Beta in Cartilage and Meniscus Degradation. *J. Orthop. Res.* **31,** 1039–1045 (2013).

147. Torzilli, P. A., Bhargava, M. & Chen, C. T. Mechanical Loading of Articular Cartilage Reduces IL-1-Induced Enzyme Expression. *Cartilage* **2,** 364–373 (2011).

148. McNulty, a L., Estes, B. T., Wilusz, R. E., Weinberg, J. B. & Guilak, F.

Dynamic loading enhances integrative meniscal repair in the presence of interleukin-1. *Osteoarthritis Cartilage* **18,** 830–8 (2010).

149. Goldring, M. B. & Marcu, K. B. Cartilage homeostasis in health and rheumatic diseases. *Arthritis Research and Therapy* **11,** 224 (2009).

150. Park, S., Krishnan, R., Nicoll, S. B. & Ateshian, G. A. Cartilage Interstitial Fluid Load Support in Unconfined Compression. *J. Biomech.* **36,** 1785–1796 (2003).

151. Sah, R. L. *et al.* Biosynthetic Response of Cartilage Explants to Dynamic Compression. *J. Orthop. Res.* **7,** 619–636 (1989).

152. Buschmann, M. D. *et al.* Stimulation of Aggrecan Synthesis in Cartilage Explants by Cyclic Loading Is Localized to Regions of High Interstitial Fluid Flow 1. *Arch. Biochem. Biophys.* **366,** 1–7 (1999).

153. Speirs, A. D., Beaulé, P. E., Ferguson, S. J. & Frei, H. Stress distribution and consolidation in cartilage constituents is influenced by cyclic loading and osteoarthritic degeneration. *J. Biomech.* **47,** 2348–2353 (2014).

154. Gottardi, R. *et al.* Supramolecular Organization of Collagen Fibrils in Healthy and Osteoarthritic Human Knee and Hip Joint Cartilage. *PLoS One* **11,** 1–13 (2016).

155. Wang, R. & Gupta, H. S. Deformation and Fracture Mechanisms of Bone and Nacre. *Ann. Rev. Mater. Res.* **41,** 41–73 (2011).

156. Seedhom, B. B. Conditioning of cartilage during normal activities is an important factor in the development of osteoarthritis. *Rheumatology* **45,** 146–149 (2006).

157. Frost, H. M. Joint Anatomy , Design , and Arthroses : Insights of the Utah Paradigm. *Anat. Rec.* **255,** 162–174 (1999).

158. Hosseini, S. M., Wilson, W., Ito, K. & Van Donkelaar, C. C. A numerical model to study mechanically induced initiation and progression of damage in articular cartilage. *Osteoarthr. Cartil.* **22,** 95–103 (2014).

159. Nikolov, B. S. *et al.* Revealing the Design Principles of High-Performance Biological Composites Using Ab initio and Multiscale Simulations : The Example of Lobster Cuticle. *Adv. Mater.* **22,** 519–526 (2010).

160. Soltz, M. a & Ateshian, G. a. Interstitial fluid pressurization during confined compression cyclical loading of articular cartilage. *Ann. Biomed. Eng.* **28,** 150–9 (2000).

Appendix

APPENDIX

A.1. Initial sample holder designs generation

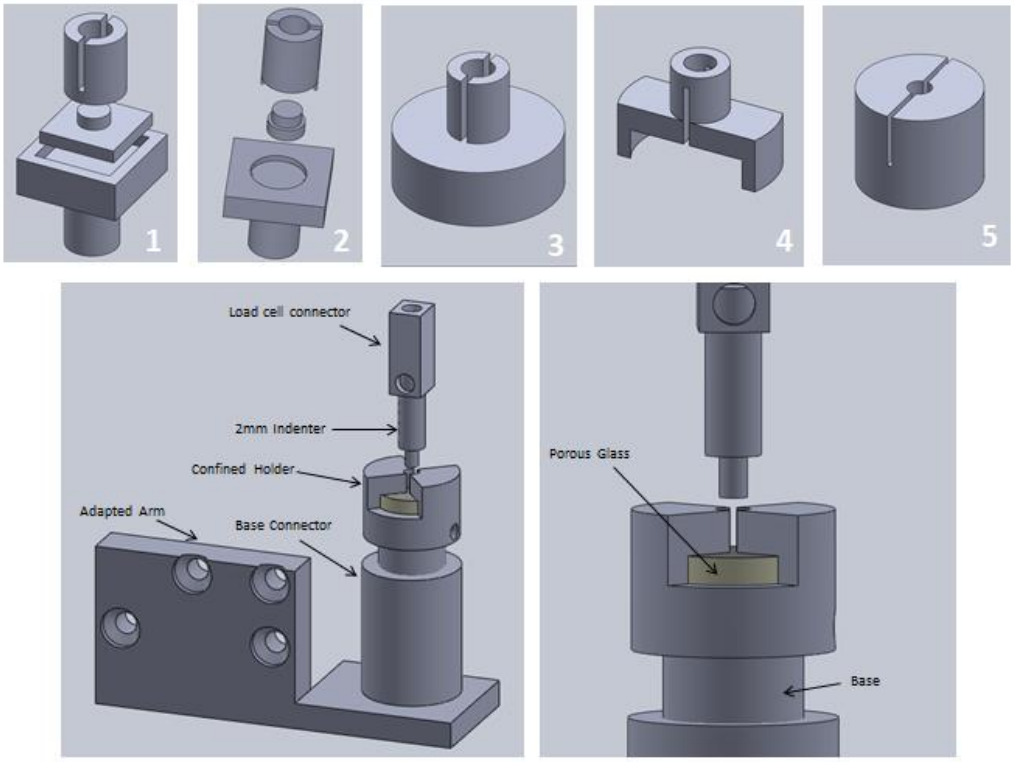

Figure A.1.1: The various concepts generated during the deign process of an in situ sample holder (1-5). A confined setup was designed and made as shown which was later simplified to unconfined.

Figure A.1.1 shows an earlier design that was manufactured but was unsuccessfully used during early experiments at DLS. The confined design included a 2mm circular indenter and a sample holder which had a small chamber in which the 2mm discs of cartilage were placed. Directly under the sample a porous glass disc was placed, to allow the applied fluid for hydration (PBS) to permeate from the tissue to the surrounding environment when placed under compression to replicate what occurs in physiological conditions (with a porosity of 40µm as used previously [160]). For hydration, a simple drip system was used to hydrate the sample as indicated in Figure

A.1.2 (1). At DLS a controlled syringe pump was used that supplied a rate of flow of PBS 0.1µl/min.

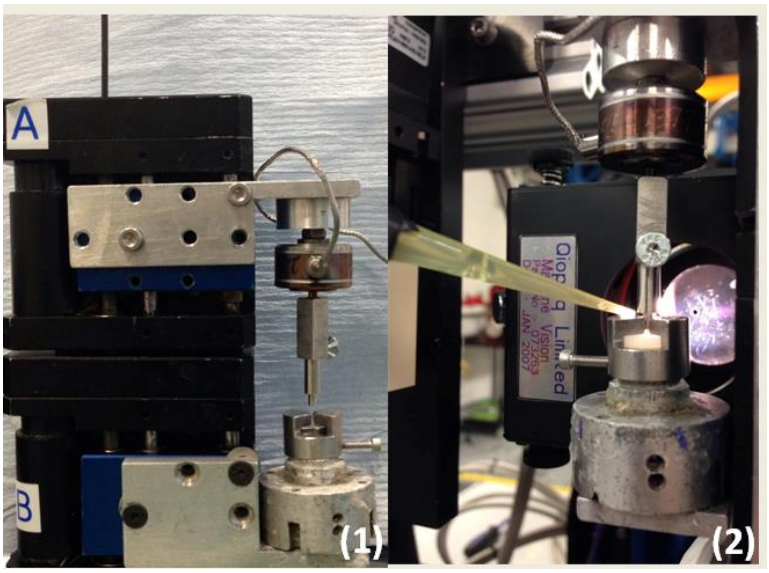

Figure A.1.2: Confined compression setup indicated in (1), view of confined chamber and syringe pump drip system used to continuously hydrate the sample during testing.

A.2. Sample holder designs generation: Drawings

A.2.1. Upper 2mm loading platen:

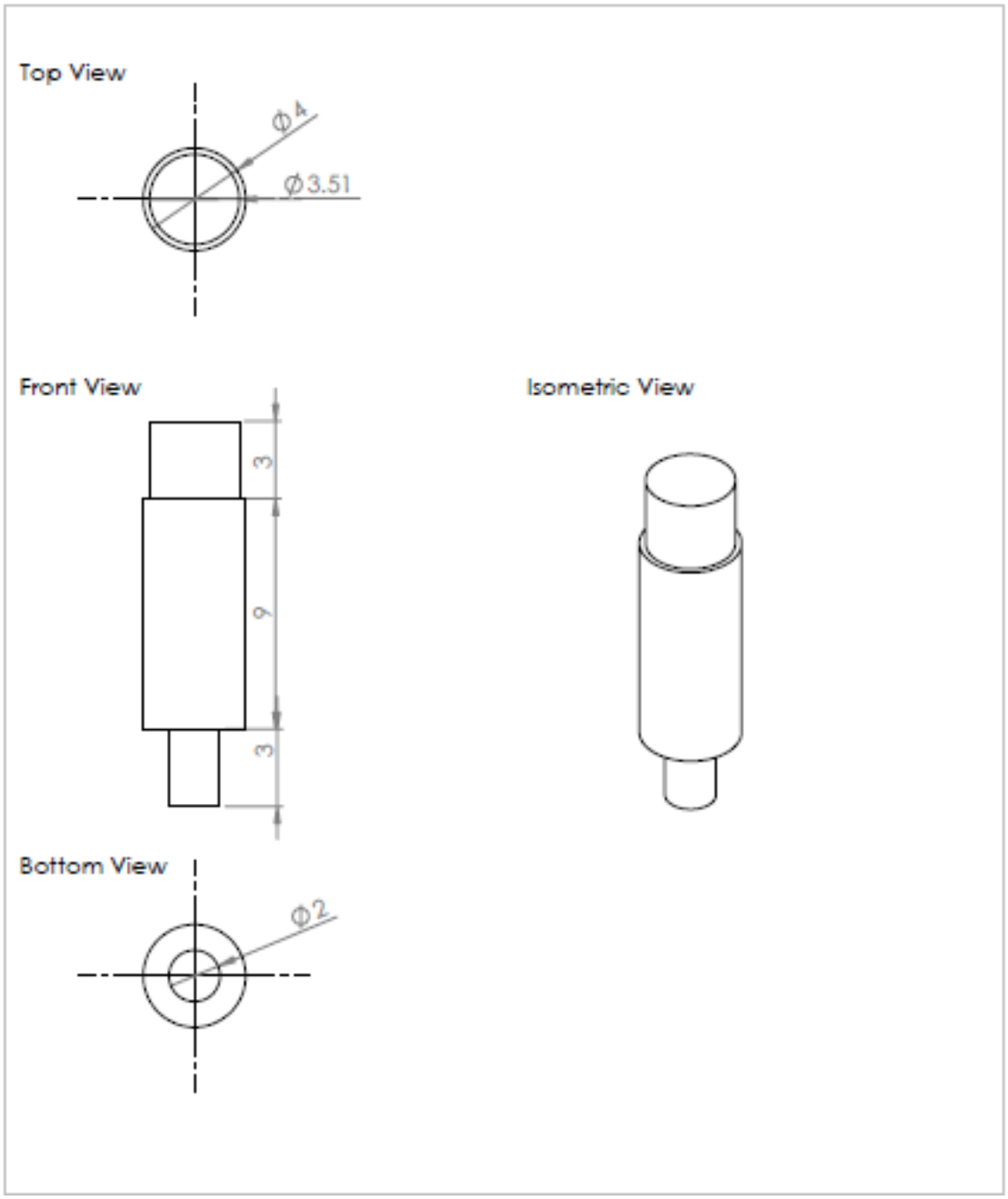

A.2.2. Upper 4mm loading platen:

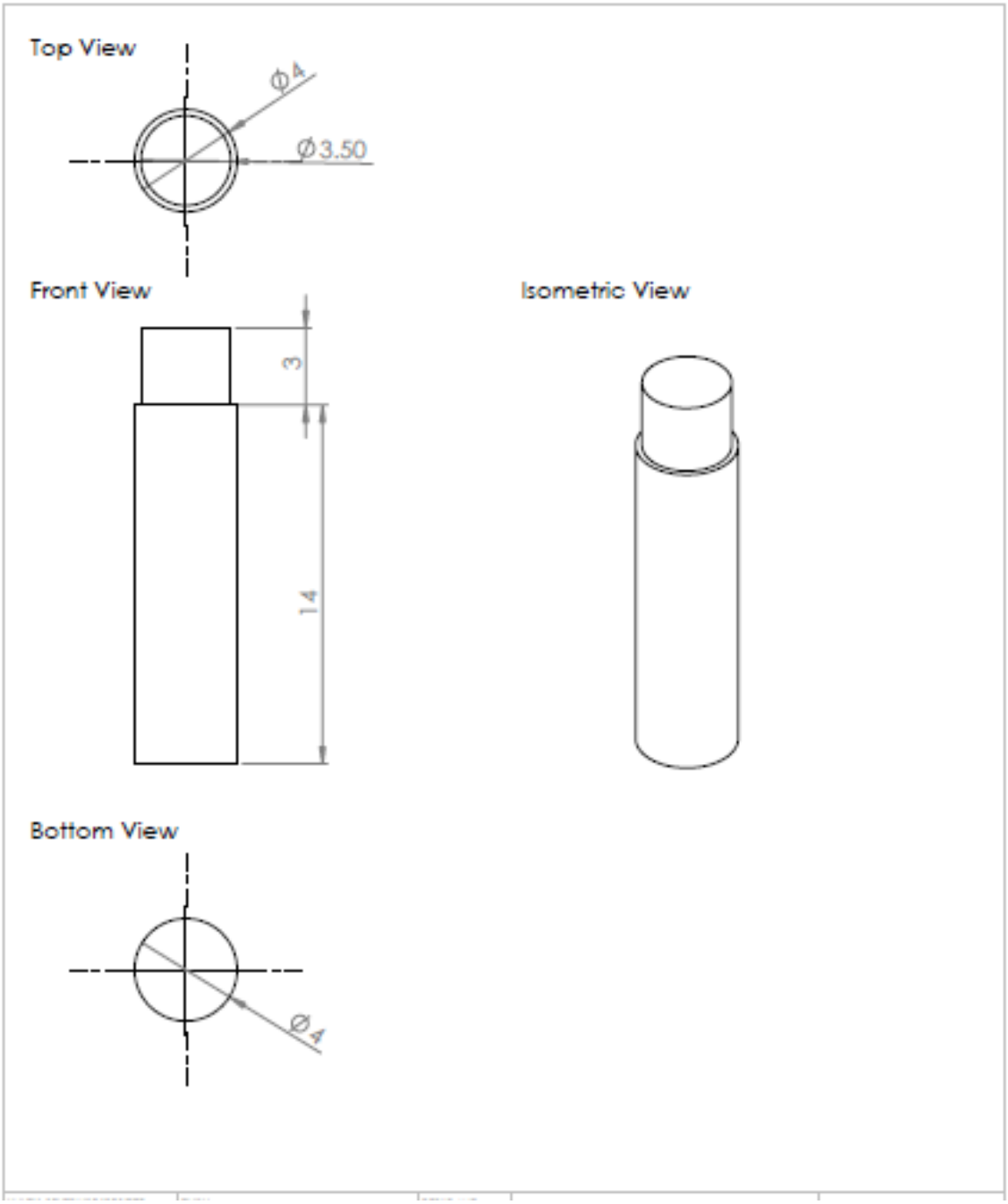

A.2.3. Load cell connector:

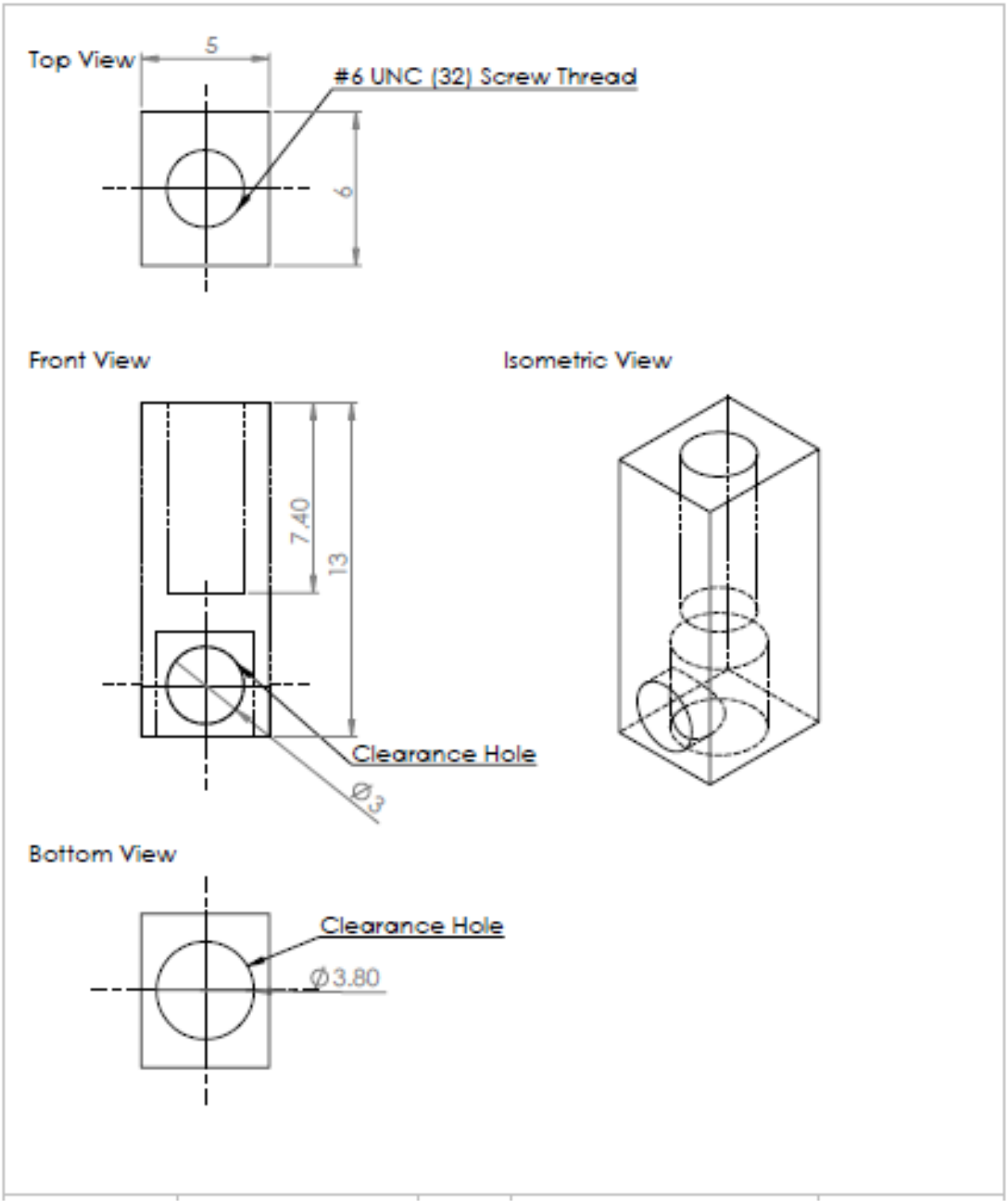

A.2.4. Base connector:

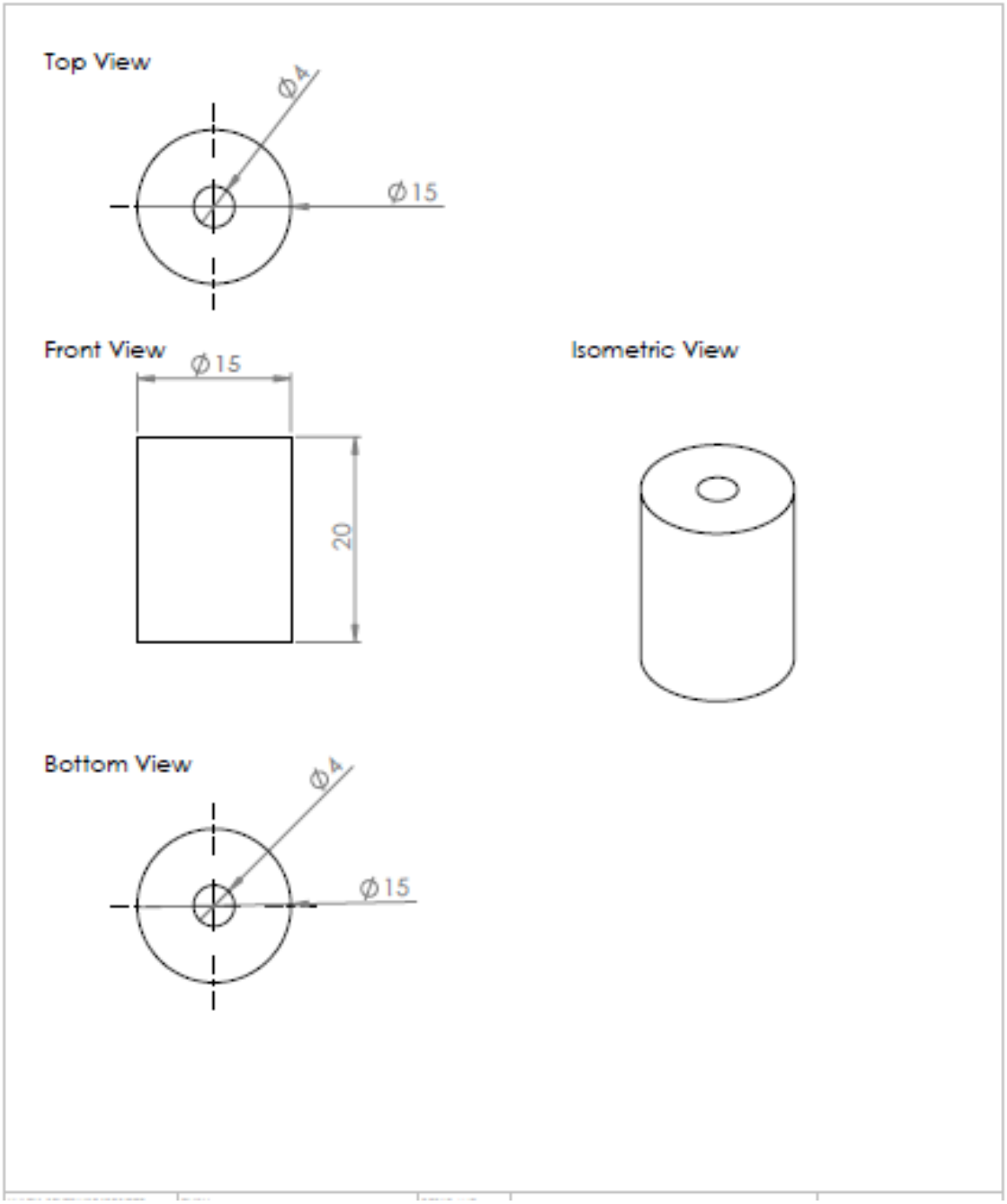

A.2.5. Base arm:

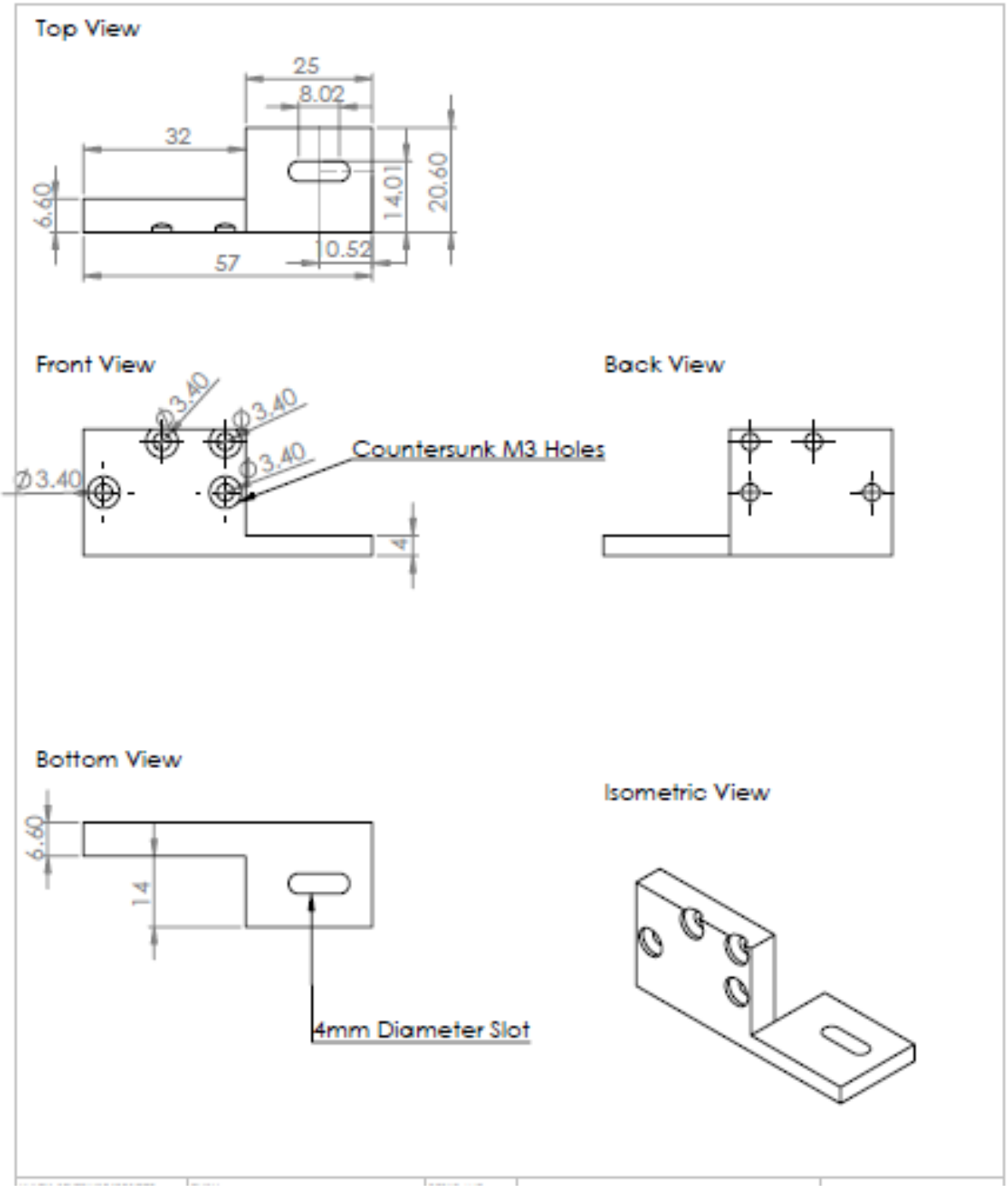
Top View
25
8.02
32
6.60
14.01
20.60
57
10.52
Front View
Ø3.40
Ø3.40
Ø3.40
Ø3.40
Countersunk M3 Holes
4
Back View
Bottom View
6.60
14
4mm Diameter Slot
Isometric View

A.2.6. Adjustable mounting block:

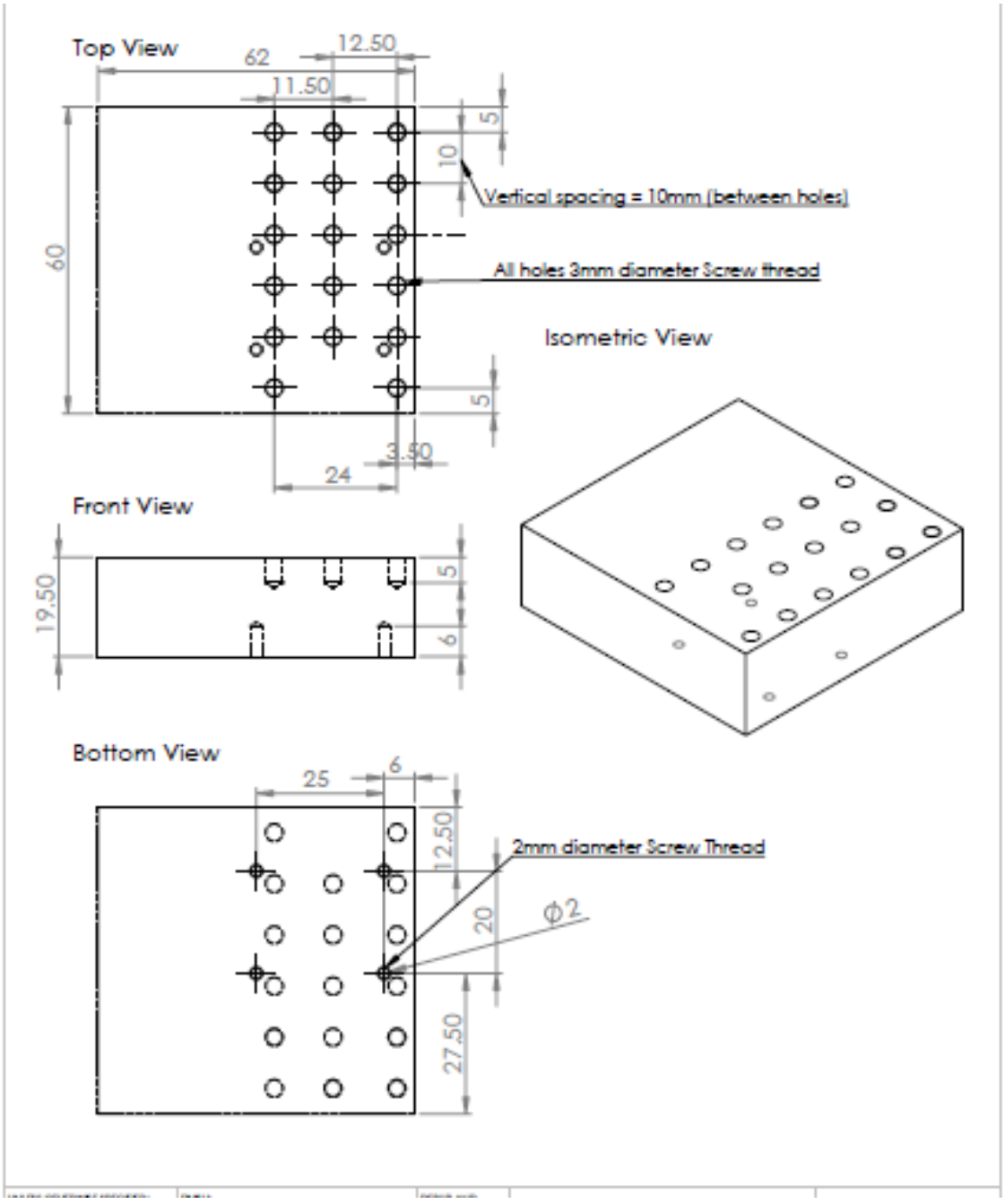

A.2.7. Sample holder base 1:

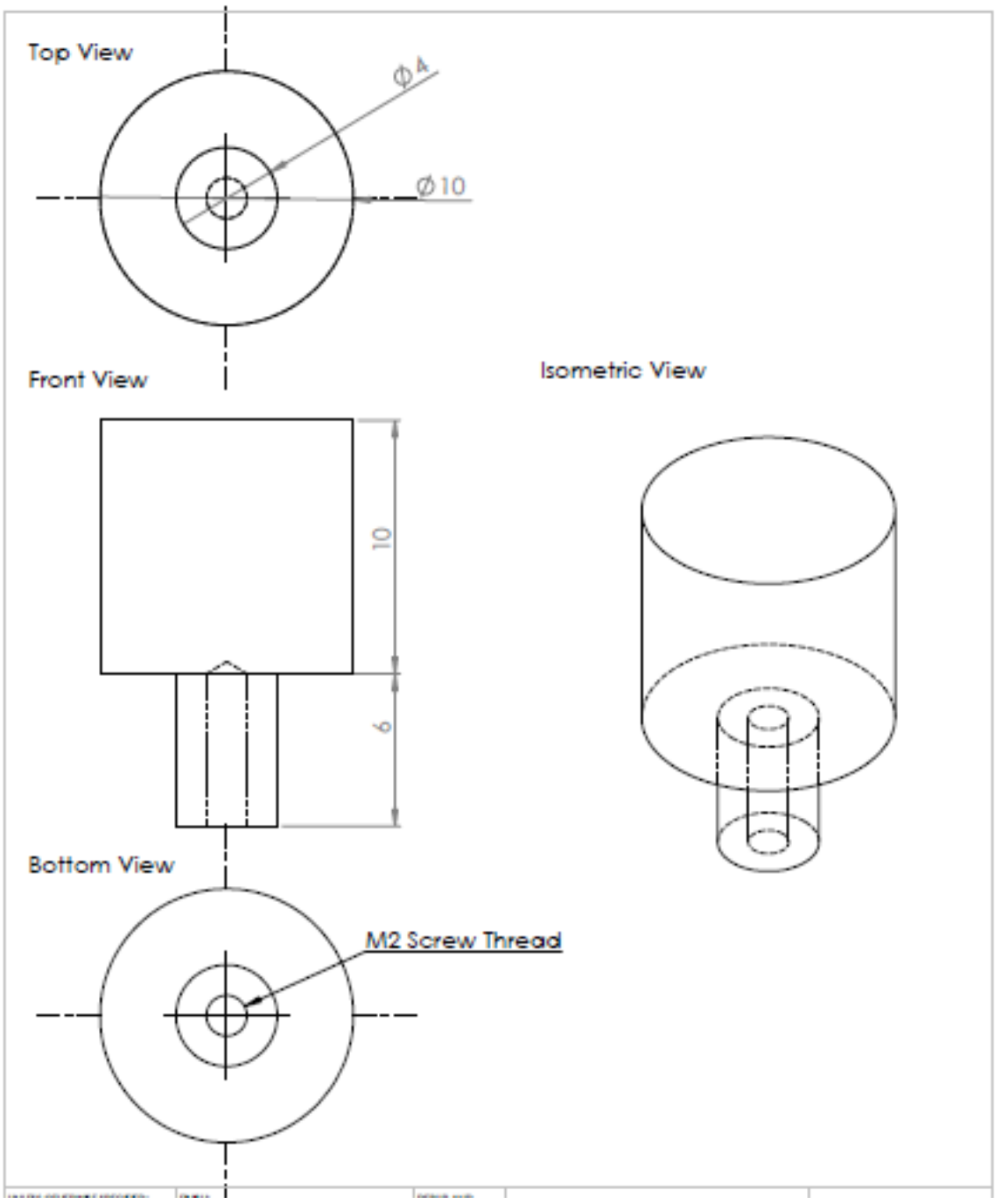

A.2.8. Sample holder base 2:

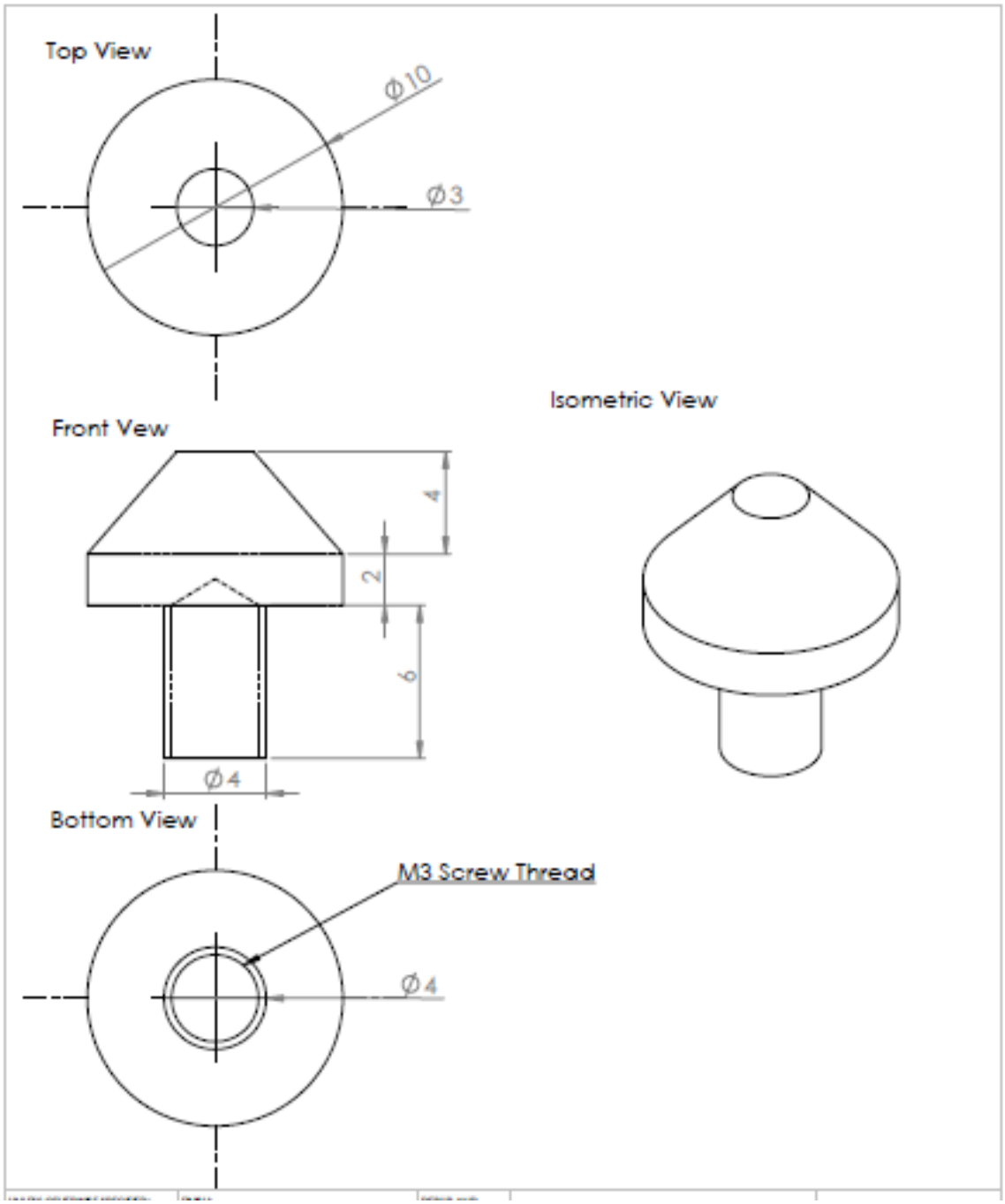

A.3. Synchrotron protocols

A.3.1 Stress-relaxation tests

Description: Performing line scans before strain application (20%) and after relaxation (900secs) in the Y direction across the full thickness of the cartilage explants.

Before The Experiment:

Preparing the script to run the scan:

The necessary scripts to run the line scan and associated diode scan before load and after relaxation. I.e. determine the Y coordinates for the start and finish (these must be displaced in the X direction for each new line scan).

Experimental Procedure:

1. Setup tensile tester within the beamline and locate region of interest and position beam, i.e. area between the loading platen and sample base.
2. Load sample onto base, hydrate sample and use the LabView programme to apply tare load (0.1N). Then allow sample to equilibrate.
3. Perform a line scan and associated diode scan in the y-direction using the prepared script. The line scan should be performed along the middle of the sample.
4. Apply pre-defined strain (20% strain at 20%/min).
5. Edit the script to offset the new line scan that will be performed following the relaxation phase.
6. Following relaxation, perform the second set of line scans using the amended script.
7. End of test.

A.3.2 Relaxation time dependent scanning

Description: Tracking the regional changes in fibrillar structure and mechanics in relation to time during the relaxation phase of an in situ stress relaxation test on bovine cartilage explants.

Before The Experiment:

Determining position of post strain scan:

The deformation within cartilage is inhomogeneous and therefore it cannot be assumed that each zone will be displaced the same amount. Using a previous set of line scans before and after relaxation, the percentage shifts in strain within each zone can be calculated. To do this, taking the SAXS patterns from before and after:

a) Integrate in χ to get the degree of orientation for each SAXS pattern.

b) Plot the orientation against the position in the sample in relation to the upper platen and lower base i.e. at the platen the position = 0 and base plate = x (where x is sample thickness).
c) By measuring the change in distance between the ROI and base, the strain within each of the three zones can be calculated, and therefore the percentage shifts.

Preparing the script to run the scan:

Experimental Procedure:

8. Setup tensile tester within the beamline and locate region of interest and position beam, i.e. area between the loading platen and sample base.
9. Load sample onto base, hydrate sample and use the LabView programme to apply tare load (0.1N). Then allow sample to equilibrate.
10. Perform a line scan in the y-direction to determine the location of each zone (superficial, middle and deep). The line scan should be performed along the middle of the sample. Identify from the SAXS patterns the point coordinate of the zone of interest i.e. the x and y coordinates.
11. Perform a line scan (and associated diode scan) in the x-direction.
    a. This should be applied along the y position determined in the previous step.
    b. The line scan should be confined within a 500µm window in the centre of the sample (therefore calculate the start and finish coordinates using central coordinate from step 3)
    c. Define the spacing between each point, and the time during relaxation for each point.
12. Re-position beam to new y coordinate to track changes in region of interest following strain application (see above for position determination).
13. Apply pre-defined strain (20% strain at 20%/min).
14. At the beginning of relaxation, run the associated script that applies a line scan in the x-direction with associated diode scans. This script should include time points derived assuming an exponential decay of time points (as described above).
15. Perform a diode line scan at the same X positions but a slightly varied Y position.

A.4. Synchrotron scripts

A.4.1 Script (1): Standard Stress-Relaxation Tests

Perform diode scan in x-direction across a lot to identify viewing range relative to the current position (this should be between 0.3-0.5mm)

i. pos pxy_x 99 (in)
ii. rscan mfstage_x -1.5 1.5 0.1 d10d2
iii. pos pxy_x 60 (out)

(following a diode scan to a) find the middle of the pin for the x coordinate, b) find the start and end of the sample according to the top platen and base. Position mfstage_x before running the script)

setTitle("Sample 1 at 0%")

inc mfstage_x 0.025 **MOVE X STAGE AFTER LOADING**

shutter "Open"

rscan mfstage_y -0.25 0.25 0.02 ncddetectors **SCAN WITHIN A 500µm IN DY**

shutter "Close"

setTitle("Sample 1 at 0% Diode)

pos pxy_x 1.159

inc mfstage_x 0.025

pos shutter "Open"

rscan mfstage_y -0.25 0.25 0.02 d10d2

pos shutter "Close"

inc pxy_x 40

(Repeat following 20% strain and relaxation- adjust script so that the x coordinate is offset once more)

A.4.2 Script (2): Relaxation Dependent Scanning

Perform diode scan in x-direction across a lot to identify viewing range relative to the current position (this should be between 0.3-0.5mm)

iv. pos pxy_x 99 (in)
v. rscan mfstage_x -1.5 1.5 0.1 d10d2
vi. pos pxy_x 60 (out)

(Following a diode scan to find the middle x position and performing a line scan in y to identify ROI, following this a calculation must be made to determine second set of y position post loading. Take a single point at the start for the SAXS pattern at 0% strain)

pos mfstage_y y

pos mfstage_x x

setTitle(“Sample 1 during relaxation”)

pos shutter “Open”

staticscan ncddetectors

pos shutter “Close”

inc mfstage_x 0.02

sleep 5

pos shutter “Open”

staticscan ncddetectors

pos shutter “Close”

inc mfstage_x 0.02

sleep 5

pos shutter “Open”

staticscan ncddetectors

pos shutter “Close”

inc mfstage_x 0.02

sleep 5

pos shutter “Open”

staticscan ncddetectors

pos shutter “Close”

inc mfstage_x 0.02

sleep 5

pos shutter “Open”

staticscan ncddetectors

pos shutter “Close”

inc mfstage_x 0.02

sleep 5

(repeat for 25 points)

A.5. Supplementary information: Chapter 5

List of Supplementary Information Topics:

A.5.1: sGAG release and mechanical alterations on chondroitinase treatment.

A.5.2: Modelling SAXD intensity changes during stress relaxation in terms of fibrillar changes

A.5.3: Intrafibrillar molecular packing and fibril orientation during stress relaxation

A.5.1: sGAG release and mechanical alterations on chondroitinase treatment:

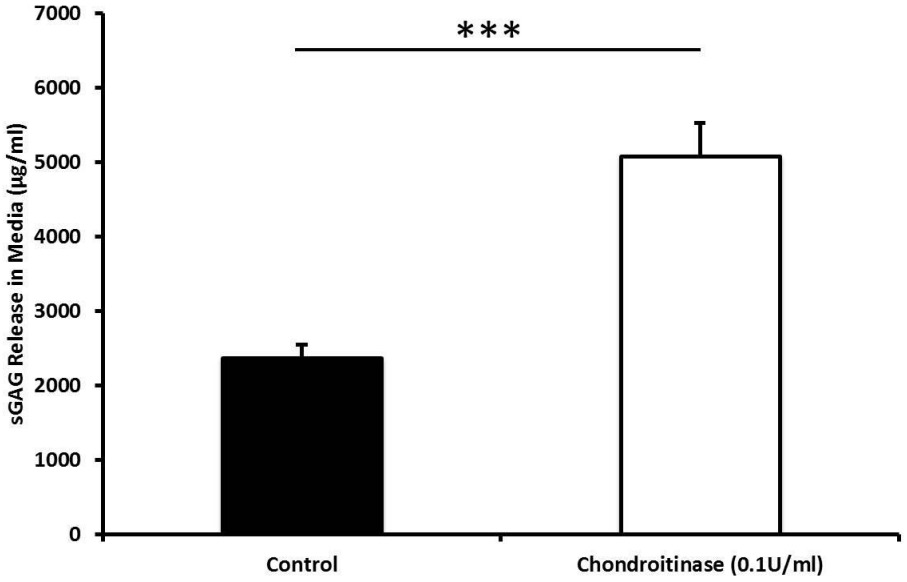

Figure A.5.1: Chondroitinase ABC treatment leads to increased sGAG release in treatment media. Values represent mean values with error bars showing SEM for n = 12/group.

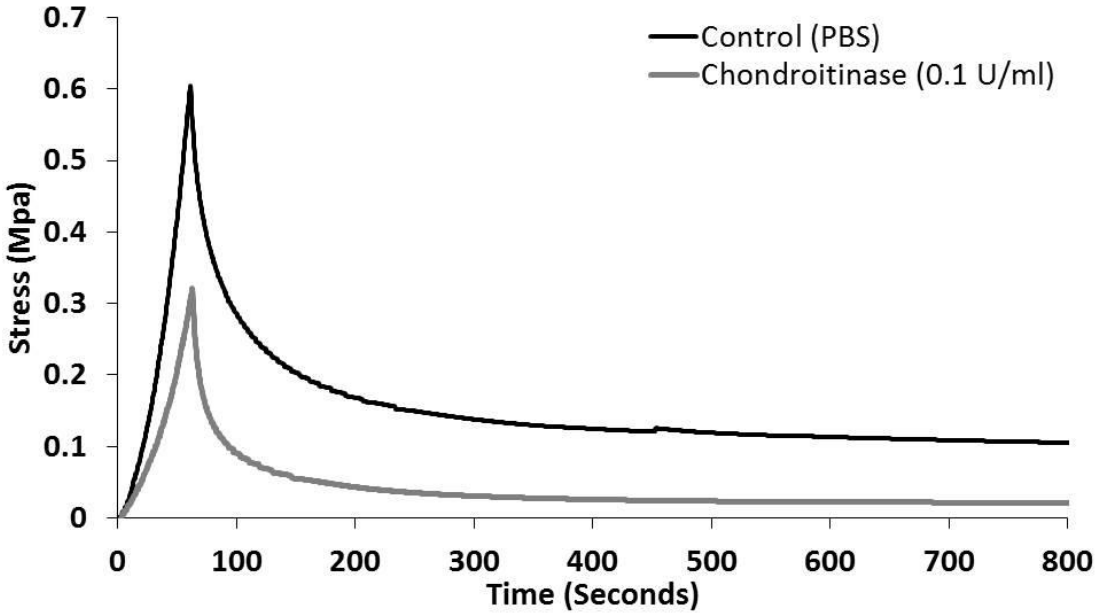

Figure A.5.2: Chondroitinase ABC treatment leads to altered stress-relaxation response. Representative macro-scale stress response in compressed cartilage during relaxation (20% strain level loaded at a rate of 20%/min).

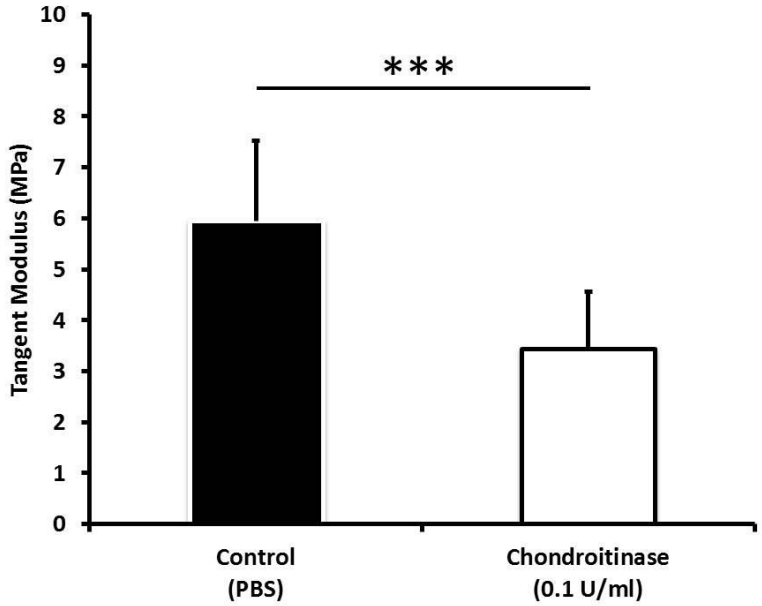

Figure A.5.3: Chondroitinase ABC treatment leads to reduced tissue stiffness. Tangent modulus is significantly reduced when explants are treated with Chondroitinase ABC at 0.1U/ml. Tangent modulus was calculated from the linear region of the stress-strain curve. Values represent mean values with error bars showing SD for n = 9/group.

A.5.2: Modelling SAXD intensity changes during stress relaxation in terms of fibrillar changes

The model in this section was developed in collaboration with the primary supervisor, Dr H.S. Gupta.

A.5.2A: Predictions of intensity ratio variation with changing O/D

Using the formulae for $\frac{I_7}{I_5}$ and $\frac{I_8}{I_5}$ derived from a step-function variation of axial electron density inside the collagen fibril, the intensity ratios can be graphed as shown below. It is clear that there is a substantial sensitivity of peak intensity ratios to the exact value of O/D. In particular, in the region between O/D = 0.40 and O/D = 0.50, which is the value observed for collagen fibrils in a close-to-physiological condition[132] , the odd-order ratio $\frac{I_7}{I_5}$ and the even-order ratio $\frac{I_8}{I_5}$ vary in opposite directions.

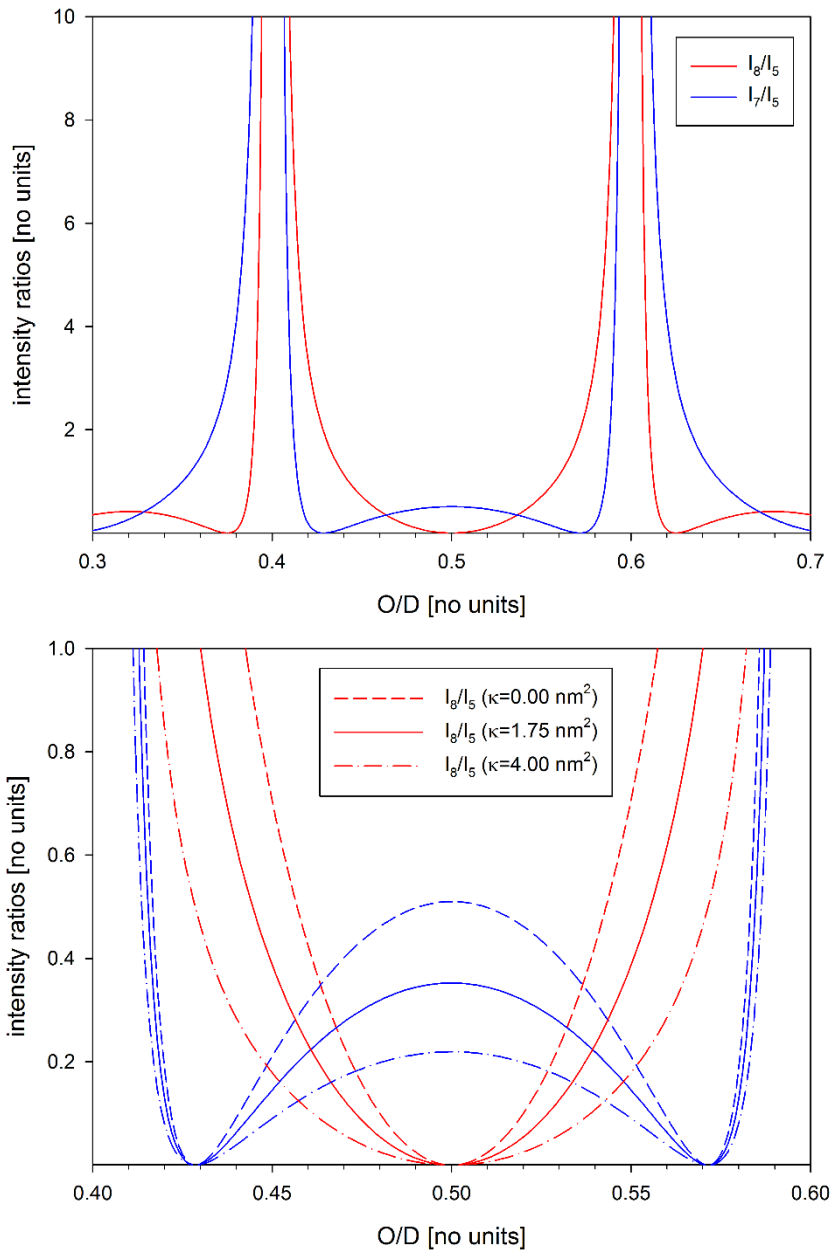

Figure A.5.4: (a) Plot of $\frac{I_7}{I_5}$ ***(blue) and*** $\frac{I_8}{I_5}$ ***(red) with zero disorder over the O/D range from 0.3 to 0.7. Note how, over the range O/D ~ 0.45 – 0.50,*** $\frac{I_7}{I_5}$ ***increases while*** $\frac{I_8}{I_5}$ ***decreases.*** $\frac{I_8}{I_5}$ ***is zero at O/D = ½, as all even orders vanish at O/D = ½. (b) Plot of the variation of*** $\frac{I_7}{I_5}$ ***(blue) and*** $\frac{I_8}{I_5}$ ***(red) for three levels of disorder (κ = 0.00 nm² (dashed), 1.75 nm² (solid), and 4.00 nm² (dash-dot)) over a narrower O/D range from 0.4 to 0.6. The plot is an expanded version (in the abscissa and ordinate scales) of Fig. 5.5D.***

A.5.2B: Estimation of changed disorder and O/D during transient D-change:

We first describe qualitatively how the changes in intensity ratios can be interpreted in terms of disorder and O/D changes (part **A.5.2B1**) followed by a quantitative modelling of the variation of these parameters in part **A.5.2B2**.

A.5.2B1:

Estimate of initial disorder: From **Figure 5.5C** (main text), at the start of the dip in D-period (leftmost side of **Figure 5.5C**), $\frac{I_7}{I_5}$ ~ 0.25 and $\frac{I_8}{I_5}$ ~ 0.15. No mutually consistent solution for O/D can be found for these values for zero disorder ($\kappa = 0.00$ nm^2; **Figure A.5.4**, dashed lines). By increasing κ, we find that at $\kappa \sim 1.75$ nm^2 (**Figure A.5.4**, solid lines), $\frac{I_7}{I_5}$ ~ 0.25 and $\frac{I_8}{I_5}$ ~ 0.15 at O/D ~ 0.466, which is a mutually consistent solution, and provides an estimate of intrinsic disorder in the collagen fibrils before any load is applied. In the current discussion, all numerical values are approximate estimates from reading off the data plots and generated model curves, and are meant to demonstrate qualitative behaviours rather than numerically precise fits to data.

Increase of disorder: In the first stage (a→ b; **Figure 5.5C**), we observe a reduction of both $\frac{I_7}{I_5}$ to ~0.20 and $\frac{I_8}{I_5}$ to ~0.10. From **Figure A.5.4**, it can be seen that such a change can be attained by keeping O/D fixed and increasing disorder from $\kappa \sim 1.75$ nm^2 to $\kappa \sim 4.00$ nm^2 (vertical downward arrows).

Reduction of O/D: In the second (middle) stage (b→ c; **Figure 5.5C**), $\frac{I_7}{I_5}$ decreases and $\frac{I_8}{I_5}$ increases till they both cross-over at ~ 0.15-0.16 at the point of minimum D. We can see from

Figs 5.5D and **A.5.4** that such a behaviour can be modelled by keeping both $\frac{I_7}{I_5}$ and $\frac{I_8}{I_5}$ on their respective $\kappa = 4.00\ nm^2$ curves, and reducing O/D till the curves intersect at ~0.457, which is also where both ratios are ~0.13.We can therefore see that the changes in peak intensity ratios during the minimum in fibrillar pre-strain in D can be explained by an initial increase in intrafibrillar disordering, followed by a reduction in O/D due axial movement of tropocollagen molecules, as shown schematically in **Figure 5.6**.

A.5.2B2:

The steps described above can be simulated, as guides to the eye rather than as a fit, by linear variations of the O/D fraction and the disorder term across the three stages, as follows.

(a → b): Denote the start and end time points of this segment to be t_1 (= 50 s) and t_2 (= 90 s). Then the rescaled time parameter can be defined as $\zeta_1 = \frac{t - t_1}{t_2 - t_1}$. With this, we have:

$$\kappa(\zeta_1) = \kappa_0 + \zeta_1(\kappa_1 - \kappa_0)$$

$$\left(\frac{I_7}{I_5}\right)_A(\zeta_1) = \left(\frac{I_7}{I_5}\right)_A(0)\exp\left(-24(\kappa(\zeta_1) - \kappa_0)\left(\frac{2\pi}{D}\right)^2\right)$$

$$\left(\frac{I_8}{I_5}\right)_A(\zeta_1) = \left(\frac{I_8}{I_5}\right)_A(0)\exp\left(-39(\kappa(\zeta_1) - \kappa_0)\left(\frac{2\pi}{D}\right)^2\right)$$

(b → c): Denote the start and end time points of this segment to be t_2 (= 90 s) and t_3 (= 110 s). Then the rescaled time parameter can be defined as $\zeta_2 = \frac{t - t_2}{t_3 - t_2}$. As over this segment, the overlap/D-period changes but the disorder remains constant, we have (abbreviating O/D as *f*):

$$f_B(t) = f_0 + \zeta_2(f_1 - f_0)$$

$$\left(\frac{I_7}{I_5}\right)_B(\zeta_2) = \left(\frac{5}{7}\right)^2\left(\frac{\sin(7\pi f_B(\zeta_2))}{\sin(5\pi f_B(\zeta_2))}\right)^2 \exp\left(-24\kappa_1\left(\frac{2\pi}{D}\right)^2\right)$$

$$\left(\frac{I_8}{I_5}\right)_B(\zeta_2) = \left(\frac{5}{8}\right)^2\left(\frac{\sin(8\pi f_B(\zeta_2))}{\sin(5\pi f_B(\zeta_2))}\right)^2 \exp\left(-39\kappa_1\left(\frac{2\pi}{D}\right)^2\right)$$

(c → d): Denote the start and end time points of this segment to be t_3 (= 110 s) and t_4 (= 150 s). If $\frac{I_8}{I_5} = \left(\frac{5}{8}\right)^2\left(\frac{\sin(8\pi f_1)}{\sin(5\pi f_1)}\right)^2 \exp\left(-39\kappa\left(\frac{2\pi}{D}\right)^2\right)$ is (approximately) constant, we can take the initial state as (κ_1, f_1), with

$$R^1_{8,5} = \left(\frac{5}{8}\right)^2\left(\frac{\sin(8\pi f_1)}{\sin(5\pi f_1)}\right)^2 \exp\left(-39\kappa_1\left(\frac{2\pi}{D}\right)^2\right)$$

If we set $R^1_{8,5}$ as a constant ~0.11, then if the ratio f varies continuously from f_1 to f_2, with a variation parameter $\zeta_3 = \frac{t - t_3}{t_4 - t_3}$,

$$f_C(t) = f_1 + \zeta_3(f_0 - f_1)$$

with $0 \le \zeta_3 \le 1$, which leads to

$$\kappa(\zeta_3) = -\frac{1}{39}\left(\frac{D}{2\pi}\right)^2 \ln\left(\frac{64\sin^2(5\pi f_C(\zeta_3))}{25\sin^2(8\pi f_C(\zeta_3))} R^1_{8,5}\right)$$

whence one can construct the trajectory for $\frac{I_7}{I_5}$

$$\left(\frac{I_7}{I_5}\right)_C(\zeta_3)=\left(\frac{5}{7}\right)^2\left(\frac{\sin\left(7\pi f_C(\zeta_3)\right)}{\sin\left(5\pi f_C(\zeta_3)\right)}\right)^2\exp\left(\frac{24}{39}\ln\left(\frac{64\sin^2\left(5\pi f_C(\zeta_3)\right)}{25\sin^2\left(8\pi f_C(\zeta_3)\right)}R_{8,5}^1\right)\right)$$

These two relations are used to complete the trajectories corresponding to the two closed curves in **Figure 5.5E**, are plotted below in **Fig A.5.5**, and are reproduced in **Figure 5.5D** as dashed model estimates. Note that by keeping $\frac{I_8}{I_5}$ constant, the disorder κ decreases from κ=4.0 nm^2 but is still lower than the initial state (a; κ~1.75 nm^2) at the end (d; κ~2.8 nm^2), which is reflected in the levels after the dip being slightly lower than before the dip in **Fig. A.5.5**.

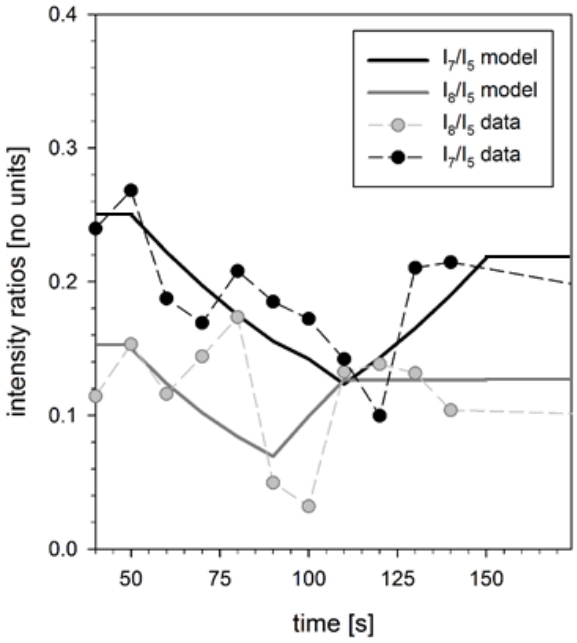

Fig A.5.5: Intensity ratio variation for measured $\frac{I_7}{I_5}$ (black symbols/dashed line) and $\frac{I_8}{I_5}$ (grey symbols/dashed line) (data from main text Fig. 5.5C), together with model predictions for $\frac{I_7}{I_5}$ (solid black line) and $\frac{I_8}{I_5}$ (solid grey line)

Parameter variation in Figs. 5.5D and A.5.5:

Stage	**O/D (*f*)** **[no units]**	**κ** **[nm^2]**	**I_7/I_5** **[no units]**	**I_8/I_5** **[no units]**
a→b	f_0	$\kappa_0 + \zeta_1(\kappa_1 - \kappa_0)$	$\left(\frac{I_7}{I_5}\right)_A(\zeta_1)$	$\left(\frac{I_8}{I_5}\right)_A(\zeta_1)$
b→c	$f_B(t) = f_0 + \zeta_2(f_1 - f_0)$	κ_1	$\left(\frac{I_7}{I_5}\right)_B(\zeta_2)$	$\left(\frac{I_8}{I_5}\right)_A(\zeta_2)$
c→d	$f_C(t) = f_1 + \zeta_3(f_0 - f_1)$	$\kappa(\zeta_3)$	$\left(\frac{I_7}{I_5}\right)_C(\zeta_3)$	$R^1_{8,5}$

Table A.5.1: Summary of the variation of overlap/D-period, disorder parameter κ, and the intensity ratios I_7/I_5 and I_8/I_5 across the loop in Figure 5.5E. The different equations for each segment (subscripted A, B, C) are given in full in the text below; lack of space prevents reporting of the full equation in the Table above. The ζ-variables are dimensionless time-variables varying from 0 to 1. Numerical values f_0, f_1 are overlap/D-period values with $f_0 = 0.466$ and $f_1 = 0.457$. Disorder parameter values are $\kappa_0 = 1.75$ nm^2 and $\kappa_1 = 4.00$ nm^2. Initial values for I_7/I_5 and I_8/I_5 (at a) are $(I_7/I_5)_0 \sim 0.25$ and $(I_8/I_5)_0 \sim 0.15$ respectively.

A.5.3: Intrafibrillar molecular packing and fibril orientation during stress relaxation

A.5.3A: Equatorial peak from intrafibrillar molecular packing:

Fig. A.5.6 shows the equatorial SAXS profile before and after subtraction of a diffuse background term (modelled as an exponential decay). After background subtraction, the equatorial peak corresponding to the intermolecular spacing d_m is clearly visible. The data can be fitted to a Gaussian profile, as shown in **Fig. A.5.6B**.

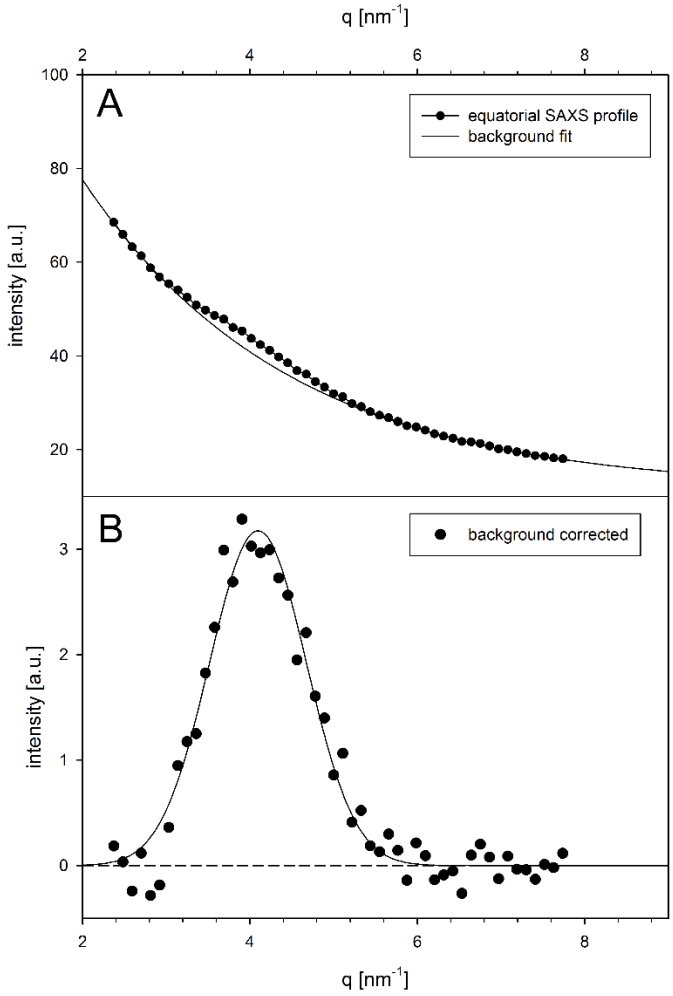

Fig A.5.6: Equatorial SAXS intensity profile for cartilage (at zero strain), before (a) and after (b) subtraction of the diffuse SAXS scattering. After subtraction, the equatorial peak is observed at q ~ 4.0 nm^{-1} corresponding to d_m ~ 1.5 nm, characteristic of the lateral intermolecular spacing in hydrated collagen[109].

A.5.3B: Variation of intermolecular spacing and fibril orientation:

Fibril orientation parameters (angular position and width) are obtained from $I(\chi)$ profiles as described in the main text, ***Materials and Methods***. Intrafibrillar molecular spacing d_m is obtained as described above in ***A.5.3A***. The variation of these parameters is shown in **Fig. A.5.7** below. **Figure A.5.7A** clearly shows that no reduction of d_m from wet to dry values occurs around the point of pre-strain reduction. Lastly, **Figure A.5.7B** shows no change in fibril orientation or width of the fibril angular distribution coinciding with the reduction in D-period.

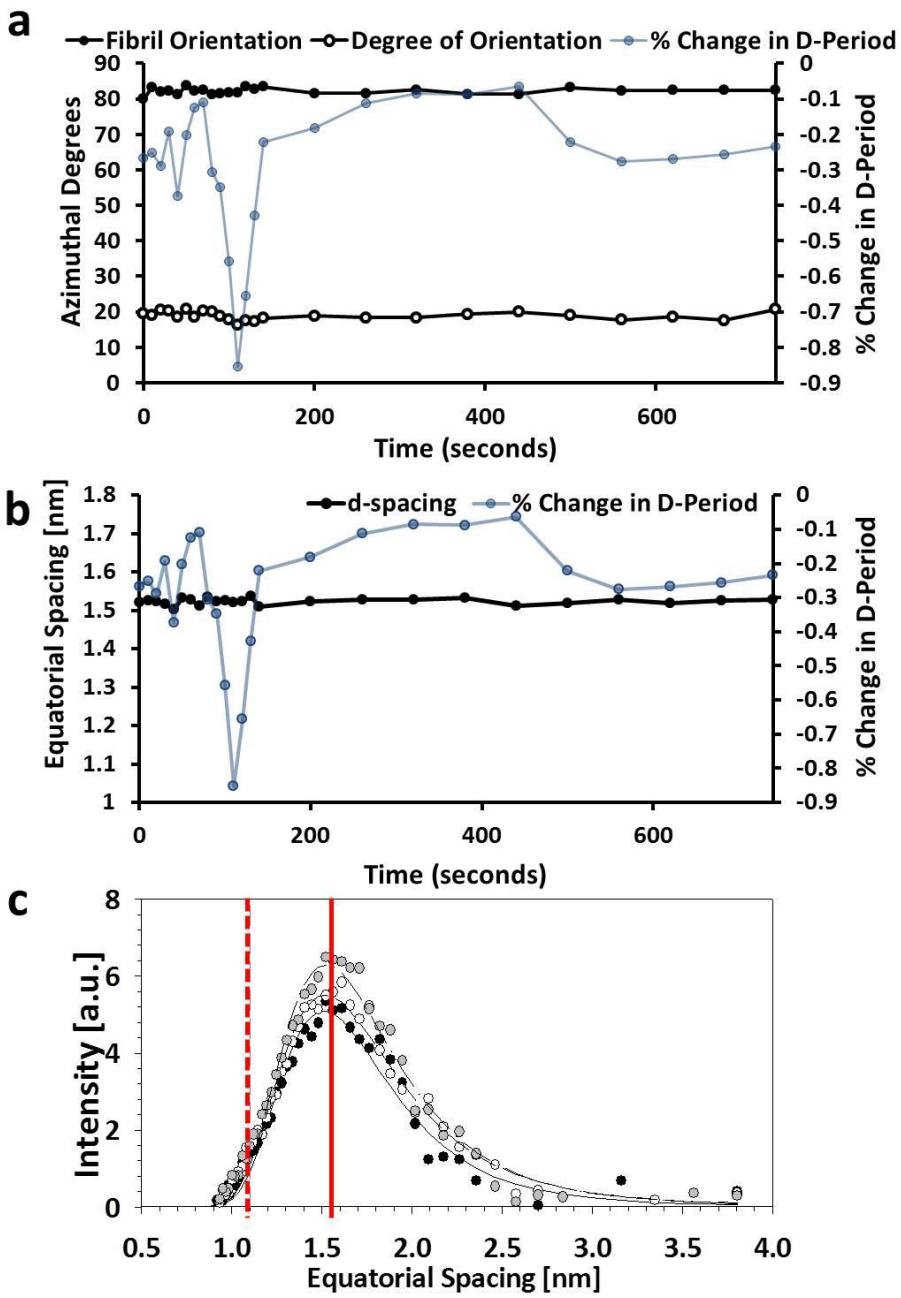

Fig A.5.7: A) Average fibril orientation (filled symbols) and angular width of the fibril distribution (open symbols) show little change at the minimum in D (gray line), B) Intermolecular spacing d_m, calculated from the peak position of the equatorial SAXS peak, plotted together with the D-period (analogous to Fig. 5.5A-B in main text). C) Equatorial SAXS peak intensity profiles It is observed that d_m remains consistently at d_m ~ 1.54 nm (solid vertical line) characteristic of wet collagen[109] (dashed line shows the value for dry collagen d_m ~ 1.1 nm), and does not change during the transient change in D (gray line). Note that the equatorial SAXS profiles are plotted with the abscissa transformed from wavevector (in which domain the Gaussian fit was performed) to equatorial spacing by $d = 2\pi/q$.